

The Analytical R-Matrix Approach to Strong Field Dynamics

vorgelegt von
B.Sc.(Hons) MAst
Lisa Tortina
Moskau, Russland

Von der Fakultät II – Mathematik und Naturwissenschaften
der Technischen Universität Berlin
zur Erlangung des akademischen Grades

Doktor der Naturwissenschaften
– Dr.rer.nat. –

genehmigte Dissertation

Promotionsausschuss:

Vorsitzende: Prof. Dr. Ulrike Woggon
Gutachterin: Dr. Olga Smirnova
Gutachter: Prof. Dr. Andreas Knorr
Gutachter: Prof. Dr. Dieter Bauer

Tag der wissenschaftlichen Aussprache: 4. Dezember 2015

Berlin 2016

ABSTRACT

In this thesis, we present a new theoretical framework for describing the electron dynamics induced when an atom or molecule is exposed to a strong low frequency laser field, focusing especially on strong field ionization. This process is at the heart of a wide variety of phenomena in the fast-developing field of attosecond science, and a good theoretical description is vital if we are to correctly interpret experimental results and understand the underlying physics. Obtaining such a description, however, poses a considerable challenge. The process is highly non-linear and although a number of methods have been developed to treat this problem, each is subject to its own limitations and caveats.

In light of this, we develop a flexible new approach to the problem, known as the Analytical R-Matrix (ARM) method. After reviewing the basic physics involved and the current theoretical state of the art, we introduce the central premise of ARM and present a first-principles derivation of its key equations. This is done first for a single-electron system and then extended to the multi-electron case – where we show how ARM can be used to describe correlation-driven excitations of the ion induced by the outgoing electron.

Having established the basic formalism, we move on to a more detailed investigation of the predictions of ARM and its physical interpretation. Focusing on circularly polarized fields, we study the effects of the ionic core on the outgoing electron and validate our theory by comparing our results with exact ab initio numerical calculations.

Finally, we proceed to apply ARM to analyze the physics behind a recently developed experimental technique known as the attoclock. This experiment aims to resolve tunnelling time delays in strong field ionization and its interpretation has attracted considerable controversy and heated debate. We show how the ARM method can be used to look inside the physics that takes place in such experiments and present a method for reconstructing ionization times from the physically measured observables. Doing so, we are able to unambiguously address the question of time delays and – by calibrating the attoclock for the one-electron case – open the way to study multielectron dynamics.

PUBLICATIONS

This cumulative thesis is based on the following publications.

- [A] L. Torlina, and O. Smirnova, Time-dependent analytical R-matrix approach for strong-field dynamics. I. One-electron systems, *Phys. Rev. A* **86**, 043408 (2012).
- [B] L. Torlina, M. Ivanov, Z. B. Walters, and O. Smirnova, Time-dependent analytical R-matrix approach for strong-field dynamics. II. Many-electron systems, *Phys. Rev. A* **86**, 043409 (2012).
- [C] L. Torlina, J. Kaushal, and O. Smirnova, Time-resolving electron-core dynamics during strong-field ionization in circularly polarized fields, *Phys. Rev. A* **88**, 053403 (2013).
- [D] L. Torlina, F. Morales, H. G. Muller, and O. Smirnova, Ab-initio verification of the Analytical R-Matrix theory for strong field ionization, *J. Phys. B: At. Mol. Opt. Phys.* **47**, 204021 (2014).
- [E] L. Torlina, F. Morales, J. Kaushal, I. Ivanov, A. Kheifets, A. Zielinski, A. Scrinzi, H. G. Muller, S. Sukiasyan, M. Ivanov, and O. Smirnova, Interpreting Attoclock Measurements of Tunnelling Times, *Nat. Phys.* **11**, 503-508 (2015).

ACKNOWLEDGMENTS

First and foremost, I would like to thank my supervisor Olga Smirnova, without whom none of this would have been possible. Thank you for introducing me to such a fascinating field, for your insights and our many stimulating discussions, for your support and encouragement, and for your endless enthusiasm. Your love of physics is inspiring and it has been a true pleasure working with you.

A big thank you also to my other main collaborators at MBI. I would like to thank Misha Ivanov for our many discussions and for always bringing fresh perspectives and new ideas: your wealth of knowledge, ability to see the bigger picture and optimism were invaluable. A very important thank you also to Felipe Morales for his amazing work on the numerical side of things: it was wonderful working with you and seeing it all come together thanks to your calculations.

More generally, I would like to thank Valeria for her friendship and for sharing so much of the PhD experience with me, Alex for being an amazing office mate, Maria for always being so lovely and taking care of everyone, Emilio for our spirited discussions, as well as Danilo, Lukas, Foudhil, Jivesh and the rest of the extended family for making my time at MBI what it was.

And last but not least, an immense thank you to my friends and family, who have supported me throughout and who, in my humble opinion, are some of the most brilliant people that there are. I hope you know who you are and how much you mean to me.

CONTENTS

i	INTRODUCTION AND SUMMARY OF PUBLICATIONS	1
1	INTRODUCTION	3
1.1	Why strong field ionization?	4
1.2	This thesis	5
2	THE PHYSICS OF STRONG FIELD IONIZATION	7
2.1	An observable and some observations	7
2.2	The photon picture	9
2.3	Some basic approximations	10
2.4	The tunnelling picture	12
2.5	A single active electron?	14
3	THEORETICAL APPROACHES	17
3.1	A tale of two potentials	17
3.2	Two- and three- step models	18
3.3	The Strong Field Approximation	29
3.4	SFA and the tunnelling picture	39
3.5	Coulomb effects in SFA	45
3.6	A new approach?	51
4	SUMMARY OF PUBLICATIONS	55
ii	THE PUBLICATIONS	65
A	Time-dependent analytical R-matrix approach for strong field dynamics. I. One-electron systems	67
B	Time-dependent analytical R-matrix approach for strong field dynamics. II. Many-electron systems	81
C	Time-resolving electron-core dynamics during strong field ionization in circularly polarized fields	93
D	Ab initio verification of the analytic R-matrix theory for strong field ionization	101
E	Interpreting attoclock measurements of tunnelling times	107
iii	CONCLUSIONS	119
5	CONCLUSIONS AND THE FUTURE	121
iv	APPENDIX	125
A	ATOMIC UNITS	127
	BIBLIOGRAPHY	129

Part I

INTRODUCTION AND SUMMARY OF
PUBLICATIONS

INTRODUCTION

This thesis starts with a very simple question. Imagine an atom or molecule – suppose, for now, that it's something simple like hydrogen or helium – and imagine that we shine some light on it. What happens? Though very simple to formulate, this question opens the door to a truly rich variety of physical phenomena, and in this thesis we will focus on exploring just a small subset of these.

Of course, the answer depends very much on the light. We know that at low to moderate field strengths, the atom-light interaction can be described as a one-photon process. In this regime, what happens relies critically on the energy of the photons, or equivalently, on the frequency of the light. If the photon energy coincides with the spacing between a pair of atomic energy levels, the atom can absorb a photon and become excited. If the photon energy exceeds the atom's ionization potential, an electron can be ejected. The latter is of course the photoelectric effect – a phenomenon studied since the earliest days of quantum mechanics. In this case, we know that the energy of the emitted photoelectron will be determined entirely by the frequency of the light and not by its intensity. Light of insufficiently high frequency will result in no ionization at all.

However, we can also ask what happens if we keep the frequency low but turn the intensity up. That is, what if rather than sending a few high energy photons at our atom, we bombard it with a large number at low energy instead? In this case, as we shall see, ionization can also occur. However, contrary to the standard photoelectric effect, this is no longer a linear process and it is possible to remove an electron even if the energy of each individual photon is insufficient to overcome the atom's binding potential. This will be the regime that we will focus on in this work.

In particular, we shall consider fields which are sufficiently strong for highly non-linear ionization processes to occur (without taking us into the relativistic regime), and frequencies well below the ionization threshold for the atom or molecule in question. To this end, we will focus on radiation in the visible and infrared range, with wavelengths of 450 nm and above, and with intensities of the order of 10^{14} W/cm². At such intensities, the field strength will be a few Volts per Angstrom – roughly an order of magnitude below the atomic field of the first Bohr orbit of hydrogen – and as a result the electronic structure of our bound states will only be slightly perturbed.

1.1 WHY STRONG FIELD IONIZATION?

Before we proceed, it is natural to ask why we should be interested in studying ionization in strong fields at all. At the most basic level, of course, investigating this regime is vital if we are to have a complete picture of atom-light interaction across all wavelengths and intensities. When the photoelectric effect was first observed, the light sources available were not powerful enough to drive non-linear ionization processes, and the physics of the time was naturally limited to the one-photon case. However, as laser technology developed and ever higher intensities became attainable, this restriction was lifted. Naturally, this raised many new questions in its stead. Can the photoelectric effect be generalized when many photons are involved? How can we understand quantum mechanics well away from the perturbative limit?

Going beyond this fundamental motivation, however, there has been a resurgence of interest in strong field ionization due to the prominent role it can play in the emerging field of attosecond science. An attosecond refers to a very short period of time indeed – 1 as = 10^{-18} s – and is the natural timescale for the motion of electrons in atoms, molecules and nanoscale structures. Ultimately, the goal of attosecond science is to image and control such electron dynamics in real time. This could involve, for example, tracking the motion of an electronic wavepacket to determine how a particular process proceeds, steering electrons within a chemical bond to control the reaction products, or time-resolving electron-electron interactions in a multielectron system. Since the motion of electrons is instrumental in nearly all processes in chemistry, biology and materials science, the ability to do so comes with far-reaching consequences indeed.

The interest in strong field ionization in the context of attosecond science is two-fold. Firstly, it stems from the experimental need for extremely short light pulses. Since pulse duration determines the fastest process that can be systematically measured, such pulses are vital for achieving the attosecond time-resolution needed to image electronic motion. In practice, one of the major ways in which attosecond pulses can be produced is via high harmonic generation (HHG) (e.g. see [1]). In this process, an electron is removed from an atom or molecule by strong field ionization and subsequently driven back to its parent ion where it recombines. Upon recombination, the excess energy the electron gained during its laser-driven travel in the continuum is emitted as light. The overall result is a very broad spectrum of radiation at odd harmonics of the driving frequency, which – given the right conditions – will produce a train of attosecond pulses in the time domain. Since strong field ionization is the first step in this process, it necessarily has a crucial role to play within attosecond science.

In addition to this, strong field ionization is itself one way in which electron motion can be initiated. This naturally leads one to ask whether we can time-resolve the resultant dynamics. Is it possible to follow the process of electron removal in real time? What can we learn about the subsequent evolution of the hole created in a multielectron system? How does the core rearrange itself once an electron has been removed? There have been a number of experimental techniques developed in recent years to address these questions, including high harmonic spectroscopy [2–6], attosecond transient absorption [7], laser-induced electron diffraction [8–10], holography [11] and the attoclock [12–14]. In each of these, electron motion is initiated by a strong field ionization process. The way in which dynamical information is subsequently deduced, however, varies considerably.

1.2 THIS THESIS

What each of the above experimental techniques has in common is the need for an excellent understanding of the underlying theory. Without this, it is not possible to extract the details of the dynamical process from the experimental observables. However, as we shall discuss, modelling strong field ionization presents a formidable challenge. Although a number of methods have been proposed to address this problem, each is subject to its own drawbacks and caveats.

In this thesis, we develop and explore a new approach to this problem. The framework we develop – known as the analytical R-matrix (ARM) – is general and flexible, and can be applied to arbitrary atoms and molecules across a broad range of pulse parameters within the strong field regime. As we shall see, the ARM method overcomes a number of limitations faced by other commonly used approaches, and in doing so will enable us to gain a deeper understanding of the physics behind some of the attosecond techniques discussed above.

The remainder of this thesis is structured as follows:

1. In Chapter 2, the basic physics behind strong field ionization is discussed, with a focus on experimental observations and physical pictures. The key approximations used when describing physics within the strong field regime are also presented.
2. Chapter 3 proceeds to examine the difficulties associated with modelling strong field dynamics theoretically, and provides an overview of current analytical approaches to this problem. Upon doing so, a number of concepts that play a central role in the context of ARM will be introduced.
3. Having established the current state of the art, Chapter 4 summarizes the key features of each of the papers upon which this thesis is based.

4. Following this, the publications themselves are presented:

- [A] The fundamental principles behind the ARM method are introduced, and key equations are derived for a one-electron system in a linearly polarized field.
- [B] The ARM method is extended to multielectron systems and a new correlation-driven ionization channel is proposed. The importance of such channels is explored for the ionization of N₂ and CO₂ molecules.
- [C] ARM is applied to long circularly polarized pulses and the effect of the electron-core interaction is investigated in detail.
- [D] The predictions of ARM are compared to ab initio numerical simulations for the ionization of hydrogen and helium.
- [E] The ARM method is used to analyse the attoclock experiment in detail. Based on this, a procedure is developed for reconstructing ionization times from the experimental observable, making it possible to study the dynamics involved with attosecond precision.

5. Finally, Chapter 5 concludes the thesis and discusses possible directions for future research.

1.2.1 A quick note on units

Throughout this thesis we will work in atomic units (a.u.), as specified by

$$m_e = 1, \quad e^2 = 1, \quad \hbar = 1, \quad k_c = \frac{1}{4\pi\epsilon_0} = 1, \quad (1.1)$$

where m_e and e refer to the mass and charge of an electron respectively, \hbar is Planck's constant divided by 2π , k_c is Coulomb's constant and ϵ_0 is the permittivity of free space. This will keep our equations as simple as possible. The relationship between atomic and S.I. units is summarized in Appendix A.

2

THE PHYSICS OF STRONG FIELD IONIZATION

2.1 AN OBSERVABLE AND SOME OBSERVATIONS

To investigate the physics that underlies ionization in strong fields, we will need a physical observable, and one of the most natural and informative choices we can make for this is the momentum distribution of the emitted photoelectrons – in other words, the angle- and energy- resolved photoelectron spectrum. This is a quantity that can be readily measured experimentally, and theoretically is simply related to the wavefunction expressed in momentum space. It will play a central role throughout this thesis. What will the photoelectron spectrum look like and what can it teach us about the underlying physics?

Let us first recall the standard photoelectric effect that we are familiar with. In the one photon case, Einstein's relationship tells us that the kinetic energy of the emitted electrons will be given by $E_k = \hbar\omega - I_p$, where ω is the angular frequency of the light and I_p is the binding energy of the atomic or molecular energy level in question. Based on this, when a single photon is absorbed, we would expect to see a single peak in the photoelectron spectrum, corresponding to the energy difference between the photon and the binding potential (or a series of peaks if a number of energy levels are accessible). If we were to decrease the frequency, the peak(s) would shift to lower energies, and eventually disappear entirely as the photon energy dropped below the ionization threshold for the most weakly bound electron. However, what if we now increase the intensity?

In fact, once the intensity becomes sufficiently high, we will again start to see ionization. Experimentally, this was first demonstrated in 1965 by Voronov and Delone who successfully ionized xenon ($I_p = 12.13$ eV) using a ruby laser (photon energy 1.78 eV) [15]. It is clear that, in this case, the process must involve the simultaneous absorption of several photons, and initially we might guess that the kinetic energy of the photoelectrons would now be given by $E_k^{\min} = N\hbar\omega - I_p$, where N is the minimum number of photons needed to overcome the ionization potential. This is the simplest generalization of the photoelectric effect: the electron absorbs just enough energy to break free from the atom and we measure the excess (some fraction of $\hbar\omega$) at the detector. Based on this, we would expect the photoelectron spectrum to consist of a single peak at E_k^{\min} . In Voronov and Delone's experiment, for example, this would correspond to $N = 7$.

However, when energy-resolved measurements of such processes were carried out, they revealed a different picture. In 1979, Agostini

et al [16] observed two discrete peaks in the photoelectron spectrum for xenon: one prominent peak at E_k^{\min} and another smaller peak at $E_k^{\min} + \hbar\omega$. This was soon found to be general. Photoelectron spectra were composed of a series of peaks, starting at E_k^{\min} and evenly spaced by the photon energy $E_k = (N + S)\hbar\omega - I_p$ [17–19]. This phenomenon was dubbed Above Threshold Ionization (ATI) [20], and has since been shown to be universal for all atoms and molecules.

2.1.1 ATI spectra

As we would expect, the precise shape of the ATI spectra depends strongly on the laser parameters.

In linearly polarized fields, early experiments at moderate intensities ($\sim 10^{11} - 10^{12} \text{ W/cm}^2$) did not find a drastic deviation from the simplest extension of the photoelectric effect mentioned above. In this regime, only a small number of ATI peaks are present, the peaks are well defined and they decrease in magnitude steadily starting from the dominant peak at E_k^{\min} [16–18]. At higher intensities ($\sim 10^{14} \text{ W/cm}^2$), however, the energy spectrum becomes considerably broader and acquires a more non-trivial shape. The distribution can extend out to several orders of magnitude above E_k^{\min} , individual peaks become less pronounced and a plateau develops at high energies [21, 22]. Angle-resolved measurements indicate that electrons are emitted primarily along the polarization axis, giving rise to a two-lobe structure in the angle-resolved spectrum, with finer features superimposed [22, 23].

In circularly polarized fields, the situation is notably different. Low energy electrons are strongly suppressed and photoelectron spectra are centred at considerably higher energies [24, 25]. If the pulse is relatively long, electrons are emitted uniformly at all angles in the plane of laser polarization and, as a result, the angle- and energy-resolved photoelectron distribution takes on a doughnut-like shape. For elliptically polarized fields, a situation intermediate between the linear and circular cases is observed (see e.g. [26]).

2.1.2 High Harmonic Generation (HHG)

Before we move on to examining the physics behind these observations, it is natural to mention another closely related phenomenon, which we have already touched upon in Section 1.1. Just like ATI, the process of high harmonic generation (HHG) is initiated by subjecting an atom or molecule to a strong low frequency laser field. However, in HHG, instead of detecting electrons, we measure the emitted light. Doing so reveals a broad spectrum of photon energies at odd harmonics of the driving frequency, which may at first glance seem reminiscent of the ATI peaks described above. Upon

closer inspection, however, we see that the basic shape of the high harmonic spectrum is qualitatively different: it falls off for the first few harmonics before forming a long plateau, which, in turn, is terminated abruptly at a sharp cutoff [27]. This basic shape is universal and – depending on the laser parameters and the atom or molecule in question – the plateau region can extend up to two orders of magnitude above the driving frequency (e.g. see [28, 29]). As discussed in Section 1.1, it is this very broad spectrum in the frequency domain that makes it possible to generate attosecond pulses using HHG. Empirically, using numerical simulations, the cutoff was shown to be well-approximated by $N_{\max} \omega = I_p + 3U_p$ [30]. Here, U_p is the ponderomotive energy, the average energy of electron oscillations in the laser field: $U_p = \langle E^2 \rangle / (2\omega^2)$, where $\langle E^2 \rangle$ is the cycle-averaged value of the electric field.

2.2 THE PHOTON PICTURE

With all of these experimental observations in hand, we are faced with the question of interpretation. How can we understand the physics behind strong field ionization?

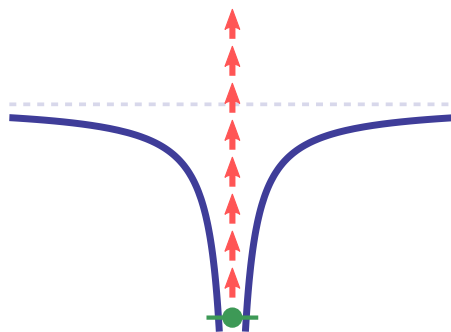


Figure 1: In the photon picture, we can understand strong field ionization as a multiphoton process. As illustrated here, the electron may absorb more photons than the minimum it needs for ionization. Each ATI peak corresponds to a different number of excess photons.

Within the photon picture, the basic process responsible for ATI seems clear: the electron has absorbed more photons than the minimum it needed to escape its parent atom or molecule. This is illustrated in Fig.1. Indeed, provided that the electron has gained sufficient energy to overcome the binding potential I_p , there is nothing to prevent it from undergoing higher order transitions in the ionization continuum [19]. Such processes were considered theoretically as early as 1965 [31], and constitute a natural non-linear generalization of the photoelectric effect. The suppression of low energy ATI peaks in circularly polarized fields can then be explained in terms of the angular momenta of the absorbed photons [25], as can the preferen-

tial ionization along the polarization axis in linearly polarized fields, which becomes more pronounced at higher orders [23].

The corresponding explanation of HHG is a simple extension of this [32]. In ATI, after absorbing $N + S$ photons, the electron carries the excess energy it has gained off towards the detector. In HHG, on the other hand, the electron instead recombines back into the bound state it departed from. Upon doing so, it emits its excess energy as a single photon of frequency $(N + S)\omega$. Assuming a symmetric potential, dipole selection rules imply that only odd harmonics are allowed, in line with observations [33].

In practice, however, as we move towards higher intensities, the photon picture soon starts to become less useful. As discussed in Section 2.1.1, ATI spectra become very broad indeed at intensities greater than $\sim 10^{13} - 10^{14} \text{ W/cm}^2$, extending out to very high orders in photon energy. In this regime, the number of photons involved is so great that any attempt to account for all possible absorption and emission processes quickly becomes impractical. Clearly, a different approach will be needed.

2.3 SOME BASIC APPROXIMATIONS

Luckily, there is another, completely different way in which we can describe the physics of strong field ionization, which will prove to be much more informative and useful in practice. In order to arrive at this description, however, we will need to rely on three basic approximations. As we shall see, these approximations are very well justified within the regime we study. As such, they underpin the overwhelming majority of current theoretical approaches to strong field phenomena, and we shall make use of them throughout this thesis.

1. Firstly, we shall work within the *semi-classical* approximation. That is, rather than speaking of photons, we shall describe light as a classical field, while treating the atom or molecule quantum mechanically. This is a good approximation provided that $F \gg (\omega^3 \Delta\omega)^{1/2}$, where F is the field strength of our light source, ω is its angular frequency and $\Delta\omega$ the bandwidth [34]. For the strong low frequency laser light we are concerned with, this approximation is very accurate indeed.
2. Secondly, we shall restrict ourselves to *non-relativistic* quantum mechanics. Relativistic effects start to come into play when $F/\omega \sim c$, where $c = 137$ is the speed of light in atomic units (e.g. see [33, 35]). At the infrared wavelengths we are interested in, this corresponds to intensities of 10^{18} W/cm^2 and above. Since we focus on ionization by fields of the order of 10^{14} W/cm^2 throughout this work, this approximation is very well justified.

Making these two approximations, the Hamiltonian for a single non-relativistic electron interacting with a classical electromagnetic field while in the presence of a binding potential $U(\mathbf{r})$ can be expressed as

$$H = \frac{1}{2}(\hat{\mathbf{p}} + \mathbf{A}(t, \mathbf{r}))^2 + U(\mathbf{r}), \quad (2.1)$$

where \mathbf{A} is the vector potential of our light field. Notice that while the momentum $\hat{\mathbf{p}} = -i\nabla$ is an operator, \mathbf{A} is an ordinary classical function here.

In fact, it turns out we can simplify our description of the light field further. Within the low frequency regime, the wavelengths of the light we are interested will be much greater than the typical length scales associated with atoms and molecules. As a result, the spatial variation of the electromagnetic field within our system will be very small.

3. This enables us to make our third approximation: the *dipole approximation*. In particular, we shall assume that $\mathbf{k} \cdot \mathbf{r} \ll 1$ and keep only the zeroth order term in the expansion of the vector potential \mathbf{A} in this quantity (here, \mathbf{k} is the wavevector for our light field and \mathbf{r} is a characteristic dimension of our system). Doing so, we find that \mathbf{A} depends only on time, and not on the spatial coordinate. This, in turn, implies that

$$\mathbf{B} = \nabla \times \mathbf{A} \approx 0. \quad (2.2)$$

That is, provided the wavelength remains large compared to the size of our system, we can neglect magnetic effects and approximate our light field as an oscillating spatially-homogeneous electric field. This will simplify our problem considerably.

Having approximated our light field in this way, we are free to choose a gauge for the vector potential \mathbf{A} in Eq.(2.1). This is typically done in one of two ways.

- (a) In the *velocity gauge*, we simply expand out (2.1) to obtain

$$H = \frac{\hat{\mathbf{p}}^2}{2} + \hat{\mathbf{p}} \cdot \mathbf{A}(t) + \frac{\mathbf{A}(t)^2}{2} + U(\mathbf{r}). \quad (2.3)$$

- (b) If we now multiply our wavefunction by the phase factor $\exp[-i\mathbf{A}(t) \cdot \mathbf{r}]$, this takes us to the *length gauge*. The Hamiltonian in this case becomes

$$H = \frac{\hat{\mathbf{p}}^2}{2} + \mathbf{r} \cdot \mathbf{E}(t) + U(\mathbf{r}), \quad (2.4)$$

where the \mathbf{E} is the electric field:

$$\mathbf{E} = -\frac{\partial \mathbf{A}}{\partial t}. \quad (2.5)$$

In both cases, we have a Hamiltonian of the form

$$H = \frac{\hat{p}^2}{2} + V_L(t) + U(r), \quad (2.6)$$

where $V_L(t)$ describes the interaction of the electron with the laser field.

Notice that in the length gauge, the Hamiltonian has a particularly simple form. It is the Hamiltonian for a particle subject to a binding potential $U(r)$ and a potential $\mathbf{r} \cdot \mathbf{E}(t)$, which varies linearly with \mathbf{r} since \mathbf{E} is spatially homogeneous. As we shall see below, this gives rise to a physical description of strong field ionization wholly different from the photon picture discussed in Section 2.2.

2.4 THE TUNNELLING PICTURE

Taking Eq.(2.4) as our starting point, consider an electron in the presence of two potentials: a binding potential and a potential which varies linearly with the spatial coordinate. As illustrated in Fig.2, the linearly varying potential effectively lowers one of the walls of the potential well, and the overall effect is the creation of a barrier. This, in turn, makes it possible to describe ionization as a tunnelling process.

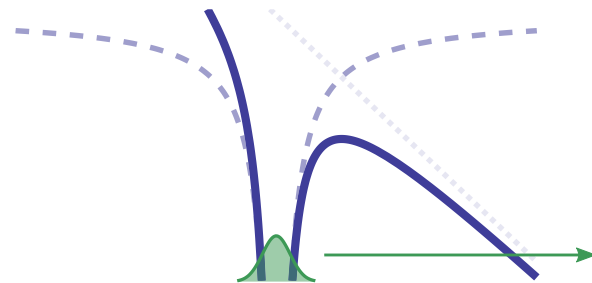


Figure 2: In the tunnelling picture of strong field ionization, the binding potential and laser potential together create a barrier. Ionization proceeds by the electron tunnelling under this barrier. Here we sketch a cut of the binding potential (dashed line), laser potential (dotted line) and total potential (solid blue line) along the direction of laser polarization at some instant in time when the laser field is near its maximum.

In this picture, the electron escapes its parent atom or molecule not by absorbing photons, but by passing under the barrier created by the laser field and the binding potential. The magnitude of $\mathbf{E}(t)$ determines the thickness of the barrier and hence the observed ionization rate: the thinner the barrier, the easier it is for the electron to tunnel out. The direction of $\mathbf{E}(t)$ determines the location of the barrier and hence the preferred tunnelling direction.

What sets this process apart from the standard tunnelling phenomena we are familiar with in quantum mechanics is that the barrier is

not stationary. Rather, as the electric field of the laser oscillates, the barrier oscillates with it. In a linearly polarized field, as \mathbf{E} changes its magnitude and sign, the barrier will periodically vary its thickness and appear and disappear on alternate sides of the potential well. This, in turn, will send bursts of electrons in opposite directions. In a circularly polarized field, on the other hand, the magnitude of \mathbf{E} is fixed and only its direction changes. The barrier will therefore maintain a constant width and rotate around the potential well. As a result, electrons will be emitted evenly in all directions in the plane of laser polarization. In an elliptically polarized field, we will have a combination of both: the barrier will rotate and change its width as it does so; a short circularly polarized pulse will produce a similar effect. Note that this immediately provides a qualitative explanation for some of the basic characteristics of photoelectron angular distributions discussed in Section 2.1.1.

As this brief discussion already suggests, the tunnelling picture provides us with a powerful yet conceptually simple way of thinking about strong field ionization. As the photon picture ceases to be useful, it gives us a new basis upon which to build our physical intuition, which is much more suited to the ionization regime we study. This is something we shall make use of throughout this thesis.

Going beyond the merely qualitative, the tunnelling picture has also given rise to a family of theoretical approaches which break the ionization process into two or three steps: the first involves quantum mechanical tunnelling and the second the propagation of classical electron trajectories in the continuum. A third step is possible if the electron subsequently revisits the atom and may involve recombination or scattering. We will discuss such models in detail in Section 3.2. It should be noted, however, that there is an important distinction between theoretical methods that explicitly assume and rely on tunnelling and those which merely make use of the tunnelling picture for their interpretation. The ARM method presented in this thesis falls into the latter category.

In fact, the tunnelling picture comes with one more important consequence. It tells us that by studying strong field ionization we are, in essence, studying tunnelling in a time dependent setting. This, in turn, is an intriguing prospect indeed since it presents the opportunity to time resolve this quantum mechanical process. How long does a particle take to pass under a barrier? Is tunnelling instantaneous, or is there an associated time delay? Such questions have been hotly debated since the early days of quantum mechanics and remain highly controversial to this day. The tunnelling picture suggests that strong field ionization could help us to find an answer, and thereby provides another important motivation for studying atom-light interactions in this regime. These questions are explored in detail in [E] in the context of the attoclock experiment.

2.5 A SINGLE ACTIVE ELECTRON?

Before we move on to a discussion of theoretical approaches, it is important to point out a fourth approximation we have made implicitly so far. In writing down a Hamiltonian of the form (2.1), we have effectively assumed that strong field ionization is a one-electron process.

In reality, of course, we know that a typical atom or molecule will contain many electrons. However, we can nevertheless describe strong field ionization using a Hamiltonian of the kind introduced in Section 2.3 if we work within the *single active electron* (SAE) approximation: that is, if we assume that only one of the electrons in our multielectron system participates actively in the ionization process. All other electrons are assumed to remain passive and fixed. They merely provide a background potential, which, together with the effect of the nucleus, is incorporated into $U(\mathbf{r})$.

Indeed, as a first approximation, the SAE approach works extremely well. To date, the majority of theoretical attempts to explain strong field phenomena have worked within this picture and have proven highly successful in doing so. However, there are nevertheless certain instances in which this approximation is clearly insufficient.

Double ionization is the classic example. Within the SAE approximation, we might try to describe double ionization as a sequential process: 1. first, one electron is removed, leaving behind a singly-charged ion in its ground state; 2. a second electron is subsequently removed from this ion at a later time. If the process is truly sequential, these two ionization steps are independent and can be treated as consecutive single-electron processes. The core is kept frozen during each step and no electron correlation effects are included. However, experimental evidence indicated that this cannot represent the full story: an excess of doubly charged ions was observed at low intensities incompatible with such a sequential SAE picture [36–38], with differences up to several orders of magnitude.

Two mechanisms were initially proposed to explain non-sequential double ionization:

1. A ‘shake-up’ process, in which the departing electron excites the ion as it departs [37, 39].
2. A recollision process, in which the first electron returns to the ion and rescatters inelastically [40].

While shake-up is the main mechanism in the single photon case, recattering was ultimately shown to dominate for strong low frequency fields [41, 42]. The first electron returns to the ion and either directly kicks out the second electron, or promotes it to an excited state from which it is readily ionized by the field [43]. Further experimental evidence suggested that the recollision was, in fact, creating doubly

excited states, from which both electrons ionize at approximately the same time [44].

Rescattering in non-sequential double ionization, however, is not the only way in which multielectron dynamics can arise in strong field ionization. Recent experiments in circularly polarized fields, for example, where the electron does not return to the core, found clear and substantial deviations from the predictions of sequential double ionization, which may be related to electron correlation [45, 46]. Furthermore, it is now well-established that, at least in the case of molecules, strong field ionization can generate ions in a superposition of different excited states, and not just in the ground state as originally supposed [3, 5, 47]. This, in turn, has given rise to a growing body of work concerned with studying the hole dynamics initiated by the ionization process. In light of this, it is interesting to note that, although negligible for small molecules, it was predicted that shake-up type processes could become important in larger molecules where the energy levels are more closely spaced [39]. Recent experimental evidence has indeed suggested that non-adiabatic excitations and electron interactions may play a role for N₂ [4].

In describing any of the scenarios above, it is clear that the SAE approximation cannot be used. Whether the ion is excited during the initial ionization step or during a recollision, electron-electron interactions play a crucial role and the core cannot be treated as frozen and fixed. What's more, from the perspective of attosecond science, these kinds of processes are hugely interesting. The problem of going beyond the SAE approximation is therefore an important one, though technically it continues to pose a considerable challenge.

In this thesis, we shall focus primarily on one-electron systems or work within the SAE approximation, in line with the vast majority of theoretical efforts to date. The important exception to this, however, is [B], where we show how the ARM method can be extended to multielectron systems and used to describe 'shake-up' type processes. Multielectron effects will also be considered in [E].

3

THEORETICAL APPROACHES

From a theoretical point of view, the problem of strong field ionization is hard. Effectively, as we saw in Section 2.3, our electron is subject to two potentials simultaneously: the attractive binding potential due to the atomic or molecular core and the potential of the laser field. Since our laser field is strong, neither of these can be said to be small in general, and accounting for both of these simultaneously is where the difficulty will lie.

3.1 A TALE OF TWO POTENTIALS

If we make the standard approximations as discussed in the previous chapter, we know that the Hamiltonian will be given by Eq.(2.6). That is, our electron feels the binding potential $U(\mathbf{r})$ and the laser potential $V_L(t)$, where V_L is large in general. How can we go about solving the corresponding Schrödinger equation $i\partial\psi/\partial t = H\psi$?

If only one of these two potentials were present, our method of solution would be relatively straightforward. For an electron subject only to a binding potential $U(\mathbf{r})$, the problem reduces to solving the time-independent Schrödinger equation. In the most basic case of hydrogen or hydrogen-like atoms, we simply have the Coulomb potential $U(\mathbf{r}) = -Q/r$. The exact analytical solution in this case is one of the standard results of quantum mechanics and can be found in any undergraduate textbook. For sufficiently large r , we have

$$\psi_{klm}(\mathbf{r}) = \kappa^{3/2} \frac{e^{-\kappa r}}{\kappa r} (\kappa r)^{Q/\kappa} Y_{lm}(\theta, \phi), \quad (3.1)$$

where Y_{lm} are the spherical harmonics. For more complicated potentials, exact analytical results are typically no longer possible, especially when multiple electrons are involved. However, in this case we can nevertheless turn to one of the well established numerical techniques developed in the quantum chemistry community.

Conversely, if the electron were moving in the presence of a laser field only, we would also be able to write down an exact analytical solution. Such solutions are known as *Volkov states* [48], and in the length gauge take the form

$$\psi_p^V(T; t, \mathbf{r}) = \langle \mathbf{r} | \mathbf{p}_T^V(t) \rangle = \frac{1}{(2\pi)^{3/2}} e^{i(\mathbf{p} + \mathbf{A}(t)) \cdot \mathbf{r}} e^{iS_V(T, \mathbf{p}; t)}, \quad (3.2)$$

where S_V is the Volkov phase

$$S_V(T, \mathbf{p}; t) = \frac{1}{2} \int_t^T d\tau (\mathbf{p} + \mathbf{A}(\tau))^2, \quad (3.3)$$

and T is an arbitrary constant. When we make use of these states later on, it will be convenient to set T equal to our observation time, so that $S_V = 0$ at the detector. Notice that these states look a lot like the plane wave solutions we are familiar with for a free particle: $\langle \mathbf{r} | \mathbf{p}(t) \rangle = e^{i(\mathbf{p} \cdot \mathbf{r} - Et)}, |\mathbf{p}(t)\rangle = e^{-iEt} |\mathbf{p}\rangle$. The only difference here is that both momentum and energy have become time-dependent. Making use of this notation, we can express the Volkov states as

$$|\mathbf{p}_V^V(t)\rangle = e^{iS_V(T, \mathbf{p}, t)} |\mathbf{p} + \mathbf{A}(t)\rangle, \quad (3.4)$$

where $|\mathbf{p} + \mathbf{A}(t)\rangle$ is the free particle basis state $\langle \mathbf{r} | \mathbf{p} + \mathbf{A}(t) \rangle = e^{i(\mathbf{p} + \mathbf{A}(t)) \cdot \mathbf{r}}$.

With either of these solutions in hand, if the other of our two potentials were small, we would again be on familiar ground. In that case, we could solve for the wavefunction of the electron using standard perturbative techniques, by breaking our Hamiltonian up as $H = H_0 + V'$, and expanding about the known solution for H_0 . However, in the case of strong field ionization, this is not the case: neither $U(\mathbf{r})$ nor $V_L(t)$ can be neglected or treated perturbatively everywhere and at all times. Solving this problem, therefore, will require a fundamentally different approach.

At present, the analytical methods used to study strong field phenomena can be roughly divided into two main categories: those which assume tunnelling and break the ionization process into two or more steps, and those based on what is known as the Strong Field Approximation (SFA). The main features, advantages and limitations of each of these will be discussed in the remainder of this chapter.

In addition to this, considerable progress has been made in developing ab initio numerical techniques for solving the time-dependent Schrödinger equation (TDSE) directly. For an overview of such numerical approaches, we direct the reader to [35, 49]. Within this thesis, we will use the results of exact ab initio simulations to validate our ARM theory and to provide ‘experimental’ data for further analysis. However, the focus throughout this work will be on analytical methods. Although inherently approximate, these methods are much less computationally intensive and, importantly, will enable us to look inside the process of ionization in a way that purely numerical calculations cannot.

3.2 TWO- AND THREE- STEP MODELS

As mentioned in Section 2.4, the tunnelling picture has inspired a series of theoretical approaches to strong field phenomena based on breaking up the process into two or three steps, and treating each on a different footing [40, 50–52]. Such models are also commonly referred to as ‘semiclassical’, not to be confused with the semiclassical approximation discussed in Section 2.3.

3.2.1 The first step

The first step in any model of this kind is tunnel ionization, in which the electron escapes its parent atom by passing under the barrier created by the laser field and the binding potential. This process is typically treated quasistatically. That is, the shape of the barrier is assumed to change negligibly during the ionization process, which makes it possible to work within the adiabatic approximation. The probability of ionization at any given time t is then simply given by instantaneous expression

$$P(t) = w_{DC}(E(t)) dt, \quad (3.5)$$

where $w_{DC}(E)$ is the tunnelling rate for the atom or molecule in the presence of a static electric field E . Clearly, this approximation is justified for low frequency fields, where the electric field $E(t)$ varies slowly with time.

More specifically, the validity of the quasistatic tunnelling picture is captured by the *Keldysh parameter* [53]:

$$\gamma = \frac{\omega}{F} \sqrt{2I_p}, \quad (3.6)$$

where ω is the frequency of the laser source, F is its field strength (the amplitude of $E(t)$) and I_p is the ionization potential of the bound state from which the electron departs. In the limit of small γ , Keldysh demonstrated that ionization is well described by a quasistatic tunnelling process [53]. This $\gamma \ll 1$ regime is commonly referred to as the tunnelling limit. Conversely, $\gamma \gg 1$ has come to be known as the multiphoton regime. Recalling our discussion of ATI spectra for linearly polarized fields in Section 2.1.1, the multiphoton regime generally encompasses the situations in which a few well-defined ATI peaks are observed, while the tunnelling limit is associated with the very broad distributions recorded at higher intensities where individual ATI peaks are washed out. Noting that the width of the barrier can be estimated by I_p/F and that $\kappa = \sqrt{2I_p}$ is the characteristic electron momentum of the bound state, we can think of γ as the ratio of the oscillation period of the laser field and the classical time the electron would have taken to traverse the tunnelling barrier given its atomic velocity, had it been allowed to do so in classical mechanics.

In practice, the static tunnelling rate is typically calculated using the approximate analytical expression obtained in [54] by Ammosov, Delone and Krainov (ADK) using the original results of Popov, Perelomov and Teren'tev [55]. It is valid for atoms and atomic ions in the limit where the electric field of the laser is weak compared to the characteristic intra-atomic field strength: $F \ll \kappa^3$ [55]. In essence, this condition implies a thick tunnelling barrier and ensures that we stay well away from the barrier-suppression regime (where the electron

escapes over the barrier rather than tunnelling through it). Modifications to extend this to molecules [56] and stronger fields [57] have since been proposed.

In fact, if we are only interested in determining the total ionization yield, then this is all we need. In this case, we simply average $w_{DC}(E(t))$ over the laser cycle and obtain

$$w_{lin}(F) = \frac{3F}{\pi\kappa^3} w_{DC}(F), \quad w_{circ}(F) = w_{DC}(F) \quad (3.7)$$

for linearly and circularly polarized fields respectively [55]. However, if we are to explain the details of the angle- and energy- resolved photoelectron spectra, it will be necessary to consider what happens to the electron next.

3.2.2 The second step

In the second step, the free electron moves off towards the detector or comes back to its parent ion (where it will ultimately rescatter or recombine). In contrast to the tunnelling step, this motion is described classically: that is, once it emerges from the tunnelling barrier, the electron is assumed to obey classical equations of motion.

In order to proceed, however, we must of course first specify the initial conditions. What is the position and momentum of the electron when it first appears in the continuum? Unfortunately, as we shall see in Sections 3.2.5 and 3.2.6, there is no clear and straightforward answer to this question. Nevertheless, making the simplest possible choice for both the initial conditions and for the equations of motion, we can already learn a great deal.

3.2.3 The simpleman model

In the most basic implementation of the two- or three- step approach, commonly referred to as the *simpleman model*, the electron is assumed to start its classical motion at the origin (which coincides with the location of its parent atom or molecule) with an initial velocity of zero:

$$\mathbf{r}(t_i) = 0; \quad \mathbf{v}(t_i) = 0. \quad (3.8)$$

Here, t_i is the moment of ionization, understood as the instant at which the electron appears in the continuum. These initial conditions were originally justified by comparing the predictions of the simpleman model with the results of ATI experiments [40, 51], and represent the simplest possible choice we can make.

Subsequent electron dynamics are then described using the classical equations of motion for a particle moving in an oscillating electric field. Both the magnetic field of the laser and the electric field of the parent ion are neglected here to keep the picture as simple as

possible. The former is justified via the dipole approximation as discussed in Section 2.3. The latter is a good approximation for strong fields once the electron has left the immediate vicinity of the atom or molecule. This same approximation will play a central role in the second major family of approaches to strong field physics discussed in Section 3.3.

Explicitly then, within the simpleman model, the motion of our classical electron is governed by

$$\frac{d\mathbf{v}}{dt} = -\mathbf{E} = \frac{d\mathbf{A}}{dt}, \quad (3.9)$$

where in the second equality we have used Eq. (2.5). The velocity of the electron is then simply given by

$$\mathbf{v}(t) = \mathbf{p} + \mathbf{A}(t), \quad (3.10)$$

where \mathbf{p} is a constant.

Essentially, we can think of \mathbf{p} as the drift momentum of our electron, which is superimposed on the oscillatory motion due to the field, given by $\mathbf{A}(t)$. At the detector, after the laser pulse has been switched off, the vector potential will vanish and only the drift momentum will remain. As a result, this is the quantity that will be measured experimentally.

Our initial condition $\mathbf{v}(t_i) = 0$, fixes the value of \mathbf{p} ; it tells us that

$$\mathbf{p} = -\mathbf{A}(t_i). \quad (3.11)$$

Notice that, as a result, \mathbf{p} is an explicit function of the ionization time t_i here, and as such directly encodes the details of the tunnelling process. This fact underpins the basic premise of the attoclock experiment, discussed in detail in [E], where this relationship is used to time-resolve ionization.

3.2.3.1 A photoelectron spectrum

Based just on the above equations, our simple model can already tell us a lot. According to the first step:

1. For any given ionization time t_i , the magnitude of the electric field $E(t_i)$ determines the thickness of the tunnelling barrier and tells us the probability that the electron departed at this instant via Eq.(3.5). In other words, it determines the ionization yield associated with a given t_i .
2. The direction of $\mathbf{E}(t_i)$ tells us the most probable tunnelling direction: the barrier is thinnest in direction $-\mathbf{E}$. Within the simpleman model, this is irrelevant since the electron is assumed to start its continuum motion at the origin. In more sophisticated models, however, $\mathbf{E}(t_i)$ can be used to define the location of the barrier exit, which determines the initial condition $\mathbf{r}(t_i)$ (see Section 3.2.5).

At the same time, Eq.(3.11) fixes the momentum we expect the electron to have when we measure it. Consequently,

3. The direction of \mathbf{p} determines the angle of detection associated with ionization time t_i .
4. The magnitude of \mathbf{p} gives us the kinetic energy $E_k = p^2/2$.

Thereby, by scanning across all possible ionization times t_i , Eq.(3.5) and Eq.(3.11) together allow us to build up an angle- and energy-resolved photoelectron spectrum based on this simple model. Note that upon inverting Eq.(3.11), there may be more than one associated ionization time t_i for any given \mathbf{p} measured at the detector.

The formulation of the simpleman model introduced above is general and can be applied for laser pulses of arbitrary polarization and duration. For illustrative purposes, let us explicitly consider long linearly- and circularly- polarized pulses.

3.2.3.2 Long linearly polarized pulse

Suppose we have long pulse linearly polarized along the z-axis:

$$\mathbf{E}(t) = F \cos(\omega t) \hat{\mathbf{z}}. \quad (3.12)$$

In the simpleman picture, the drift momentum of the electron would then be given by

$$\mathbf{p} = -\mathbf{A}(t_i) = \frac{F}{\omega} \sin(\omega t_i) \hat{\mathbf{z}}. \quad (3.13)$$

Using our second initial condition $\mathbf{r}(t_i) = 0$, we have the corresponding electron trajectory:

$$z(t) = p_z(t - t_i) + \frac{F}{\omega^2} (\cos(\omega t) - \cos(\omega t_i)). \quad (3.14)$$

In this case, the magnitude of the electric field oscillates with time. Consequently, recalling that $E(t_i)$ determines the ionization probability, we would expect ionization to occur in bursts, centred about the times $t_i = 0, \pm\pi/\omega, \pm2\pi/\omega, \dots$ where $E(t)$ attains its maximum.

At these times, $\mathbf{p} = 0$ so the photoelectron spectrum should have a peak at zero kinetic energy. From Eq.(3.13), we also see that the p must range between 0 and F/ω , which tells us that the energy distribution must have a cutoff at $E_k^{\max} = 1/2(F/\omega)^2 = \langle E^2 \rangle / \omega^2 = 2U_p$, where U_p is the ponderomotive energy introduced in Section 2.1.2. Recalling our discussion in Section 2.1.1 we see that, at least at low energies, the overall shape is qualitatively similar to the experimentally observed ATI spectra. However, the plateau observed at higher energies, which extends the energy distribution out beyond $2U_p$, is missing here (e.g. see [21]). We will discuss the origin of this shortly.

In terms of the angular distribution, Eq. (3.13) tells us that electrons will be emitted along the plane of laser polarization: the angle of detection will switch from $+z$ to $-z$ as the sign of \mathbf{p} changes (note that, depending on the quarter cycle, this will either be the same or opposite to the tunnelling direction). Roughly speaking, this coincides with the observed two lobe structure for linearly polarized fields discussed in Section 2.1.1. Note, however, that in this very simple model, while the energy spectrum has a finite width and a non-trivial shape, the angular distribution is essentially a delta-function.

3.2.3.3 Long circularly polarized pulse

Consider now a circularly polarized field polarized in the x - y plane. If

$$\mathbf{E}(t) = F(-\sin(\omega t), \cos(\omega t)), \quad (3.15)$$

the drift momentum will be

$$\mathbf{p} = -\mathbf{A}(t_i) = \frac{F}{\omega}(\cos(\omega t_i), \sin(\omega t_i)), \quad (3.16)$$

and the corresponding electron trajectory takes the form

$$x(t) = p_x(t - t_i) - \frac{F}{\omega^2}(\sin(\omega t) - \sin(\omega t_i)) \quad (3.17)$$

$$y(t) = p_y(t - t_i) + \frac{F}{\omega^2}(\cos(\omega t) - \cos(\omega t_i)). \quad (3.18)$$

We immediately see that the situation in this case is quite different. The magnitudes of both \mathbf{E} and \mathbf{p} are now fixed in time. The former tells us that electrons will be emitted at a constant rate as the electric field rotates. The latter implies that the kinetic energy distribution will consist of a single spike at $E_k = 1/2(F/\omega)^2 = \langle E^2 \rangle / (2\omega^2) = U_p$. The angle at which the electrons will be detected is now given by

$$\theta_{\text{det}} = \theta_p = \tan^{-1} \left(\frac{p_y}{p_x} \right) = \omega t_i, \quad (3.19)$$

which varies at a constant rate with the time of ionization. Putting these facts together, we see the angle- and energy- resolved photoelectron spectrum must now be a thin ring with radius $1/2(F/\omega)^2$ and of equal height everywhere. Again, roughly speaking, this reproduces the doughnut-like photoelectron spectrum we saw for circularly polarized fields in Section 2.1.1.

Notice that this is the opposite situation to the linearly polarized case: we now have a non-trivial angular distribution, while the energy spectrum has reduced to a delta-function. To put it another way, for circularly polarized fields, ionization time is mapped into angle rather than energy. Within the simpleman model, this mapping is exceedingly simple. As we see from Eq.(3.19), the angle of detection is directly proportional to the time of ionization. It will be this mapping

that underpins the attoclock experiment, which we analyse in detail in [E].

As a final remark, note that for any given ionization time t_i , the drift momentum \mathbf{p} is always perpendicular to $\mathbf{E}(t_i)$. We therefore expect to detect the electron in a direction perpendicular to its tunnelling direction.

3.2.4 A possible third step

In the simpleman picture discussed above, we have neglected the atomic or molecular ion after the ionization step. It is as if the atom or molecule vanishes completely as soon as the electron has tunnelled out from its bound state. Clearly, at least to first approximation, this picture will be adequate if the electron rapidly moves away from its parent ion and never returns. Indeed, as we can deduce from Eqs. (3.17) and (3.18), this is always the case for circularly polarized fields.

For linearly polarized fields, however, this is not always so. Using Eq. (3.14), we find that when ωt_i is in the first or the third quadrant, trajectories will at some time again pass through $\mathbf{r} = 0$. In this case, neglecting the ion is certainly not justified. Upon re-encountering its parent atom or molecule, we know that the electron can either rescatter or recombine and release a photon. Fortunately, it is possible to incorporate such effects into the simpleman model by adding a third step.

In particular, for any given trajectory $\mathbf{r}(t; t_i)$ associated with ionization time t_i , we can deduce a lot if we know the velocity \mathbf{v}_r the electron has when it returns to the ion. In the case of HHG, the electron will radiatively recombine and emit a photon of energy $E_r + I_p$, where $E_r = v_r^2/2$ is the electron's kinetic energy at the time of return. If it rescatters instead, \mathbf{v}_r will determine the details of the rescattering process. In practice, finding \mathbf{v}_r within the simpleman model is straightforward: we simply solve $\mathbf{r}(t_r; t_i) = 0$ for the return time t_r and evaluate the corresponding velocity $\mathbf{v}_r = \mathbf{v}(t_r; t_i) = \mathbf{p}(t_i) + \mathbf{A}(t_r)$.

Doing so, we find that there is a maximum recombination energy E_r^{\max} , which depends on the frequency and intensity of the laser field. This, in turn, directly yields the location of the cutoff in HHG: $N_{\max} \omega = I_p + E_r^{\max}$. By running many classical trajectories, it was possible to show that $E_r^{\max} \approx 3.17U_p$ [40, 52], which is in excellent agreement with the empirically derived relation presented in Section 2.1.2.

Rescattering can be treated in a similar way. Taking into account the velocity of the returning electron upon impact, and considering both elastic and inelastic collisions, it was shown [21, 40, 58] that rescattering gives rise to electrons with energies much greater than the $2U_p$ cutoff we found for linear fields in Section 3.2.3.2. Indeed, it is now well established that rescattered electrons are responsible

for the high energy plateau in ATI spectra discussed in Section 2.1.1. Furthermore, taking into account the energy of the returning electron and considering inelastic collisions, it is possible to make predictions regarding non-sequential double ionization [40], discussed in Section 2.5.

3.2.5 Going beyond the simpleman

Given its highly primitive nature, the simpleman model works remarkably well. As we have seen, it successfully reproduces the basic features of both ATI and HHG spectra – offering qualitative if not quantitative agreement – correctly predicts the location of the cutoff in HHG, and has been able to explain the high energy plateau in ATI as well as non-sequential double ionization in terms of electron rescattering. The side lobe structures observed in angle-resolved ATI spectra have also been addressed in terms of electron recollisions using this simple approach [59]. Despite these successes, however, it is clear that the simpleman model provides us with a rather crude picture. It captures the essence of the basic physics, but cannot offer quantitative agreement in general.

In light of this, more sophisticated versions of the two- and three-step approach have been developed (e.g. see [14, 60–70]). Typically, in such models:

1. The interaction of the outgoing electron with the parent ion is no longer neglected in the second step: the electron is described as a classical particle moving in the presence of both an oscillating electric field and the attractive Coulomb potential of the core.
2. Rather than starting the electron's classical motion at the origin $\mathbf{r} = 0$, electron trajectories are assumed to begin at the tunnel exit. The electron therefore starts at some distance from the ion, rather than directly on top of it. This is clearly necessary if Coulomb interactions with the core are to be included. Note that the precise location of the tunnel exit is model dependent – it is intimately linked to the way in which the tunnelling step is described.
3. Many electron trajectories are propagated for each ionization time t_i , weighted by some probability distribution.

In the simpleman model, we assumed a unique set of initial conditions for an electron that appears in the continuum at any given time t_i : $\mathbf{r}(t_i) = 0, \mathbf{v}(t_i) = 0$. These, in turn, gave rise to a single classical trajectory. From the point of view of quantum mechanics, however, something is amiss here: the Heisenberg uncertainty principle tells us that we cannot simultaneously

know both the position and momentum of a particle with perfect precision.

In light of this, we can instead consider a distribution of initial positions and, more commonly, velocities for the electron wavepacket at the exit of the tunnelling barrier (the particular shape of the distribution will again depend strongly on the model). This will generate a set of electron trajectories, weighted by the probability for each pair of initial conditions, which can be propagated according to the classical equations of motion. Doing so ensures that the photoelectron distribution has a non-trivial width, in contrast to what we saw for the simpleman model.

Clearly, the critical step here is describing the electron wavepacket at the barrier exit – in other words, specifying a distribution of initial conditions $\{r(t_i), v(t_i)\}$ for classical propagation. Indeed, this is the primary way in which models of this sort differ from each other. Some of the most common choices are discussed below.

3.2.5.1 The barrier exit

The exit of the tunnelling barrier is often estimated by assuming the electron tunnels in the direction of the field [60, 62–64]. This gives rise to a simple 1D picture: if r is the coordinate in the tunnelling direction and $E(t_i)$ is the magnitude of the field at time t_i , the exit of the barrier should solve $rE(t_i) - U(r) = I_p$. For a Coulomb potential of the form $U(r) = -Z/r$, for example, this implies

$$r_{\text{exit}} = \frac{I_p + \sqrt{I_p^2 - 4ZE(t_i)}}{2E(t_i)}. \quad (3.20)$$

For a short range potential, $U(r) = -\delta(r)$, or in the limit of relatively weak fields, $F \ll I_p$, this reduces to

$$r_{\text{exit}}^0 = \frac{I_p}{E(t_i)}. \quad (3.21)$$

However, a different expression for the barrier exit is obtained if the tunnelling problem is instead considered in parabolic coordinates. This is one of the key features of the recently developed TIPIS model, for example, which also takes into account Stark shifts of the bound state and the induced dipole of the ion [14, 68]. Within this model, the barrier exit takes the form

$$r_{\text{exit}} = \frac{I_p + \sqrt{I_p^2 - 4\beta_2 E(t_i)}}{2E(t_i)}, \quad (3.22)$$

where $\beta_2 = Z - (1 + |m|)\sqrt{I_p/2}$ and the ionization potential $I_p = I_p(E)$ varies with the field strength. This expression has, in turn, been

shown to give rise to a notably different angular distribution for ionization by nearly-circularly polarized pulses [14].

Note that, typically, only a single value is assumed for r_{exit} for each t_i , since it is not immediately clear what the shape and width of a distribution in the exit coordinate should be. There are exceptions to this, however – for example, a Gaussian distribution of width $(2E)^{-1/3}$ was used in [61].

3.2.5.2 An initial velocity distribution

The initial distribution of velocities perpendicular to the laser polarization (and hence to the tunnelling direction) – commonly referred to as the transverse or lateral velocity distribution – is almost universally assumed to coincide with the result presented in [71]. Experiments have indeed shown good (though not always perfect) agreement with this picture, especially when interactions with the ion are taken into account [62, 72].

The longitudinal velocity distribution – that is, the velocity parallel to the field polarization – is considerably less straightforward since the electron is accelerated by the field as it tunnels out [73]. It is often assumed to be identically zero, with no distribution about this value [60, 63, 65, 68, 70]. Exceptions again exist, however: for example, a Gaussian distribution about zero was used in [61, 64], different values were tested in [62], and it was claimed in [69] that using a non-zero initial longitudinal velocity gives better agreement with experimental results.

3.2.5.3 An alternative description of the tunnelling step

Finally, it is worth mentioning another branch of approaches, based on a quasi-classical description of the tunnelling step and known as Classical Trajectory Monte Carlo with Tunnelling (CTMC-T) [66, 67]. These use a microcanonical ensemble to represent the initial bound state, and allow tunnelling to occur at the classical turning points with a probability based on the WKB approximation. It is assumed that tunnelling occurs instantaneously and that the electron continues its motion in the continuum with the same velocity it had prior to tunnelling. Essentially, this corresponds to yet another set of probability-weighted initial conditions for classical propagation.

3.2.6 Strengths and limitations

Improved two- and three- step models of the kind discussed above have proven highly successful on a number of fronts. They have been able to explain numerous strong field phenomena using a highly intuitive and transparent physical picture and achieved quantitative agreement with experimental results in many instances. For ex-

ample, this has included double ionization [61], frustrated tunnelling [63], low energy structures in ATI spectra [64, 65], Coulomb focussing [60, 62] and the shape of the transverse momentum distribution [67, 74], among others. Importantly, the classical computations involved are considerably more tractable compared with solving the fully quantum TDSE problem directly, and tend to offer much more physical insight. Moreover, these models are well-suited for describing electron rescattering and double ionization, and – unlike the SFA approach we shall discuss in Section 3.3 – can readily account for the Coulomb potential of the core both during the tunnelling step and in the continuum.

However, they also come with a number of fundamental limitations. One of the most significant, which has been mentioned already, is the problem of specifying initial conditions when the quantum and classical steps are matched. Although this issue has received considerable attention, there is an inherent ambiguity here. We are, in essence, breaking up what is a single quantum process in an artificial way, and proceeding to treat the two parts using entirely different physics. Unavoidably, then, the initial conditions must be chosen in an ad hoc manner. This problem is particularly important since the predictions of two- and three- step models can be highly sensitive to the initial conditions used. For example, simulations in [62] indicated that the degree of Coulomb focussing depends critically on the initial longitudinal velocity assumed for the electron, while [68] showed that the final momentum distribution for a short elliptically polarized pulse is highly sensitive to whether Eq.(3.20) or Eq.(3.22) is used for the barrier exit. Turning the problem around, this sensitivity could be used to empirically estimate the correct initial conditions based on experimental data – indeed, this was done in [69]. Nevertheless, all reconstructions of this kind remain fundamentally model-dependent.

In addition to this, there are inherent limitations associated with working within the tunnelling picture. As discussed in Section 3.2.1, the first ionization step is treated quasistatically: the probability of ionization is given by the static tunnelling rate associated with the magnitude of the laser field at that instant. Necessarily, therefore, non-adiabatic effects will be missed by this description. Since such effects should become more prominent at higher frequencies, where the barrier oscillates more rapidly, models of this kind are fundamentally restricted to the long wavelength limit or, more precisely, the limit $\gamma \ll 1$.

Furthermore, the tunnelling description of ionization, at least in its original form, is very much based on a single-electron picture. Although recollision-induced multielectron processes can be taken into account during the classical propagation step, it is not clear, for example, how ionic excitations during the ionization step (cf. shake-up, see Section 2.5) could be incorporated.

3.3 THE STRONG FIELD APPROXIMATION

The other main branch of theoretical approaches to strong field ionization (besides numerically solving the TDSE) is based on a set of closely related theories, originally developed by Keldysh [53], Perelomov, Popov and Terent'ev [55, 75], Faisal [76] and Reiss [77]. Together, these are commonly referred to as KFR or the Strong Field Approximation (SFA).

Unlike the two- and three- step models discussed in the previous section, the SFA approach, does not, from its outset, make any assumptions about the process that underlies ionization. In particular, it does not rely on the tunnelling picture. Rather, it starts directly from the Schrödinger equation and proceeds to modify it on physical grounds, either by neglecting the outgoing electron's interaction with the core after the instant of ionization or neglecting the influence of the laser field on the initial bound state. As we shall see, both of these approximations are justified for a short range potential and lead to the same physical result, up to a prefactor and a choice of gauge. In doing so, the problem is simplified considerably and it becomes possible to apply an analytical approach.

3.3.1 *The basic result and its derivation*

The basic equation of this theory was first formulated by Keldysh in 1965 [53]. It describes the transition amplitude between an initial bound state $|\psi_i\rangle$ and a continuum state with momentum \mathbf{p} at the detector. At some time T after the laser has been switched off, the SFA ionization amplitude takes the form

$$a_{\mathbf{p}}(T) = \langle \mathbf{p} | \psi(T) \rangle = -i \int_{-\infty}^T \langle \mathbf{p}_T^V(t') | V_L(t') | \psi_b(t') \rangle dt', \quad (3.23)$$

where $|\mathbf{p}_T^V\rangle$ is a Volkov state – the exact solution for a free electron moving in the presence of an oscillating field, as defined in Eq.(3.2) – and $|\psi_b\rangle$ is a field-free bound state – our initial state evaluated at some time t' . The potential V_L describes the electron's interaction with the laser field. As discussed in Section 2.3, the particular form it takes will depend on the choice of gauge.

Of course, once we know $a_{\mathbf{p}}(T)$, finding our physical observables is easy. We obtain the angle- and energy- resolved photoelectron spectrum by taking the square modulus $|a_{\mathbf{p}}(T)|^2$, and the total ionization rate can be calculated by integrating over all momenta:

$$w = \int |a_{\mathbf{p}}(T)|^2 d\mathbf{p}. \quad (3.24)$$

As mentioned above, the expression for $a_{\mathbf{p}}(T)$ can be derived in two different ways [55, 77], each of which makes use of a different ap-

proximation. Both, however, draw on one important fact from our discussion from the start of this chapter. In particular, recall the Hamiltonian we introduced in Section 2.3. In its most general form, it can be expressed as

$$H = \frac{\hat{p}^2}{2} + V_L(t) + U(r), \quad (3.25)$$

where $V_L(t)$ and $U(r)$ represent the laser and binding potentials respectively. As we saw in Section 3.1, solving the Schrödinger equation would generally be straightforward if only one of $V_L(t)$ or $U(r)$ were present. That is, we know (or can obtain) solutions corresponding to

$$H_0^c = \frac{\hat{p}^2}{2} + U(r) \quad (3.26)$$

and

$$H_0^L = \frac{\hat{p}^2}{2} + V_L(t). \quad (3.27)$$

The Volkov states $|\mathbf{p}_T^V(t)\rangle$ solve (3.27), while field-free bound states $|\psi_b\rangle$ are solutions to (3.26).

In standard perturbation theory, we would need to know the solution for only one of H_0^c or H_0^L , provided that the remaining potential was small. As discussed earlier, however, this is not the case for either $V_L(t)$ or $U(r)$. In contrast, the derivations of Eq.(3.23) rely on the knowledge of *both* of the above solutions, along with the nature of the particular problem at hand. The key features of each of these derivations are summarized below.

3.3.1.1 The SFA derivation

Let us begin with the derivation that gives the strong field approximation its name, proposed originally by Reiss in 1980 [77]. In this case, we start by breaking up the Hamiltonian (3.25) as follows:

$$H = H_0^c + V_L(t). \quad (3.28)$$

The solution to the time dependent Schrödinger equation $i\partial\psi/\partial t = H\psi$ can then be written as

$$|\psi(T)\rangle = U(T, t_0) |\psi(t_0)\rangle \quad (3.29)$$

$$= U_0^c(T, t_0) |\psi(t_0)\rangle - i \int_{t_0}^T dt' U(T, t') V_L(t') U_0^c(t', t_0) |\psi(t_0)\rangle, \quad (3.30)$$

where U and U_0^c are the propagators corresponding to H and H_0^c respectively.

While we know the solution for U_0^c , the $U(T, t')$ in the second term remains a problem. If $V_L(t')$ were small, of course, we could take the standard perturbation theory approach from here – to first order, for example, this would simply mean replacing U by the field-free

propagator \mathcal{U}_0^c . However, in the strong field regime, this is clearly not justified.

Instead, we proceed by making use of the physical interpretation of the integrand in Eq.(3.30):

1. The electron starts in some initial bound state $|\psi(t_0)\rangle = |\psi_b(t_0)\rangle$ and undergoes field free evolution until time t' , described by the propagator \mathcal{U}_0^c .
2. At time t' , it is kicked by the laser field via the laser potential $V_L(t')$, which may cause a transition to a continuum state. It is natural to think of this as the ionization time.
3. After time t' , the electron evolves according to the full propagator \mathcal{U} – that is, in the presence of both the laser field and the potential of the core – until the observation time T .
4. By integrating over all times t' , we are essentially integrating over all possible instants of ionization.

With the above picture in mind, we can think of $\mathcal{U}(T, t')$ as describing the electron's motion in the continuum which, as we know, should be dominated by the strong laser field (this is where the strong field part of the strong field approximation comes in). This, in turn, motivates the replacement of $\mathcal{U}(T, t')$ by $\mathcal{U}_0^L(T, t')$, the propagator corresponding to H_0^L . Effectively, in doing so, we are ignoring the interaction of the departing electron with the core after ionization has occurred. This is the same approximation we made in the second step of the simpleman model in Section 3.2.3 of course. Note that, rigorously speaking, the above replacement is only suitable for a short or zero range potential. It is this requirement, in fact, rather than a restriction to strong fields, that is imperative to obtain the SFA result [78].

Having made the above approximation, writing down a solution for $a_p(T)$ becomes easy. Assuming our initial field-free bound state $|\psi_b\rangle$ is a stationary solution of H_0^c with energy I_p ,

$$\mathcal{U}_0^c(t, t_0) |\psi_b(t_0)\rangle = |\psi_b(t)\rangle = e^{iI_p t} |\psi_b\rangle. \quad (3.31)$$

The solution for \mathcal{U}_0^L is also something we know. We can express it in terms of the Volkov functions as follows:

$$\mathcal{U}_0^L(t_2, t_1) = \theta(t_2 - t_1) \int d\mathbf{k} |\mathbf{k}_T^V(t_2)\rangle \langle \mathbf{k}_T^V(t_1)|, \quad (3.32)$$

where $\theta(t_2 - t_1)$ is the Heaviside step function which ensures time-ordering.

Substituting these expressions into (3.30) and projecting onto a final field-free continuum state with momentum \mathbf{p} at the detector, we obtain the following expression for the ionization amplitude:

$$a_p(T) = -i \int^T dt' \int d\mathbf{k} \langle \mathbf{p} | \mathbf{k}_T^V(T) \rangle \langle \mathbf{k}_T^V(t') | V_L(t') | \psi_b(t') \rangle. \quad (3.33)$$

If we assume that our observation time T occurs after the laser pulse has been switched off, $|k_T^V(T)\rangle = |k\rangle$ and Eq.(3.33) reduces to the Keldysh postulate (3.23) we introduced at the beginning of this section.

3.3.1.2 The PPT derivation

An alternative derivation was proposed by Popov, Perelomov and Teren'tev (PPT) in 1966 [55]. In this case, the Hamiltonian (3.25) is split up in a different way:

$$H = H_0^L(t) + U(r), \quad (3.34)$$

and the solution to the Schrödinger equation is written as

$$|\psi(T)\rangle = U_0^L(T, t_0)|\psi(t_0)\rangle - i \int_{t_0}^T dt' U_0^L(T, t')U(r)U(t', t_0)|\psi(t_0)\rangle, \quad (3.35)$$

where U_0^L is the propagator for H_0^L .

Again, the problem we face is the full propagator U in the second term. This time, however, it will be the binding potential $U(r)$ that saves us. To see the reason for this, it is useful to rewrite Eq.(3.35) in position space:

$$\begin{aligned} \psi(r, T) &= \int dr' G_0^L(r, T; r', t_0)\psi(r', t_0) \\ &\quad - i \int_{t_0}^T dt' \int dr' G_0^L(r, T; r', t')U(r')\psi(r', t'), \end{aligned} \quad (3.36)$$

where G_0^L is the Green's function corresponding to the Hamiltonian H_0^L and $\psi(r', t') = \langle r' | U(t', t_0) | \psi(t_0) \rangle$ in the second term. If $U(r)$ is a short range potential, only the immediate vicinity of the atom will contribute to the integral over r' : $U(r)$ will kill off the ionized or polarized tail of the full wavefunction $\psi(r', t')$ everywhere else. Within this region, provided the binding potential is sufficiently deep and the extent of $U(r)$ is sufficiently small, the influence of the laser field should be unimportant. Working in the length gauge, this motivates the replacement of the full propagator $U(t', t_0)$ by its laser-free counterpart $U_0^c(t', t_0)$, and the full wavefunction $\psi(r', t')$ by the field-free bound state $\psi_b(r', t')$.

Again, we have reduced the problem to quantities we can evaluate: namely, the solutions for H_0^L and H_0^c . Inserting the expression for U_0^L (3.32) and projecting onto a continuum state with momentum p as before, we obtain

$$a_p(T) = -i \int^T \langle p_T^V(t') | U(r) | \psi_b(t') \rangle dt'. \quad (3.37)$$

Notice that this is different to the Keldysh result (3.23) introduced at the start of this section: $V_L(t')$ has been replaced by the binding

potential $U(\mathbf{r})$. Nevertheless, it can be readily taken to that form using the fact that $|\psi_b\rangle$ and $|\mathbf{p}_T^V\rangle$ are solutions to the time-dependent Schrödinger equation specified by (3.26) and (3.27) respectively¹:

$$U(\mathbf{r}) |\psi_b(t')\rangle = \left(i \frac{\partial}{\partial t} - \frac{\hat{\mathbf{p}}^2}{2} \right) |\psi_b(t')\rangle \quad (3.38)$$

$$\langle \mathbf{p}_T^V(t') | \left(i \frac{\partial}{\partial t} - \frac{\hat{\mathbf{p}}^2}{2} \right) = \langle \mathbf{p}_T^V(t') | V_L(t'). \quad (3.39)$$

Substituting this into Eq.(3.37), we reproduce Eq.(3.23). As a result, PPT and length gauge SFA yield identical results for the short-range potential [79].

3.3.2 Evaluating the integral

Arriving at Eq.(3.23) is only part of the battle, of course. Although we have derived an expression for the SFA ionization amplitude, in order to evaluate it in practice we must integrate over all possible ionization times t' .

Let us begin by rewriting Eq.(3.23) more explicitly. Using Eq.(3.4) for $|\mathbf{p}_T^V(t')\rangle$ and Eq.(3.31) for $|\psi_b(t')\rangle$, we obtain

$$a_p(T) = -i \int_t^T dt' R(\mathbf{p}, t') e^{-iS^{SFA}(T, \mathbf{p}; t')}, \quad (3.40)$$

where S^{SFA} is the SFA phase

$$S^{SFA}(T, \mathbf{p}; t) = S_V(T, \mathbf{p}; t) - I_p t \quad (3.41)$$

$$= \frac{1}{2} \int_t^T (\mathbf{p} + \mathbf{A}(\tau))^2 d\tau - I_p t. \quad (3.42)$$

The prefactor $R(\mathbf{p}, t')$ depends on the choice of gauge. In the length gauge, we have

$$R_{lg}(\mathbf{p}, t') = \langle \mathbf{p} + \mathbf{A}(t') | \mathbf{E}(t') \cdot \mathbf{r} | \psi_b \rangle, \quad (3.43)$$

while in the velocity gauge,

$$R_{vg}(\mathbf{p}, t') = \langle \mathbf{p} | \mathbf{p} \cdot \mathbf{A}(t') + \frac{\mathbf{A}(t')^2}{2} | \psi_b \rangle. \quad (3.44)$$

In principle, it is possible to evaluate the above integral (3.40) exactly. For a long monochromatic pulse, for example, the solution can be expressed in terms of Bessel functions (e.g. see [77]) and calculated numerically. However, this is not the route that we shall pursue

¹ Note, however, that in practice the PPT approach employs the time *independent* Schrödinger equation for the bound state $|\psi_b\rangle$ instead. This yields $U(\mathbf{r})|\psi_b\rangle = -(\hat{\mathbf{p}}^2/2 + I_p)|\psi_b\rangle$, which greatly simplifies the analytical treatment when used to evaluate Eq.(3.37).

here. Instead, we shall take an approximate approach based on what is known as the saddlepoint method, or equivalently the method of stationary phase or steepest descents. As we shall see, this gives rise to much simpler analytic expressions for the ionization amplitude, works for arbitrary pulse shapes, and comes with a natural and highly insightful physical interpretation.

3.3.2.1 The saddlepoint method

Consider an integral of the form

$$I = \int g(t)e^{i\lambda f(t)} dt, \quad (3.45)$$

where λ is large, and $g(t)$ is a well-behaved function that varies slowly with t . The principle of stationary phase states that the major contribution to the integral will come from the point(s) where the derivative of the phase vanishes: that is, the points t_s where $f'(t_s) = 0$. These points turn out to be saddlepoints in the complex plane, lending the method its name. Based on this, we can approximate the integral by expanding f to second order about t_s and integrating the resulting Gaussian:

$$I \approx g(t_s)e^{i\lambda f(t_s)} \int e^{i\lambda f''(t_s)(t-t_s)^2} dt \quad (3.46)$$

$$= \sqrt{\frac{2\pi i}{\lambda f''(t_s)}} g(t_s) e^{i\lambda f(t_s)}. \quad (3.47)$$

If more than one saddlepoint is present (provided they are sufficiently far apart), the contribution from each can simply be summed.

Our ability to apply the saddlepoint method when evaluating the ionization amplitude is a consequence of the strong low frequency fields we are dealing with. For large F and small ω , the SFA phase (3.42) will be large in magnitude and our expression for $a_p(T)$ (3.40) will be of the form (3.45). In this case, applying the argument above, we know that the majority of our integral will be accumulated in the vicinity of saddlepoint times t_s where the SFA phase vanishes. These times solve the saddlepoint equation

$$\left. \frac{\partial S^{\text{SFA}}}{\partial t'} \right|_{t'=t_s} = 0 \Rightarrow \frac{1}{2}(\mathbf{p} + \mathbf{A}(t_s))^2 = -I_p. \quad (3.48)$$

Immediately, the perfect square on the LHS and the fact that $I_p > 0$ tell us that we will not find a real t_s to satisfy this condition. A solution is always possible, however, if we allow t_s to be complex:

$$t_s(\mathbf{p}) = t_i(\mathbf{p}) + i\tau_T(\mathbf{p}). \quad (3.49)$$

In general, the solutions will come in complex conjugate pairs; however, since $\text{Im}(t_s) < 0$ leads to exponential growth instead of decay,

we exclude all t_s with a negative imaginary part by restricting our integration contour to the upper half plane. Even so, given the periodic nature of $\mathbf{A}(t)$, there will typically be many possible solutions for any given \mathbf{p} . For a long pulse of frequency ω , for example, if t_s is a solution, so is $t_s + 2n\pi/\omega$. In addition to this, depending on the particular form of the vector potential $\mathbf{A}(t)$, there may be more than one solution t_s within a single laser period (e.g. see [80]). Explicit analytical solutions for long linearly and circularly polarized pulses are presented in [A] and [C] respectively.

3.3.3 SFA ionization amplitude

Having found our saddlepoints in this way, we can evaluate the SFA ionization amplitude using Eq.(3.47). The contribution to the integral from each saddlepoint $t_s^\alpha(\mathbf{p})$ is given by

$$a_p^\alpha(T) = \sqrt{\frac{2\pi}{iS_V''(t_s^\alpha)}} R(\mathbf{p}, t_s^\alpha) e^{-iS^{\text{SFA}}(T, \mathbf{p}; t_s^\alpha)}, \quad (3.50)$$

and the overall result is determined by summing the above:

$$a_p(T) = \sum_{\alpha} a_p^\alpha(T). \quad (3.51)$$

Note that, in a long pulse, the interference of saddlepoint contributions from consecutive laser periods gives rise to a series of delta peaks, evenly spaced by the laser frequency ω :

$$a_p(T) \propto \sum_n \delta \left(\frac{\mathbf{p}^2}{2m} + U_p + I_p - n\omega \right) \sum_i a_p^i(T), \quad (3.52)$$

where the sum over i includes only those saddlepoints that lie within a single laser period, $0 < \text{Re}(t_s^i) < 2\pi/\omega$ (e.g. see [78]). These delta peaks are, of course, precisely the ATI peaks we discussed in Section 2.1. For a short pulse, the peaks become progressively less defined and the interference pattern is gradually lost.

3.3.4 Rescattering and recombination

In our formulation of the SFA so far, we have assumed that no further interactions with the core take place after the instant of ionization. Just like in the two-step simpleman model, it is as if the parent ion has vanished as soon as ionization has occurred. However, as we saw in Section 3.2.4, working under this assumption misses a great deal of important physics, such as high harmonic generation and the high energy plateau in ATI spectra. It was only by adding a third step – describing recombination or rescattering respectively – that these effects could be accounted for.

Fortunately, extending the SFA formalism in an analogous way is relatively straightforward. To incorporate rescattering, for example, we can simply go back to Eq.(3.30) in Section 3.3.1.1. Now, instead of merely replacing the full propagator $\mathcal{U}(T, t')$ by the laser-only propagator $\mathcal{U}_0^L(T, t')$, we treat the potential $U(\mathbf{r})$ describing electron-ion interactions as a small perturbation [81–83]. Expanding $\mathcal{U}(T, t')$ to first order in $U(\mathbf{r})$ and substituting this into Eq.(3.30), we obtain the following correction to the ionization amplitude:

$$a_{\mathbf{p}}^{(1)}(T) = - \int_{-\infty}^T dt' \int_{t'}^T dt'' \langle \mathbf{p}_T^V(t'') | U(\mathbf{r}) \mathcal{U}_0^L(t'', t') V_L(t') | \psi_b(t') \rangle. \quad (3.53)$$

To describe high harmonic generation, we can again return to Eq.(3.30). This time, we are interested in the response of our atom or molecule, which is proportional to the induced dipole $\mathbf{D}(t) = \langle \psi(t) | \hat{\mathbf{d}} | \psi(t) \rangle$, where $\hat{\mathbf{d}} = -\hat{\mathbf{r}}$ is the dipole operator. If we substitute our formal solution (3.30) into this, and again replace the full propagator $\mathcal{U}(t, t')$ by its laser-only counterpart $\mathcal{U}_0^L(t, t')$, we obtain

$$\mathbf{D}(t) \approx -i \int_{t_0}^t dt' \langle \psi_b(t) | \hat{\mathbf{d}} \mathcal{U}_0^L(t, t') V_L(t') | \psi_b(t') \rangle + c.c. \quad (3.54)$$

In the above, we have assumed that there is no permanent dipole in our initial bound state $|\psi_b\rangle$, and that the contribution of the continuum-continuum transitions to the dipole is negligible (which is justified provided that ionization is relatively weak). The harmonic spectrum $I(N\omega) \propto (N\omega)^4 |D(N\omega)|^2$ can then be determined by taking the Fourier transform:

$$D(N\omega) = \int dt e^{iN\omega t} D(t). \quad (3.55)$$

In both problems above, we have two integrals over time to evaluate (together with an implicit integral over momentum coming from the propagator \mathcal{U}_0^L , as defined by Eq.(3.32)). Again, as discussed in Section 3.3.2, we can either attempt to evaluate these exactly [81, 82], or apply the saddlepoint approximation [84, 85]. In the latter case, the above analysis was used to derive a HHG cutoff law of the form $N_{\max}\omega \approx 1.3I_p + 3.17U_p$ [84], which again coincides well with the empirically derived expression in Section 2.1.2. For a much more detailed account of rescattering and HHG in the context of SFA, see [86] and [87] respectively.

3.3.5 Strengths and Limitations

Compared with the two- and three- steps models of Section 3.2, the SFA approach comes with a distinct advantage. The derivation begins with the Schrödinger equation, remains fully quantum throughout, and makes no assumptions about the physical process by which ionization proceeds. In particular, it is entirely independent of the

tunnelling picture. Essentially, as underlined by the PPT derivation, the only assumption it requires, beyond the standard approximations discussed in Sections 2.3 and 2.5, is that of a short range potential. There are number of things we gain as a result.

Firstly, unlike two-step models which propagate classical trajectories, the SFA description is able to take into account quantum interference effects. As we saw in Section 3.3.3, for example, this gives rise to the ATI peaks which we previously interpreted in terms of photon absorption. In addition to this, the SFA has been able to predict quantum interferences arising from saddlepoints t_s^i that lie within the same laser cycle [79]. Although generally washed out in linearly polarized fields due to their dependence on laser intensity, such interferences have been indeed been observed for elliptically polarized fields [80, 86].

Secondly, since tunnelling is not assumed in the SFA picture, we are no longer restricted to the tunnelling limit $\gamma \ll 1$. Indeed, the SFA imposes no special limits on the laser frequency. At one extreme, for example, it is possible to show that the SFA result reproduces the static tunnelling rate for a short range potential in the $\gamma \ll 1$ limit [55]. On the other hand, when applied to a zero range potential in a weak field, the Keldysh ansatz (3.23) reduces to the first order perturbation theory result for one photon absorption [78]. This fact gives the SFA a considerably broader range of applicability compared to two- and three- step approaches. Note, in particular, that since the SFA does not rely on a quasistatic description of the ionization process, non-adiabatic effects missed in tunnelling-based models are naturally accounted for here.

In addition to this, within the SFA we completely avoid the problem of specifying initial conditions at the exit of the barrier, necessary for matching the quantum and classical steps within tunnelling-based approaches. Indeed, the SFA result is independent of any physical picture and requires no knowledge of the internal details of the ionization process. A single mathematical framework is used throughout, and the derivation proceeds based on one well-defined approximation, which can be rigorously justified for a short range potential. This leaves no room for ad hoc assumptions or the ambiguity associated with the choice of initial conditions.

3.3.5.1 Short range vs long range potentials

There is an elephant in the room, however, that we have been carefully avoiding in our discussion so far. As we saw, the crucial approximation within the SFA derivation was that of a short range potential. In practice, however, we know that the core potential the electron sees during ionization will typically have a long range Coulomb tail. In light of this, it is natural to ask: how well does the SFA work in practice and under what conditions can it be applied?

As we would expect, for systems truly characterized by a short or zero range potential, the SFA works very well indeed. For a δ -function potential, in fact, it coincides with the exact result, up to the Stark shift of the ground state [88]. Since the photodetachement of negative ions is naturally described in terms of a short-range interaction, this process provides a strict test of the theory. Indeed, in this case the SFA has been shown to produce quantitatively accurate results: excellent agreement has been demonstrated in comparisons with both numerical simulations of photodetachment [79, 89] and experimental data (once rescattering is accounted for as described in Section 3.3.4) [83, 90].

When applied to systems described by a long-range potential, however, the SFA method clearly suffers. An immediate sign that something is amiss is the magnitude of the first order rescattering correction (3.53). Whereas for short range potentials this term is indeed perturbative, for Coulomb potentials it can dominate the zeroth order expression (3.23) [78]. Another fundamental problem becomes apparent if we compare the expressions for a_p obtained in the length and velocity gauges (see Eq.(3.50), (3.43) and (3.44)). Although the exponential factor $\exp[-iS^{\text{SFA}}]$ is the same in both cases, the prefactor $R(\mathbf{p}, t_s)$ produces notably different results in general. Indeed, the SFA is only exactly gauge invariant in the case of a zero range potential (which admits a single s-state solution) [78, 79]; even for short range potentials, the length and velocity gauges can produce qualitatively different results. From a physical point of view, of course, this also rings alarm bells. For short range potentials, the length gauge has been shown to be the correct choice [91–93]. For long range potentials, however, comparison with the known static tunnelling rate in the $\gamma \ll 1$ limit suggests that the prefactors in *both* gauges are incorrect [53, 78]. As a result, the SFA can only provide exponential accuracy when a long-range potential is involved.

In light of this, the predictions of the SFA for the strong field ionization of atoms or molecules must be taken with a grain of salt. Qualitatively, the theory presented above has been able to reproduce many observed features of photoelectron spectra, such as the bell-shaped energy distribution in circularly polarized fields [94], quantum interference effects in elliptically polarized field fields [80], and ring-like angular distributions [85] and low energy structures in linearly polarized fields [95]. Significantly, when extended to describe recombination as discussed in Section 3.3.4, it also correctly predicts the cutoff law for HHG [84]. Quantitative agreement, however, is generally lacking. The total ionization rate, for example, is notably underestimated, typically by several orders of magnitude [96], and the precise shape of the spectra does not coincide with the exact result in general (e.g. see [97, 98]). Certain qualitative effects are missing as well, such as

the asymmetry in the angular distributions for elliptically polarized fields [99].

Of course, we should not find this surprising. We have already seen in the context of two-step models that neglecting the long range electron-core interaction leads to a rather crude picture. Within the SFA, however – in contrast to the tunnelling-based approaches – this approximation is built in at the most basic level, which makes this problem a fundamental one.

Given its otherwise notable advantages, there have been a number of attempts to modify the SFA to non-perturbatively account for the Coulomb interaction between the departing electron and the core. The most important of these, along with their respective strengths and shortcomings will be discussed in Section 3.5. Before we move on to this, however, it will prove rewarding to consider one more aspect of the SFA.

3.4 SFA AND THE TUNNELLING PICTURE

In our discussion so far, one feature of the two- and three- step models discussed in Section 3.2 has not yet been directly touched upon in the context of the SFA: namely, that of a simple and readily accessible physical interpretation. In the former, the tunnelling picture was assumed from the outset and formed the backbone for all subsequent calculations – without this physical interpretation, no two- or three-step model could exist. As we have emphasized above, this is very much not the case for the SFA. Instead, the key results can be derived on purely mathematical grounds (based on the assumption of a short range potential) and allow us to calculate any observable we choose with no reference to any underlying physical process.

However, as we shall see, there is nevertheless a natural way to assign a physical interpretation to the quantities within SFA and to connect them to the tunnelling picture in particular. Indeed, besides computational tractability, this is one of the key advantages of this analytical approach compared to directly solving the TDSE by numerical means.

3.4.1 *A complex ionization time?*

The way in which the SFA can be interpreted was already hinted at in Section 3.3.1.1. There, we identified the integration variable t' with the time at which ionization takes place. Let us now take this notion further.

When we used the saddlepoint method to evaluate the integral over t' , we found that the major contribution came from certain points t_s that satisfy the saddlepoint equation (3.48). If the integral over t'

represents all possible instants of ionization, this suggests that we can think of t_s as the most likely time(s) for ionization to occur.

In light of this interpretation, we can compare Eq.(3.48) to its counterpart in the simpleman model Eq.(3.11). In both cases, these equations connect the ionization time to the experimentally measured momentum \mathbf{p} . Indeed, these equations become equivalent if we set $I_p = 0$. There is a crucial difference however. Whereas in the simpleman model we only consider real times t_i , in the SFA case, we have no choice but to allow our saddlepoint solutions t_s to be complex. How can we understand this?

Generally speaking, the appearance of complex quantities suggests that a non-classical process is involved. Notice, for example, that the saddlepoint equation (3.48) takes the form of a conservation of energy condition: it tells us that the energy of the electron in its initial bound state (RHS) must equal the kinetic energy of the Volkov state it is excited to (LHS) at the time at which the transition takes place (t_s). The fact that kinetic energy is negative here is typical of a tunnelling process. Note that it implies a purely imaginary velocity $v(t) = \mathbf{p} + \mathbf{A}(t)$:

$$v(t_s) = i\sqrt{2I_p} = i\kappa. \quad (3.56)$$

The question remains, however: can we assign a physical interpretation to the complex ‘ionization time’ t_s , and is there a way to connect this to the time t_i in the simpleman model? In fact, the answer to both of these questions turns out to be yes.

3.4.1.1 *The real part*

The interpretation of the real part of the saddlepoint solution $\text{Re}(t_s) = t_i$ is a natural one. We can think of it as the direct SFA counterpart to the (real) time of ionization t_i in the two- and three- step models discussed in Section 3.2.3: that is, the time at which the tunnelling step is completed and the electron begins its motion in the continuum. The notation we chose was not coincidental, of course.

This idea is motivated further if we examine the explicit expressions for the SFA ionization times $t_i(\mathbf{p})$. Comparing Eq.(4) in [C] with Eq.(3.19) in Section 3.2.3.3, we find that SFA and simpleman t_i coincide exactly for circularly polarized fields. For linearly polarized fields, the SFA result (given by Eq.(41) in [A]) is, in general, of a more complicated form than its simpleman counterpart (defined by Eq.(3.13) in Section 3.2.3.2); however, it is easy to check that the SFA expression reduces to the simpleman result in the tunnelling limit $\gamma \ll 1$.

Why the discrepancy? An explanation is suggested if we recall one of the key differences between the two approaches. In a linearly polarized field, the width of the barrier oscillates with time and, consequently, away from the $\gamma \ll 1$ limit, non-adiabatic effects can become more important. Such effects are naturally accounted for within

the SFA but missed entirely in the quasistatic tunnelling description. In a circularly polarized field, this is less of an issue since, as discussed in Section 2.4, the width of the barrier is fixed (it merely rotates with time), and as a result the situation more closely resembles static tunnelling.

3.4.1.2 The imaginary part

The interpretation of the imaginary part is somewhat less straightforward. In the $\gamma \ll 1$ limit, it is possible to show that τ_T reduces to the Keldysh tunnelling time

$$\tau_K = \frac{r_{\text{exit}}^0}{\kappa/2} = \frac{\kappa}{F} = \frac{\gamma}{\omega}, \quad (3.57)$$

where r_{exit}^0 is the width of the tunnelling barrier for a short range potential (see Eq.(3.21)) and $\kappa = \sqrt{2I_p}$ is the atomic velocity (see Eq.(3.56)). Essentially, this is the time it would take a classical particle to traverse a distance of r_{exit}^0 if its initial velocity (3.56) were real. Alternatively, we can think of $i\tau_T$ as the imaginary time a particle moving with an imaginary velocity would need to cover a real distance.

In a more practical sense, τ_T tells us how much the wavefunction decays in passing under the barrier via the terms

$$|a_p|^2 \propto e^{2\text{Im}[S^{\text{SFA}}(p, t_s)]} = e^{2\text{Im}[S_V(t_i, \tau_T)]} e^{-2I_p \tau_T}. \quad (3.58)$$

Generally speaking, the larger τ_T , the more suppressed ionization will be. As we see from Eq.(3.57), it scales with the width of the barrier that the electron has to traverse, as we would expect.

3.4.2 The PPT picture

In fact, it is possible to take the interpretation above one step further: following the work of PPT [75, 96], we can link a particular integration contour in SFA with the steps that make up the tunnelling-based models of Section 3.2.

To understand the basic concept, let us go back to the expression for the ionization amplitude given by Eq.(3.50). In the exponential part, we have an integral coming from the Volkov phase of the form

$$S_V(T, p; t_s) = \frac{1}{2} \int_{t_s}^T (\mathbf{p} + \mathbf{A}(\tau))^2 d\tau. \quad (3.59)$$

The complex saddlepoint t_s in the lower limit tells us that we have a complex integral on our hands, and since our integrand is analytic, we are free to deform our integration contour as we please. Following PPT, let us do this as follows:

1. First, integrate parallel to the imaginary axis, down from our complex saddlepoint $t_s = t_i + i\tau_T$ to the point t_i on the real axis.
2. Next, integrate along the real axis from the point t_i to our observation time T .

This contour is illustrated in Fig.3(a). Having done so, we can rewrite Eq.(3.59) as

$$S_V(T, \mathbf{p}; t_s) = \frac{i}{2} \int_{\tau_T}^0 (\mathbf{p} + \mathbf{A}(t_i + i\xi))^2 d\xi + \frac{1}{2} \int_{t_i}^T (\mathbf{p} + \mathbf{A}(\tau))^2 d\tau. \quad (3.60)$$

Notice, now, that while the first term includes both real and imaginary parts, the integral along the second leg of the contour is purely real. Since only the imaginary part of the SFA phase contributes to our observable $|\alpha_p|^2$, this, in turn, suggests that ionization is essentially concluded by the time we reach t_i on the real axis. Beyond this time, as we move along the real axis, the electron merely acquires an overall phase.

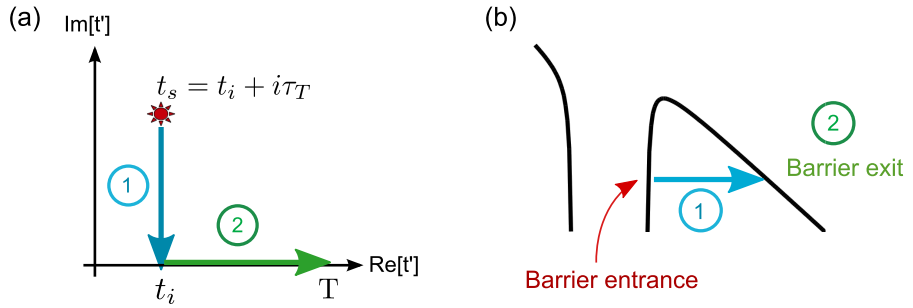


Figure 3: The PPT picture of strong field ionization. (a) The integration contour we choose in the complex plane. (b) The interpretation of each leg of this contour in terms of the tunnelling picture.

This fact motivates the following interpretation, illustrated in Fig.3(b):

1. The first leg of the contour, describing the evolution in imaginary time, is associated with the electron's motion under the barrier. This is accompanied by a decay of the ionization amplitude α_p . Note that this interpretation is particularly natural if we recall our discussion of τ_T as a tunnelling time – that is, the (imaginary) time it takes to cross the tunnelling barrier.
2. At time t_i , when the contour hits the real axis, the electron exits the barrier and appears in the continuum. This is what we think of as the ionization time, as discussed above.
3. The second leg of the contour, where time evolves along the real axis, describes the electron's subsequent evolution in the continuum. Since the ionization process is concluded by this stage, no further changes to $|\alpha_p|^2$ take place.

3.4.3 Trajectories and initial conditions

With this picture in mind, it is also possible to introduce the concept of trajectories into the SFA framework. As PPT pointed out [75], the exponential factor in the SFA expression for the ionization amplitude (3.50) can be thought of in terms of a classical action. To see this explicitly, we can rewrite the SFA phase (3.42) as follows [78]:

$$S^{\text{SFA}}(\mathbf{p}, T; t_s) = - \int_{t_s}^T \left(\frac{1}{2} \mathbf{v}_p^2 + \dot{\mathbf{v}}_p \cdot \mathbf{r}_p \right) dt' + [\mathbf{r}_p \cdot \mathbf{v}_p]_{t_s}^T - I_p t_s, \quad (3.61)$$

where we have defined

$$\mathbf{v}_p(t) = \mathbf{p} + \mathbf{A}(t) = \dot{\mathbf{r}}_p(t) \quad (3.62)$$

and integrated \mathbf{v}_p^2 by parts. Making use of the fact that $\dot{\mathbf{v}}_p = d\mathbf{A}/dt = -\mathbf{E}(t)$, this becomes

$$S^{\text{SFA}}(\mathbf{p}, T; t_s) = - \left(\int_{t_s}^T \mathcal{L}(\mathbf{r}_p, \mathbf{v}_p, t') dt' + I_p t_s \right) + [\mathbf{r}_p \cdot \mathbf{v}_p]_{t_s}^T, \quad (3.63)$$

where \mathcal{L} is the Lagrangian

$$\mathcal{L} = \frac{1}{2} \mathbf{v}_p^2 - \mathbf{E} \cdot \mathbf{r}_p. \quad (3.64)$$

As we see from Eq.(3.63) and (3.64), the SFA phase contains the classical action for a particle moving in an oscillating electric field. The electron's velocity $\mathbf{v}_p(t)$ is fixed by the final condition at the detector $\mathbf{v}_p(T) = \mathbf{p} + \mathbf{A}(T) = \mathbf{p}$ and the initial condition is determined by $\mathbf{v}_p^2(t_s) = -\kappa^2$. The corresponding trajectories \mathbf{r}_p are then given by

$$\mathbf{r}_p(t) = \mathbf{r}_0 + \int_{t_s}^t \mathbf{v}_p(t') dt' = \mathbf{r}_0 + \int_{t_s}^t (\mathbf{p} + \mathbf{A}(t')) dt', \quad (3.65)$$

where $\mathbf{r}_0 = \mathbf{r}_0(\mathbf{p})$ is an arbitrary constant that determines the initial condition $\mathbf{r}_p(t_s) = \mathbf{r}_0$.

Such trajectories \mathbf{r}_p can be understood along similar lines to the saddlepoint times t_s . Just as t_s represent the most likely times of ionization – which increasingly dominate the integral as we move towards the classical $S^{\text{SFA}} \gg 1$ limit – \mathbf{r}_p represents the trajectories that contribute most strongly to the ionization amplitude. This is a concept familiar from the path integral formulation of quantum mechanics.

How do these trajectories compare to those within two-step models of ionization? Formally, it is clear that \mathbf{r}_p satisfies exactly the same classical equations of motion as the continuum trajectories within the simpleman model. The initial conditions, however, are notably different: they are now defined at the saddlepoint time t_s and are complex in general.

To see the connection to tunnelling-based models more explicitly, it will be useful to split up the integral for \mathbf{r}_p in the same way we did for S_V in the previous section. This yields trajectories \mathbf{r}_1 and \mathbf{r}_2 , describing the electron's motion under the barrier and in the continuum respectively. The situation now differs from the two-step model of ionization in two important ways:

1. The trajectories in PPT describe motion under the barrier, not just in the continuum.
2. Depending on the choice of initial condition \mathbf{r}_0 , PPT trajectories will, in general, have a non-zero imaginary part. This is the case not only under the barrier, but in the continuum as well. In fact, as we shall see in the context of the ARM theory, these imaginary parts can play a vital role in describing the physics of strong field ionization.

Notice, also, that within the PPT picture all values of \mathbf{p} are allowed since we can always solve the saddlepoint equation (3.48) for a complex t_s . As a result, we find many different trajectories with the same t_i (but different τ_T), and obtain a photoelectron spectrum with a finite width. This is in contrast to the simpleman model, where \mathbf{p} was completely constrained by (3.11), which, in turn, gave rise to a delta-like photoelectron distribution. Essentially, this difference is equivalent to having a non-trivial distribution of initial conditions for propagation in the continuum. Here, however, this initial distribution is not postulated but stems directly from the complex-valued saddlepoint equation (3.48).

To complete our comparison with two-step models, it would be helpful to know the SFA distribution of initial conditions at the ionization time explicitly. Luckily, finding them within the PPT picture is relatively straightforward. As mentioned above, for any given t_i we can find a set of corresponding trajectories $\mathbf{r}_s(\mathbf{p})$. Associated with each of these, we have an initial velocity $\mathbf{v}(\mathbf{p}, t_i) = \mathbf{p} + \mathbf{A}(t_i)$ and a barrier exit, which can be determined by evaluating $\text{Re}[\mathbf{r}_s(\mathbf{p}, t_s; t_i)]$. The relative weighting for each of these initial conditions (parametrised by the final momentum \mathbf{p}) is then given by the probability distribution $|a_{\mathbf{p}}|^2$.

It is possible to show that in the tunnelling limit (and for an appropriate choice of \mathbf{r}_0), these initial conditions indeed reduce to a simple version of the two-step model: the barrier exit approaches the static result for a short-range potential (3.21) and the initial velocity distribution is centred about $v = 0$. However, moving towards larger values of γ , both the barrier exit and the initial velocity start to deviate increasingly from these values (e.g. see [78] and [100] for a discussion relating to linearly and circularly polarized fields respectively). Again, the implication seems clear. Non-adiabatic effects missed by the quasistatic tunnelling description must be coming into play. This

is a limitation of the two-step approach that we have have touched upon before, of course. Now, however, thanks to the PPT picture, we can explicitly see and quantify such effects.

3.5 COULOMB EFFECTS IN SFA

As we have seen in Sections 3.3.5 and 3.4, the SFA approach for describing strong field dynamics is a powerful one in many respects. It is a fully quantum theory, derived directly from the Schrödinger equation and applicable across a considerable range of parameters from the multiphoton to the tunnelling regime, which nevertheless comes with a natural interpretation in terms of the tunnelling picture. Importantly, in contrast to two- and three- step models, the physical picture is not postulated but emerges directly from the mathematical formulation of the theory, leaving no room for ambiguity or ad hoc assumptions.

However, we also know that the SFA comes with an Achilles heel. In its original form, it cannot account for the long range interaction between the departing electron and the ionic core. Since we know that, outside of photodetachment, neglecting such effects leads to quantitatively (and sometimes qualitatively) incorrect results, it is natural to ask whether it might be possible to modify the SFA in some way to take Coulomb interactions into account. Indeed, several approaches to this problem have been developed, each with their own strengths and caveats. We discuss the most prominent of these below.

3.5.1 A preliminary result: ionization in a static field

To obtain an estimate for the Coulomb correction to the rate of ionization, it is natural to begin by considering the case we know how to solve: namely ionization in a static field. This is, of course, precisely what we used to describe the tunnelling step in two- or three-step approaches, as discussed in Section 3.2.1. If we compare the expressions for a short-range and a Coulomb binding potential derived in [55], we find that the rates differ by the factor [96]

$$\frac{w_{\text{stat}}^{\text{C}}}{w_{\text{stat}}^{\text{sr}}} = \left(\frac{2\kappa^3}{F} \right)^{2Q/\kappa}, \quad (3.66)$$

where the rates are again calculated for $F \ll \kappa^3$. Immediately, this tells us that the Coulomb potential gives rise to a notable enhancement in the ionization rate compared to the short-range result, as mentioned in Section 3.3.5.1. Indeed, we can understand this if we compare the shape of the tunnelling barriers in each of the two cases. For a given ionization potential I_p , the barrier for a Coulomb potential will be lower than its short-range counterpart, making it easier for the electron to tunnel out. Since we know that the SFA result reduces to the

static tunnelling rate when $\gamma \ll 1$, we would expect any Coulomb correction to SFA to coincide with the above expression in the tunnelling limit.

3.5.2 The PPT approach

Some of the earliest attempts to correct the SFA result for electron-core interactions were made by PPT [96]. Their approach – which also underpins the Coulomb-corrected SFA (CCSFA) method discussed in the next section – relies directly on the interpretation of the SFA amplitude in terms of a classical action and electron trajectories, introduced in Section 3.4.3. In our discussion, we focussed on using the trajectory picture to interpret the results of SFA and to compare them to the two-step model. PPT turned this argument around. They started with the premise that the exponential part of the ionization amplitude can be determined by evaluating an appropriate classical action. The problem of accounting for the Coulomb potential then becomes one of correcting this action.

In particular, PPT focussed on deriving the correction to the total ionization rate in the tunnelling limit [96]. To do this, they considered a single trajectory \mathbf{r}_p , associated with the highest probability of ionization $|a_p|^2$: for a linearly polarized field this corresponds to $\mathbf{p} = t_i = 0$. Setting $\mathbf{r}_0 = 0$, this optimal trajectory is purely real for all times along the real axis and since, as we know, only the imaginary component of the SFA phase contributes to the ionization probability, PPT restricted their attention to the first leg of integration contour introduced in Section 3.4.2.

Under these conditions, they showed that the first order correction to the classical action in Eq.(3.63) due to a binding potential $U(\mathbf{r})$ would take the form

$$\delta S = \int_{t_s}^{t_i=0} dt U(\mathbf{r}_{p=0}(t)), \quad (3.67)$$

where $\mathbf{r}_{p=0} = \int_{t_s}^t \mathbf{A}(t') dt'$ is the Coulomb-free trajectory of the electron (see Eq.(3.65)). According to PPT, the Coulomb correction to the SFA ionization rate (3.24) should then be given by $\exp[2\text{Im}(\delta S)]$.

If we want to evaluate Eq.(3.67), however, we face a problem. If $U(\mathbf{r})$ is the Coulomb potential, we know that the integral will diverge at the lower limit where $\mathbf{r}_p(t_s) = 0$. This is not surprising, of course: as long as the trajectory \mathbf{r}_p remains close to the core, treating the Coulomb interaction as a first-order correction to the action is clearly not justified. Indeed, Eq.(3.67) can only be applied when the potential $U(\mathbf{r})$ is small along the entire trajectory, which is the case only as long as $r \gtrsim 1/\kappa$ [96].

To resolve this issue, PPT made use of a matching argument. They considered the wavefunction at a coordinate r_1 such that

$$\frac{1}{\kappa} \ll r_1 \ll r_{\text{exit}}^{\text{SFA}} \quad (3.68)$$

where $r_{\text{exit}}^{\text{SFA}} = r_{p=0}(0)$ is the barrier exit in the PPT picture, as discussed in Section 3.4.3. Under these conditions, $U(\mathbf{r})$ is still sufficiently small for Eq.(3.67) to apply; however the influence of the laser field can already be neglected. The latter implies that we can describe the wavefunction at r_1 using the asymptotic expression for our initial bound state (see Eq.(3.1)):

$$\psi(r_1) \sim (\kappa r_1)^{Q/\kappa-1} e^{-\kappa r_1} = \frac{1}{r_1} e^{-\kappa r_1 + Q/\kappa \ln(\kappa r_1)} = \frac{1}{r_1} e^{\text{Im}S(r_1)}. \quad (3.69)$$

In a short range potential, the second term in the exponential vanishes. This motivated PPT to interpret it as the bound state contribution to δS , allowing them to rewrite Eq.(3.67) as

$$\delta S = -i \frac{Q}{\kappa} \ln \kappa r_1 + \int_{t_1}^0 dt U(\mathbf{r}_{p=0}(t)), \quad (3.70)$$

where t_1 satisfies $r_{p=0}(t_1) = r_1$. Evaluating the integral above exactly for the Coulomb potential $U(\mathbf{r}) = -Q/r$ and taking the tunnelling limit, the dependence on r_1 could be eliminated and PPT arrived at the result

$$e^{2\text{Im}\delta S} = \left(\frac{2\kappa^3}{F} \right)^{2Q/\kappa}, \quad (3.71)$$

which coincides with the static case (3.66), as we would expect.

3.5.3 Coulomb-corrected SFA (CCSFA)

Of course, while the above calculation nicely confirms the correct result in the tunnelling limit and provides a good benchmark for the Coulomb enhancement of the total ionization rate, it has clearly not solved our overall problem. It has no ability to explain the qualitative and quantitative differences between the shapes of photoelectron spectra predicted by SFA and measured experimentally, and cannot be trusted away from the $\gamma \ll 1$ limit.

The basic premise of the PPT approach, however, is a general one. As we have already seen in Section 3.4.3, the idea of interpreting the SFA amplitude in terms of a classical action is by no means limited to the tunnelling limit or to the optimal trajectory. In light of this, the method described in Section 3.5.2 above has more recently been generalized to arbitrary values of γ and \mathbf{p} . The resultant theory is known as the Coulomb-corrected strong field approximation (CCSFA) [11, 101–104] or trajectory-based Coulomb-SFA (TCSFA) [105, 106].

This theory takes the SFA ionization amplitude for a short range potential as its starting point, and proceeds to modify it based on the PPT arguments introduced above. In particular, the binding potential $U(\mathbf{r})$ is added to the Lagrangian in Eq.(3.63) and the trajectories $\mathbf{r}_p(t)$ are modified to take the Coulomb interaction into account $\mathbf{r}_p \rightarrow \mathbf{r} = \mathbf{r}_p + \mathbf{r}_1$, where the correction \mathbf{r}_1 satisfies

$$\dot{\mathbf{r}}_1 = -\nabla U(\mathbf{r}_p(t)). \quad (3.72)$$

Notice that the photoelectron momentum $\mathbf{p} = \dot{\mathbf{r}} - \mathbf{A}$ is now no longer conserved: it satisfies $\dot{\mathbf{p}} = \dot{\mathbf{r}}_1$ and varies as we move along the trajectory. As a result, the value of \mathbf{p} used when evaluating the saddlepoint time t_s cannot be the same as the momentum measured at the detector. With this in mind, S^{SFA} is replaced by

$$S^{\text{CCSFA}}(\mathbf{p}_d, T) = S^{\text{SFA}}(T, \mathbf{p}_0; t_s(\mathbf{p}_0)) + \int_{t_s(\mathbf{p}_0)}^T U(\mathbf{r}(t')) dt', \quad (3.73)$$

where the momentum at the detector \mathbf{p}_d is related to the momentum \mathbf{p}_0 via $\mathbf{p}_d = \mathbf{p}_0 + \dot{\mathbf{r}}_1$. In principle, therefore, the problem of Coulomb-correcting the SFA amplitude reduces to determining the appropriate \mathbf{p}_d for a given \mathbf{p}_0 (or vice versa) and evaluating the integral over the binding potential $U(\mathbf{r})$. Following PPT, the integration contour is chosen as described in Section 3.4.2.

Note, however, that there is an ambiguity in this approach that we have glossed over so far: namely, the choice of initial conditions for the trajectory \mathbf{r} . When we first introduced the trajectory picture in Section 3.4.3, we saw that the saddlepoint equation (3.56) defined the initial condition for the velocity. However, there was nothing to tell us what the initial condition $\mathbf{r}_0 = \mathbf{r}_p(t_s)$ for the trajectory should be. Indeed, in the context of SFA, we are free to add any constant we like to $\mathbf{r}_p(t)$ – doing so does not affect the SFA phase overall.

For the Coulomb-corrected action S^{CCSFA} , in contrast, this is no longer the case. It is clear from the second term in Eq.(3.73) that the choice of $\mathbf{r}(t_s)$ can have a profound effect on the result. In practice, the initial condition in CCSFA is chosen on physical grounds. The simplest and most natural choice would require that the electron starts its motion from the origin, where the atom or molecule is located: $\mathbf{r}_p(t_s) = \mathbf{r}_0 = 0$. In this case, however, we find that trajectories in general have a constant non-zero imaginary component $i\rho_p$ in the continuum (indeed, this is the case for all trajectories except the optimal). Accumulated under the barrier, we can express this imaginary constant as

$$\rho_p = \text{Im}[\mathbf{r}_p(t_i)] = \text{Im} \int_{t_s}^{t_i} \mathbf{v}_p(\tau) d\tau. \quad (3.74)$$

To simplify calculations and provide a more direct link to two-step models of ionization, the trajectories in CCSFA are instead defined to ensure that continuum trajectories are purely real for real times. This

can be achieved by subtracting off $i\rho_p$ for each trajectory or, in other words, setting the initial condition to be $\mathbf{r}_p(t_s) = \mathbf{r}_0 = -i\rho_p$.

3.5.3.1 Ionization rate for arbitrary γ

Based on this formalism, an expression for the Coulomb correction to the total ionization rate was derived for arbitrary values of γ [102, 103]. The derivation was entirely analogous to the original PPT calculation in the tunnelling limit, discussed in Section 3.5.2. Equation (3.73) was evaluated for the optimal trajectory (for which $\rho_p = 0$) and the action was expanded to first order, so that the trajectory \mathbf{r} along which the integral over the binding potential is evaluated was replaced by the Coulomb-free trajectory \mathbf{r}_{p_d} . As in the PPT derivation, only the first under-barrier leg of the integration contour was considered, and the divergence at $t_s(\mathbf{p}_d)$ was taken care of by matching with the asymptotic tail of the bound wavefunction. In essence, the key difference stemmed from the replacement $\mathbf{p}_d \rightarrow \mathbf{p}_0$ in the SFA part of the action.

Doing so, the PPT result for the tunnelling limit (3.71) was modified as follows:

$$\frac{w^C}{w^{sr}} \approx \left(\frac{2\kappa^3}{F} \right)^{2Q/\kappa} \left(1 + \frac{2}{e} \gamma \right)^{-2Q/\kappa}, \quad (3.75)$$

where e is Euler's number $e = 2.718\dots$. Note that Eq.(3.75) implies that the ionization rate is relatively suppressed as we move away from the tunnelling limit.

3.5.3.2 Photoelectron spectra

To determine the effect of the long range Coulomb interaction on photoelectron spectra, it is necessary to go beyond the optimal trajectory and consider the case for general \mathbf{p} . Reasoning that the first leg of the integration contour over $U(\mathbf{r})$ affects the overall ionization rate but should have a relatively weak effect on the shape of the distribution, only the second leg – between t_i and the observation time T – was considered in [11, 104, 105]. As discussed above, the initial conditions were defined to ensure that trajectories were purely real in the continuum. With no complex quantities and no divergences to worry about, the problem of evaluating the Coulomb-corrected phase (3.73) amounted to solving Newton's equations for the trajectory \mathbf{r} and evaluating a real integral. This was done for elliptically polarized fields in [104] and linearly polarized fields in [11, 105].

More recently, there have also been attempts to extend this to include the contribution coming from the first leg of the integration contour over $U(\mathbf{r})$ – that is, to determine the under-the-barrier Coulomb-correction for general \mathbf{p} , not just the optimal trajectory [106]. In this case, the action was again expanded to first order (so that the integral over U was evaluated along the Coulomb-free trajectory \mathbf{r}_p). However,

in this case no matching procedure was carried out since the postulated initial condition $\mathbf{r}_p(t_s) = -i\rho_p$ ensured that the integral did not diverge at the lower limit.

3.5.3.3 Successes and limitations

To date, the CCSFA approach has successfully reproduced a number of features of photoelectron spectra in strong field ionization. Quantitative agreement has been demonstrated between numerical TDSE calculations and the total rate predicted by Eq.(3.75) [102, 103], the asymmetry of the spectrum for elliptically polarized fields was accurately described [104], and in the case of linear polarization CCSFA was able to explain low energy structures [105] and side lobes [11] in terms of new kinds of trajectories that arise due to the Coulomb interaction and the way in which they interfere. More recently, by considering the under-barrier effect on spectra, CCSFA was used to qualitatively explain the location of interference fringes coming from different trajectories within the same laser cycle [106]. In the latter case, however, quantitative agreement with TDSE calculations was lacking, and the method was found to break down for $\gamma > 1$ when too many unphysical caustic structures began to appear in the spectrum.

As a theory, CCSFA unites elements of both two-step models and the SFA. Like the two-step approach, it is based on a clearly defined physical picture and involves the propagation of classical trajectories in the continuum. However, the way in which these trajectories are treated in this case allows them to retain some of their quantum mechanical nature. This, in turn, makes it possible to describe interference effects missed by the two-step model. In addition to this, since it is based on the SFA rather than the quasistatic tunnelling picture, CCSFA naturally incorporates non-adiabatic effects. As a result, like the SFA, it can be applied well beyond the $\gamma \ll 1$ tunnelling limit.

However, although these factors represent a notable improvement over the two-step model, the CCSFA also suffers from some of its shortcomings. In contrast to the SFA, which was derived directly from the Schrödinger equation, the CCSFA correction to ionization amplitude was postulated on physical grounds, based on well-motivated yet heuristic arguments. One of the consequences of this, for example, is the ambiguity in the choice of initial condition $\mathbf{r}(t_s)$, which can clearly have a considerable effect on the results.

3.5.4 The Coulomb-Volkov approximation (CVA)

Before concluding this section, it is worth mentioning one more approach that has been used to account for Coulomb interactions in strong field ionization, known as the Coulomb-Volkov approximation (CVA) [98, 107–112]. While the CCSFA took the SFA ionization amp-

litude for a short range potential as its starting point, the CVA instead modifies the continuum wavefunction. Recall that the key approximation within the SFA derivation presented in Section 3.3.1.1 consisted of replacing the exact propagator after time t' by the Volkov propagator. Since the true wavefunction should take into account both the laser field and the ionic potential, the use of Volkov states essentially amounts to neglecting the interaction of the outgoing electron with the core. In light of this, the CVA postulates an alternative wavefunction for the continuum, making use of the Coulomb scattering eigenstates $\phi_{\mathbf{k}}^-$, for which an explicit analytical expression is well known. The original SFA ansatz (3.23) is then modified according to

$$a_p^{\text{CVA}}(T) = -i \int_{-\infty}^T \langle \psi_p^{\text{CVA}}(t') | V_L(t') | \psi_b(t') \rangle dt', \quad (3.76)$$

where

$$\psi_p^{\text{CVA}}(\mathbf{r}, t) = \phi_{\mathbf{k}}^-(\mathbf{r}) e^{i\mathbf{A}(t) \cdot \mathbf{r}} e^{iS_V(t, \mathbf{p})}. \quad (3.77)$$

This approach has been used to explain the origin of the asymmetry in elliptically polarized fields [109, 110], and has seen some success in describing the photoelectron spectra in linearly polarized fields [98, 112]. However, the CVA faces a serious problem: the postulated function ψ_p^{CVA} is not a solution to any form of the Schrödinger equation, and as a result it is difficult to assess the accuracy of this approximation or to formulate the conditions under which it can be applied [78]. In [113], it was proposed that the CVA should work reasonably well when $F \ll \omega$, while [111] suggested that it is best applied for very short pulses. In general, however, the applicability of the CVA remains uncertain [78].

3.6 A NEW APPROACH?

As we have seen, the problem of modelling strong field ionization is a difficult one. If we are to simultaneously take into account the strong laser field and the long-range potential of the ionic core, all in the context of an analytical theory, sacrifices will inevitably have to be made. Ideally, however, we would like a theory that

- C₁ Is derived from first principles, based on well-defined approximations. The way in which this is done should leave no room for ambiguity or free parameters.
- C₂ Is a quantum theory, which can, for example, account for interference effects.
- C₃ Works for a broad range of parameters within the strong field regime. In particular, we would like a theory that can be applied beyond the tunnelling limit and is capable of accounting for non-adiabatic effects.

- C₄ Comes with a natural and intuitive physical interpretation.
- C₅ Can account for the long-range Coulomb interaction between the outgoing electron and the core.
- C₆ Has the capacity to take us beyond the single active electron approximation.

Of the above criteria, two step models satisfy only C₄ and C₅. The SFA does considerably better. As we have seen, it fulfils C₁-C₄, though it fails C₅ badly. The CCSFA, which takes the SFA as a starting point, does very well indeed, although in resolving the issue with C₅ it sacrifices C₁ to an extent. Finally, ab initio techniques – though capable of yielding the exact solution (which is a powerful thing indeed) – suffer when it comes to C₄, and begin to face issues with numerical convergence at long wavelengths, which limits their applicability somewhat in terms of C₃.

The final requirement C₆ is something of a wildcard. All theoretical methods discussed so far have described ionization as a one-electron process only. When applied to a multielectron system, this amounts to treating all electrons but one as passive and fixed. However, as we saw Section 2.5, there are certain instances when this treatment is known to be insufficient. The ability to go beyond the SAE is therefore an enticing prospect, particularly in the context of attosecond science.

In light of this, we are prompted to ask: can we do better? Can we go back to first principles and develop a new theory that will allow us to satisfy the above criteria to a greater extent?

In fact, the conceptual ingredients needed to do this have been with us all along. To see this, we need simply go back to our discussion in Section 3.1. There, we argued that simultaneously accounting for $U(\mathbf{r})$ and $V_L(t)$ presents us with a formidable challenge provided that these potentials are of comparable strength and neither can be treated as a small correction. However, even for a strong field, we know that this is not the case everywhere. What saves us is the fact that the binding potential $U(\mathbf{r})$ is localized in space. As a result, in the immediate vicinity of the core, $U(\mathbf{r})$ will dominate and the relative contribution from the laser potential V_L will be small. Conversely, as we move away from the origin, V_L will start to take over as $U(\mathbf{r})$ gradually fades away.

Although it was not emphasized at the time, this argument is, in some sense, integral to the SFA as well. This becomes apparent if we recall the PPT derivation outlined in Section 3.3.1.2. There, the key step relied on assuming that $U(\mathbf{r})$ was a short range potential, which vanished entirely outside of a small region centred about $\mathbf{r} = 0$. Provided this region was sufficiently small, the influence of the laser field could be neglected therein, which made it possible to write down an approximate solution in terms of field-free bound states.

For a Coulomb potential, we know that such an assumption cannot be justified. No matter how far we move away from the atom, the Coulomb tail will still be present. However, the notion of using the spatial localization of the binding potential $U(\mathbf{r})$ to simplify our problem is a powerful one. In particular, it makes it possible to use different approximations in different regions of space. Provided solutions in the two regions can be matched, this in turn enables us to build up a complete, flexible and fully quantum theory, which is nevertheless capable of accounting for the long range interaction of the outgoing electron with the core.

This is the basic idea that underpins the ARM approach to strong field ionization to which the remainder of this thesis is devoted. With it in mind, we are now ready to proceed to the derivation and exploration of the ARM theory itself.

4

SUMMARY OF PUBLICATIONS

[A] TIME-DEPENDENT ANALYTICAL R-MATRIX APPROACH FOR STRONG FIELD DYNAMICS. I. ONE-ELECTRON SYSTEMS

In this paper, the basic ideas and equations of the ARM approach are derived and presented for the first time. In essence, there are two key ingredients which go into making this theory, without which the ARM derivation could not proceed:

1. *The R-matrix method.* Already well established in the numerical community, this approach is based on the idea of partitioning space into different regions and treating each on a different footing [114]. The basic principles of this method lie at the core of ARM and make it possible to formalize our discussion from Section 3.6.
2. *The eikonal-Volkov approximation (EVA).* Within this approximation, the laser field is treated exactly while the electron-core interaction is described using the eikonal approximation [115]. It is accurate as long as the electron remains sufficiently far from the singularity at $r = 0$, and as such will play a crucial role in describing our wavefunction away from the immediate vicinity of the core.

With both of these in hand, the ARM derivation proceeds as follows:

1. First, space is split into two regions, separated by a spherical boundary of radius $r = a$. The inner region encloses the atom or molecule; the outer region comprises the rest of space.
2. In the inner region, the binding potential will dominate. As a result, provided that we have chosen our boundary a correctly, we can neglect V_L or treat it within the quasistatic approximation. The solutions in this region are then simply the bound states of $U(r)$, with a possible correction for Stark shifts and depletion. In general, this is a good approximation for $a \ll I_p/F$: that is, as long as we remain well away from the exit of the tunnelling barrier.
3. In the outer region, in contrast, it will be the laser field that dominates, allowing us to approximate the solution using EVA states. Roughly speaking, this is accurate provided we are sufficiently far from the atom or molecule compared to the characteristic size of the bound state: that is, for $a \gg 1/\kappa$.

4. Following standard R-matrix arguments, the wavefunction in the inner region is projected onto the boundary at $r = a$ and propagated outwards using the EVA propagator. The integral over t' that appears is evaluated using the saddlepoint method as discussed in Section 3.3.2.1.
5. Finally, the a -dependence is eliminated by matching the tail of the bound wavefunction with the Coulomb part of the appropriate EVA solution. The argument we follow here proceeds along similar lines to those used in [96, 102] and sketched in Section 3.5.2. In our case, however, we do not restrict ourselves to the optimal trajectory, but carry out the matching procedure for all values of \mathbf{p} .

The final step is, in fact, the crucial one. In essence, the success of the ARM method hinges on being able to match the inner and outer region solutions. Note that it is only thanks to the Coulomb correction within the EVA that this becomes possible.

Proceeding as outlined above, we arrive at the central result of the one-electron ARM theory:

$$a_p(T) = a_g(t_s) R_{klm}(\mathbf{p}, t_s) e^{-iS^{SFA}(T, \mathbf{p}; t_s)} e^{-iW_C(T, \mathbf{p}; t_s)}, \quad (4.1)$$

Here, $a_g(t_s)$ accounts for Stark shifts and depletion, $R_{klm}(\mathbf{p}, t_s)$ is a prefactor that encodes the angular structure of the initial bound state, S^{SFA} is the SFA phase as defined in Eq.(3.42) and t_s is the complex solution to the SFA saddlepoint equation (3.48). Finally, W_C is the Coulomb phase

$$W_C(T, \mathbf{p}; t_s) = \int_{t_s - i/\kappa^2}^T dt U(r_s(\mathbf{p}, t, t_s)), \quad (4.2)$$

where $r_s(\mathbf{p})$ coincides with the Coulomb-free trajectory r_p defined by Eq.(3.65) if $r_0 = 0$. Note that although Eq.(4.1) was derived for a linearly polarized field in [A], the result above is general. An analogous derivation for circularly polarized fields is presented in [116]. Note also that if we define the subcycle ionization amplitude $a_p(t)$ by projecting the wavefunction at time t onto the plane wave basis $|\mathbf{p} + \mathbf{A}(t)\rangle$, we find that it takes precisely the same form as our expression for $a_p(T)$ above. As such, Eq.(4.1) can be applied for arbitrary t , not just large T after the laser pulse has been switched off.

From the above, it is immediately clear that ARM has a lot in common with the SFA. Indeed, when W_C vanishes, it is straightforward to check that Eq.(4.1) coincides exactly with the PPT result for a short range potential [55]. Compared with CCSFA, the similarities are even greater. Recalling our discussion in Section 3.5.3, we see that the Coulomb phase W_C is of the same form as the second term in the CCSFA action (3.73) when it is expanded to first order.

However, there are also a number of decisive differences. Perhaps the most important is the fact that, in contrast to CCSFA, in ARM we are not free to choose the initial conditions for the trajectories \mathbf{r}_s at will. Instead, they are completely fixed by the matching procedure, such that $\mathbf{r}_s(t_s) = 0$. As a consequence, we find that the trajectories in ARM have a non-zero imaginary component in the continuum in general, in sharp contrast to the trajectories defined in CCSFA. Indeed, we can see this explicitly in Eq.(84) in [A], which gives the analytical expression for \mathbf{r}_s for a long linearly polarized pulse. If we note that $p_z = F/\omega \sin \phi_i \cosh \phi_\tau$ and $\phi \equiv \omega t$, we find that the real part of the continuum trajectory \mathbf{r}'_2 almost exactly coincides with the simpleman expression (3.14). The only difference is the $\cosh \phi_\tau$ in the second term, which accounts for the location of the barrier exit. However, on top of this, we also have a constant imaginary component \mathbf{r}''_2 which is not present in any two- or three- step model or in the CCSFA. This is not a matter of convention, but a fundamental feature of the ARM theory. As we shall see in Papers [C],[D] and [E], these complex components have a crucial role to play in describing the interaction between the departing electron and the core, and consequently in producing quantitatively accurate results.

[B] TIME-DEPENDENT ANALYTICAL R-MATRIX APPROACH FOR STRONG FIELD DYNAMICS. II. MANY-ELECTRON SYSTEMS

Up until this point, all theoretical approaches considered in this thesis have worked within the SAE approximation. However, as we saw in Section 2.5, this may not always tell the whole story. In light of this, in [B] we show how the ARM method can be extended to multielectron systems, and in particular how it can be used to describe excitations of the ionic core induced by the outgoing electron. Such excitations are closely related to the shake-up process discussed in Section 2.5.

In the multielectron case, we assume that both the outgoing photo-electron and the ion it leaves behind can be measured. To find our observable, we therefore project our full N-electron wavefunction onto a quasistatic ionic basis labelled by n and the final state of the continuum electron $|\mathbf{p}\rangle$. Using the Dyson series to expand this to first order in interactions between the outgoing electron and the electrons that remain in the ion, we obtain the ionization amplitude as a sum of two contributions:

1. First, we have the direct channel, given by

$$a_n^{(d)}(\mathbf{p}, t) = \langle n_t | U^{N-1}(t, t_s) | n_{t_s} \rangle e^{-iE_n t_s} a_n^{(1e)}(\mathbf{p}, t) \quad (4.3)$$

Here $a_n^{(1e)}$ is the one-electron ionization amplitude, as derived in [A], where the remaining electrons are fixed in ionic state n . In this case, no excitation is induced by the outgoing electron

– the ion remains in state n throughout – and the SAE result is simply corrected by a factor describing the evolution of the ionic core in the laser field. Treated quasistatically, the prefactor accounts for Stark shifts and the laser polarization of the ion.

2. Second is the correlation-driven channel – the central result of [B]:

$$a_{mn}^{(c)}(\mathbf{p}, t) = c_{mn}(t, t_s) e^{-iE_n t_s} a_n^{(1e)}(\mathbf{p}, t), \quad (4.4)$$

where

$$c_{mn}(t, t_s) = -i \int_{t_s}^t dt'' \langle m_{t,t''} | V_{ee}^n(\mathbf{r}_s(t'')) | n_{t'', t_s} \rangle \times e^{-iQ_{mn}(t'')}. \quad (4.5)$$

Here, V_{ee}^n describes the Coulomb interaction between the photoelectron and the electrons which remain in the ion. It is evaluated along the departing electron's trajectory \mathbf{r}_s . The correction $Q_{mn}(t'')$, defined by Eq.(49) in [B], accounts for the difference between the effective potential experienced by the departing electron when the ion is in state m and n respectively. We expect it to have a relatively minor effect on results. Note, also, that we have used the shorthand $|n_{t_2, t_1}\rangle = U^{N-1}(t_2, t_1)|n_{t_1}\rangle$ when describing the evolution of our ionic states in Eq.(4.5).

The above result captures the situation in which the ion transitions from state n to state m during the course of the ionization process due to an interaction with the outgoing electron. Drawing on the same reasoning that allowed us to interpret t' as the time of ionization in Section 3.3.1.1, we can think of the time t'' as the time at which this excitation occurred.

Importantly, Eq.(4.4) tells us that the ionization amplitude in the correlation driven channel again factorizes into the SAE result and an additional term describing the dynamics of the ion, just like it did in the direct case. As a result, the problem of determining the contribution of correlation-driven excitations reduces to evaluating the matrix element $\langle m | V_{ee}^N(\mathbf{r}_s) | n \rangle$ along the trajectory of the departing electron.

Having established the basic equations of multielectron ARM, the remainder of [B] is dedicated to exploring the relative importance of the correlation-driven channel for the strong field ionization of N_2 and CO_2 molecules. The results indicate that, depending on the way in which the molecule is aligned relative to the laser field and the shape of the orbitals in question, the correlation-driven channel can indeed become important under typical experimental conditions.

[C] TIME-RESOLVING ELECTRON-CORE DYNAMICS DURING STRONG FIELD IONIZATION IN CIRCULARLY POLARIZED FIELDS

In [C], we turn our attention to the calculation of photoelectron spectra for strong field ionization by a long circularly polarized pulse. This represents the most natural place to begin our exploration of the ARM theory and its predictions for a reason that harks back to our discussion in Section 3.2.4. There, we noted that trajectories in circularly polarized fields never return to the core. As a result, we do not have to worry about recombination or rescattering, which simplifies things considerably.

As we have already discussed, it is the Coulomb correction term W_C that distinguishes the one-electron ARM theory from the SFA and related approaches. Here, we begin exploring some of its major features and physical consequences. To do so, it is sufficient to consider the simplest case of a spherically symmetric state with $l = m = 0$ and to neglect the prefactor $a_g(t_s)$. When calculating the ionization amplitude we also focus only on saddlepoints that lie within a single laser cycle: for a long circularly polarized pulse, there will be one such solution for each final momentum \mathbf{p} . In doing so, we effectively obtain the ARM equivalent to $a_p^i(T)$ in Eq.(3.52) – that is, the envelope of the photoelectron spectrum, onto which ATI peaks are superimposed.

To evaluate the complex integral in W_C , we choose the same contour introduced in Section 3.4.2, again associating each of the two legs with the electron's motion under the barrier and in the continuum respectively. Just as in the linear case, we find that the real parts of the continuum trajectories coincide with their simpleman counterparts (given by Eq.(3.17), (3.18) in Section 3.2.3.3), with the exception of a $\cosh \phi_\tau$ term that accounts for the location of the barrier exit. However, in addition to this, we again have a constant imaginary component in the continuum which varies with \mathbf{p} and only vanishes for the optimal SFA trajectory. Do these imaginary components have a physical significance or is this merely a mathematical curiosity?

Our results clearly demonstrate the former to be the case. In particular, we observe that during the continuum leg

1. The Coulomb correction term shifts the SFA distribution to lower momenta as the electron moves away from its parent atom. The physical interpretation here is clear: the electron is decelerated by the positively charged ion on its way to the detector.
2. The total ionization rate continues to vary for $t > t_i$, before asymptoting to a final value. This suggests that, in contrast to our discussion in Section 3.4.2, ionization isn't fully completed by time t_i when a long-range potential is involved. We propose that this might reflect the transient trapping of the outgoing electron into Rydberg states.

Within ARM, both of these very physical effects are a direct consequence of the imaginary components of the continuum trajectories. Indeed, if r_s were purely real, we would accumulate only a phase in the continuum, and neither the shape nor the magnitude of $a_p(t)$ would be affected after time t_i . The importance of such effects is validated in [D] and [E], where we compare the predictions of ARM with exact ab initio simulations.

As a final remark, note that due to the complex nature of our trajectories, it is necessary to use an analytical continuation for the potential $U(r)$. Upon doing so, it is important to pay attention to branch cuts and singularities when choosing the integration contour.

[D] AB INITIO VERIFICATION OF THE ANALYTIC R-MATRIX THEORY FOR STRONG FIELD IONIZATION

Having developed a procedure for calculating photoelectron spectra, another question naturally arises: how well does the ARM theory work in practice? After reviewing some of the most important features of the ARM approach, we address this question in [D]. In particular, we compare the predictions of ARM with exact ab initio TDSE calculations for the strong field ionization of hydrogen and helium atoms by long circularly polarized laser pulses. Focussing on energy-resolved photoelectron spectra, we find excellent agreement across a range of parameters.

[E] INTERPRETING ATTOCLOCK MEASUREMENTS OF TUNNELLING TIMES

So far, our discussion of the ARM theory has primarily focussed on computing physical observables. In this capacity, we have seen that ARM is able to produce highly accurate photoelectron spectra using only a fraction of the time and computational resources required for the exact ab initio calculation. However, as already discussed in the context of two-step models and the SFA, analytical approaches come with another distinct advantage over their fully numerical counterparts – namely, the ability to look inside the ionization process itself. In [E], it will be this aspect of the ARM theory that comes into its own.

In particular, in this paper we focus on exploring the physics behind a recently developed experimental setup known as the attoclock [12–14], which aims to time-resolve ionization in the strong field regime. The basic idea is a simple one. If we describe ionization as a tunnelling process, we know that a circularly polarized field creates a barrier that rotates with time at a constant rate. Since the orientation of the barrier determines the direction in which the electron tunnels, this gives us a mapping between angle and time, just like a regular

analogue clock. The only other ingredient we need is the ability to resolve this – that is, we would like the probability of ionization to vary with time as well. The latter is achieved by the use of a short pulse, which ensures that the width of the barrier changes as it rotates. The resultant photoelectron spectrum is then maximized at some angle θ_{peak} , as shown in Fig.1.(c) in [E].

Having obtained a photoelectron spectrum, the next step is the crucial one. Given a particular angle of detection, we would like to know what the corresponding time of ionization was. Since time itself is not an observable, this is only possible by using a theory in which the concept of ionization times is well defined. As we have seen, this is indeed the case for two-step models, as well as the SFA and related approaches. Ab initio numerical methods, on the other hand, remain silent in this regard. Note also that, inherently, the accuracy of the reconstruction will only be as good as the theory we use.

In the context of both the simpleman model and the SFA, we have explicitly come across a relationship between angle and ionization time already. Recalling our discussion in Sections 3.2.3.3 and 3.4.1.1, we find that in both cases we have the very simple mapping given by Eq.(3.19):

$$t_i^{\text{SFA}} = \frac{\theta}{\omega}. \quad (4.6)$$

Based on this relationship, if the laser field reaches its maximum intensity at $t = 0$, we would at least naively expect the photoelectron spectrum to attain its maximum at $\theta_{\text{peak}} = 0$.

Exact ab initio calculations, however, reveal a different picture. As Fig.3 in [E] shows, offset angles θ_{peak} for the hydrogen atom are positive across all intensities, ranging from 5 to 17 degrees. Based on the above SFA mapping, this would suggest that ionization occurred ~ 100 attoseconds after the peak of the pulse. Could this represent a real tunnelling delay, or is there another factor at play?

In [E], we address this question by using the ARM theory in conjunction with exact numerical simulations. As we have discussed extensively throughout this thesis, the key shortcoming of the SFA, like the simpleman model before it, is the neglect of the long-range Coulomb interaction between the outgoing electron and the core. At the same time, as depicted schematically in Fig.1(b) in [E], it is apparent that deflection by the positively charged ion could also lead to positive values for θ_{peak} . To what extent could such electron-core interactions be responsible for the offset angles we observe?

As a first step towards answering this question, the numerical calculations for hydrogen were repeated for a short-range Yukawa potential. In this instance, the tunnelling barrier is still present (albeit with a somewhat altered shape); however, the long-range interaction between the core and the outgoing electron is completely suppressed. As shown in Fig.3 in [E], we find that offset angles in this case vanish across all intensities. This, in turn, is a strong indication that it is the

Coulomb interaction that is responsible for the positive offset angles we saw for hydrogen.

Although this is a powerful result, such numerical calculations cannot directly say anything about the ionization times themselves. To do so, we now turn to ARM. Here, following the same logic as Section 3.4, we can interpret the real part of the saddlepoint solution as the time of ionization, just as we did for the SFA. This, in turn, will provide us with the ARM equivalent to Eq.(4.6): a mapping $t_i = t_i(\theta, p)$ between the experimental observables and the time at which the electron appeared in the continuum.

In our investigation of the ARM theory so far, we have been evaluating the ionization amplitude (4.1) at the SFA saddlepoint t_s^{SFA} . Since W_C represents a relatively small correction to the SFA phase, this is indeed adequate when describing photoelectron spectra for long pulses, as we have seen. To accurately model the attoclock, however, we need to do better: we must go back to the full saddlepoint equation

$$\frac{\partial S^{\text{SFA}}}{\partial t'} \Big|_{t'=t_s} + \frac{\partial W_C}{\partial t'} \Big|_{t'=t_s} = 0 \quad (4.7)$$

and Coulomb-correct our saddlepoints as well. Upon doing so, Eq.(4.6), is modified as follows:

$$t_i(\theta, p) = \frac{\theta}{\omega} + \Delta t_i^{\text{env}}(\theta, p) + \Delta t_i^C(\theta, p), \quad (4.8)$$

where Δt_i^{env} and Δt_i^C are corrections coming from the pulse envelope and the Coulomb phase W_C respectively. In practice, Δt_i^{env} is found by numerically solving the SFA saddlepoint equation for a given pulse shape, while the $\Delta t_i^C = \text{Re}[\Delta t_s^C]$ can be evaluated using

$$\Delta t_s^C = -\frac{dW_C|_{\kappa=\text{const.}}}{dI_p}. \quad (4.9)$$

With this improved mapping in hand, it is possible to use the ARM theory to reconstruct the most probable time of ionization for any given photoelectron spectrum: we do this by evaluating $t_i(\theta_{\text{peak}}, p_{\text{peak}})$. Using the exact numerical calculations for hydrogen as our source of experimental data, the results of this reconstruction are presented in Fig.5(a) in [E]. Notice, now, that the ionization times are never positive: they vanish at moderate intensities and become slightly negative for $I > 1.5 \times 10^{14} \text{ W/cm}^2$. This tells us that the electrons appeared in the continuum either exactly at the peak of the pulse or slightly earlier – where the latter observation can be explained by the depletion of the ground state, along with possible non-adiabatic dynamics of the kind discussed in [C]. In both cases, however, our results imply the absence of real tunnelling delays associated with the electron's motion under the barrier, thereby addressing what is a highly controversial and longstanding question in quantum mechanics. By

calibrating the attoclock experiment for the single-electron case, this work also opens the way to study multielectron dynamics.

Part II
THE PUBLICATIONS

Time-dependent analytical *R*-matrix approach for strong-field dynamics. I. One-electron systems

Lisa Torlina and Olga Smirnova

Max Born Institute, Max Born Strasse 2a, 12489 Berlin, Germany

(Received 2 May 2012; published 5 October 2012)

We develop a flexible analytical approach to describe strong-field dynamics in atoms and molecules. The approach is based on the ideas of the *R*-matrix method. Here, we illustrate and validate our approach by applying it to systems with one active electron bound by the Coulomb potential and benchmark our results against the standard theory of Perelomov, Popov, and Terent'ev [Sov. Phys. JETP 23, 924 (1966)]. We discuss corrections to the ionization amplitude associated with the interplay of the Coulomb potential and the laser field on the sub-laser cycle time scale and the shape of the tunneling wave packets associated with different instants of ionization.

DOI: 10.1103/PhysRevA.86.043408

PACS number(s): 32.80.Rm, 42.50.Hz, 33.80.Wz

I. INTRODUCTION

One of the most powerful ideas in describing scattering and ionization in multielectron systems is embedded in the *R*-matrix method [1], which partitions the space into outer and inner regions. This partitioning reflects different dynamics of the two interacting subsystems, for example, ion and liberated electron in the case of one-electron ionization. The outer region corresponds to the electron being sufficiently far away from the ionic core. The words “*sufficiently far*” imply that a simplified description of the electron-core interaction is possible, for example, neglecting electron exchange. Dynamics in the inner region, on the other hand, could be very complex, but the limited volume of the inner region offers important simplifications, such as the possibility to use the theoretical machinery already developed for bound states of multielectron systems.

The goal of this paper is to develop an analytical description that would take advantage of the *R*-matrix concept: the analytical *R*-matrix method (ARM). When it comes to analytical or semianalytical methods in strong laser fields, dividing the space into inner and outer regions also offers benefits. Indeed, the root difficulty of analytical approaches in strong-field dynamics is the need to include both types of electron interactions—with the laser field and with the ionic core—beyond the standard time-dependent perturbation theory. This difficulty is naturally resolved in the outer region, where the electron is sufficiently far away from the Coulomb singularity of the ionic core. In this region, the strong-field eikonal-Volkov approximation [2] becomes quite accurate [3]. Thus, the separation of space into inner and outer regions naturally accommodates the possibility of an analytical or semianalytical description in the outer region. Correlation-induced coupling between different ionization and/or scattering channels in the outer region can also be included, for example, within first-order perturbation theory in correlations between the outgoing and core electrons. This is the subject of our companion paper [4], which looks at correlation-induced excitation of the ion during ionization [5,6].

In the context of using an analytical description for laser-driven dynamics in the outer region, we bring the reader's attention to the series of papers by A. Scrinzi and co-workers [7–10]. The numerical t-SURFF approach developed in these papers applies an *R*-matrix-type principle and uses Volkov states to propagate the continuum wave function in the outer region. Transfer onto the Volkov states is done at the boundary

between inner and outer regions. Since Volkov states are exact solutions for the laser-driven continuum dynamics in the absence of interaction with the core, the boundary of the outer region has to be chosen beyond the range of the core potential. However, even for the long-range Coulomb potential, accurate results can be achieved with a very reasonable size of the inner region (~ 100 a.u.), turning off the interaction beyond the boundary. The major advantage of the method is that propagation in the outer region is fully analytic, making this approach computationally very efficient.

The introduction of inner and outer regions naturally leads to the idea of electron trajectories which enter and leave the inner region under the action of the strong laser field (see below). The wave function is naturally decomposed into a sum of components associated with a different number of returns into the inner region. From the perspective of the electron-ion recollision model in the strong laser field [11–13], the ARM formulation allows one to separate electron collisions with the parent ion into soft and hard. Soft collisions correspond to trajectories that stay outside the inner region; hard collisions correspond to those trajectories that cross into the inner region. With the dynamics built around semiclassical trajectories, hard collisions correspond to small impact parameters and lead to large-angle scattering. Following large-angle scattering, the scattered electron acquires high energy from the strong laser field and leaves the interaction region for good; a second hard collision is highly unlikely. Thus, the expansion of the wave function in the number of hard collisions should converge quickly.

The development of consistent approximations for the inner region must take into account the energy of the electron entering this region. During the ionization step, when the total electron energy is negative, the wave function in the inner region is dominated by the initial bound state, introducing a well-defined source term for the outer region. If the electron is driven back into the inner region by the laser field, one can rely on the fact that the electron spends only a short time in the inner region, and hence treat the effects of the laser field perturbatively during that time (see, e.g., [14]). To zeroth order, this treatment corresponds to the ansatz of so-called quantitative rescattering theory [15], which uses field-free scattering and/or recombination amplitudes and cross sections for describing the recollision step. Short scattering times justify this approach [14,16]. At the same time, such important effects in laser-driven recollision as Coulomb-laser coupling [17] and

laser-assisted Coulomb focusing [18] (which increase overall recollision cross sections by orders of magnitude [14]), absent in quantitative rescattering theory, can naturally be included as they are dominated by dynamics in the outer region. The ARM is also well suited for the description of strong-field driven time-resolved electron holography [19,21], which focuses on the interference of the strongly scattered object wave and the weakly scattered reference wave. The reference wave is the component of the wave function that stays in the outer region at all times. The object wave is the component of the wave function re-entering the inner region after ionization.

Finally, the emergence of electron trajectories originating from the inner region naturally suggests the application of semiclassical approaches in the spirit of techniques developed in [21–23]. In this context, one can use the analytical description of the wave packet created during the ionization step as the initial condition for trajectory-based techniques. The ionization step is challenging for trajectory-based methods as it often involves tunneling. The structure of the wave packet as it emerges from the classically forbidden region is analyzed in Sec. IV.

The paper is organized as follows: Section II outlines the main ideas and the basic formalism of the ARM. Section III applies this formalism to the canonical problem of strong field ionization from a Coulomb potential and compares results with the standard theory of Perelomov, Popov, and Terent'ev (PPT) [24]. Section IV analyzes the subcycle tunneling dynamics and shows how different momentum components of the tunneled wave packet are formed. Section V describes sublaser cycle effects associated with the long-range tail of the Coulomb potential, absent in standard PPT theory. Section VI concludes the paper.

II. BASIC FORMALISM AND APPROXIMATIONS

We partition the configuration space into an inner (1) and an outer region (2), separated along the boundary of a sphere with radius a [Fig. 1(a)]. Usually, dealing with laser-induced dynamics, one attempts to solve the initial value problem:

$$i \frac{\partial}{\partial t} \Psi(\mathbf{r}, t) = \hat{H} \Psi(\mathbf{r}, t), \quad (1)$$

$$\Psi(\mathbf{r}, t = t_0) = \Psi_g(\mathbf{r}), \quad (2)$$

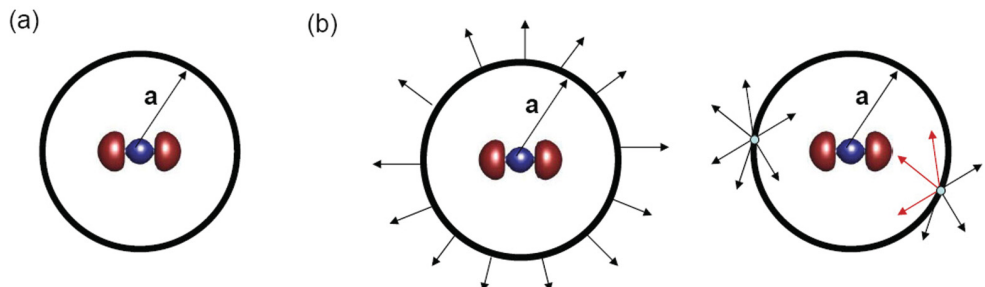


FIG. 1. (Color online) (a) Partitioning of the configuration space. (b) Schematic representation of the boundary condition for the exact Green's function (left) and the approximate eikonal-Volkov Green's function used in this paper (right). Note that the eikonal-Volkov approximation includes unwanted incoming solutions, indicated by the red arrows. However, in strong-field ionization problems, such pathways have to traverse the classically forbidden region to reach the origin. Therefore, they are strongly suppressed and introduce only exponentially small errors.

where \hat{H} is the Hamiltonian of the system and Ψ_g is its ground state, where the system resides prior to the turning on of all laser pulses.

However, if we want to find a solution of Eq. (1) in the outer region (2), we have to take into account that, due to the presence of the boundary, the operator \hat{H} is not Hermitian in both region (1) and region (2) separately [25] (see Appendix A; the culprit is the radial part \hat{K}_r of the kinetic energy operator \hat{K}). Hermiticity is recovered if we compensate for the boundary terms which result from \hat{K}_r acting in the half space. The compensation is achieved by adding the Bloch operator [1,25]

$$\hat{L}^\pm(a) = \pm \delta(r - a) \hat{B}, \quad (3)$$

where the differential operator at the boundary in the r representation is

$$\hat{B} = \frac{d}{dr} + \frac{1 - b}{r}. \quad (4)$$

Here, b is an arbitrary constant (which we later fix), and the δ function is defined such that

$$\int_a^\infty dr \delta(r - a) = \int_0^a dr \delta(r - a) = \frac{1}{2} \quad (5)$$

(see Appendix A for detailed discussion and derivation). The operator $\hat{L}^+(a)$ makes the Hamiltonian Hermitian in the inner region, while $\hat{L}^-(a) = -\hat{L}^+(a)$ does the same for the outer region.

Thus, we rewrite the time-dependent Schrödinger equation (TDSE) as follows:

$$i \frac{\partial}{\partial t} \Psi(\mathbf{r}, t) = [\hat{H} + \hat{L}^\pm(a)] \Psi(\mathbf{r}, t) - \hat{L}^\pm(a) \Psi(\mathbf{r}, t), \quad (6)$$

for the inner (+) and outer (−) region. We can now use the Bloch operator to reformulate Eq. (1) as a boundary problem [25]:

$$\begin{aligned} i \frac{\partial}{\partial t} \Psi(\mathbf{r}, t) - \hat{\mathcal{H}}^{(\pm)} \Psi(\mathbf{r}, t) &= -\hat{L}^\pm(a) \Psi(\mathbf{r}, t) \\ &= \mp \delta(r - a) B(a, \theta, \phi, t), \\ B(a, \theta, \phi, t) &= \hat{B} \Psi(\mathbf{r}, t)|_{r=a} \\ &= \left(\frac{d}{dr} + \frac{1 - b}{r} \right) \Psi(\mathbf{r}, t)|_{r=a}. \end{aligned} \quad (7)$$

The Hermitian Hamiltonian $\hat{\mathcal{H}}^{(+)} = \hat{H} + \hat{L}^+(a)$ describes electron dynamics in the inner region, while in the outer region we have the Hermitian Hamiltonian $\hat{\mathcal{H}}^{(-)} = \hat{H} + \hat{L}^-(a) = \hat{H} - \hat{L}^+(a)$. The solution of the inhomogeneous equation with the boundary condition Eqs. (7) can be written via the Green's function $\mathcal{G}^a(\mathbf{r}, \mathbf{r}', t, t')$ of the corresponding homogenous equation. For the outer region we have

$$\Psi_{\text{out}}(\mathbf{r}, t) = -i \int d\mathbf{r}' \int_{-\infty}^t dt' \mathcal{G}_{\text{out}}^a(\mathbf{r}, t, \mathbf{r}', t') \times [-\hat{L}^-(a)\Psi(\mathbf{r}', t')]_{r'=a}, \quad (8)$$

where the Green's function in the outer region,

$$\mathcal{G}_{\text{out}}^a(\mathbf{r}, t, \mathbf{r}', t') = \langle \mathbf{r} | e^{-i \int_{t'}^t \hat{\mathcal{H}}^{(-)} d\tau} | \mathbf{r}' \rangle, \quad (9)$$

incorporates the boundary (note the Hamiltonian $\mathcal{H}^{(-)}$) and should describe waves outgoing from the boundary at t' [Fig. 1(b)]. Thanks to the localized action of the Bloch operator, the solution is obtained as long as we know the wave function $\Psi(\mathbf{r}, t)_{r=a}$ and its derivative at any time t at the boundary $r = a$. Note that the required wave function at the boundary is exact and, formally, fully incorporates effects of the laser field. Equation (8) is complemented by the wave function in the inner region,

$$\Psi_{\text{in}}(\mathbf{r}, t) = -i \int d\mathbf{r}' \int_{-\infty}^t dt' \mathcal{G}_{\text{in}}^a(\mathbf{r}, t, \mathbf{r}', t') \times [-\hat{L}^+(a)\Psi(\mathbf{r}', t')]_{r'=a} \quad (10)$$

with

$$\mathcal{G}_{\text{in}}^a(\mathbf{r}, t, \mathbf{r}', t') = \langle \mathbf{r} | e^{-i \int_{t'}^t \hat{\mathcal{H}}^{(+)} d\tau} | \mathbf{r}' \rangle. \quad (11)$$

In the numerical implementation of the R -matrix approach, both time-independent [1] and the recently developed time-dependent method [26], the boundary of the sphere is taken rather far from the core. In our analytical work, however, we keep the boundary relatively close (the exact conditions will be defined later). We can then use Eqs. (8) and (10) to develop a series in the number of “crossings” of the boundary, leading to hard collisions.

First, the exact laser-dressed wave function at the boundary is approximated with its ground-state component, leading to the following solution in the outer region:

$$\Psi_{\text{out}}^{(1)}(\mathbf{r}, t) = i \int d\mathbf{r}' \int_{-\infty}^t dt' \mathcal{G}_{\text{out}}^a(\mathbf{r}, t, \mathbf{r}', t') \times [\hat{L}^-(a)\psi_g(\mathbf{r}')]_{r'=a} a_g(t') e^{-iE_g t'}. \quad (12)$$

Here $a_g(t)$ includes the Stark shift of the field-free ground-state energy E_g and the decay of the norm of the ground-state component $\phi_g(\mathbf{r}')$ of the total wave function in the inner region. This approximation is reasonably far from saturation, when most of the wave function resides in the laser-polarized ground state. The expression is similar to the starting point of effective-range theory [27–29] for strong-field dynamics in short-range potentials, which are described by the effective boundary condition. The difference, however, is that here the wave function on the left-hand side of Eq. (12) is defined only outside the boundary.

In turn, $\Psi_{\text{out}}^{(1)}(\mathbf{r}, t)$ can be substituted into the equation for the inner region [Eq. (10)], describing the wave packet entering

the inner region from the outside

$$\Psi_{\text{in}}^{(2)}(\mathbf{r}, t) = i \int d\mathbf{r}' \int_{-\infty}^t dt' \mathcal{G}_{\text{in}}^a(\mathbf{r}, t, \mathbf{r}', t') [\hat{L}^+(a)\Psi_{\text{out}}^{(1)}(\mathbf{r}', t')]_{r'=a}. \quad (13)$$

The next term in the series is $\Psi_{\text{out}}^{(3)}(\mathbf{r}, t)$, describing the wave packet that escapes into the outer region for the second time [$\Psi_{\text{out}}^{(1)}(\mathbf{r}, t)$ being the first]. Limiting the series to one “hard recollision” implies that it is terminated at $\Psi_{\text{in}}^{(2)}(\mathbf{r}, t)$ for the inner region and $\Psi_{\text{out}}^{(3)}(\mathbf{r}, t)$ for the outer region.

The utility of this series becomes clear when the semi-classical approximation is used for the propagators. Then tunneling is described by trajectories moving in complex time (see [24,30]). Once one is able to (i) introduce trajectories leaving the inner region for the first time in Eq. (12) and (ii) describe their motion through the classically forbidden region analytically, further evolution of these trajectories in real time can be described numerically without further partitioning the coordinate space into regions (1) and (2), incorporating the ionization step into the trajectory-based methods developed in [21,22].

Let us now replace $\mathcal{G}_{\text{out}}^a$ in Eq. (8) by an approximate Green's function for the outer region. To this end, we use the eikonal-Volkov approximation (EVA) [2]. We have shown that the EVA propagator $\mathcal{U}^{\text{EVA}}(t, T)$ is accurate for describing strong-field ionization for nonsingular core potentials $U(\mathbf{r})$ [3]. Thus, it is natural to apply it in the outer region. As Fig. 1(b) shows, unlike the true propagator, our approximation allows incoming as well as outgoing solutions at the boundary. However, in strong-field ionization such undesirable incoming pathways have to traverse an additional classically forbidden region. As a result, they decay exponentially and only introduce exponentially small errors in our calculations (see Appendix B).

The propagator $\mathcal{U}^{\text{EVA}}(t, T)$ is constructed using the EVA to find eigenstates (quasienergy states) of the time-dependent Hamiltonian describing an arbitrary one-electron system bound by a potential $U(\mathbf{r})$ and interacting with a strong laser field $V_L(t) = \mathbf{r} \cdot \mathbf{F}(t) \cos(\omega t)$:

$$\hat{H} = \frac{\hat{\mathbf{p}}^2}{2} + U(\mathbf{r}) + \mathbf{r} \cdot \mathbf{F}(t) \cos(\omega t). \quad (14)$$

Here $\mathbf{F}(t) = \mathbf{F} f_L(t)$ includes the field envelope $f_L(t)$, \mathbf{F} is the peak field strength, and ω is the laser field frequency. The EVA states $|\mathbf{p}_T^{\text{EVA}}(t)\rangle$ are defined via backpropagation of field-free eikonal continuum states $|\mathbf{p}^E\rangle$ from time $t = T$ after the end of the laser pulse to time t , when the pulse is on:

$$|\mathbf{p}_T^{\text{EVA}}(t)\rangle = \mathcal{U}^{\text{EVA}}(t, T)|\mathbf{p}^E\rangle, \quad (15)$$

where $\mathcal{U}^{\text{EVA}}(t, T)$ is the EVA propagator. The field-free states $|\mathbf{p}^E\rangle$ are characterized by their asymptotic momentum \mathbf{p} , and the superscript E in $|\mathbf{p}^E\rangle$ stands for “eikonal.” In coordinate representation

$$\langle \mathbf{r} | \mathbf{p}^E \rangle = (2\pi)^{-3/2} e^{i\mathbf{p} \cdot \mathbf{r}} e^{iG_{0\mathbf{p}}(\mathbf{r})}, \quad (16)$$

where the $G_{0\mathbf{p}}(\mathbf{r})$ describes the distortion of the phase front, compared to the plane wave, at position \mathbf{r} . Equation (16) sets the initial condition for the propagation of EVA states at $t = T$.

The states are [2]

$$\langle \mathbf{r} | \mathbf{p}_T^{\text{EVA}}(t) \rangle = \left[\frac{1}{(2\pi)^{3/2}} e^{i(\mathbf{p} + \mathbf{A}(t)) \cdot \mathbf{r} - \frac{i}{2} \int_t^T d\tau [\mathbf{p} + \mathbf{A}(\tau)]^2} \right] \\ \times e^{-i \int_t^T d\tau U(\mathbf{r}_L(\tau; \mathbf{r}, \mathbf{p}, t))} e^{i G_{0p}(\mathbf{r}_L(T; \mathbf{r}, \mathbf{p}, t))}. \quad (17)$$

The term in square brackets is the usual Volkov wave function, with the vector-potential $\mathbf{A}(t)$ defined as $\mathbf{F}(t) = -\frac{d}{dt} \mathbf{A}(t)$. In this paper we consider the laser field linearly polarized along the z axis. The next-to-last term in Eq. (17) represents the core potential-induced distortion of the phase front along electron trajectories in the laser field \mathbf{r}_L . The trajectory $\mathbf{r}_L(\tau) \equiv \mathbf{r}_L(\tau; \mathbf{r}, \mathbf{p}, t)$ starts at the point \mathbf{r} at the moment t and is characterized by the asymptotic (canonical) momentum \mathbf{p} :

$$\mathbf{r}_L(\tau; \mathbf{r}, \mathbf{p}, t) = \mathbf{r} + \int_t^\tau dt'' [\mathbf{p} + \mathbf{A}(t'')]. \quad (18)$$

The last term in Eq. (17) is associated with the phase distortion of the field-free states and ensures continuity of the solutions given by Eq. (17) at $t = T$. Improper choice of the initial condition would, in general, degrade the accuracy of the approximation [2]. However, if T is sufficiently large and the drift momentum of the electron is nonzero, $\mathbf{r}_L(T; a, \mathbf{p}, t) \rightarrow \infty$ for $T \rightarrow \infty$ and $G_{0p}(\mathbf{r}_L(T; \mathbf{r}, \mathbf{p}, t)) \rightarrow 1$, which is equivalent to substituting the eikonal initial condition by the plane wave at very large distances. The relevant distortion of the plane wave front is then accumulated under the combined action of both the core potential and the laser field, as the wave front is backpropagated towards the core.

Using the EVA states, we can write the following EVA Green's function:

$$G^{\text{EVA}}(\mathbf{r}, t, \mathbf{r}', t') = \langle \mathbf{r} | \mathcal{U}^{\text{EVA}}(t, t') | \mathbf{r}' \rangle \\ = \theta(t - t') \int d\mathbf{p} \langle \mathbf{r} | \mathbf{p}_T^{\text{EVA}}(t) \rangle \langle \mathbf{p}_T^{\text{EVA}}(t') | \mathbf{r}' \rangle. \quad (19)$$

This expression can then be substituted into Eq. (12) to calculate the wave function in the outer region. Thanks to the boundary nature of the Bloch operator, the trajectories \mathbf{r}_L around which the EVA states and EVA propagator are built originate from the boundary. The approximation requires that they stay outside the inner region and hence describes only the so-called “direct” electrons, which do not experience hard recollisions with the core. The expression for $\Psi_{\text{out}}^{(1)}(\mathbf{r}, t)$ (12) using the EVA Green's function introduced above (19) can be effectively analyzed using the saddle-point method as we discuss below.

The ionization amplitude is obtained by projecting $\Psi_{\text{out}}(\mathbf{r}, t)$ on the field-free eikonal states $|\mathbf{p}^E\rangle$ in the same region:

$$a_p(T) = \int_a d\mathbf{r} \langle \mathbf{p}^E | \mathbf{r} \rangle \Psi_{\text{out}}(\mathbf{r}, T), \quad (20)$$

where the \int_a implies integration over the outer region only, which can be extended to all of space if the electron has left the inner region, for example, as $T \rightarrow \infty$. Since at $T \rightarrow \infty$ the electron wave packet is far from the core, projection onto the plane-wave continuum states is also adequate:

$$a_p(T) = \int d\mathbf{r} \langle \mathbf{p} | \mathbf{r} \rangle \Psi_{\text{out}}(\mathbf{r}, T). \quad (21)$$

Substituting in G^{EVA} (19) in our expression for Ψ_{out} (8) and keeping in mind the orthogonality of the EVA states, the ionization amplitude becomes

$$a_p(T) = -i \int^T dt' e^{-\frac{i}{2} \int_{t'}^T d\tau [\mathbf{p} + \mathbf{A}(\tau)]^2} \\ \times \int \frac{d\mathbf{r}'}{(2\pi)^{3/2}} e^{-i \int_{t'}^T d\tau U[\mathbf{r}_L(\tau)]} e^{-i[\mathbf{p} + \mathbf{A}(t')] \cdot \mathbf{r}'} \\ \times \delta(r' - a) \hat{B} \Psi_{\text{in}}(\mathbf{r}', t'). \quad (22)$$

The expression for $a_p(T)$ does not account for hard recollisions, but is well-suited for calculating the ionization yield, which is not affected by hard recollisions, and for the spectra of “direct” electrons.

III. STRONG FIELD IONIZATION: DERIVATION OF STANDARD RESULTS

The goal of this section is to both illustrate and test this approach. To this end, we derive ionization amplitudes in strong low-frequency fields. Our approach is most naturally used in the time domain. Thus, we shall look at the contribution to the ionization amplitude accumulated over a single half cycle of the laser pulse and then show how these results yield the standard results of PPT theory [24] developed for continuous laser radiation.

As mentioned before, we use the same approximation as [24] and replace the exact wave function at the boundary $\Psi(r' = a, t')$ with its ground-state component,

$$\Psi_{\text{in}}(\mathbf{r}', t') \simeq e^{i I_{p,t'}} a_g(t') \psi_g(\mathbf{r}'). \quad (23)$$

The Stark shift and depletion of the ground state should be incorporated into the amplitude $a_g(t)$, while $\psi_g(\mathbf{r})$ determines the spatial structure of the ground state [31]. To compare with standard PPT results for the Coulomb potential $U(r) = -Q/r$, we use the hydrogenic expression

$$\psi_g(\mathbf{r}) = \psi_{k,l,m}(\mathbf{r}) = \varphi_{k,l}(r) Y_{lm}(\theta, \phi) \\ = \varphi_{k,l}(r) N_{lm} P_l^m(\cos \theta) \frac{e^{im\phi}}{\sqrt{2\pi}}, \quad (24)$$

$$\varphi_{k,l}(r) = C_{kl} \kappa^{3/2} \frac{e^{-\kappa r}}{\kappa r} (\kappa r)^{Q/\kappa}, \quad (25)$$

$$N_{lm} = \sqrt{\frac{(2l+1)(l-m)!}{2(l+m)!}}. \quad (26)$$

Here $\kappa = \sqrt{2I_p}$ determines the size of the bound state $\sim 1/\kappa$, and C_{kl} is a constant.

Note that setting $b = Q/\kappa$ in Eq. (4) yields the simple result

$$\hat{B} \varphi_{k,l}(r) = -\kappa \varphi_{k,l}(r). \quad (27)$$

Before we commence our calculation of the ionization amplitude, let us first consider our choice of a , the radius of the sphere separating the inner and outer regions. At a , we would like to match a bound field-free solution in the inner region, with an outer solution that captures the laser field fully but treats the Coulomb interaction as a small correction. To do this successfully, a must lie inside the classically forbidden region, sufficiently far from both the entrance and the exit of the tunneling barrier. Specifically, to apply the eikonal

approximation, we must ensure that $a\kappa \gg 1$ or alternatively $|U(a)| \ll I_p$; that is, we are sufficiently far from the atom compared to the characteristic size of bound state and the Coulomb potential is no longer very important. On the other hand, the use of the field-free state in the inner region requires that $Fa \ll I_p$. The change in the electron energy due to the work of the electric field must be negligible compared to the energy of the bound state. Note that F/I_p roughly corresponds to the exit of the tunneling barrier (for sufficiently small values of the Keldysh parameter $\gamma = \omega\sqrt{2I_p}/F$). Putting this together, we require $1/\kappa \ll a \ll \kappa^2/2F$. Note that these conditions together impose an important restriction on the field strengths for which our analysis is justified, $F \ll \kappa^3$.

With approximation (23), the expression for the ionization amplitude Eq. (22) takes the form

$$a_{\mathbf{p}}(T) = \frac{i\kappa}{(2\pi)^{3/2}} \int dt' a_g(t') \int d\mathbf{r}' e^{-iS(T,t',\mathbf{r}',\mathbf{p})} \times \delta(r' - a)\varphi_{\kappa,l}(r') Y_{lm}(\theta, \phi), \quad (28)$$

where the phase of the integrand $S(T,t',\mathbf{r}',\mathbf{p})$ is determined by the action of a particle moving with canonical momentum \mathbf{p} and having position \mathbf{r}' at the moment t' :

$$S(T,t',\mathbf{r}',\mathbf{p}) = \frac{1}{2} \int_{t'}^T d\tau [\mathbf{p} + \mathbf{A}(\tau)]^2 + \int_{t'}^T d\tau U[\mathbf{r}_L(\tau)] + [\mathbf{p} + \mathbf{A}(t')] \cdot \mathbf{r}' - I_p t'. \quad (29)$$

Energy is calculated relative to that of the ground state. We let the field $F \cos \omega t$ be linearly polarized along the z axis. The corresponding vector potential is

$$\mathbf{A}(t) = -\frac{F}{\omega} \sin \omega t \hat{\mathbf{e}}_z. \quad (30)$$

A. Temporal integration

Using the δ function to evaluate the radial integral over r' , we can rewrite the ionization amplitude as

$$a_{\mathbf{p}}(T) = \frac{i\kappa}{(2\pi)^{3/2}} a^2 \varphi_{\kappa,l}(a) e^{-i\frac{p_\perp^2}{2}T} \times \int_0^\pi d\theta \int_0^{2\pi} d\phi \sin \theta Y_{lm}(\theta, \phi) e^{-ia p_\perp \sin \theta \cos(\phi - \phi_p)} \times \int_{t'}^T dt' a_g(t') e^{-iS_V(T,t',\mathbf{p})} e^{-i\sigma_U(t')} e^{-iv_z(t')a \cos \theta}, \quad (31)$$

where

$$S_V(T,t',\mathbf{p}) = \frac{1}{2} \int_{t'}^T d\tau v_z(\tau)^2 - I_{p,\text{eff}} t', \quad (32)$$

$$I_{p,\text{eff}} = I_p + \frac{p_\perp^2}{2}, \quad (33)$$

$$v_z(t') = p_\parallel + A(t'), \quad (34)$$

$$\sigma_U(t') = \int_{t'}^T d\tau U[\mathbf{r}_L(\tau; \theta, \mathbf{p}, t')], \quad (35)$$

$p_\parallel = p_z$, $p_\perp^2 = p_x^2 + p_y^2$, and ϕ_p is the polar angle the momentum p_\perp makes with the x axis. The contributions S_V and σ_U describe the Volkov part of the action and the correction from the core potential, respectively.

Fast oscillations of the phase in strong low-frequency fields allow one to use the saddle-point method to evaluate the integral over time. Such analysis can be done by treating the phase $\sigma_U(t')$ as a relatively slow function of t' and hence ignoring its contribution to the saddle points. This treatment is a natural first step within the eikonal approximation and proves accurate: The standard results of PPT theory are obtained using the saddle points found to zeroth order in $U(\mathbf{r}_L)$. Corrections to the saddle points can then be introduced perturbatively. Such an iterative treatment may further improve the original results of PPT theory, extending their applicability to the case of very large Keldysh parameter $\gamma = \omega\sqrt{2I_p}/F \gg 1$ as recently shown in [30].

We focus on the contribution from a half-cycle interval $-\pi/2 < \omega t < +\pi/2$, where $\cos \omega t \geq 0$ and hence the electron should start moving in the negative- z direction.

Differentiating the phase with respect to t' and treating $\sigma_U(t')$ as slow compared to $S_V(t')$, we obtain the saddle-point equation, $\partial S/\partial t' = 0$:

$$\frac{1}{2}[p_\parallel + A(t')]^2 + \left[I_p + \frac{p_\perp^2}{2} + Fa \cos \theta \cos \omega t' \right] = 0. \quad (36)$$

Using this, we can approximate the solution as

$$a_{\mathbf{p}}(T) = \frac{i\kappa}{(2\pi)^{3/2}} a^2 \varphi_{\kappa,l}(a) e^{-i\frac{p_\perp^2}{2}T} \times \int_0^\pi d\theta \int_0^{2\pi} d\phi \sin \theta Y_{lm}(\theta, \phi) e^{-ia p_\perp \sin \theta \cos(\phi - \phi_p)} \times \frac{\sqrt{2\pi} a_g(t_a)}{\sqrt{|S''_V(t_a) + A''(t_a)a \cos \theta|}} \times e^{-iS_V(t_a)} e^{-i\sigma_U(t_a)} e^{-iv_z(t_a)a \cos \theta}, \quad (37)$$

where t_a solves Eq. (36).

There are a number of important observations. First, note that any deviation from the optimal tunneling direction $p_\perp = 0$ and $\cos \theta = -1$ leads to an increased effective I_p in Eq. (36) and therefore to an exponentially increased cost for tunneling. Consequently, tunneling will be dominated by small perpendicular momenta and angles $\theta \sim \pi$. We shall come back to this fact when we integrate over the surface of our sphere $r' = a$.

Second, recall that the use of the unperturbed ground state in the inner region requires that $Fa \ll I_p$. The final term in Eq. (36) should therefore represent only a small correction to I_p . From this, we can deduce that the solution t_a must lie near the saddle point $t_s = t_i + i\tau_T$ determined by the equation

$$[p_\parallel + A(t_i + i\tau_T)]^2 = -[2I_p + p_\perp^2] = -2I_{p,\text{eff}}. \quad (38)$$

This can be rewritten as

$$v_z(t_s) = p_\parallel - \frac{F}{\omega} \sin(\omega t_i + i\omega\tau_T) = \pm i\sqrt{2I_{p,\text{eff}}} = \pm i\kappa_{\text{eff}}. \quad (39)$$

For $\cos \omega t_i > 0$, $v_z(t_s) = -i\kappa_{\text{eff}}$ is the correct choice, ensuring that the landscape of the imaginary phase in the vicinity of $t_s = t_i + i\tau_T$ with positive imaginary part indeed corresponds to the saddle, and vice versa for $\cos \omega t_i < 0$. This choice, in turn, leads to an exponentially small ionization amplitude and exponential decay of the outgoing wave function for complex

times and $|r'| > a$. We can summarize this as

$$v_z(t_s) = i\alpha\kappa_{\text{eff}}, \quad (40)$$

where $\alpha = -\text{sign}(\cos \omega t_i)$.

In general, the solution for t_s is

$$\begin{aligned} \phi_i \equiv \omega t_i &= \beta \arcsin \left(\sqrt{\frac{P-D}{2}} \right) + (n-1)\pi, \\ \phi_\tau \equiv \omega\tau_T &= \text{arcosh} \left(\sqrt{\frac{P+D}{2}} \right), \\ P &= \bar{p}_\parallel^2 + \gamma_e^2 + 1, \quad D = \sqrt{P^2 - 4\bar{p}_\parallel^2}, \end{aligned} \quad (41)$$

where $\gamma_e = \sqrt{2I_{p,\text{eff}}}\omega/F$ is the Keldysh parameter [32] for the effective ionization potential, $\bar{p}_\parallel = p_\parallel/p_0$ is the momentum measured in units of $p_0 = F/\omega$, and $\beta = \text{sgn}(\sin \phi_i)$. The solution is given not only for the specific half cycle we have been focusing on, but also for other half cycles.

With this in mind, let us expand t_a in powers of $(Fa/I_{p,\text{eff}})$ and write $t_a = t_s + \Delta t_a$. We find that

$$\Delta t_a = -i\alpha \frac{a}{\kappa_{\text{eff}}} \cos \theta \quad (42)$$

solves Eq. (36) to first order in $(Fa/I_{p,\text{eff}})$. Note that $a/\kappa_{\text{eff}} \ll \kappa/2F < \tau_T$, so Δt_a represents only a small correction to t_s .

Thanks to the stationarity of S_V at t_s , the shift Δt_a of the complex saddle point only contributes at second order to the phase $S_V + v_z a \cos \theta$. Thus, keeping only terms linear in $(Fa/I_{p,\text{eff}})$ and focusing on the half cycle where $\cos \omega t' \geq 0$, we have

$$S_V(t_a) + v_z(t_a)a \cos \theta \approx S_V(t_s) - i\kappa_{\text{eff}} a \cos \theta. \quad (43)$$

To lowest order in $(Fa/I_{p,\text{eff}})$, we can also approximate $S''_V(t_a) + A''(t_a)a \cos \theta \approx S''_V(t_s)$ and $a_g(t_a) = a_g(t_s)$. Finally, taking into account that $p_\perp^2/\kappa^2 \ll 1$, we have $\kappa_{\text{eff}} \approx \kappa$.

B. Spatial integration

Given the above approximations, we can now rewrite the ionization amplitude (37) as

$$\begin{aligned} a_p(T) &= \frac{i\kappa}{(2\pi)^{3/2}} a^2 \varphi_{\kappa,l}(a) \frac{a_g(t_s)}{\sqrt{|S''_V(t_s)|}} e^{-iS_V(t_s)} e^{-i\frac{p_\perp^2}{2}T} e^{im\phi_p} N_{l,m} \\ &\times \int_0^\pi d\theta \sin \theta P_l^m(\cos \theta) e^{-\kappa a \cos \theta} e^{-i\sigma_U(t_a, \theta)} \\ &\times \int_0^{2\pi} d\phi' e^{im\phi'} e^{-ia p_\perp \sin \theta \cos \phi'}. \end{aligned} \quad (44)$$

The integral over ϕ yields the Bessel function:

$$\int_0^{2\pi} d\phi' e^{-ia p_\perp \sin \theta \cos \phi' + im\phi'} = 2\pi(-i)^m J_m(p_\perp a \sin \theta). \quad (45)$$

Now, to evaluate the remaining integral over θ , notice that the integrand contains the term $\exp[-\kappa a \cos \theta]$. If we recall the condition $\kappa a \gg 1$, we see that this naturally confines the integral to the vicinity of $\theta = \pi$, where the exponent has a maximum. Let us therefore change the integration variable from θ to $\theta' = \pi - \theta \ll 1$ and take small-angle expansions.

First, consider the Coulomb term, $\exp[-i\sigma_U]$. Keeping only the lowest order term in θ' in the argument of $U(\mathbf{r}_L)$ and assuming that p_\perp is small, we can approximate $\mathbf{r}_L(\tau)$ with the optimal tunneling trajectory $z_L(\tau)$ starting at $\mathbf{r}' = -a\hat{\mathbf{e}}_z$ with $p_\perp = 0$,

$$\mathbf{r}_L(\tau; \theta, \mathbf{p}, t_a) \simeq z_L(\tau; -a, p_\parallel, t_a) = -a + \int_{t_a}^\tau dt'' (p_\parallel + A(t'')). \quad (46)$$

For the remaining θ -dependent terms, we can use the following small-angle expansions (see [33] for Legendre polynomials [34]),

$$\begin{aligned} J_m(p_\perp a \sin(\pi - \theta')) &\simeq \frac{(p_\perp a \theta'/2)^m}{\Gamma(m+1)}, \\ P_l^m(\cos(\pi - \theta')) &\simeq (-1)^l \left(\frac{(l+m)!}{2^m m! (l-m)!} \right) (\theta')^m, \quad (47) \\ e^{-\kappa a \cos \theta} &\simeq e^{\kappa a} e^{-\kappa a \frac{\theta'^2}{2}}, \quad \sin(\pi - \theta') = \theta'. \end{aligned}$$

Note that the above approximation works very well for $l = m = 0$ even for modest κa but starts to increasingly overestimate the integral for larger l, m , unless κa is sufficiently large. As discussed before, the competing limit $aF/I_p \ll 1$ implies that F/κ^3 must, in turn, be suitably small for both conditions on a to be simultaneously satisfied.

Using the above, we are now able to evaluate the integral over θ . If we take into account that

$$\begin{aligned} \int_0^\pi d\theta \theta \left[\frac{\theta^2}{2} \right]^m e^{-\kappa a \theta^2/2} &\simeq \left[\frac{1}{\kappa a} \right]^{m+1} \\ \int_0^\infty e^{-t} t^m dt &= \left[\frac{1}{\kappa a} \right]^{m+1} \Gamma(m+1), \end{aligned} \quad (48)$$

we obtain

$$\begin{aligned} a_p(T) &\simeq \frac{(-1)^{l+m} i^{m+1}}{\sqrt{|S''_V(t_s)|}} C_{lm} e^{im\phi_p} e^{-i\frac{p_\perp^2}{2}T} \left[\frac{p_\perp}{\kappa} \right]^m \\ &\times e^{-i\frac{1}{2} \int_{t_a}^T d\tau [p_\parallel + A(\tau)]^2 + iA(t_a)} a_g(t_s) \\ &\times [\varphi_{\kappa,l}(a) a e^{\kappa a} e^{-i \int_{t_a}^T d\tau U(-a + \int_{t_a}^\tau [p_\parallel + A(t'')] dt'')}], \end{aligned} \quad (49)$$

where

$$C_{lm} = \frac{1}{2^m m!} \sqrt{\frac{(2l+1)(l+m)!}{4\pi(l-m)!}}. \quad (50)$$

C. Independence of the boundary

Had we used the exact wave function at the boundary [35], the smooth continuation of the wave function from the inner to the outer region would have been naturally expected. Equally automatic would have been the independence of ionization amplitudes on the position of the boundary. However, we have used an unperturbed wave function in the inner region while taking full account of the laser field in the outer region. Thus, the independence of the results on the position of the boundary is neither ensured nor obvious.

The expression in square brackets in Eq. (49),

$$F_{\kappa,l} = \varphi_{\kappa,l}(a) a e^{\kappa a} e^{-i \int_{t_a}^T d\tau U(-a + \int_{t_a}^\tau [p_\parallel + A(t'')] dt'')}, \quad (51)$$

contains the terms which still depend on the position of the boundary. Recalling the expression for the bound wave function $\varphi_{\kappa,l}(a)$ (25), this simplifies to

$$F_{\kappa,l} = C_{\kappa,l} \kappa^{1/2} (\kappa a)^{\frac{Q}{\kappa}} e^{-i \int_{t_a}^T d\tau U[-a + \int_{t_a}^\tau [p_\parallel + A(t'')] dt''].} \quad (52)$$

Note that both the remaining a -dependent terms are associated with the Coulomb potential. We now show that their combination is (approximately) a independent. We do this in a general way, applicable for any potential U .

First, note that the trajectory in the argument of U can be rewritten via t_s :

$$e^{-i \int_{t_a}^T d\tau U[-a + \int_{t_a}^\tau [p_\parallel + A(t'')] dt'']} = e^{-i \int_{t_a}^T d\tau U[\int_{t_s}^\tau [p_\parallel + A(t'')] dt''].} \quad (53)$$

Now let us look at the Coulomb term in the bound wave function, $(\kappa a)^{\frac{Q}{\kappa}}$. This can be rewritten as

$$(\kappa a)^{\frac{Q}{\kappa}} = e^{\frac{Q}{\kappa} \int_{1/\kappa}^a \frac{dz}{z}} = e^{-\frac{1}{\kappa} \int_{1/\kappa}^a U(z) dz}. \quad (54)$$

That is, the wave function contains the integral of the Coulomb potential between $z = 1/\kappa$ and the boundary. This asymptotic form is not special for the Coulomb potential, but is dictated by the general behavior of bound states in the classically forbidden region. The effective lower limit of the integral here is $z_\kappa = 1/\kappa$; for other potentials it could be different, but the general behavior is the same. For $z < 0$, relevant to our problem, the same applies:

$$(\kappa a)^{\frac{Q}{\kappa}} = e^{\frac{1}{\kappa} \int_{-1/\kappa}^{-a} U(z) dz}. \quad (55)$$

Keeping in mind that the electron velocity is $-i\kappa$, we can rewrite the spatial integral as an integral in the time domain,

$$(\kappa a)^{\frac{Q}{\kappa}} = e^{-i \int_{t_a}^{t_s} d\tau U[\int_{t_s}^\tau (-ik) dt'']}, \quad (56)$$

where the lower limit of the outer integral is $t_s = t_a + \Delta t_\kappa$,

$$\Delta t_\kappa = \frac{-1/\kappa}{-i\kappa} = -i \frac{1}{\kappa^2}. \quad (57)$$

Now we see that the product of the two potential-dependent terms is a independent, and we have

$$F_{\kappa,l} = C_{\kappa,l} \kappa^{1/2} e^{-i \int_{t_a}^T d\tau U[\int_{t_s}^\tau [p_\parallel + A(t'')] dt''].} \quad (58)$$

As is clear from the derivation, this result is general. The bound wave function in the region beyond the size of the bound state can always be written via the spatial integral of the core potential in this region, starting from some initial point, for the Coulomb potential equal to $1/\kappa$. The spatial integral across the inner region, at the boundary $a \gg 1/\kappa$, can then be rewritten as a time integral, keeping in mind that the electron velocity is nearly constant. Matching this integral to the corresponding time integral in the outer region is natural. The caveat is in the fact that electron motion in the outer region includes the laser field, while in the inner region this field was ignored. Thus, one has to watch for artifacts introduced by ignoring the effect of the laser field in the inner region, as we have done here.

D. Comparison with PPT results

The ionization amplitude we have just derived, computed for a single half cycle of the laser field and hence for a single “ionization burst,” is

$$\begin{aligned} a_{\mathbf{p}}(T) &\simeq a_g(t_s) \left(\frac{(-1)^{l+m} i^{m+1}}{\sqrt{|S_V''(T, t_s)|}} C_{lm} e^{im\phi_p} e^{-i \frac{p_\perp^2}{2} T} \left[\frac{p_\perp}{\kappa} \right]^m C_{\kappa l} \kappa^{1/2} \right) \\ &\times \left[e^{-i \int_{t_a}^T d\tau U[\int_{t_s}^\tau [p_\parallel + A(t'')] dt'']} \right] e^{-i \frac{1}{2} \int_{t_s}^T d\tau [p_\parallel + A(\tau)]^2 + i I_{p,\text{eff}} t_s}. \end{aligned} \quad (59)$$

The first from the right is the familiar Keldysh exponent $\exp[-i S_V(T, t_s, \mathbf{p})]$ calculated for the specific momentum \mathbf{p} , identical to that in the standard theory. Note that $t_s = t_s(\mathbf{p}) = t_i(\mathbf{p}) + i\tau_T(\mathbf{p})$ is determined by the equation

$$p_\parallel - \frac{F}{\omega} \sin(\omega t_i + i\omega\tau_T) = \alpha i \sqrt{2I_{p,\text{eff}}} = \alpha i \kappa_{\text{eff}}, \quad (60)$$

where $\alpha = -\text{sgn}(\cos \omega t_i)$.

The second term, in square brackets, is the contribution of the Coulomb potential. For the maximum of the momentum distribution $p = 0$, which corresponds to ionization at the peak of the oscillating field, it is identical to the familiar Coulomb correction of PPT theory [36,37]. In our derivation, the Coulomb correction is \mathbf{p} dependent. Since different final momenta \mathbf{p} can be associated with different moments of ionization within the laser half cycle, we have access to the subcycle dependence of the Coulomb corrections.

Finally, the leftmost group of terms, also in brackets, is related to the angular structure of the wave function and is common for ionization from both long-range and short-range potentials. Comparing it with PPT theory, we should keep in mind that our calculations are done in the time domain, and that our expression gives the contribution to $a(\mathbf{p})$ from a single ionization burst during one half cycle of the laser field. The results of PPT theory [24] are, on the other hand, derived for an infinitely long pulse. They provide the ionization rate as a sum over all multiphoton channels:

$$\begin{aligned} \Gamma^{\text{PPT}} &= \sum_n \Gamma_n^{\text{PPT}}, \\ \Gamma_n^{\text{PPT}} &= 2\pi \int d\mathbf{p} |F_n(p)|^2 \delta\left(\frac{p^2}{2} - (n - n_0)\omega\right) \\ &= 2\pi p_n \int d\Omega |F_n(p)|^2, \\ E_n &= \frac{p_n^2}{2} = (n - n_0)\omega. \end{aligned} \quad (61)$$

Here $n_0 = \frac{I_p + 2U_p}{\omega}$ is the minimum number of absorbed photons.

To compare the two results, we should calculate the contribution to the n -photon peak, sandwiched between the energies $E_n \pm \omega/2$, during one laser half cycle. In PPT theory, this contribution is

$$w_n = \frac{\pi}{\omega} \Gamma_n^{\text{PPT}} = \frac{2\pi^2}{\omega} p_n \int d\Omega |F_n(p)|^2, \quad (62)$$

where $d\Omega$ implies integration over solid angle. In our approach, the same quantity is

$$w_n = \int_{E_n - \omega/2}^{E_n + \omega/2} d\mathbf{p} |a_{\mathbf{p}}(T)|^2 \simeq \omega p_n \int d\Omega |a_{\mathbf{p}}(T)|^2|_{p=p_n}. \quad (63)$$

Thus, the connection between the two results should be

$$|a_{\mathbf{p}}(T)|^2 = \frac{\omega^2}{2\pi^2} |F_n(\mathbf{p})|^2, \quad (64)$$

for $\mathbf{p}^2/2 = p_n^2/2$, where $|F_n(p)|^2$ is given by Eq. (53) of [24]. This is indeed the case, up to notation.

IV. SUBCYCLE IONIZATION DYNAMICS AND THE STRUCTURE OF THE TUNNELING WAVE PACKET

Our approach gives insight into the instantaneous ionization dynamics and the shape of the electronic wave packet as it tunnels. Let us analyze how the ionization amplitudes Eq. (59) are formed. First, we rewrite this result in a more compact form,

$$a_{\mathbf{p}}(T) = a_g(t_s) R_{klm}(\mathbf{p}) e^{-i \int_{t_s}^T d\tau U(\int_{t_s}^{\tau} dt'' [\mathbf{p} + \mathbf{A}(t'')])} \\ \times e^{-\frac{i}{2} \int_{t_s}^T d\tau [\mathbf{p} + \mathbf{A}(\tau)]^2 + i I_p t_s}, \quad (65)$$

where we have restored the full momentum dependence in the Coulomb term. The prefactor

$$R_{klm}(\mathbf{p}) = \frac{(-1)^{l+m} i^{m+1}}{\sqrt{|S_V''(T, t_s)|}} C_{lm} e^{im\phi_p} \left[\frac{p_{\perp}}{\kappa} \right]^m C_{kl} \kappa^{1/2} \quad (66)$$

encodes the impact of angular structure of the ionizing state on ionization. The prefactor $R_{klm}(\mathbf{p})$ also appears in the analysis of Murray *et al.* for static fields [20]. This work shows how the static approach developed in [20] extends to oscillating fields.

The wave function at time T , determined by these amplitudes, represents the wave packet $|\Delta\Psi(T)\rangle$ associated with a single ionization burst around one of the instantaneous maxima of the oscillating laser field,

$$|\Delta\Psi(T)\rangle = \int d\mathbf{p} a_{\mathbf{p}}(T) |\mathbf{p}\rangle. \quad (67)$$

Since the EVA wave functions $|\mathbf{p}_T^{\text{EVA}}(t)\rangle$ are approximate solutions of the TDSE in the outer region, we can use them to propagate the wave packet Eq. (67) backward in time until some moment t , yielding $|\Delta\Psi(t)\rangle$. This is, of course, only possible as long as the electron trajectories in the argument of $U(\dots)$ stay outside the inner region. We can then project the result of this propagation on the plane wave basis $|\mathbf{p} + \mathbf{A}(t)\rangle$, gaining insight into the momentum composition of the wave packet after it emerges in the continuum.

This procedure yields the expression

$$a_{\mathbf{p}}(t) \equiv \langle \mathbf{p} + \mathbf{A}(t) | \Delta\Psi(t) \rangle = \langle \mathbf{p} + \mathbf{A}(t) | \int d\mathbf{k} a_{\mathbf{k}}(T) |\mathbf{k}_T^{\text{EVA}}(t)\rangle \\ = \frac{1}{(2\pi)^3} \int d\mathbf{r} e^{-i\mathbf{p}\cdot\mathbf{r}} \int d\mathbf{k} e^{i\mathbf{k}\cdot\mathbf{r}} a_g(t_s) R_{klm}(\mathbf{k}) e^{iI_p t_s} \\ \times e^{-\frac{i}{2} \int_{t_s}^t [\mathbf{k} + \mathbf{A}(t'')]^2 dt''} e^{-iW_c(t, \mathbf{r}, \mathbf{k}, T)}, \quad (68)$$

where the term associated with the core potential is

$$W_c = \int_T^t U(\mathbf{r}_L(\tau; \mathbf{r}, \mathbf{k}, t)) d\tau \\ + \int_{t_s}^T d\tau U \left(\int_{t_s}^{\tau} dt'' [\mathbf{k} + \mathbf{A}(t'')] \right). \quad (69)$$

Notice that the two integrals in Eq. (68) are very nearly direct and inverse Fourier transforms. It is only the r dependence of W_c which prevents this from being the case.

In particular, the first term in Eq. (69) contains the trajectory $\mathbf{r}_L(\tau; \mathbf{r}, \mathbf{k}, t)$, which is characterized by canonical momentum \mathbf{k} at infinity and coordinate \mathbf{r} at the moment t . Integration over \mathbf{r} means that all trajectories are sampled. In contrast, only a single trajectory $\mathbf{r}_L(\tau; 0, \mathbf{k}, t_s)$ appears in the argument of the second integral. This starts at t_s at the origin. As we will see, evaluating the integrals in Eq. (68) using the saddle-point (stationary phase) method will select precisely the trajectory that matches $\mathbf{r}_L(\tau; 0, \mathbf{k}, t_s)$ in the first term.

Let us now evaluate $a_{\mathbf{p}}(t)$ in the case $m = 0$ by applying the saddle-point method to both \mathbf{r} and \mathbf{k} integrals simultaneously. The integrand contains $\exp[-i\Theta(\mathbf{r}, \mathbf{k})]$, where

$$\Theta(\mathbf{r}, \mathbf{k}) = \frac{1}{2} \int_{t_s}^t [\mathbf{k} + \mathbf{A}(t'')]^2 dt'' - \mathbf{k} \cdot \mathbf{r} + \mathbf{p} \cdot \mathbf{r} \\ + W_c(t, \mathbf{r}, \mathbf{k}, T), \quad (70)$$

and to zeroth order with respect to W_c , we have the following saddle-point equations:

$$\frac{\partial}{\partial \mathbf{k}} \Theta(\mathbf{r}, \mathbf{k})|_{\mathbf{r}_s, \mathbf{k}_s} = \int_{t_s}^t [\mathbf{k}_s + \mathbf{A}(t'')] dt'' - \mathbf{r}_s = 0, \\ \frac{\partial}{\partial \mathbf{r}} \Theta(\mathbf{r}, \mathbf{k})|_{\mathbf{r}_s, \mathbf{k}_s} = \mathbf{p} - \mathbf{k}_s = 0. \quad (71)$$

Note that even though $t_s = t_s(\mathbf{k})$, the phase is stationary with respect to t_s and hence $\partial/\partial t_s$ does not contribute here. These equations select a unique trajectory in the final expression for $a_{\mathbf{p}}(t)$,

$$\mathbf{r}_s(\mathbf{p}, t) = \mathbf{r}_L(t; 0, \mathbf{p}, t_s) = \int_{t_s}^t [\mathbf{p} + \mathbf{A}(t'')] dt'', \quad (72)$$

and lead to the following simple expression for the Coulomb term:

$$W_c(r_s(\mathbf{p}, t)) = \int_{t_s}^t d\tau U \left(\int_{t_s}^{\tau} dt'' [\mathbf{p} + \mathbf{A}(t'')] \right). \quad (73)$$

Thus, within the saddle-point method, the amplitude can be approximated as

$$a_{\mathbf{p}}(t) \simeq a_g(t_s) e^{-iW_c(r_s(\mathbf{p}, t))} e^{iI_p t_s} \\ \times \frac{1}{(2\pi)^3} \int d\mathbf{r} e^{-i\mathbf{p}\cdot\mathbf{r}} \int d\mathbf{k} e^{i\mathbf{k}\cdot\mathbf{r}} R_{kl0}(\mathbf{k}) e^{-\frac{i}{2} \int_{t_s}^t [\mathbf{k} + \mathbf{A}(t'')]^2 dt''}, \quad (74)$$

which leads to the final result

$$a_{\mathbf{p}}(t) \simeq a_g(t_s) e^{-iW_c(r_s(\mathbf{p}, t))} e^{iI_p t_s} R_{kl0}(\mathbf{p}) e^{-\frac{i}{2} \int_{t_s}^t [\mathbf{p} + \mathbf{A}(t'')]^2 dt''}. \quad (75)$$

This expression is applicable for all times t as long as the saddle point $t_s = t_s(p)$ of the original time integral is fully passed. Note that for $t = T$, this expression is, in fact, identical to $a_{\mathbf{p}}(T)$, the ionization amplitude we derived for large T

[Eq. (65)]. It is also applicable along the contour connecting the complex saddle point $t_s = t_i + i\tau_T$ to the point t_i on the real time axis. Thus, it allows us to analyze how the amplitudes and the wave packet $\Delta\Psi$ are formed during tunneling.

For this purpose, it is useful to study the integrals in Eq. (68) in more detail. In particular, let us now evaluate $a_p(t)$ by first integrating over \mathbf{k} and then over \mathbf{r} . This analysis also illustrates a technical issue related to the applicability of the saddle-point (stationary phase) analysis to the double integral, given that the \mathbf{r} integral on its own does not appear to contain fast-oscillating terms.

Again, we set the magnetic quantum number $m = 0$. Hence, $R_{k,l,m}$ is independent of k_\perp . Applying the stationary phase method to the \mathbf{k} integral in Eq. (68), we obtain the stationary phase equation

$$\int_{t_s}^t [\mathbf{k} + \mathbf{A}(t'')] dt'' - \mathbf{r} = 0, \quad (76)$$

which determines the stationary momentum $\mathbf{k}_s = \mathbf{k}_s(\mathbf{r})$,

$$\mathbf{k}_s = \frac{\mathbf{r} - \int_{t_s}^t \mathbf{A}(t'') dt''}{t - t_s}. \quad (77)$$

The result of \mathbf{k} integration is

$$a_p(t) \simeq \int d\mathbf{r} \left(a_g(t_s) \frac{R_{k,l,0} e^{-iW_c - i\pi/4 + iI_p t_s}}{[2\pi(t - t_s)]^{3/2}} \right) \times e^{-i\mathbf{p} \cdot \mathbf{r}} e^{i\mathbf{k}_s \cdot \mathbf{r}} e^{-\frac{i}{2} \int_{t_s}^t [\mathbf{k}_s + \mathbf{A}(t'')]^2 dt''}. \quad (78)$$

Using our expression for \mathbf{k}_s and completing the square in the exponent, we can rewrite this as

$$a_p(t) \simeq \int d\mathbf{r} \left(a_g(t_s) \frac{R_{k,l,0} e^{-iW_c - i\pi/4 + iI_p t_s}}{[2\pi(t - t_s)]^{3/2}} \right) \times e^{\frac{i}{2} \frac{(\mathbf{r} - \mathbf{r}_s(\mathbf{p}, t))^2}{(t - t_s)}} e^{-\frac{i}{2} \int_{t_s}^t (\mathbf{p} + \mathbf{A}(t''))^2 dt''}, \quad (79)$$

where we have defined

$$\mathbf{r}_s(\mathbf{p}, t) \equiv \int_{t_s}^t [\mathbf{p} + \mathbf{A}(t'')] dt''. \quad (80)$$

First, this expression clearly justifies the application of the saddle-point method for integration over \mathbf{r} . Second, it shows that during its motion in the classically forbidden region, when times are complex-valued, $t - t_s = -i\xi$, the wave

packet is a Gaussian $\exp[-(\mathbf{r} - \mathbf{r}_s(\mathbf{p}, t))^2/2\xi]$ that surrounds the trajectory $\mathbf{r}_s(\mathbf{p}, t)$ and spreads as $(t - t_s)^{-3/2}$. This explains why a single trajectory can be used to evaluate the contribution of the core potential to the ionization amplitude as we discussed before. It also indicates how each momentum component a_p is formed. In particular, we see that each momentum component after tunneling can be associated with a Gaussian wave packet emerging from the classically forbidden region and then spreading. Note that we can now apply the stationary phase method to the integral over \mathbf{r} , reproducing the result (75) for $a_p(t)$.

V. SUBCYCLE COULOMB EFFECTS

Trajectory-based techniques for strong-field ionization use quantum ionization amplitudes as input for ensembles of trajectories [21,22], which are then propagated classically. So far, the subcycle dynamics of the interaction between the departing electron and the core during tunneling has been ignored. The Coulomb effects in ionization are evaluated along a trajectory departing at the maximum of the oscillating laser field. This is an excellent approximation for the total ionization yield, even for large Keldysh parameter γ [30]. However, for problems such as high harmonic generation, where trajectories leaving the core after the instantaneous maximum of the oscillating field are very important, including those starting substantially past the maximum (short trajectories), such an approximation is not necessarily adequate. Our analysis allows us to evaluate the subcycle role of the Coulomb potential for instantaneous ionization amplitudes. We assume that $p_\perp = 0$.

The subcycle contribution from the Coulomb potential is given by $\exp[-iW_c]$, where

$$W_c(p) = \int_{t_k}^t d\tau U \left(\int_{t_s}^\tau dt'' [p_\parallel + A(t'')] \right) \quad (81)$$

is evaluated along the complex-valued trajectory that starts at the origin at $t_s(p_\parallel) = t_i(p_\parallel) + i\tau_T(p_\parallel)$. Integration over τ is performed from t_k until t . We choose our integration contour such that it has two sections. Its first leg starts at $t_k = t_i + i\tau_T - i/\kappa^2$ and descends parallel to the imaginary time axis, until it hits t_i on the real time axis. The second leg continues along the real time axis from t_i to t (see Fig. 2).

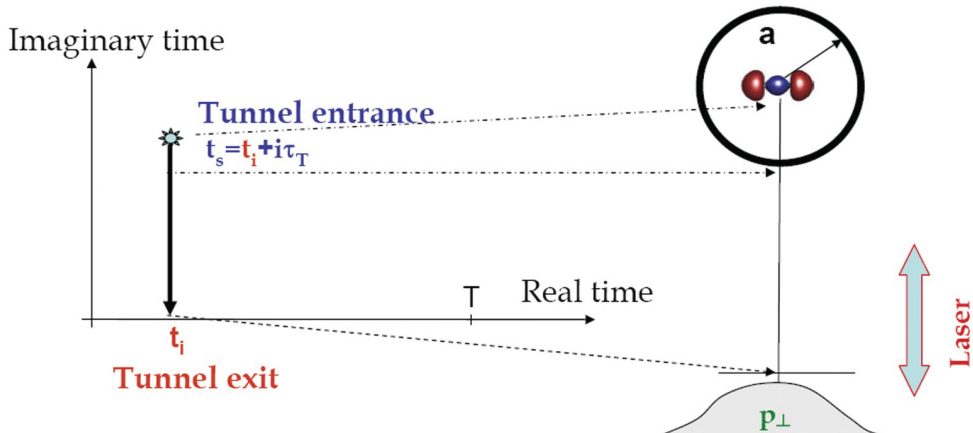


FIG. 2. (Color online) The integration contour for integral Eq. (81) and its relation to the boundary of the outer region.

While for the instantaneous maximum of the laser field $F \cos \omega t$ the trajectory is real-valued, in general it is complex. Therefore, the Coulomb potential should be analytically continued to the complex plane. In particular, $V_C(x) = -Q/|x|$ is continued as $V_C(x + iy) = -Q/\sqrt{(x + iy)^2} = -\text{sgn}(x)Q/(x + iy)$.

We focus here on the imaginary part of the Coulomb phase which is responsible for the contribution to the ionization rate. For the maximum of the field, the imaginary part is accumulated only along the first section of the integration contour. In general, however, both sections contribute. In particular, the Coulomb correction to the ionization probability $|a_p(t)|^2$ can be written as $e^{2W_{C1}+2W_{C2}}$, where

$$W_{C1} = \frac{Q}{\omega} \int_0^{\phi_i} \frac{|r'_1| d\phi}{r'^2_1 + r''^2_1}, \quad (82)$$

$$W_{C2} = \frac{Q}{\omega} \int_{\phi_i}^{\omega t} \text{sgn}(r'_2) \frac{r''_2 d\phi'}{r'^2_2 + r''^2_2}. \quad (83)$$

Here we have introduced dimensionless times $\phi_\kappa = \omega\tau_\kappa = \omega(\tau_T - 1/\kappa^2)$, $\phi_\tau = \omega\tau_T$, and $\phi_i = \omega t_i$ and the imaginary r'' and real r' parts of electron trajectories along the two sections of the integration contour:

$$r'_1 = \alpha \frac{F}{\omega^2} |\cos \phi_i| (\cosh \phi_\tau - \cosh \phi),$$

$$r''_1 = \beta \frac{F}{\omega^2} |\sin \phi_i| (\sinh \phi_\tau - \sinh \phi + \cosh \phi_\tau (\phi - \phi_\tau)),$$

$$\begin{aligned} r'_2 &= \frac{F}{\omega^2} [\cos \phi - \cos \phi_i \cosh \phi_\tau + \sin \phi_i \cosh \phi_\tau (\phi - \phi_i)], \\ r''_2 &= \beta \frac{F}{\omega^2} |\sin \phi_i| [\sinh \phi_\tau - \phi_\tau \cosh \phi_\tau]. \end{aligned} \quad (84)$$

Here, $\alpha = -\text{sgn}(\cos \phi_i)$ and $\beta = \text{sgn}(\sin \phi_i) = \text{sgn}(p_{||})$. α is related to the sign of the electric field at the moment of ionization and gives the direction of electron escape. On the other hand, β encodes the sign of the electron's drift momentum.

Note that there are two possible scenarios here. If $\alpha = \beta$, the electron escapes in the negative (positive) z -direction with negative (positive) drift velocity and does not return to the core. This occurs for ionization times $\phi_i \in (-\pi/2, 0), (\pi/2, \pi), \dots$, that is, for ionization when the barrier is “opening”. On the other hand, if $\alpha \neq \beta$ and the barrier is “closing”, the electron emerges with a drift velocity back towards the ion. Such electrons will re-encounter the parent ion, and to treat this, we would need to account for recollisions. Here, we consider direct electrons only and hence restrict our attention to the first case. Note that in this instance $\text{sgn}(r'_2) = \alpha = \beta$.

Let us now consider the Coulomb correction terms, W_{C1} and W_{C2} , in more detail. The first correction [Eq. (82)] is always positive and therefore increases the ionization rate compared to the short-range potential. It is equal to:

$$W_{C1} = \int_0^{\phi_i} d\phi \frac{(Q\omega/F)|\cos \phi_i|(\cosh \phi_\tau - \cosh \phi)}{\cos \phi_i^2 [\cosh \phi_\tau - \cosh \phi]^2 + \sin \phi_i^2 [\sinh \phi_\tau - \sinh \phi + \cosh \phi_\tau (\phi - \phi_\tau)]^2}. \quad (85)$$

This correction changes weakly within the cycle.

The subcycle dynamics of the second correction (accumulated along the real time axis) depend on whether the drift velocity is directed towards or away from the ion:

$$W_{C2} = \int_{\phi_i}^{\omega t} d\phi \text{sgn}(r'_2) \beta \frac{(Q\omega/F)|\sin \phi_i|[\sinh \phi_\tau - \phi_\tau \cosh \phi_\tau]}{[\cos \phi + \cosh \phi_\tau ((\phi - \phi_i) \sin \phi_i - \cos \phi_i)]^2 + \sin \phi_i^2 (\sinh \phi_\tau - \phi_\tau \cosh \phi_\tau)^2}. \quad (86)$$

Note that, since $\phi_\tau \geq 0$, $(\sinh \phi_\tau - \phi_\tau \cosh \phi_\tau)$ is always negative. For direct ionization ($\alpha = \beta = \text{sgn}(r'_2)$), we therefore have $W_{C2} < 0$. That is, ionization is suppressed. This correction is intrinsically non-adiabatic. As the barrier is opening (becoming narrower), we can think of it as pulling the electrons back and causing additional trapping.

The nonadiabatic Coulomb correction $e^{2W_{C2}}$ does not affect electrons born around the maximum of the laser field (see Fig. 3). However, the probability of ionization for electrons born at the beginning of the ionization window is suppressed by about three times for typical experimental conditions.

VI. CONCLUSIONS

One of the key properties of our approach is its gauge invariance, as opposed to the standard methods based on the strong-field approximation (SFA). The difference between the results for ionization amplitudes calculated in the length and velocity gauges in the SFA originates from a combination

of two factors. First, in the integral expressions for the ionization amplitude that serve as the starting point of the SFA theory, the initial bound state of the system is laser field free. That, in itself, is not an approximation as long as the final state is treated exactly. Second, the final continuum state is approximated by the Volkov state that ignores the effect of the core potential on the electron. This approximation brings the gauge noninvariance. The Volkov states are themselves gauge invariant in the sense that they yield gauge-independent answers for observables, as long as one is dealing with the free electron. However, they do contain the gauge-dependent factor in their spatial part: The spatial part is $\exp(i\mathbf{p} \cdot \mathbf{r})$ in the velocity gauge and $\exp(i(\mathbf{p} + \mathbf{A}(t)) \cdot \mathbf{r})$ in the length gauge. The factor $\exp(i\mathbf{A}(t) \cdot \mathbf{r})$ disappears from all matrix elements where initial and final states are the Volkov states. However, in the SFA this difference cannot be compensated by the same gauge-dependent term in the initial state, since the latter is field free. In contrast, in our formulation the wave function in the inner region is exact, dressed by the laser field.

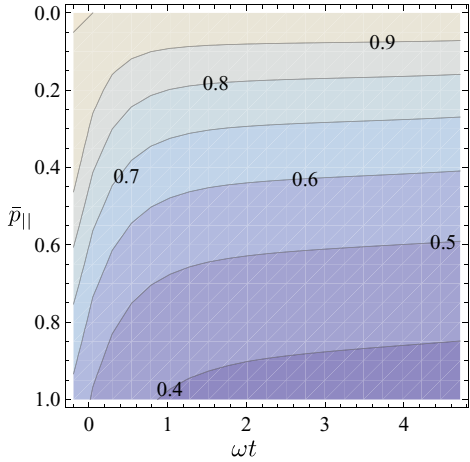


FIG. 3. (Color online) Nonadiabatic Coulomb correction $e^{2W_{C2}}$, plotted against time after ionization ωt , and scaled electron momentum, $\bar{p}_{||} = p_{||}/p_0$, $p_0 = F/\omega$. We consider only those electrons which leave in the negative z direction with negative momentum. This corresponds to ionization times $\phi_i \in (-\pi/2, 0)$. Note that we must have $\omega t > \phi_i$. We assume an 800-nm laser field with intensity 1.3×10^{14} W/cm² and an ionization potential $I_p = 0.57$.

Therefore, transformation between length and velocity gauges will add the exact same gauge-related term to both bound and continuum states, compensating their contribution in the bound-free matrix element.

Our approach also demonstrates how the quasiclassical nature of tunneling in strong laser fields establishes a hierarchy of trajectories. Formally, the ionization amplitudes are determined by integrating over all \mathbf{r} and hence over all trajectories. The interaction of the outgoing electron with the core incorporates all of them. However, the exponential cost of deviating from the optimal tunneling trajectory ensures that the tunneling wave packets associated with different ionization times have a Gaussian shape surrounding the optimal trajectory. Consequently, for each ionization time, the contributions from all possible trajectories to the interaction with the core are dominated by a single trajectory, which leaves the boundary between inner and outer regions along the direction of the field. The same conclusion will apply to effects associated with electron-electron correlation during ionization: the dynamic interaction of the outgoing electron with the electrons remaining in the core. These are the subject of the companion paper [4].

The formalism developed in this paper is naturally suited for multichannel ionization. Insight into the structure of the wave packet in complex time and the ability to evaluate the interaction of the core with the departing electron along characteristic tunneling trajectories are the key implications of our analysis. They show how the picture of non-interacting channels should be amended to include electron-electron correlation during tunneling.

ACKNOWLEDGMENTS

O.S. gratefully acknowledges DFG Grant No. Sm 292/2-1. L.T. acknowledges support from DiNL. O.S. and L.T. thank M. Ivanov for fruitful discussions.

APPENDIX A: DERIVATION OF THE BLOCH OPERATOR

To investigate the Hermiticity of the Hamiltonian H in the inner (outer) region we have to check that

$$C = \int d\mathbf{r} \Psi_1^*(\mathbf{r})(H\Psi_2(\mathbf{r})) - \int d\mathbf{r} (H\Psi_1(\mathbf{r}))^* \Psi_2(\mathbf{r}) = 0. \quad (\text{A1})$$

Taking into account that the radial part of the Laplace operator has the form $\Delta = \frac{1}{r} \frac{d^2}{dr^2} r$, we obtain for the inner region

$$\begin{aligned} C &= \frac{1}{2} \int_0^a r^2 dr \Psi_1^*(\mathbf{r}) \Delta \Psi_2(\mathbf{r}) - \frac{1}{2} \int_0^a r^2 dr \Delta \Psi_1^*(\mathbf{r}) \Psi_2(\mathbf{r}) \\ &= \frac{1}{2} (r \Psi_1^*(\mathbf{r}))' \Psi_2(\mathbf{r})|_0^a - \frac{1}{2} r \Psi_1^*(\mathbf{r}) (\Psi_2(\mathbf{r})r)'|_0^a \\ &= \frac{1}{2} a^2 (\Psi_1'^*(a) \Psi_2(a) - \Psi_1^*(a) \Psi_2'(a)) \neq 0. \end{aligned} \quad (\text{A2})$$

Thus, to compensate the boundary terms we should add the Bloch operator to the Hamiltonian:

$$\widehat{L}^+(a) = \delta(r - a) \left(\frac{d}{dr} + \frac{1-b}{r} \right). \quad (\text{A3})$$

Indeed,

$$\begin{aligned} &\int_0^a r^2 dr \Psi_1^*(\mathbf{r}) L^+(a) \Psi_2(\mathbf{r}) \\ &= \frac{1}{2} \Psi_1^*(a) \Psi_2'(a) a^2 + \frac{1-b}{2} \Psi_1^*(a) \Psi_2(a) a, \end{aligned} \quad (\text{A4})$$

if we define our δ function such that $\int_0^a dr \delta(r - a) = \frac{1}{2}$. Note that the second term will always cancel with a corresponding term from the Hermitian conjugate, leaving us free to choose the constant b as we like.

To derive the Bloch operator for outer region we note that $\int_0^\infty dr = \int_0^a dr + \int_a^\infty dr$ and therefore for the outer region the Bloch operator differs only by sign:

$$\widehat{L}^-(a) = -\delta(r - a) \left(\frac{d}{dr} + \frac{1-b}{r} \right). \quad (\text{A5})$$

It is possible to show that $\int_a^\infty dr \delta(r - a) = \frac{1}{2}$, and correspondingly $\int_0^a dr \delta(r - a) = \frac{1}{2}$, if $\delta(r - a) \equiv \frac{1}{2\pi} \int_{-\infty}^\infty dq e^{iq(r-a)}$.

APPENDIX B: SOLUTION OF THE BOUNDARY PROBLEM FOR A TEST CASE

As an example, consider the simplest possible problem: that of a single state in a short-range potential. Our goal is to show that the approximation of using the full space Green's function, which does not incorporate the Bloch operator, to solve for the wavefunction in the outer region, leads to exponentially small errors.

Suppose we know the wave function of a particle at any moment of time at the boundary given by a sphere with radius $r = a$. In particular, consider $\Psi(a, t') = e^{iI_p(t'-t_0)} e^{-ka}/a$, the solution for a short-range potential. We would now like to find the wave function of this particle outside the sphere for the Hamiltonian $H = \widehat{p}^2/2$ corresponding to free motion.

To this end, we would first have to find the outer region Green's function $\mathcal{G}^a(\mathbf{r}, t, \mathbf{r}', t')$, which corresponds to

the Hamiltonian $H + \hat{L}^-(a)$ and satisfies the appropriate boundary conditions. However, instead, we shall simply use the Green's function $G(\mathbf{r}, t, \mathbf{r}', t')$ for the Hamiltonian $H = \hat{p}^2/2$, given by:

$$G(\mathbf{r}, t, \mathbf{r}', t') = \frac{1}{(2\pi)^3} \theta(t-t') e^{-\varepsilon(t-t')} \int d\mathbf{k} e^{i\mathbf{k}\cdot(\mathbf{r}-\mathbf{r}')} e^{-ik^2(t-t')/2}. \quad (\text{B1})$$

where $\varepsilon \rightarrow 0$ and $\exp(-\varepsilon(t-t'))$ removes transient effects as $t - t' \rightarrow \infty$. This Green's function is defined on all of space, not just in the outer region. It propagates solutions outwards in all directions, and as a result, each point on the boundary effectively acts as a point source (see rightmost image in Fig. 1).

We shall now show that this approximation yields a solution with exponentially small errors if (i) the wave-function at the boundary corresponds to the bound state, (ii) the radius of the sphere is sufficiently large compared to the characteristic size of this bound state: $a\kappa \gg 1$, where $\kappa = \sqrt{2I_p}$ and $E = -I_p$ is the energy of this state.

To obtain an expression for $\Psi(\mathbf{r}, t)$ using this Green's function, we have to insert a decomposition of unity over all of space, $\int d\mathbf{r}' |\mathbf{r}'\rangle \langle \mathbf{r}'|$,

$$\begin{aligned} \langle \mathbf{r} | \Psi(t) \rangle &= i \int_{-\infty}^t dt' \langle \mathbf{r} | e^{-i\hat{H}(t-t')} \hat{L}^- | \Psi_{\text{in}}(t') \rangle \\ &= i \int_{-\infty}^t dt' \int d\mathbf{r}' \langle \mathbf{r} | e^{-i\hat{H}(t-t')} | \mathbf{r}' \rangle \langle \mathbf{r}' | \hat{L}^- | \Psi_{\text{in}}(t') \rangle \\ &= i \int_{-\infty}^t dt' \int d\mathbf{r}' G(\mathbf{r}, \mathbf{r}', t, t') \delta(r' - a) e^{iI_p t'} \kappa \frac{e^{-\kappa a}}{a}, \end{aligned} \quad (\text{B2})$$

where in the last line we have used the fact that $\langle \mathbf{r}' | \hat{L}^- | \Psi_{\text{in}} \rangle = \delta(r' - a)\kappa \Psi(a, t')$ if we choose b appropriately in our definition of \hat{L}^- .

Evaluating the integral over time t' first, we get

$$\Psi(\mathbf{r}, t) = \frac{\kappa e^{iI_p t - \kappa a}}{a(2\pi)^3} \int d\mathbf{r}' \int d\mathbf{k} e^{i\mathbf{k}\cdot(\mathbf{r}-\mathbf{r}')} \frac{2}{\mathbf{k}^2 + \kappa^2}. \quad (\text{B3})$$

Now we integrate over \mathbf{k} . First, integrate over angular coordinates θ and ϕ between the vectors $\mathbf{r} - \mathbf{r}'$ and \mathbf{k} :

$$\begin{aligned} \int d\mathbf{k} \frac{1}{(2\pi)^3} \frac{2e^{i\mathbf{k}\cdot(\mathbf{r}-\mathbf{r}')}}{\kappa^2 + k^2} &= \frac{-i}{4\pi^2 |\mathbf{r} - \mathbf{r}'|} \int_0^\infty dk \frac{2k}{\kappa^2 + k^2} \\ &\times [e^{ik|\mathbf{r}-\mathbf{r}'|} - e^{-ik|\mathbf{r}-\mathbf{r}'|}]. \end{aligned} \quad (\text{B4})$$

Next, observe that the integrand is an even function of k and extend the limits of integration to $\pm\infty$,

$$\int_0^\infty dk \frac{k}{\kappa^2 + k^2} [e^{ik|\mathbf{r}-\mathbf{r}'|} - e^{-ik|\mathbf{r}-\mathbf{r}'|}] = \int_{-\infty}^\infty dk \frac{k}{\kappa^2 + k^2} e^{ik|\mathbf{r}-\mathbf{r}'|}. \quad (\text{B5})$$

Now we can use the residue theorem and take the outgoing solution corresponding to the pole $k = i\kappa$, completing the integration contour in the upper half plane:

$$\int_{-\infty}^\infty dk \frac{2k}{\kappa^2 + k^2} e^{ik|\mathbf{r}-\mathbf{r}'|} = \frac{2\pi i}{\kappa} e^{-\kappa|\mathbf{r}-\mathbf{r}'|}. \quad (\text{B6})$$

Substituting these results into Eq. (B3) and performing spatial integration, we get

$$\Psi(\mathbf{r}, t) = e^{iI_p t} \frac{e^{-\kappa r}}{r} (1 - e^{-2\kappa a}). \quad (\text{B7})$$

Thus, assuming $a\kappa \gg 1$, deviation from the exact result $\Psi(\mathbf{r}, t) = e^{iI_p t} \frac{e^{-\kappa r}}{r}$ is exponentially small. The error term represents the contribution of the undesirable inwards moving solutions discussed above [the red arrows in Fig. 1(b)].

-
- [1] P. G. Burke and J. Tennyson, *Mol. Phys.* **103**, 2537 (2005).
 - [2] O. Smirnova, M. Spanner, and M. Ivanov, *Phys. Rev. A* **77**, 033407 (2008).
 - [3] O. Smirnova, M. Spanner, and M. Ivanov, *J. Phys. B* **39**, S307 (2006).
 - [4] L. Torlina, M. Ivanov, Z. Walters, and O. Smirnova, following paper, *Phys. Rev. A* **86**, 043409 (2012).
 - [5] Z. Walters and O. Smirnova, *J. Phys. B* **43**, 161002 (2010).
 - [6] J. Eberly (private communication).
 - [7] A. Scrinzi (private communication).
 - [8] L. Tao and A. Scrinzi, *New J. Phys.* **14**, 013021 (2012).
 - [9] A. Scrinzi, *Phys. Rev. A* **81**, 053845 (2010).
 - [10] J. Caillat, J. Zanghellini, M. Kitzler, O. Koch, W. Kreuzer, and A. Scrinzi, *Phys. Rev. A* **71**, 012712 (2005).
 - [11] M. Yu. Kuchiev, Sov. Phys. JETP Lett. **45**, 404 (1987).
 - [12] P. B. Corkum, *Phys. Rev. Lett.* **71**, 1994 (1993).
 - [13] K. Kulander, in *Super-Intense Laser-Atom Physics Proceedings of a NATO ARW held in Han-sur-Lesse, Belgium, January 8–14, 1993*, edited by A. L'Huillier, Bernard Piraux, and Kazimierz Rzazewski, NATO Science Series B: Physics Vol. 316 (Kluwer, Dordrecht, 1993).
 - [14] G. L. Yudin and M. Yu. Ivanov, *Phys. Rev. A* **63**, 033404 (2001).
 - [15] A. T. Le, R. R. Lucchese, S. Tonzani, T. Morishita, and C. D. Lin, *Phys. Rev. A* **80**, 013401 (2009).
 - [16] M. V. Frolov, N. L. Manakov, T. S. Sarantseva, M. Y. Emelin, M. Y. Ryabikin, and A. F. Starace, *Phys. Rev. Lett.* **102**, 243901 (2009).
 - [17] O. Smirnova, A. S. Mouritzen, S. Patchkovskii, and M. Ivanov, *J. Phys. B* **40**, F197 (2007).
 - [18] T. Brabec, M. Y. Ivanov, and P. B. Corkum, *Phys. Rev. A* **54**, R2551 (1996).
 - [19] M. Spanner, O. Smirnova, P. B. Corkum, and M. Yu. Ivanov, *J. Phys. B* **37**, L243 (2004).
 - [20] R. Murray, M. Spanner, S. Patchkovskii, and M. Yu. Ivanov, *Phys. Rev. Lett.* **106**, 173001 (2011).
 - [21] Y. Huismans *et al.*, *Science* **331**, 61 (2011).
 - [22] S. V. Popruzhenko and D. Bauer, *J. Mod. Opt.* **55**, 2573 (2008).
 - [23] A. Kirrander and D. V. Shalashilin, *Phys. Rev. A* **84**, 033406 (2011).
 - [24] A. M. Perelomov, V. S. Popov, and M. V. Terent'ev, *Sov. Phys. JETP* **23**, 924 (1966).

- [25] C. Bloch, *Nucl. Phys.* **4**, 503 (1957).
- [26] L. R. Moore, M. A. Lysaght, J. S. Parker, H. W. van der Hart, and K. T. Taylor, *Phys. Rev. A* **84**, 061404 (2011).
- [27] N. L. Manakov and L. P. Rapoport, Sov. Phys. JETP **42**, 430 (1975).
- [28] M. V. Frolov, N. L. Manakov, E. A. Pronin, and A. F. Starace, *Phys. Rev. Lett.* **91**, 053003 (2003).
- [29] M. V. Frolov, N. L. Manakov, E. A. Pronin, and A. F. Starace, *J. Phys. B* **36**, L419 (2003).
- [30] S. V. Popruzhenko, V. D. Mur, V. S. Popov, and D. Bauer, *Phys. Rev. Lett.* **101**, 193003 (2008).
- [31] In PPT theory $a_g(t)$ is omitted. It can be incorporated as shown in [3].
- [32] L V Keldysh, Sov. Phys. JETP **20**, 1307 (1965).
- [33] Alan Jeffrey and Daniel Zwillinger (eds.), *Gradshteyn and Ryzhik's Table of Integrals, Series, and Products*, 6th ed. (Academic Press, San Diego, 2000).
- [34] The factor $(-1)^l$ accounts for the negative sign of the lobe of the electron wave function for $\theta = \pi$.
- [35] The use of an approximate Green's function should introduce only an exponentially small error (see Appendix B).
- [36] V. S. Popov, *Phys. Usp.* **42**, 733 (1999).
- [37] A. Becker and F. Faisal, *J. Phys. B* **38**, R1 (2005).

Time-dependent analytical *R*-matrix approach for strong-field dynamics. II. Many-electron systems

Lisa Tortlina,¹ Misha Ivanov,^{1,2,3} Zachary B. Walters,^{4,1} and Olga Smirnova¹

¹Max Born Institute, Max Born Strasse 2a, 12489 Berlin, Germany

²Department of Physics, Humboldt University, Newtonstrasse 15, 12489 Berlin, Germany

³Department of Physics, Imperial College London, South Kensington Campus, SW7 2AZ London, United Kingdom

⁴Max Planck Institute for the Physics of Complex Systems, Nöthnitzer Strasse 38, 01187 Dresden, Germany

(Received 2 May 2012; published 5 October 2012)

Ionization of atoms and molecules in intense low-frequency fields is a multielectron process which may leave the ion in different excited states. Within the adiabatic perspective on strong-field ionization, usually referred to as optical tunneling, electrons remaining in the molecular ion are assumed to be frozen during the ionization process. In this case, the only way to excite the molecular ion during ionization is to remove an electron from a lower-lying molecular orbital. The higher ionization potential corresponding to such processes implies that such channels are exponentially suppressed during tunneling. Here we show that correlation-induced coupling between the departing electron and the core electrons removes the exponential penalty for ionic excitations, resulting in complex attosecond dynamics of core rearrangement during strong-field ionization. We develop a multichannel theory of strong-field ionization and demonstrate the importance of correlation-induced excitations in the multiphoton and tunneling regimes for N₂ and CO₂ molecules.

DOI: 10.1103/PhysRevA.86.043409

PACS number(s): 32.80.Rm, 42.50.Hz, 33.80.Wz

I. INTRODUCTION

Ionization is a ubiquitous phenomenon in laser-matter interaction, underlying such diverse processes as the photoelectric effect, radiation damage, tunneling microscopy, and laser-based mass spectroscopy, as well as many others. Even if only one electron escapes the core, ionization at its heart involves interaction between all electrons of the original system. This interaction has been long appreciated in the case of single photon ionization, where different mechanisms such as “shake-up” and postionization interaction (“knock-out” or “two-step-one” process) play a crucial role in describing the rearrangement of the core that may accompany ionization (e.g., see [1–3]).

In most pathways, electron-electron correlation plays a key role. In shake-up, for example, this correlation occurs prior to the absorption of the photon. In simple terms, the “core” electrons feel the presence of the “active” electron before ionization and feel its absence afterwards. The absence is felt in the form of a modified potential, which no longer experiences the contribution of the liberated electron. The old wave function is then projected onto eigenfunctions of the new potential. For shake-up to occur, the active electron must escape more quickly than the core electrons can adjust to its absence, so that the core wave function does not change during the ionization process.

Interaction between the outgoing electron and electrons in the core can also occur after the photon has been absorbed. Part of the departing electron’s energy is transmitted to the core, changing the state of the ion in what is essentially a half-collision. Unlike shake-up, this postionization interaction can take time: The long range of the Coulomb interaction allows the escaping electron to interact with the core as it departs.

How will this picture change when not one but many photons are absorbed? For a low-frequency field, the minimum number of photons needed for ionization, $N_0 = I_p/\omega$, may be very large. Here I_p is the ionization potential and ω is the laser frequency. Because multiple photons are absorbed, there are now multiple instances when electron-electron correlation may

be felt. If we were to treat the electron-electron correlation perturbatively, we would have the following intuitive picture: N_1 photons could be absorbed before electron-electron correlation and N_2 photons could be absorbed after for any combination such that $N_1 + N_2 = N_0$. How do such pathways add up? Is it possible for electron-electron interaction to change the state of the core more than once? How important would such higher-order terms in electron-electron correlations be? Here we address these questions.

We apply the time-dependent analytical *R*-matrix (ARM) approach developed in our companion paper [4], generalizing it to N electron systems with one departing electron and $N - 1$ core electrons. Our results generalize the analytical theory of strong-field ionization already developed for single-electron systems [4–7] to the multielectron, multichannel case. In this way, we are able to describe electron rearrangement in the core of an atom or molecule which accompanies strong-field ionization, going beyond the picture of direct ionization developed in [8–11] (see also the so-called SU1 contribution in Ref. [12]). The picture of direct ionization is widely applied in molecules, where it is often viewed (interpreted) as tunneling from a particular molecular orbital. From the perspective of different contributions during tunneling described in Ref. [12], our analysis explicitly incorporates electron-electron interaction throughout the whole motion across the tunneling barrier, not only correlation after the electron emerges from the classically forbidden barrier region (called the SU2 contribution in [12]).

In theories based on the single active electron approximation, excitation of the core during strong-field ionization has long been assumed to be negligible. This is most easily understood in the following simple picture. The binding potential and the time-dependent laser field combine to create an oscillating barrier through which the electron must escape. Aside from the oscillation, this picture is reminiscent of tunnel ionization in static fields. The transmission rate through such a barrier is exponentially suppressed with respect to I_p , not only for static electric fields but also for oscillating laser fields [5]. It has therefore been a nearly universal assumption that the

removal of the least bound electron from the molecule is exponentially dominant, leaving the resulting ion in its lowest electronic state.

The exponential penalty arises in the standard theory of strong-field ionization because the core is either assumed to be frozen during the tunneling process or is described using self-consistent field (see, e.g., [13] for a recent application of this approximation to strong-field ionization). Within the self-consistent field approach, the electron would have to tunnel from a more deeply bound orbital to leave the core in an excited state. Thus, contrary to single-photon ionization, multiphoton ionization in low-frequency fields (optical tunneling) is conventionally treated as an adiabatic process. This perspective is embedded in the theory of inelastic tunneling of [8–11].

Interestingly, this adiabatic picture contradicts the well-known perspective on atom-ion collisions with charge exchange, where the tunneling of an electron from an atom to an ion may involve substantial excitations of the donor [14,15]. Recent experimental advances have also begun to challenge the picture of strong-field ionization as an adiabatic process (see, e.g., [16,17] for the latest evidence of nonadiabatic multielectron dynamics during strong-field ionization).

A nonadiabatic multielectron response implies the presence of excited states of the ion after ionization. In principle, these states could be detected by examining the photoelectron spectra, as done for single-photon ionization. However, the highly nonlinear nature of the strong-field interaction makes such analysis very challenging, obscuring the identification of different ionic states [18]. Alternatively, one could attempt to identify excited states in molecules by the fragmentation channels to which they correlate (see, e.g., Ref. [12]). However, these techniques do not generally allow one to experimentally distinguish ionic excitations that occur during ionization from those that occur after. These problems have now been addressed using coincidence techniques [19], which allow one to correlate energies in the photoelectron spectra with ionic fragments, “cleaning up” the photoelectron spectra and making it possible to distinguish ionic excitations that have occurred during or after ionization. Together with alternative evidence [20–26], experiments have now unambiguously demonstrated a significant contribution of multiple ionization channels, which correspond to a population of different electronically excited states during ionization. Strong experimental arguments suggest that, just like one-photon ionization, multiphoton ionization is not an adiabatic process [16,17,24].

To address these issues, it is necessary to not only consider multiple ionization channels associated with different final states of the ion, but also to include the interaction between these channels during ionization. Loosely speaking, these channels correspond to the removal of electrons from different orbitals. Rigorously, they correspond to different final states of the ion. Interaction between channels is associated with the excitation and deexcitation of the ion, that is, moving the hole from one orbital to another during the ionization process. The importance of channel coupling due to the laser field has been emphasized theoretically in [24,27,28]. The combined effect of the strong laser field and channel coupling on the recombination step of high harmonic generation has been discussed in Ref. [29]. Reference [24] suggested the importance

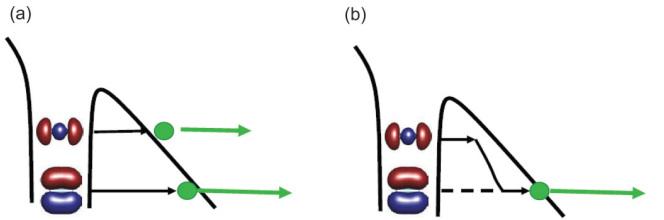


FIG. 1. (Color online) An illustration of the direct (a) and correlation-driven (b) channels in tunnel ionization.

of electron correlations during tunneling and provided the first experimental indication of nontrivial dynamics induced by this coupling. The theory presented below lays the foundation for the analysis and interpretation of these dynamics.

Qualitatively, allowing the state of the ion to evolve during ionization may significantly alter the likelihood of ionizing to an excited final state. Electron-electron correlation between the ion and the departing electron can induce nonadiabatic dynamics as the electron leaves the core. As a result of this excitation, which can happen at any point during ionization (tunneling), the creation of excited ionic states is not subject to the full exponential suppression accompanying direct ionization from more deeply bound orbitals. Figure 1 shows an illustration of this nonadiabatic, correlation-driven pathway. The left panel shows the usual direct adiabatic tunneling channels, corresponding to the removal of an electron from the highest occupied molecular orbital (HOMO) and the one just below it (HOMO-1). A thinner tunneling barrier for the highest orbital gives the first channel an exponential advantage over the second. The right panel shows the nonadiabatic correlation-driven channel. Here the electron leaves from the HOMO. However, before exiting the tunneling barrier, it interacts with the core electrons and excites the ionic core. The tunneling electron then loses its energy and has to pass through a thicker barrier, which corresponds to the HOMO-1 being vacant. However, this thicker barrier appears only at the end, so that the nonadiabatic channel does not incur the full exponential penalty characteristic of the direct HOMO-1 channel.

This paper is organized as follows. Sections II and III present a multichannel theory of strong-field ionization which includes electron-electron correlation during tunneling. In Secs. IV and V we perform saddle-point analysis of the general expressions in the spirit of Perelomov, Popov, and Terent'ev (PPT) theory [6,7] and derive simple analytical expressions for direct and correlation-driven channels in strong-field ionization. Section VI illustrates the importance of correlation-induced excitations for tunnel ionization of N₂ and CO₂ molecules. Section VII discusses the role of this channel in strong-field phenomena.

II. BASIC EQUATIONS

We use the analytical time-dependent *R*-matrix approach (ARM) [4] and the saddle-point method to develop a multichannel theory of strong-field ionization. First, we introduce the Hamiltonian of an *N*-electron neutral molecule interacting

with a laser field:

$$\begin{aligned} H^N &= T_e^N + V_C^N + V_{ee}^N + V_L^N, \\ V_C^N &= - \sum_{m,i=1}^{i=N} Z_m / |\mathbf{R}_m - \mathbf{r}_i|, \\ V_{ee}^N &= \sum_{i \neq j}^N 1 / |\mathbf{r}_i - \mathbf{r}_j|, \quad V_L^N = \sum_i \mathbf{F}(t) \cdot \mathbf{r}_i. \end{aligned} \quad (1)$$

Here the nuclei with charges Z_m are frozen at positions \mathbf{R}_m . Index m enumerates the nuclei, while i, j label the electrons. Superscript N indicates the number of electrons involved. T_e^N is the electron kinetic energy operator, V_C^N describes the Coulomb potential of the nuclei, V_{ee}^N describes the electron-electron interaction, and V_L^N describes the interaction with the laser field.

We also use the Hamiltonian of the ion in the laser field H^{N-1} and the Hamiltonian of an electron H_e interacting with the laser field, the nuclei, and the ($N - 1$) electrons of the ion, $H_e = H^N - H^{N-1}$.

Our goal is to solve the time-dependent Schrödinger equation for the N -electron wave function of the molecule, initially in its ground electronic state $\Psi_g(\mathbf{r})$:

$$i \frac{\partial}{\partial t} |\Psi^N(t)\rangle = \hat{H}^N |\Psi^N(t)\rangle, \quad (2)$$

$$|\Psi^N(t=0)\rangle = |\Psi_g\rangle. \quad (3)$$

Let us now apply the time-dependent ARM approach [4]. We begin by reformulating the initial value problem as a boundary problem. We divide the space into inner and outer regions and introduce the Bloch operator for the outer region $\hat{L}^-(a)$,

$$\hat{L}^-(a) = - \sum_{i=1}^N \hat{\Delta}_i(a) \hat{B}_i, \quad (4)$$

where the index i labels each of the N electrons. In coordinate representation we have

$$\langle \mathbf{r} | \hat{\Delta}_i(a) | \mathbf{r}' \rangle = \delta(r_i - a) \langle \mathbf{r} | \mathbf{r}' \rangle = \delta(r_i - a) \delta(\mathbf{r} - \mathbf{r}'), \quad (5)$$

$$\langle \mathbf{r} | \hat{B}_i | \mathbf{r}' \rangle = \left(\frac{d}{dr_i} - \frac{b_0 - 1}{r_i} \right) \delta(\mathbf{r} - \mathbf{r}'). \quad (6)$$

Here b_0 is an arbitrary constant (see, e.g., [4] for discussion). We use the shorthand notation $\hat{\Delta}(a) \hat{B} \equiv \sum_i \hat{\Delta}_i(a) \hat{B}_i$ to imply summation over all electrons. The δ function is defined such that

$$\int_a^\infty dr \delta(r - a) = \int_0^a dr \delta(r - a) = \frac{1}{2}. \quad (7)$$

Adding and subtracting the Bloch operator to the Hamiltonian, we can rewrite Eqs. (2) and (3) as

$$\begin{aligned} i \frac{\partial}{\partial t} |\Psi^N(t)\rangle &= [\hat{H}^N + \hat{L}^-(a)] |\Psi^N(t)\rangle - \hat{L}^-(a) |\Psi^N(t)\rangle, \\ |\Psi^N(t=0)\rangle &= |\Psi_g^N\rangle. \end{aligned} \quad (8)$$

The boundary nature of the Bloch operator allows one to reformulate Eqs. (8) as a boundary value problem, with the

formal solution

$$|\Psi^N(t)\rangle = -i \int_{-\infty}^t dt' U^N(t, t') \hat{\Delta}(a) \hat{B} |\Psi^N(t')\rangle. \quad (9)$$

Here $U^N(t, t')$ is the N -electron propagator in the outer region, corresponding to the outer-region Hamiltonian $\hat{\mathcal{H}}^N = \hat{H}^N + \hat{L}^-(a)$.

We now use the same approach as in the one-electron case [4] and approximate the wave function on the right-hand side of Eq. (9) with the ground state of the neutral atom, $|\Psi^N(t')\rangle \simeq e^{-iE_g t'} a_g(t') |\psi_g^N\rangle$, yielding

$$|\Psi^N(t)\rangle = -i \int_{-\infty}^t dt' U^N(t, t') \hat{\Delta}(a) \hat{B} |\psi_g^N\rangle a_g(t') e^{-iE_g t'}, \quad (10)$$

where E_g is the energy of the ground state and $a_g(t')$ incorporates Stark shift and the depletion of the ground state. Our next step is to introduce a multichannel expansion into the above equation.

III. MULTICHANNEL FORMALISM

A. Selection of channels

At this point, we need to identify the ionization channels associated with different states of the ion. The key aspect we have to consider is the presence of the strong laser field, which can induce multiple transitions in the ion and in the continuum.

At first glance, one might like to introduce channels which (i) incorporate the effects of the strong laser field fully and (ii) lead to well-defined field-free states of the ion at the end of interaction $t = T$. Referring to Eq. (10), this implies projecting the final wave function $|\Psi^N(T)\rangle$ on the field-free ionic states $\langle n |$ at $t = T$. According to Eq. (10), these states $\langle n |$ would then have to be propagated back in time from T to t' , with potentially complex evolution. Each channel defined in this way may incorporate not only multiple bound but also continuum states of the ion. Such complexity is undesirable.

To avoid backpropagation, one could instead project onto field-free states of the ion at the moment t' , as the wave function is transferred through the boundary between the inner and outer regions. However, given our goal of an analytical description, this standard choice is also far from ideal. Indeed, since the ion is created in the presence of a strong laser field, ionic states populated during ionization are likely to be far from their field-free counterparts. Distortion of the field-free ionic states has to be included in the ionization step.

To find a good compromise, we recall the dynamics of single-channel strong-field ionization. First, ionization occurs in bursts centered around the instantaneous maxima of the oscillating laser field. Second, the transition to the continuum during each ionization burst is described by trajectories moving in complex time, with the ionization step essentially completed when the trajectory descends to the real time axis. This time interval constitutes a small fraction of the laser period. Thus, the required ionic basis states should (i) be relatively straightforward to find, (ii) incorporate the strong laser field, and (iii) minimize laser-induced transitions during

the (complex-valued) fraction of the laser cycle associated with the ionization step itself: the electron motion in the classically forbidden region. For these reasons, we associate different channels with quasistatic states of the ion, also known as “field-polarized” and/or “adiabatic.”

These states, denoted as $|n_t\rangle$, satisfy the stationary Schrödinger equation for the time-dependent ionic Hamiltonian H^{N-1} which includes the laser field. They are defined by the equation

$$H^{N-1}|n_t\rangle = E_n^{N-1}(t)|n_t\rangle \quad (11)$$

and follow the laser field adiabatically. They are found by diagonalizing the Hamiltonian of the ion in the laser field H^{N-1} at each moment of time. In practice, such diagonalization requires knowledge of the ionic field-free states, including their energies and transition dipoles between them. These can be obtained using quantum chemistry approaches. At the end of the laser pulse the quasistatic states $|n_t\rangle$ turn into the field-free states $|n\rangle$, which are the eigenvectors of the field-free ionic Hamiltonian.

For the continuum electron, we use an approach similar to the one we have already used for the single-electron problem [4]. For the multichannel case, we define the continuum states as solutions of the channel-specific one-electron TDSE

$$i|\dot{\mathbf{k}}_t^n\rangle = H_e^n|\mathbf{k}_t^n\rangle, \quad (12)$$

where the one-electron Hamiltonian, defined as

$$H_e^n \equiv \langle n_t | H^N - H^{N-1} | n_t \rangle, \quad (13)$$

describes the dynamics of the electron in the laser field, the Coulomb potential of the nuclei $V_C(\mathbf{r}) = -\sum_m^{i=N} Z_m / |\mathbf{R}_m - \mathbf{r}|$, and the Hartree potential of the core electrons,

$$V_H^n(t) \equiv \langle n_t | V_{ee} | n_t \rangle. \quad (14)$$

The electron-electron operator $V_{ee} \equiv V_{ee}^N - V_{ee}^{N-1}$ describes the Coulomb interaction between the departing electron and all the electrons left in the ion. Note that the Hartree potential [Eq. (14)] is defined for the quasistatic states of the ion and hence includes polarization of the core by the laser field.

In practice, for analytical calculations we approximate $|\mathbf{k}_t^n\rangle$ with channel specific one-electron eikonal-Volkov states [30], as in the one-electron case. The eikonal-Volkov approximation works well for strong-field ionization [31,32] and laser-assisted one-photon XUV ionization [33–35]. These states are obtained by backpropagating field-free continuum solutions defined at a time T after the laser field has been switched off. For large $T \rightarrow \infty$, these field-free solutions can be well approximated by plane waves, characterized by a momentum \mathbf{k} . Under this assumption, we can express the EVA states at any general time t as

$$\begin{aligned} \langle \mathbf{r} | \mathbf{k}_n^{EVA}(t) \rangle &= \frac{1}{(2\pi)^{3/2}} e^{i(\mathbf{k} + \mathbf{A}(t)) \cdot \mathbf{r} - \frac{i}{2} \int_T^t d\tau [\mathbf{k} + \mathbf{A}(\tau)]^2} \\ &\times e^{-i \int_T^t d\tau U_n(\mathbf{r}_L(\tau, \mathbf{r}, \mathbf{k}, t))}, \end{aligned} \quad (15)$$

where

$$\mathbf{r}_L(\tau; \mathbf{r}, \mathbf{k}, t) = \mathbf{r} + \int_t^\tau dt'' [\mathbf{k} + \mathbf{A}(t'')] \quad (16)$$

and U_n is the effective ionic potential experienced by the departing electron in channel n .

By introducing a basis of laser dressed states for the ion and electron, we imply that, in the absence of electron-electron correlation which couples these systems, the laser-induced dynamics can be modeled accurately. While for analytical calculations we use approximate eikonal-Volkov states, the single-electron problem can be solved efficiently and the dynamics of the continuum electron can be accurately described numerically. Bound-state dynamics in the ion are also reasonably simple as long as they require only a limited set of ionic states; that is, the ion can be modeled as a multilevel system in a laser field.

B. Multichannel amplitudes

Having defined the channels, we can now introduce the channel projector:

$$\hat{I} = \int d\mathbf{k} \sum_n \mathbb{A} |n_t \otimes \mathbf{k}_t^n\rangle \langle n_t \otimes \mathbf{k}_t^n| \mathbb{A}. \quad (17)$$

Here the integration is over all asymptotic momenta \mathbf{k} , which characterize each channel-specific continuum state $|\mathbf{k}_t^n\rangle$. Equation (17) implies an (over)complete basis of the quasistatic states for the ion and the active electron, including continuum states of the ion and bound states of the active electron. Operator \mathbb{A} antisymmetrizes electrons and removes basis set overcompleteness [36]. Inserting \hat{I} into Eq. (10) gives a multichannel representation of the time-dependent wave function (omitting the \otimes sign):

$$\begin{aligned} |\Psi(t)\rangle &= -i \sum_n \int d\mathbf{k} \int_{-\infty}^t dt' U^N(t, t') \mathbb{A} |n_t \mathbf{k}_t^n\rangle \\ &\times \langle n_{t'} \mathbf{k}_{t'}^n | \mathbb{A} \hat{\Delta}(a) \hat{B} | \psi_g^N \rangle a_g(t') e^{-i E_g t'}. \end{aligned} \quad (18)$$

Before proceeding further, consider the matrix element determined by the Bloch operator, which is a single-particle operator acting on all N electrons. This matrix element includes two groups of terms. The first group contains those terms where an electron i crossing the boundary $r_i = a$ is projected onto the continuum state, while the other $N - 1$ electrons staying inside the inner region are projected onto the ionic state $n_{t'}$. The second group includes exchange-like terms, where an electron $j \neq i$ from the inner region is projected onto the continuum state, while the electron i at the boundary is projected onto the bound ionic state. It is straightforward to check that for a sufficiently large radius a of the boundary ($\kappa a \gg 1$), the second group of terms gives an exponentially small contribution compared to the first group.

The equivalence of electrons ensures that all N terms in the first group are identical, and we can label r_1 the electron that leaves the inner region and $i = 2, \dots, N$ the electrons that stay inside the ion at the moment t' . Recalling the normalization factor $1/\sqrt{N}$ coming from antisymmetrization and introducing channel-specific Dyson orbitals for the quasistatic state of the ion,

$$|n_{t'}^D\rangle = \sqrt{N} \langle n_{t'} | \psi_g^N \rangle, \quad (19)$$

we rewrite Eq. (18) as

$$|\Psi(t)\rangle = -i \sum_n \int d\mathbf{k} \int_{-\infty}^t dt' U^N(t,t') |\mathbf{n}_{t'} \mathbf{k}_{t'}^n\rangle \\ \times \langle \mathbf{k}_{t'}^n | \hat{\Delta}_1(a) \hat{B}_1 | \mathbf{n}_{t'}^D \rangle a_g(t') e^{-iE_g t'}. \quad (20)$$

Next, let us turn our attention to the N -electron propagator U^N , which acts on the $N - 1$ core electrons and one outgoing electron. Their interaction introduces correlation-induced coupling between the channels. To single out the contribution of these dynamics, for each channel n , we split up our full Hamiltonian (1) as

$$H^N = H_n^N + V_{ee}^n(t). \quad (21)$$

Here, H_n^N is the “correlation-free” Hamiltonian for channel n . It is a sum of the Hamiltonian for the $N - 1$ electrons which remain in the ion and the Hamiltonian for the continuum electron moving in the self-consistent field of the core,

$$H_n^N \equiv H^{N-1} + H_e^n. \quad (22)$$

This Hamiltonian fully describes laser-induced dynamics in the ion, as well as the dynamics of the continuum electron in the laser field, the field of the nucleus and the Hartree potential [Eq. (14)] for channel n . However, it ignores coupling between the electrons in the ion and the departing electron. Correspondingly, the propagator $U_n^N(t,t')$ will be a product of the propagator for the continuum electron $U_e^n(t,t')$ and for the ion $U^{N-1}(t,t')$, $U_n^N(t,t') = U^{N-1}(t,t') U_e^n(t,t')$.

The second term,

$$V_{ee}^n(t) \equiv V_{ee} - \langle \mathbf{n}_t | V_{ee} | \mathbf{n}_t \rangle, \quad (23)$$

describes correlations between the outgoing electron and the electrons which remain.

With this in mind, we can introduce the following channel-specific Dyson expansion of the full propagator

$$U^N(t,t') = -i \int_{t'}^t dt'' U^N(t,t'') V_{ee}^n(t'') U_n^N(t'',t') + U_n^N(t,t'). \quad (24)$$

This allows us to rewrite the total wave function (20) as a sum of two contributions. The first is the “direct” contribution which does not include electron-electron correlation,

$$|\Psi^{(1)}(T)\rangle = -i \sum_n \int d\mathbf{k} \int dt' U^{N-1}(T,t') |\mathbf{n}_{t'}\rangle \\ \times U_e^n(T,t') |\mathbf{k}_{t'}^n\rangle \langle \mathbf{k}_{t'}^n | \hat{\Delta}_1(a) \hat{B}_1 | \mathbf{n}_{t'}^D \rangle a_g(t') e^{-iE_g t'}. \quad (25)$$

The second is the “indirect” correlation-driven contribution that we are interested in,

$$|\Psi^{(2)}(T)\rangle = - \sum_n \int d\mathbf{k} \int^T dt'' \int^{t''} dt' U^N(T,t'') V_{ee}^n(t'') \\ \times U^{N-1}(t'',t') |\mathbf{n}_{t'}\rangle U_e^n(t'',t') |\mathbf{k}_{t'}^n\rangle \langle \mathbf{k}_{t'}^n | \hat{\Delta}_1(a) \\ \times \hat{B}_1 | \mathbf{n}_{t'}^D \rangle a_g(t') e^{-iE_g t'}. \quad (26)$$

IV. DIRECT IONIZATION AMPLITUDES

Let us begin with the first term, Eq. (25). Direct ionization amplitudes are obtained by projecting $|\Psi^{(1)}(T)\rangle$ onto the final states of the continuum electron and the ionic core. However, we should keep in mind that the quasistatic states we have used to define the ionization channels represent a good basis only for a fraction of the laser cycle. They do not include real laser-induced excitations which develop on the time scale of a laser cycle and longer. These transitions can redistribute the amplitude associated with a particular ionization channel between other channels on the time scale of several cycles after the ionization itself has been completed, obscuring the picture.

To obtain meaningful channel-specific direct ionization amplitudes $a_n(\mathbf{p})$, we recall the results obtained for the single-electron case [4]. For a given final momentum \mathbf{p} , the integral over time t' has contributions associated with different periodically spaced saddle points $t_s(\mathbf{p})$, where $t_s(\mathbf{p}) = t_i(\mathbf{p}) + i\tau_T(\mathbf{p})$ satisfies

$$(\mathbf{p} + \mathbf{A}(t_s))^2 = -2I_p \quad (27)$$

and I_p is the ionization potential. Each saddle point, associated with some final momentum \mathbf{p} , corresponds to a particular ionization burst centered around one of the instantaneous maxima of the oscillating laser field. Ionization is essentially completed when the complex-valued trajectory associated with the saddle point $t' = t_s(\mathbf{p})$ descends to the real time axis. We therefore rewrite the ionic propagator as $U^{N-1}(T,t') = U^{N-1}(T,t_0) U^{N-1}(t_0,t')$. The moment t_0 is selected on the real time axis, ensuring that the saddle-point region around $t_s(\mathbf{p})$ is passed. For the calculations described below, we use $t_0 = \text{Re}[t_s(\mathbf{p})] = t_i$.

We now project the wave function at the moment T onto the ionic basis $U^{N-1}(T,t_0) |\mathbf{m}_{t_0}\rangle$ and the final state of the continuum electron $|\mathbf{p}\rangle$ to obtain the ionization amplitude associated with the continuum electron with momentum \mathbf{p} . Since we are interested only in the contribution of a single ionization burst near t_0 to the total ionization amplitude, we restrict our t' integral to the vicinity of a single saddle point $t_s(\mathbf{p})$ by introducing the contour $C(\mathbf{p},t_0)$. This fact is stressed by keeping t_0 in the argument of $a_{mn}^{(1)}(\mathbf{p},t_0)$:

$$a_{mn}^{(1)}(\mathbf{p},t_0) = -i \int d\mathbf{k} \int_{C(\mathbf{p},t_0)} dt' \langle \mathbf{m}_{t_0} | U^{N-1}(t_0,t') | \mathbf{n}_{t'}\rangle \\ \times \langle \mathbf{p} | U_e^n(T,t') |\mathbf{k}_{t'}^n\rangle \langle \mathbf{k}_{t'}^n | \hat{\Delta}_1(a) \hat{B}_1 | \mathbf{n}_{t'}^D \rangle a_g(t') e^{-iE_g t'}. \quad (28)$$

Note that this amplitude correlates to the final state of the ion $|\tilde{m}(T,t_0)\rangle = U^{N-1}(T,t_0) |\mathbf{m}_{t_0}\rangle$, where $|\tilde{m}(T,t_0)\rangle$ is some superposition of field-free states. The amplitude is formed by the time t_0 . From t_0 to T , only phase is accumulated in the matrix element $\langle \mathbf{p} | U_e^n(T,t') |\mathbf{k}_{t'}^n\rangle$ (up to a nonadiabatic Coulomb correction, discussed in [4], which is unimportant for ionization near the peak of the laser field), accompanied by unitary evolution of the ion $U^{N-1}(T,t_0) |\mathbf{m}_{t_0}\rangle$.

Equation (28) accounts for the fact that the laser field can induce transitions between different quasistatic states during the time interval $t_0 - t_s(\mathbf{p})$. However, in all cases considered below, such transitions are negligible during the short time interval $t_0 - t_s(\mathbf{p})$. One can therefore use the quasistatic

approximation for the short-time propagator $U^{N-1}(t_0, t')$ and the matrix elements $\langle \mathbf{m}_{t_0} | U^{N-1}(t_0, t') | \mathbf{n}_{t'} \rangle$:

$$\begin{aligned} \langle \mathbf{n}_{t_0} | U^{N-1}(t_0, t') | \mathbf{m}_{t'} \rangle &= \delta_{mn} b_m(t_0, t') e^{-i E_m(t_0 - t')} \\ &= \delta_{mn} e^{-i \int_{t'}^{t_0} \Delta E_m^{(\text{St})}(\tau) d\tau - i E_m(t_0 - t')}. \end{aligned} \quad (29)$$

Here E_m is the field-free energy of the ionic state $|m\rangle$. The additional factor $b_m(t_0, t')$ accounts for the quasistatic Stark shift $\Delta E_m^{(\text{St})}(\tau)$.

In practice (see Sec. VI), we will not make the quasistatic approximation when calculating the matrix element Eq. (29). However, off-diagonal contributions will be negligible. The diagonal contribution is

$$\begin{aligned} a_{nn}^{(1)}(\mathbf{p}, t_0, T) &= -i \int d\mathbf{k} \int_{C(\mathbf{p}, t_0)} dt' b_n(t_0, t') e^{-i E_n(t_0 - t')} \\ &\times \langle \mathbf{p} | U_e^n(T, t') | \mathbf{k}_{t'}^n \rangle \langle \mathbf{k}_{t'}^n | \hat{\Delta}_1(a) \hat{B}_1 | \mathbf{n}_{t'}^D \rangle a_g(t') \\ &\times e^{-i E_g t'}. \end{aligned} \quad (30)$$

Orthogonality of the continuum states $|\mathbf{k}_{t'}^n\rangle$ means that this expression simplifies to

$$\begin{aligned} a_{nn}^{(1)}(\mathbf{p}, t_0, T) &= -i \int_{C(\mathbf{p}, t_0)} dt' b_n(t_0, t') e^{-i E_n(t_0 - t')} \\ &\times \langle \mathbf{p}_{t'}^n | \hat{\Delta}_1(a) \hat{B}_1 | \mathbf{n}_{t'}^D \rangle a_g(t') e^{-i E_g t'}. \end{aligned} \quad (31)$$

The amplitude $a_{nn}^{(1)}(\mathbf{p})$ is very similar to the single active electron (SAE) case (see, e.g., our companion paper [4]). The difference is the extra phase evolution in the ionic channel n . First, it encodes the field-free ionization potential for this channel,

$$I_{p,n} = E_n - E_g. \quad (32)$$

Second, the Stark shifts of both neutral and ionic states are also present, via $a_g(t')$ and $b_n(t_0, t')$, respectively. Treating both $a_g(t')$ and $b_n(t_0, t')$ as slow functions and evaluating the t' integral using the saddle-point method, we can express the ionization amplitude $a_{nn}^{(1)}$ via its SAE counterpart a_{SAE} ,

$$a_{nn}^{(1)}(\mathbf{p}, t_0) = a_g(t_s) b_n(t_0, t_s) e^{-i E_n t_0} a_{\text{SAE}}(\mathbf{p}; I_{p,n}, t_0). \quad (33)$$

Note that in our companion paper [4], $a_g(t_s)$ was included in a_{SAE} . The role of the ground-state wave function in the single-electron ionization amplitude is played by the Dyson orbital for the channel, and the unperturbed ionization potential is $I_{p,n}$. Both amplitudes refer to the contribution of a single ionization burst around $t_0 = \text{Re } t_s(\mathbf{p})$.

V. CORRELATION-DRIVEN INDIRECT IONIZATION AMPLITUDES

Consider now the correlation-driven contribution to the total wave function:

$$\begin{aligned} |\Psi^{(2)}(T)\rangle &= - \sum_n \int d\mathbf{k} \int^T dt'' \int^{t''} dt' U^N(T, t'') V_{ee}^n(t'') \\ &\times U^{N-1}(t'', t') | \mathbf{n}_{t'} \rangle U_e^n(t'', t') | \mathbf{k}_{t'}^n \rangle \langle \mathbf{k}_{t'}^n | \hat{\Delta}_1(a) \\ &\times \hat{B}_1 | \mathbf{n}_{t'}^D \rangle a_g(t') e^{-i E_g t'}. \end{aligned} \quad (34)$$

In this exact expression, propagation between t' and t'' is correlation-free, but includes the effect of the self-consistent

field of the core on the outgoing electron. Correlation can induce transitions at an instant moment t'' , after which the full propagator is applied.

Let us now project this wave function onto the ionic basis $U^{N-1}(T, t_0) | \mathbf{m}_{t_0} \rangle$ and the final state of the continuum electron $|\mathbf{p}\rangle$ at time T , just as we did for the direct channel. To first order in electron-electron correlation, we can approximate the full propagator after t'' as

$$U^N(T, t'') \simeq U^{N-1}(T, t'') U_e^m(T, t''). \quad (35)$$

Doing this, we obtain the correlation-induced transition amplitude from the quasistatic ionic state n to the quasistatic state m :

$$\begin{aligned} a_{mn}^{(2)}(\mathbf{p}, t_0) &= - \int d\mathbf{k} \int^{t_0} dt'' \int^{t''} dt' \langle \mathbf{p}_{t''}^m | \langle \mathbf{m}_{t_0} | U^{N-1}(t_0, t'') \\ &\times | V_{ee}^n(t'') U^{N-1}(t'', t') | \mathbf{n}_{t'} \rangle | \mathbf{k}_{t'}^n \rangle \langle \mathbf{k}_{t'}^n | \hat{\Delta}_1(a) \\ &\times \hat{B}_1 | \mathbf{n}_{t'}^D \rangle a_g(t') e^{-i E_g t'}. \end{aligned} \quad (36)$$

Here, we have again restricted our time integral by setting the upper limit of the t'' integral to t_0 . This allows us to compute the contribution from a particular ionization burst as the continuum electron is moving away and eliminates the contribution of the electron-ion recollision which happens after the laser field turns the outgoing electron around and brings it back to the core. Such contributions, responsible for nonsequential double ionization [37], are described by an equation similar to Eq. (36), except that the corresponding contribution to the t'' integral comes from later times $t'' > t_0$, separated from t_0 by about half a laser cycle or more. Restricting the inner (i.e., t') integral to the vicinity of a single saddle point effectively sets the lower limit of the outer t'' integral to $t_s(\mathbf{p})$.

Finally, let us explicitly factor out the phases associated with the channel energies,

$$\begin{aligned} U^{N-1}(t'', t') | \mathbf{n}_{t'} \rangle &= e^{-i E_n(t'' - t')} b_n(t'', t') | \mathbf{n}(t'', t') \rangle, \\ \langle \mathbf{m}_{t_0} | U^{N-1}(t_0, t'') &= e^{-i E_m(t_0 - t'')} b_m(t_0, t'') \langle \mathbf{m}(t_0, t'') |, \end{aligned} \quad (37)$$

where slow functions b_k incorporate Stark shifts of the quasistatic channels. Note that states $|\mathbf{n}(t'', t')\rangle$ and $|\mathbf{m}(t'', t_0)\rangle$ defined by the above equations may be superpositions of different quasistatic states. With this notation, we get

$$\begin{aligned} a_{mn}^{(2)}(\mathbf{p}, t_0) &= - \int d\mathbf{k} \int^{t_0} dt'' \int^{t''} dt' b_m(t_0, t'') e^{-i E_m(t_0 - t'')} \\ &\times \langle \mathbf{m}(t_0, t'') | \langle \mathbf{p}_{t''}^m | V_{ee}^n(t'') | \mathbf{n}(t'', t') \rangle | \mathbf{k}_{t'}^n \rangle b_n(t'', t') \\ &\times e^{-i E_n(t'' - t')} \langle \mathbf{k}_{t'}^n | \hat{\Delta}_1(a) \hat{B}_1 | \mathbf{n}_{t'}^D \rangle a_g(t') e^{-i E_g t'}. \end{aligned} \quad (38)$$

The integral over t' , as we will soon see, is again accumulated near the saddle point $t_s(\mathbf{p})$. Pre-empting this, for convenience of notation, we can therefore take the slow function $b_n(t'', t')$ out of the t' integral at the saddle point, replacing it with $b_n(t'', t_s)$. The same is done with $|\mathbf{n}(t'', t')\rangle$. Recalling that $V_{ee}^n = V_{ee}^n(\mathbf{r}, \dots, \mathbf{r}_N)$ and inserting the identity on the coordinates of the departing electron, $\int d\mathbf{r} |\mathbf{r}\rangle \langle \mathbf{r}|$, we can rewrite

Eq. (38) as

$$\begin{aligned} a_{mn}^{(2)}(\mathbf{p}, t_0) &= -i \int^{t_0} dt'' e^{-iE_m t_0} b_m(t_0, t'') b_n(t'', t_s) e^{i(E_m - E_n)t''} \\ &\times \int d\mathbf{r} \int d\mathbf{k} \langle \mathbf{p}_{t''}^m | \mathbf{r} \rangle \langle \mathbf{m}(t_0, t'') | V_{ee}^n(t'', \mathbf{r}) | \mathbf{n}(t'', t_s) \rangle \langle \mathbf{r} | \mathbf{k}_{t''}^n \rangle \\ &\times \left[(-i) \int^{t''} dt' \langle \mathbf{k}_{t'}^n | \hat{\Delta}_1(a) \hat{B}_1 | \mathbf{n}_{t'}^D \rangle a_g(t') e^{iI_{p,n}t'} \right]. \end{aligned} \quad (39)$$

The operator $V_{ee}^n(t'', \mathbf{r})$ in Eq. (39) acts on all electrons but the notation explicitly stresses the coordinate \mathbf{r} of the outgoing electron.

The expression in square brackets in Eq. (39) is almost exactly the SAE ionization amplitude $a_{\mathbf{k}}(T)$, which we calculated in the companion paper [4], with the hydrogen bound state replaced by a Dyson orbital $|\mathbf{n}_{t'}^D\rangle$. The main difference here is that the upper limit of the t' integral is t'' ; the form of the t' integrand itself is identical. However, as we saw in [4] and as we discussed for the direct channel, the contribution to the integral over t' comes only from the saddle-point region $t_s(\mathbf{p})$, determined by Eq. (27). Thus, assuming we choose the contour for t'' appropriately, this upper limit should not affect the value of our integral. We can therefore replace the expression in square brackets by $a_{\mathbf{k}}(T)$,

$$\begin{aligned} a_{mn}^{(2)}(\mathbf{p}, t_0) &= -i \int^{t_0} dt'' e^{-iE_m t_0} b_m(t_0, t'') b_n(t'', t_s) e^{i(E_m - E_n)t''} \\ &\times V_{mn}(\mathbf{p}, t''), \end{aligned} \quad (40)$$

where we have introduced

$$\begin{aligned} V_{mn}(\mathbf{p}, t'') &= \int d\mathbf{r} \int d\mathbf{k} \langle \mathbf{m}(t_0, t'') | V_{ee}^n(t'', \mathbf{r}) | \mathbf{n}(t'', t_s) \rangle \\ &\times \langle \mathbf{p}_{t''}^m | \mathbf{r} \rangle \langle \mathbf{r} | \mathbf{k}_{t''}^n \rangle a_{\mathbf{k}}(T). \end{aligned} \quad (41)$$

Let us now look more closely at the integrals over \mathbf{k} and \mathbf{r} above. To evaluate these explicitly, we use eikonal-Volkov states (15) for $\langle \mathbf{p}_{t''}^m | \mathbf{r} \rangle$ and $\langle \mathbf{r} | \mathbf{k}_{t''}^n \rangle$ and quote the following analytical result for $a_{\mathbf{k}}(T)$ from [4]:

$$\begin{aligned} a_{\mathbf{k}}(T) &= a_g(t_s) R_n(\mathbf{k}) e^{-\frac{i}{2} \int_{t_s}^T d\tau [\mathbf{k} + \mathbf{A}(\tau)]^2 + iI_{p,n}t_s} \\ &\times e^{-i \int_{t_s}^T d\tau U(\int_{t_s}^\tau dt' [\mathbf{k} + \mathbf{A}(t')])}. \end{aligned} \quad (42)$$

Here, $R_n(\mathbf{k})$ is a term that encodes the impact of the angular structure of our channel- n Dyson orbital on ionization exactly as $R_{klm}(\mathbf{k})$ did for hydrogen bound states in [4]. The implementation for calculating $R_n(\mathbf{k})$ terms here will be analogous to the one discussed by Murray *et al.* for static fields [38], showing how the static approach extends to oscillating fields.

Substituting in these expressions, we obtain

$$\begin{aligned} V_{mn}(\mathbf{p}, t'') &= e^{-i/2 \int_{t''}^T (\mathbf{p} + \mathbf{A}(\tau))^2 d\tau} \frac{1}{(2\pi)^3} \int d\mathbf{r} \\ &\times \int d\mathbf{k} e^{i(\mathbf{k} - \mathbf{p}) \cdot \mathbf{r}} e^{-i/2 \int_{t_s}^{t''} (\mathbf{k} + \mathbf{A}(\tau))^2 d\tau} e^{iI_{p,n}t_s} \\ &\times a_g(t_s) R_n(\mathbf{k}) \langle \mathbf{m}(t_0, t'') | V_{ee}^n(t'', \mathbf{r}) | \mathbf{n}(t'', t_s) \rangle \\ &\times e^{-iW_c^{mn}(t'', \mathbf{r}, \mathbf{k}, T)}, \end{aligned} \quad (43)$$

where

$$\begin{aligned} W_c^{mn}(t'', \mathbf{r}, \mathbf{k}, T) &= \int_{t''}^T d\tau U_m \left(\mathbf{r} + \int_{t''}^\tau d\zeta [\mathbf{p} + \mathbf{A}(\zeta)] \right) \\ &+ \int_T^{t''} d\tau U_n \left(\mathbf{r} + \int_{t''}^\tau d\zeta [\mathbf{k} + \mathbf{A}(\zeta)] \right) \\ &+ \int_{t_s}^T d\tau U_n \left(\int_{t_s}^\tau d\zeta [\mathbf{k} + \mathbf{A}(\zeta)] \right). \end{aligned} \quad (44)$$

If we now compare this to $a_{\mathbf{p}}(t)$ in [4], we see that the integrals we have to evaluate are entirely analogous. We have simply gained the factor $\langle \mathbf{m}(t_0, t'') | V_{ee}^n(t'', \mathbf{r}) | \mathbf{n}(t'', t_s) \rangle$, and W_c now has an additional U_m -dependent term. Both these terms, however, can be treated as slow prefactors and will not affect our saddle-point analysis. Thus, following the derivation in [4], we shall proceed by integrating first over \mathbf{k} and then over \mathbf{r} .

Applying the saddle-point method for the integral over \mathbf{k} , assuming that $R_n(\mathbf{k})$ is slowly varying and well-behaved, we find

$$\begin{aligned} V_{mn}(\mathbf{p}, t'') &\simeq e^{-i/2 \int_{t''}^T (\mathbf{p} + \mathbf{A}(\tau))^2 d\tau} \int d\mathbf{r} \frac{e^{-i\pi/4}}{[2\pi(t'' - t_s)]^{3/2}} \\ &\times e^{\frac{i(\mathbf{r} - \mathbf{r}_s(\mathbf{p}, t''))^2}{t'' - t_s}} e^{-i/2 \int_{t_s}^{t''} (\mathbf{p} + \mathbf{A}(\tau))^2 d\tau} e^{iI_{p,n}t_s} \\ &\times a_g(t_s) R_n(\mathbf{k}_s) \langle \mathbf{m}(t_0, t'') | V_{ee}^n(t'', \mathbf{r}) | \mathbf{n}(t'', t_s) \rangle \\ &\times e^{-iW_c^{mn}(t'', \mathbf{r}, \mathbf{k}_s, T)}, \end{aligned} \quad (45)$$

where the stationary momentum \mathbf{k}_s is given by

$$\mathbf{k}_s = \frac{\mathbf{r} - \int_{t_s}^{t''} \mathbf{A}(\tau) d\tau}{t'' - t_s}, \quad (46)$$

and

$$\mathbf{r}_s(\mathbf{p}, t'') = \int_{t_s}^{t''} [\mathbf{p} + \mathbf{A}(\tau)] d\tau. \quad (47)$$

The presence of the wave packet $\exp[\frac{i(\mathbf{r} - \mathbf{r}_s(\mathbf{p}, t''))^2}{t'' - t_s}] / [2\pi(t'' - t_s)]^{3/2}$ above allows us to evaluate the \mathbf{r} integral using the saddle-point method, where the saddle point is given by Eq. (47) above. Note that in the classically forbidden region $t'' - t_s = -i\xi$, this wave packet becomes a Gaussian. It is the presence of this term which allows us to use a single tunneling trajectory, as defined by Eq. (47), to evaluate the contribution of the core potential to the SAE ionization amplitude $a_{\mathbf{p}}(t)$ in [4]. For exactly the same reason, we can also substitute it in the correlation-driven matrix element $\langle \mathbf{m}(t_0, t'') | V_{ee}^n(\mathbf{r}) | \mathbf{n}(t'', t_s) \rangle$ here. Doing this, and noting that Eqs. (46) and (47) together imply $\mathbf{k}_s = \mathbf{p}$, we obtain the final result

$$\begin{aligned} V_{mn}(\mathbf{p}, t'') &\simeq a_g(t_s) R_n(\mathbf{p}) e^{-i/2 \int_{t_s}^T (\mathbf{p} + \mathbf{A}(\tau))^2 d\tau} e^{iI_{p,n}t_s} \\ &\times \langle \mathbf{m}(t_0, t'') | V_{ee}^n(\mathbf{r}_s(t'')) | \mathbf{n}(t'', t_s) \rangle \\ &\times e^{-i \int_{t''}^T d\tau U_m(\mathbf{r}_s(\mathbf{p}, \tau))} e^{-i \int_{t_s}^{t''} d\tau U_n(\mathbf{r}_s(\mathbf{p}, \tau))}. \end{aligned} \quad (48)$$

Introducing the correction factor,

$$Q_{mn}(t'') \equiv \int_{t''}^T d\tau [U_m(\mathbf{r}_s(\tau)) - U_n(\mathbf{r}_s(\tau))], \quad (49)$$

we can express this as

$$\begin{aligned} V_{mn}(\mathbf{p}, t'') \simeq & [a_g(t_s) R_n(\mathbf{p}) e^{-i/2 \int_{t_s}^T (\mathbf{p} + A(\tau))^2 d\tau} e^{i I_{p,n} t_s} \\ & \times e^{-i \int_{t_s}^T d\tau U_n(\mathbf{r}_s(\mathbf{p}, \tau))}] \langle m(t_0, t'') | V_{ee}^n(\mathbf{r}_s(t'')) \\ & \times | n(t'', t_s) \rangle e^{-i Q_{mn}(t'')}. \end{aligned} \quad (50)$$

Comparing the first term [in brackets] to Eq. (42), we see that this is simply the SAE ionization amplitude for channel n , $a_p(T) = a_g(t_s) a_{SAE}(\mathbf{p}; I_{p,n}, t_0)$. Thus, we can now write down a simple expression for our correlation-driven multichannel ionization amplitude:

$$\begin{aligned} a_{mn}^{(2)}(\mathbf{p}, t_0) = & -i \int_{t_s}^{t_0} dt'' e^{-i E_m t_0} b_m(t_0, t'') b_n(t'', t_s) e^{i(E_m - E_n)t''} \\ & \times a_g(t_s) a_{SAE}(\mathbf{p}; I_{p,n}, t_0) \langle m(t_0, t'') | V_{ee}^n(\mathbf{r}_s(t'')) \\ & \times | n(t'', t_s) \rangle e^{-i Q_{mn}(t'')}. \end{aligned} \quad (51)$$

Recalling our final result for the direct channel ionization amplitude Eq. (33), we can express this as

$$a_{mn}^{(2)}(\mathbf{p}, t_0) = c_{mn}(t_0, t_s) b_n^{-1}(t_0, t_s) a_{nn}^{(1)}(\mathbf{p}, t_0), \quad (52)$$

where

$$\begin{aligned} c_{mn}(t_0, t_s) = & -i \int_{t_s}^{t_0} dt'' \langle m(t_0) | U^{(N-1)}(t_0, t'') V_{ee}^n(\mathbf{r}_s(t'')) \\ & \times U^{(N-1)}(t'', t_s) | n(t_s) \rangle e^{-i Q_{mn}(t'')} \end{aligned} \quad (53)$$

or, explicitly writing out phases associated with the unperturbed energies of the channels,

$$\begin{aligned} c_{mn}(t_0, t_s) = & -i \int_{t_s}^{t_0} dt'' b_m(t_0, t'') b_n(t'', t_s) e^{-i(E_m - E_n)(t_0 - t'')} \\ & \times \langle m(t_0, t'') | V_{ee}^n(\mathbf{r}_s(t'')) | n(t'', t_s) \rangle e^{-i Q_{mn}(t'')}. \end{aligned} \quad (54)$$

Note that both t_s and $t_0 = \text{Re}[t_s]$ are determined by the momentum \mathbf{p} .

The amplitude c_{mn} describes correlation-induced transitions between the quasistatic electronic states of the ion. The field responsible for these transitions is created by the departing electron, which arrives at the detector with momentum \mathbf{p} . The transitions occur while the tunneling electron is moving away from the core via the classically forbidden region and result in correlation-driven ionization into channel m .

The evolution of the states $\langle m(t_0, t'') \rangle$ and $| n(t'', t_s) \rangle$ is exact. The t'' integral is taken in complex time, from the saddle point $t_s = t_0 + i\tau_T(\mathbf{p})$ to $t_0 = \text{Re}[t_s]$. Consequently, $t_0 - t'' = -i\xi$ and the factor $\exp(-i(E_m - E_n)(t_0 - t''))$ in the integrand becomes $\exp(-(E_m - E_n)\xi)$. This results in the exponential suppression of the excitation amplitude $c_{mn}(\mathbf{p})$ if the eigenstate $|m\rangle$ has higher energy than the eigenstate $|n\rangle$ [39], that is, $\Delta I_p \equiv E_m - E_n > 0$.

Consider ionization at the maximum of the instantaneous laser field, when $\mathbf{p}/v_0 = \mathbf{p}/\sqrt{4U_p} \simeq 0$, with $U_p = F^2/4\omega^2$ the ponderomotive potential. In this case $t_s = i\tau_T$ and $t_0 = 0$. Changing the integration variable to imaginary $\xi = i(t_0 - t'')$, we see that when the laser-induced Stark shifts in the ion and the difference between the core potentials for different

ionization channels are neglected, we have

$$c_{mn} = \int_{\tau_T}^0 d\xi e^{-\Delta I_p \xi} \langle m | V_{ee}^n(\mathbf{r}_s(\xi)) | n \rangle. \quad (55)$$

This expression shows that the exponential suppression factor $e^{-\Delta I_p \xi}$ favors excitation which occurs close to the exit from the tunnel ($\xi = 0$). The role of this factor is discussed in our short report [40].

It will be convenient to evaluate the strength of the indirect channel $n \rightarrow m$ by normalizing the corresponding amplitude with respect to the direct ionization amplitude associated with the “parent” channel n . Using the results above, this ratio is

$$\begin{aligned} \tilde{a}_{mn}^{(2)}(\mathbf{p}) &= a_{mn}^{(2)}(\mathbf{p}) / a_{nn}^{(1)}(\mathbf{p}) \\ &= c_{mn}(t_0, t_s) / b_n(t_0, t_s) \equiv c_{mn}(\mathbf{p}) / b_n(\mathbf{p}), \end{aligned} \quad (56)$$

where in the last equality we have stressed that both t_s and $t_0 = \text{Re}[t_s]$ are determined by the final momentum \mathbf{p} .

VI. RESULTS

The central result of this work is given by Eqs. (52)–(54), which connect the correlation-induced indirect ionization amplitude with the amplitude for direct ionization from the parent channel. In this section, we analyze the role of the correlation-induced channel in strong-field ionization of N₂ and CO₂ molecules. As we will see, this depends strongly on the electronic structure of the molecule and the details of the laser field parameters. Direct ionization amplitudes are calculated using the analytical approach developed in Refs. [38,41]. We include the effect of Stark shifts, encoded in the direct ionization amplitude via coefficients b_n . Other approaches supplying single-channel ionization amplitudes [28,42,43] could also be used for this purpose.

As an example we consider the contribution to ionization from the instantaneous maximum $t = 0$ of the laser field $F(t) = F_0 \cos(\omega t)$, leading to $\mathbf{p} \simeq 0$. We neglect the correction factor $e^{-i Q_{mn}}$ throughout.

To begin with, consider the case when only two ionic states are involved. Denoting the relevant quasistatic states as $|1\rangle$ and $|2\rangle$, the expressions for c_{mn} and b_n become

$$\begin{aligned} c_{21}(\mathbf{p} = 0) &= \int_{\tau_T}^0 d\xi \langle 2 | U^{N-1}(0, \xi) V_{ee}^1(\mathbf{r}_s(\xi)) U^{N-1}(\xi, \tau_T) | 1 \rangle, \\ b_1(\tau_T) &= \langle 1 | U^{N-1}(0, \tau_T) | 1 \rangle. \end{aligned} \quad (57)$$

Physically, such a system could describe N₂ aligned at 90°, where essentially only two states are coupled by the laser field: the ground state X(X²Σ_g) and the first excited state A(A²Π_u) separated from the ground state by 1.3 eV. Here, the correlation-driven excitation channel corresponds to the ionic state changing from X to A during ionization.

In order to calculate the amplitude for correlation-induced excitation at (imaginary) time ξ , it is necessary to propagate state $|1\rangle$ in (imaginary) time from $t_s = i\tau_T$ to $t'' = i\xi$ and state $|2\rangle$ from $t_0 = 0i$ to $t'' = i\xi$:

$$U^{N-1}(i\xi, i\tau_T) | 1 \rangle = \alpha_{11}(\xi) | X \rangle + \alpha_{21}(\xi) | A \rangle, \quad (58)$$

$$2 | U^{N-1}(0, i\xi) = [\langle X | \beta_2^*(\xi) + \langle A | \beta_{22}^*(\xi)] e^{-\Delta I_p^{XA}\xi}. \quad (59)$$

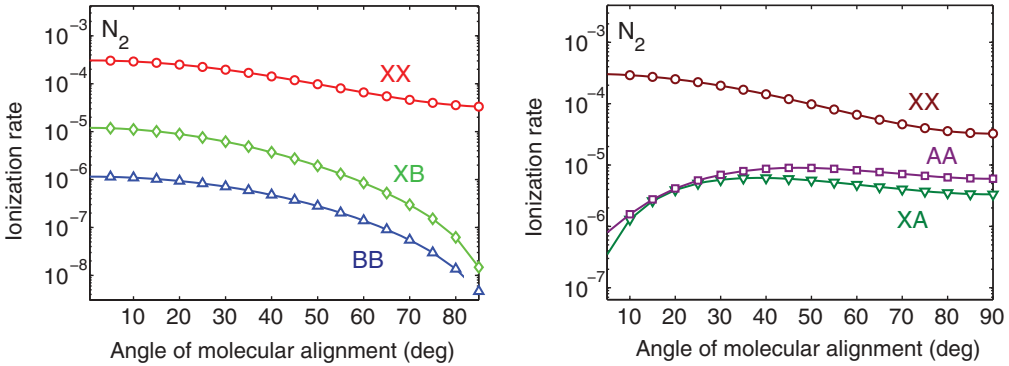


FIG. 2. (Color online) Molecular alignment-dependent ionization rates for direct XX (red circles), AA (violet squares), BB (blue triangles) and correlation-driven channels XB (a) (green diamonds) and XA (b) (green inverted triangles) in N_2 . Laser parameters are in the regime of nonadiabatic tunneling ($\gamma \geq 1$): $\lambda = 800$ nm, $I = 0.8 \times 10^{14}$ W/cm 2 .

Here the amplitudes $\alpha_{ij}(\xi)$, $\beta_{ij}(\xi)$ reflect the time-dependent evolution in the basis of field-free ionic states $|A\rangle$, $|X\rangle$, due to propagation in the laser field. The field-free energies of the two levels are set to $E_X = 0$ and $E_A = \Delta I_p^{XA}$, where $\Delta I_p^{XA} > 0$ is the field-free difference in ionization potentials for channels X and A. Initial conditions for forward and backward propagation in Eqs. (58) and (59) are determined by the projection of the quasistatic eigenstate $|1_{t_s}^{qs}\rangle$ at time $t_s = i\tau_T$ and eigenstate $|2_0^{qs}\rangle$ at time $t_i = 0$ onto the field-free states: $\alpha_{11}(\tau_T) = \langle X|1_{i\tau_T}^{qs}\rangle$, $\alpha_{21}(\tau_T) = \langle A|1_{i\tau_T}^{qs}\rangle$, $\beta_{22}^*(0) = \langle 2_0^{qs}|A\rangle$, $\beta_{21}^*(0) = \langle 2_0^{qs}|X\rangle$. In Eq. (57) the transition between quasistatic states occurs at (imaginary) time ξ . Using Eqs. (58) and (59), the integrand in Eq. (57) can be simplified to yield a “polarized” correlation potential $V_{21}(\xi)$, calculated between the laser-dressed states of the ion:

$$V_{21}(\xi) = \beta_{21}^* \langle X|V_{ee}|X\rangle \alpha_{11} + \beta_{22}^* \langle A|V_{ee}|X\rangle \alpha_{11} + \beta_{21}^* \langle X|V_{ee}|A\rangle \alpha_{21} + \beta_{22}^* \langle A|V_{ee}|A\rangle \alpha_{21}, \quad (60)$$

$$c_{21}(\mathbf{k}_f) = \int_{\tau}^0 d\xi V_{21}(\xi) e^{-\Delta I_p^{XA}\xi}. \quad (61)$$

Here all time-dependent amplitudes α_{ij}, β_{ij} are taken at imaginary time $i\xi$. If the states of the ion are not coupled by the laser field ($\alpha_{21} = 0, \beta_{21}^* = 0, \alpha_{11} = 1, \beta_{22}^* = 1$), only the second term $\beta_{22}^* \langle A|V_{ee}|X\rangle \alpha_{11} \equiv \langle A|V_{ee}|X\rangle$, corresponding to the field-free correlation potential, contributes.

The dependence of polarized and field-free correlation potentials for N_2 and CO_2 on the alignment and electronic structure of the molecule has been discussed in our short report [40]. Here we focus on the comparison of direct and indirect pathways which leave the ion in an excited state.

The vertical ionization potential for channels X, A, and B (corresponding to the ion left in the ground and first and second excited electronic states, respectively) are known spectroscopically: 15.6, 16.9, and 19.1 eV for N_2 and 13.8, 17.3, and 18.1 eV for CO_2 . To calculate the effects of the laser field, we use complete active space self-consistent field (CASSCF) values for the dipole matrix elements calculated by S. Patchkovskii for these molecules in our previous works [21,24]. For N_2 , the dipole coupling vectors between the ionic states are $d_{XA}^{CAS} = (0.25, 0, 0)$, $d_{XB}^{CAS} = (0, 0, 0.72)$, while for CO_2 , they are $d_{XA}^{CAS} = (0, 0, 0.46)$, $d_{XB}^{CAS} = (0.27, 0, 0)$. The first component in the brackets is perpendicular and the last is

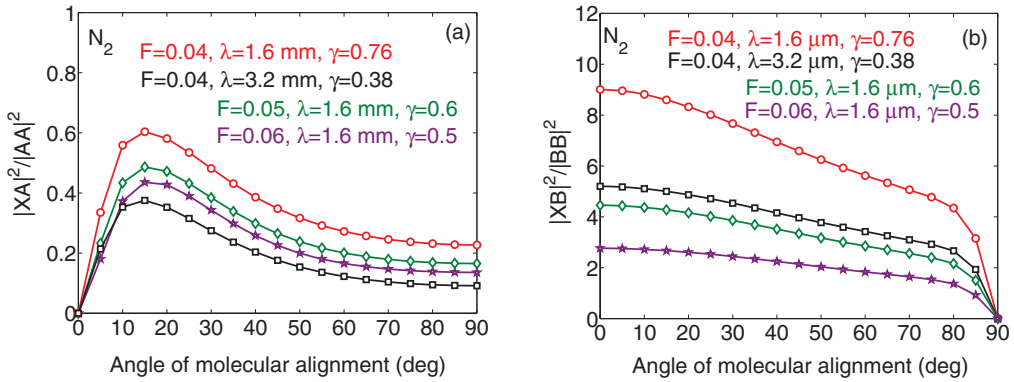


FIG. 3. (Color online) The ratio of ionization rates for correlation-driven and corresponding direct channels leading to the production of N_2^+ ions in excited states A (a) and B (b) for different laser parameters in the tunneling regime ($\gamma < 1$). (a) $F = 0.04$ a.u., $\lambda = 1.6 \mu m$ (red circles); $F = 0.04$ a.u., $\lambda = 3.2 \mu m$ (black squares); $F = 0.05$ a.u., $\lambda = 1.6 \mu m$ (green diamonds); $F = 0.06$ a.u., $\lambda = 1.6 \mu m$ (violet stars). (b) $F = 0.04$ a.u., $\lambda = 1.6 \mu m$ (red circles); $F = 0.04$ a.u., $\lambda = 3.2 \mu m$ (black squares); $F = 0.05$ a.u., $\lambda = 1.6 \mu m$ (green diamonds); $F = 0.06$ a.u., $\lambda = 1.6 \mu m$ (violet stars).

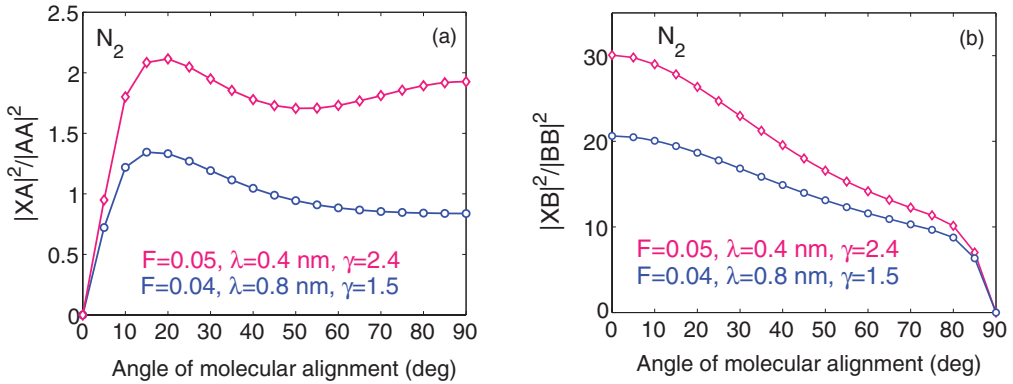


FIG. 4. (Color online) The ratio of ionization rates for correlation-driven and corresponding direct channels leading to the production of N_2^+ ions in excited states A (a) and B (b), for different laser parameters in the regime of nonadiabatic tunneling ($\gamma \geq 1$). (a) $F = 0.05$ a.u., $\lambda = 0.4 \mu\text{m}$ (pink diamonds); $F = 0.04$ a.u., $\lambda = 0.8 \mu\text{m}$ (blue circles). (b) $F = 0.05$ a.u., $\lambda = 0.4 \mu\text{m}$ (pink diamonds); $F = 0.04$ a.u., $\lambda = 0.8 \mu\text{m}$ (blue circles).

parallel to the molecular axis. It is important to use the more accurate dipoles, because the Hartree-Fock approximation overestimates the strength of the dipole couplings: for the XA transition in CO_2 by a factor of 3.5, for the XB transition in N_2 by a factor of 2.2. Hartree-Fock dipoles would thus overestimate laser-induced dynamics in our molecular ions.

When calculating correlation potentials, here we use the Hartree-Fock orbitals of the neutral molecules. The correlation potential calculated using these orbitals,

$$V_{mn}^{ee}(t) = \int d\mathbf{r} \frac{\phi_m^*(\mathbf{r})\phi_n(\mathbf{r})}{|\mathbf{r}_s(t) - \mathbf{r}|}, \quad n,m = \text{X, A, B}, \quad (62)$$

approaches $V_{mn}^{ee}(t) \approx d_{mn}/r_s^2$ for large r_s , where d_{mn} are the Hartree-Fock dipoles. Thus, it is likely that the unadjusted correlation potential will lead to an overestimation of the correlation effects. This overestimation of the electronic coupling strength is likely to affect any method based on the expectation values of the Hartree Fock orbitals, and may be responsible for the strong laser-induced coupling between the X and A channels in CO_2 reported in Ref. [28]. To correct this problem, we scale the value of the correlation potential by the ratio of the CASSCF and Hartree Fock dipoles; using the full CASSCF correlation potentials is the planned next step.

To calculate angle-resolved ionization rates for the direct ionization channels, we use analytical formulas derived by Murray and Ivanov [38,41]. The Stark shifts of the neutral molecule and of the ion are included in the same way as in our previous work [21,24].

As correlation-driven excitation is not subject to the full exponential suppression characteristic of direct ionization from lower orbitals, it becomes particularly important for low fields and high $\Delta I_p \tau$, that is, in the regime of nonadiabatic tunneling. However, our results indicate that this channel is also important in the tunneling regime $\gamma < 1$.

We first consider N_2 , where correlation-driven channels are particularly strong. We treat the N_2^+ ion as a three-level system, in the same manner as the two-level system discussed earlier. The correlation potentials are

$$V_{\mathfrak{A}\mathfrak{X}}(\xi) = \sum_{m,i,j,l=1,3} \langle A_{\xi=0}^{qs} | m^{N-1} \rangle b_{mj}(0,\xi) V_{ji}^{ee} b_{il}(\xi, \tau_T) \times \langle l^{N-1} | X^{qs}_{\xi=\tau_T} \rangle, \quad (63)$$

$$V_{\mathfrak{B}\mathfrak{X}}(\xi) = \sum_{m,i,j,l=1,3} \langle B_{\xi=0}^{qs} | m^{N-1} \rangle b_{mj}(0,\xi) V_{ji}^{ee} b_{il}(\xi, \tau_T) \times \langle l^{N-1} | X^{qs}_{\xi=\tau_T} \rangle. \quad (64)$$

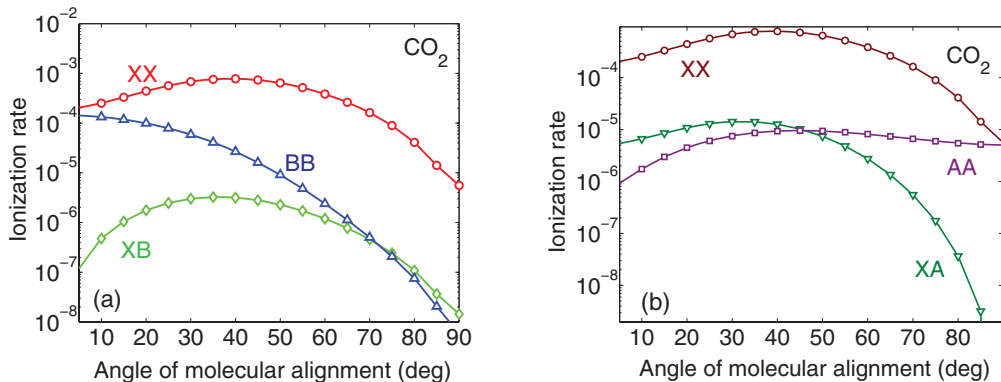


FIG. 5. (Color online) Angular-dependent ionization rates for direct XX (red circles), AA (violet squares), BB (blue triangles), and correlation-driven channels XB (a) (green diamonds) and XA (b) (green inverted triangles) in CO_2 . Laser parameters are in the regime of nonadiabatic tunneling ($\gamma \geq 1$): $\lambda = 800 \text{ nm}$, $I = 0.8 \times 10^{14} \text{ W/cm}^2$ laser field.

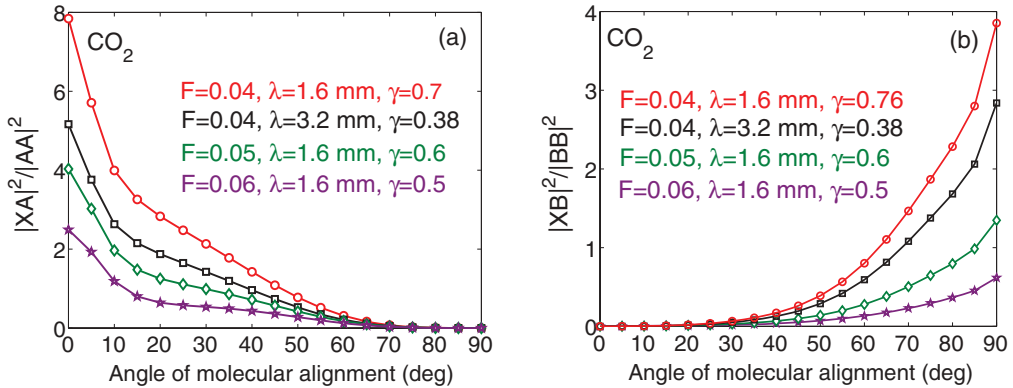


FIG. 6. (Color online) The ratio of ionization rates for correlation-driven and corresponding direct channels leading to the production of CO_2^+ in excited states A (a) and B (b) for different laser parameters in tunneling regime ($\gamma < 1$). (a) $F = 0.04$ a.u., $\lambda = 1.6 \mu\text{m}$ (red circles); $F = 0.04$ a.u., $\lambda = 3.2 \mu\text{m}$ (black squares); $F = 0.05$ a.u., $\lambda = 1.6 \mu\text{m}$ (green diamonds); $F = 0.06$ a.u., $\lambda = 1.6 \mu\text{m}$ (violet stars). (b) $F = 0.04$ a.u., $\lambda = 1.6 \mu\text{m}$ (red circles); $F = 0.04$ a.u., $\lambda = 3.2 \mu\text{m}$ (black squares); $F = 0.05$ a.u., $\lambda = 1.6 \mu\text{m}$ (green diamonds); $F = 0.06$ a.u., $\lambda = 1.6 \mu\text{m}$ (violet stars).

Detailed analysis of the properties of these potentials can be found in [40]. The excitation amplitude is given by their time integrals.

As seen in Fig. 2, correlation-driven channels play a very important role in the strong-field ionization of N_2 . Here the correlation-driven XA channel is comparable to the the direct AA channel, while XB *always* dominates the direct BB channel. In this figure, we used laser parameters similar to experimental parameters in [24], which put the system in the regime of nonadiabatic tunneling ($\gamma \geq 1$). As seen in Figs. 3 and 4, respectively, correlation-driven channels play a significant role in tunneling ($\gamma < 1$) and multiphoton regimes ($\gamma \sim 3$) as well.

In CO_2 , shown in Figs. 5 and 6, the XB channel is significant for large but not for small alignment angles. The suppression at small alignment angles is due to the dipole coupling between the X and B states of the ion, which is maximized when the molecule is aligned perpendicular to the laser field and is zero for parallel alignment. For the same reason, the XA channel dominates at small angles, but drops at large angles. As seen in Fig. 6, a similar angular dependence applies in the tunneling regime. Note that the contribution of the direct BB channel shown in Fig. 5(a) is enhanced due to the Stark shift.

VII. CONCLUSIONS

Strong-field ionization is an intrinsically multielectron process. In contrast to the usual SAE approximation, the state of the electrons which do not escape the ion may evolve due to interactions with the departing electron, causing excitation of the ion and leading to attosecond dynamics of core rearrangement. These dynamics determine the initial conditions and the coherence of the hole created upon ionization. Novel ultrafast imaging techniques may allow one to time resolve core rearrangements upon strong-field ionization [21,24] and characterize the coherence of hole motion [25]. Thus, understanding multielectron excitations during strong-field ionization is crucial for controlling and imaging hole dynamics and its coherence [44] in atoms [25] and molecules. It is also important for applications such as

mass spectrometry with femtosecond infrared pulses. Here fragmentation patterns will strongly depend on the excitations of the molecular ions during ionization.

To describe these multielectron dynamics, we have developed a multichannel theory of strong-field ionization. In this theory, interaction with the departing electron couples different ionization channels and leads to new ionization pathways, which may compete with or even dominate the direct channels for ionization to a particular final state. We obtained simple analytical expressions for the ionization amplitudes for these channels using a saddle-point method in the spirit of PPT theory, well known for accurately describing strong-field ionization in single-electron systems.

Using this theory, we find that nonadiabatic excitations of the core are important under typical experimental conditions. Compared with direct tunneling from more deeply bound orbitals, the correlation-driven channel does not suffer the full exponential suppression accompanying the thicker tunneling barrier. This effect appears to be particularly strong for large values of the Keldysh parameter γ and large ΔI_p . When important, correlation-driven channels approximately follow the angular dependence of their parent direct channels.

We are now in a position to address the questions asked in the Introduction. Because the exponential suppression accompanying an excited ionic state is minimized if the excitation occurs just before the tunneling exit, diagrams where N_1 (the number of photons absorbed before electron-electron correlation) approaches $N_0 = I_p/\omega$ (the total number of photons required for ionization) will be favored over those with small N_1 . Note that the derived analytical expressions incorporate all such pathways. This insight also sheds light on the question of higher-order contributions of the electron-electron correlation. Here, powers of the correlation which contribute to the direct amplitude by returning the core to its original state describe polarization of the ionic core induced by the outgoing electron. After accounting for the effects of this polarization, correlation-induced change of the ionic state is dominated by first-order terms, as higher-order diagrams are likely to involve the electron spending more time under a thicker tunneling barrier, with the accompanying exponential suppression.

Note added in proof. We would like to draw the reader's attention to a recent paper by M. Amusia [45]. It points out that the exchange between an electron tunneling from a deeply bound orbital and an electron in the HOMO, mediated by the electron-electron interaction, can enhance the amplitude of the deeply bound electron orbital in the classically forbidden region, leading to slower exponential decay in the classically forbidden region, consistent with the behaviour of the HOMO. The enhancement is proportional to the matrix element of the electron-electron interaction between the two electrons, and is mathematically similar to the enhancement discussed in this paper. We note, however, the fundamentally dynamic

nature of effect discussed in our paper. We also bring the reader's attention to [46], where a similar effect and its role in double ionization has been analyzed classically and termed "precollision" [47].

ACKNOWLEDGMENTS

We are grateful to S. Patchkovskii for useful comments. O.S. gratefully acknowledges support from DFG Grant No. Sm292/2-1. M.I. acknowledges support of EPSRC Programme Grant EP/I032517/1. L.T. acknowledges support from DiNL.

-
- [1] J. A. Tanis *et al.*, *Phys. Rev. Lett.* **83**, 1131 (1999).
 - [2] T. Schneider, P. L. Chocian, and J.-M. Rost, *Phys. Rev. Lett.* **89**, 073002 (2002).
 - [3] T. Schneider and J.-M. Rost, *Phys. Rev. A* **67**, 062704 (2003).
 - [4] L. Torlina and O. Smirnova, preceding paper, *Phys. Rev. A* **86**, 043408 (2012).
 - [5] L. V. Keldysh, Sov. Phys. JETP **20**, 1307 (1965).
 - [6] A. M. Perelomov, V. S. Popov, and M. V. Terentiev, *Zh. Eksp. Teor. Fiz.* **50**, 1393 (1966) [Sov. Phys. JETP **23**, 924 (1966)].
 - [7] S. V. Popruzhenko, V. D. Mur, V. S. Popov, and D. Bauer, *Phys. Rev. Lett.* **101**, 193003 (2008).
 - [8] B. A. Zon, Sov. Phys. JETP **91**, 899 (2000).
 - [9] A. S. Kornev, E. B. Tulenko, and B. A. Zon, *Phys. Rev. A* **68**, 043414 (2003).
 - [10] A. S. Kornev, E. B. Tulenko, and B. A. Zon, *Phys. Rev. A* **69**, 065401 (2004).
 - [11] A. S. Kornev, E. B. Tulenko, and B. A. Zon, *Phys. Rev. A* **79**, 063405 (2009).
 - [12] I. V. Litvinyuk, F. Legare, P. W. Dooley, D. M. Villeneuve, P. B. Corkum, J. Zanghellini, A. Pegarkov, C. Fabian, and T. Brabec, *Phys. Rev. Lett.* **94**, 033003 (2005).
 - [13] N. Pfeiffer Adrian, Claudio Cirelli, Mathias Smolarski, Darko Dimitrovski, Mahmoud Abu-samha, Lars Bojer Madsen, and Ursula Keller, *Nat. Phys.* **8**, 76 (2012).
 - [14] V. N. Ostrovskii, *Zh. Eksp. Teor. Fiz.* **84**, 1323 (1983) [Sov. Phys. JETP **57**, 766 (1983)].
 - [15] M. Ya. Ovchinnikova and D. V. Shalashilin, *Khim. Fiz.* **7**, 175 (1988).
 - [16] A. N. Pfeiffer, C. Cirelli, M. Smolarski, R. Dörner, and U. Keller, *Nat. Phys.* **7**, 428 (2011).
 - [17] A. N. Pfeiffer, C. Cirelli, M. Smolarski, Xu Wang, J. H. Eberly, R. Dörner, and U. Keller, *New J. Phys.* **13**, 093008 (2011).
 - [18] H. Rottke, J. Ludwig, and W. Sandner, *J. Phys. B* **29**, 1479 (1996).
 - [19] A. E. Boguslavskiy, J. Mikosch, A. Gijsbertsen, M. Spanner, S. Patchkovskii, N. Gador, M. J. J. Vrakking, and A. Stolow, *Science* **335**(6074), 1336 (2012).
 - [20] L. Young, D. A. Arms, E. M. Dufresne, R. W. Dunford, D. L. Ederer, C. Hohr, E. P. Kanter, B. Krassig, E. C. Landahl, E. R. Peterson, J. Rudati, R. Santra, and S. H. Southworth, *Phys. Rev. Lett.* **97**, 083601 (2006).
 - [21] O. Smirnova, Y. Mairesse, S. Patchkovskii, N. Dudovich, D. Villeneuve, P. Corkum, and M. Yu. Ivanov, *Nature (London)* **460**, 972 (2009).
 - [22] H. Akagi, T. Otobe, A. Staudte, A. Shiner, E. Turner, R. Dorner, D. Villeneuve, and P. Corkum, *Science* **325**, 1364 (2009).
 - [23] S. Haessler, J. Caillat, W. Boutu, C. Giovanetti-Texeira, T. Ruchon, T. Auguste, Z. Diveki, P. Breger, A. Maquet, and B. Carre, *Nat. Phys.* **6**, 200 (2010).
 - [24] Y. Mairesse, J. Higuet, N. Dudovich, D. Shafir, B. Fabre, E. Mevel, E. Constant, S. Patchkovskii, Z. Walters, M. Y. Ivanov, and O. Smirnova, *Phys. Rev. Lett.* **104**, 213601 (2010).
 - [25] E. Goulielmakis *et al.*, *Nature (London)* **466**, 739 (2010).
 - [26] C. Wu, H. Zhang, H. Yang, Q. Gong, D. Song, and H. Su, *Phys. Rev. A* **83**, 033410 (2011).
 - [27] M. Spanner and S. Patchkovskii, *Phys. Rev. A* **80**, 063411 (2009).
 - [28] S. Petretti, Y. V. Vanne, A. Saenz, A. Castro, and P. Decleva, *Phys. Rev. Lett.* **104**, 223001 (2010).
 - [29] S. Patchkovskii, O. Smirnova, and M. Spanner, *J. Phys. B* **45**, 131002 (2012).
 - [30] O. Smirnova, M. Spanner, and M. Ivanov, *Phys. Rev. A* **77**, 033407 (2008).
 - [31] S. V. Popruzhenko and D. Bauer, *J. Mod. Opt.* **55**, 2573 (2008).
 - [32] O. Smirnova, M. Spanner, and M. Ivanov, *J. Phys. B* **39**, S307 (2006).
 - [33] O. Smirnova, M. Spanner, and M. Yu. Ivanov, *J. Phys. B* **39**, S323 (2006).
 - [34] Olga Smirnova *et al.*, *J. Phys. B* **40**, F197 (2007).
 - [35] Misha Ivanov and Olga Smirnova, *Phys. Rev. Lett.* **107**, 213605 (2011).
 - [36] A. Friedman William, *Ann. Phys.* **45**, 265 (1967).
 - [37] C. Figueira de Morisson Faria and X. Liu, *J. Mod. Opt.* **58**, 1076 (2011).
 - [38] R. Murray, M. Spanner, S. Patchkovskii, and M. Yu. Ivanov, *Phys. Rev. Lett.* **106**, 173001 (2011).
 - [39] We use $|m^{N-1}\rangle$, $|n^{N-1}\rangle$ to represent field-free states of the ion and $|n_{\ell''}^{N-1}\rangle$, $|m_{\ell''}^{N-1}\rangle$, for quasistatic states of the ion.
 - [40] Z. Walters and O. Smirnova, *J. Phys. B* **43**, 161002 (2010).
 - [41] R. Murray, W. K. Liu, and M. Y. Ivanov, *Phys. Rev. A* **81**, 023413 (2010).
 - [42] Z. X. Zhao, X. M. Tong, and C. D. Lin, *Phys. Rev. A* **67**, 43404 (2003).
 - [43] M. Abu-samha and L. B. Madsen, *Phys. Rev. A* **80**, 023401 (2009).
 - [44] N. Rohringer and R. Santra, *Phys. Rev. A* **79**, 053402 (2009).
 - [45] M. Ya. Amusia, *JETP Lett.* **90**, 161 (2009).
 - [46] Xu. Wang and J. H. Eberly, arXiv:1102.0221 [physics.atom-ph].
 - [47] J. Eberly (private communication).

Time-resolving electron-core dynamics during strong-field ionization in circularly polarized fields

Lisa Torlina, Jivesh Kaushal, and Olga Smirnova

Max Born Institute, Max Born Strasse 2a, 12489, Berlin, Germany

(Received 5 August 2013; published 4 November 2013)

Electron-core interactions play a key role in strong-field ionization and the formation of photoelectron spectra. We analyze the temporal dynamics of strong-field ionization associated with these interactions using the time-dependent analytical R -matrix (ARM) method, developed in our previous work [Phys. Rev. A **88**, 013421 (2013)]. The approach is fully quantum but includes the concept of trajectories. However, the trajectories are not classical in the sense that they have both real and imaginary components all the way to the detector. We show that the imaginary parts of these trajectories, which are usually ignored, have a clear physical meaning and are crucial for the correct description of electron-core interactions after ionization. In particular, they give rise to electron deceleration, as well as dynamics associated with electron recapture and release. Our approach is analytical and time dependent and allows one to gain access to the electron energy distribution and ionization yield as a function of time. Thus we can also rigorously answer the question: when is ionization completed?

DOI: [10.1103/PhysRevA.88.053403](https://doi.org/10.1103/PhysRevA.88.053403)

PACS number(s): 32.80.Rm, 42.50.Hz, 33.80.Wz

I. INTRODUCTION

We address the effects of electron-core interaction in strong-field ionization by circular fields. These effects play a crucial role in the dynamics of electron release and hole formation by strong-field ionization. They determine the structure of photoelectron spectra, ionization delays, and the effects of electron recapture into bound states. Understanding these effects is one of the key components of attosecond imaging.

In addition to the direct *ab initio* solution of the time-dependent Schrödinger equation (TDSE) (see, e.g., Refs. [1,2]), standard approaches to calculating photoelectron spectra in strong-field ionization rely on the two-step model. The first step involves ionization in a static field. This step is treated within the quantum approach and is often viewed as the electron tunneling through the barrier created by the laser field and the core potential. The second step describes electron dynamics after ionization and is treated classically by propagating classical trajectories from the “exit” of the tunneling barrier to the detector. A more advanced approach (CCSFA) involves classical Monte Carlo-type simulations, with the additional capability of treating nonadiabatic effects during ionization, keeping track of phases accumulated along each trajectory, and treating dynamics inside and outside the barrier on an equal footing by using complex times [3–5]. Using this method, good agreement between theory and experiment has been demonstrated for elliptically polarized field [6]. The appeal of these models is in the accessibility of the physical picture. However, the difficult lies in separating the process into quantum and classical steps. For the case of a long-range electron-core interaction, the two-step model does not provide a unique recipe for merging the quantum and classical treatments.

We overcome these difficulties in our approach, which provides a consistent quantum treatment, yet includes the concept of trajectories. However, in our case, the trajectories are not classical in the sense that they have both real and imaginary components all the way to the detector. Usually, the imaginary components of trajectories outside the barrier are excluded by redefining the initial conditions prior to ionization [7,8]. Here, we show that the imaginary parts are in fact responsible for a

number of effects, including electron recapture and rerelease during ionization, and the redistribution of electrons over continuum states after ionization, which corresponds to their deceleration due to the interaction with the core.

We investigate the effect of the Coulomb correction on ionization amplitudes in circularly polarized field using results obtained within the formalism of the time-dependent analytical R -matrix [9–11]. The time-dependent analytical R -matrix (ARM) method provides an opportunity to develop a consistent theory of strong-field ionization for arbitrary core potentials in the time domain. In the spirit of R -matrix theory, the configuration space is split into two regions: an inner region enclosing the atom or molecule, and an outer region, remote from the singularity of the core. The remoteness of the outer region allows one to use propagators based on the eikonal-Volkov (EVA) states. The latter are known to perform well for soft-core potentials [12] and to allow one to introduce and analyze the subcycle ionization yield [13]. The matching of inner-region solutions to outer-region EVA states occurs at the R -matrix boundary a , which is placed in the asymptotic region $a \gg 1/\kappa$, where $1/\kappa$ is the size of the ground state. Technically, matching is achieved using the Bloch operator.

In Ref. [11], we derived an expression for ionization amplitudes in circularly polarized field using the ARM approach, and analyzed the effect of the long-range electron-core interaction on ionization times, the initial conditions for electron continuum dynamics, and the ratio of ionization rates from p^- and p^+ orbitals. Here, we focus on nonadiabatic Coulomb effects in photoelectron spectra and investigate subcycle variations in the total ionization rate. This analysis enables us to gain insight into the temporal dynamics of ionization, making it possible to address the question of when ionization is completed and to explore how this depends on the laser parameters.

This paper is organized as follows: In Sec. II we present and discuss the expression for the ionization amplitude derived in our previous work [11]. In Sec. III, we introduce the concept of electron trajectories and analyze the Coulomb-correction term in detail. In Sec. IV, we investigate the resulting effects on electron spectra and time-resolved ionization rates. Section V concludes the paper.

II. IONIZATION AMPLITUDES FOR CIRCULAR FIELDS

The relevant quantity for studying ionization rates and electron spectra is the ionization amplitude, $a_{\mathbf{p}}(T) = \langle \mathbf{p} | \Psi(T) \rangle$, where $|\Psi(T)\rangle$ is the wave function of the liberated electron at some time T after the laser field has been switched off. An analytic expression for this was derived in Ref. [11] using the ARM approach.

In particular, if our field is given by $\mathbf{E} = F[-\sin(\omega t)\hat{\mathbf{x}} + \cos(\omega t)\hat{\mathbf{y}}]$, with corresponding vector potential

$$\mathbf{A} = -A_0[\cos(\omega t)\hat{\mathbf{x}} + \sin(\omega t)\hat{\mathbf{y}}], \quad (1)$$

the expression for the ionization amplitude takes the following form:

$$a_{\mathbf{p}}(T) = \langle \mathbf{p} | \Psi(T) \rangle = R_{\text{klm}}(\mathbf{p}) e^{-iW_C(T,\mathbf{p})} e^{-iS_{\text{SFA}}(T,\mathbf{p})}. \quad (2)$$

Let us briefly review each part of this expression in turn.

First, $e^{-iS_{\text{SFA}}}$ is the standard exponential factor that arises in the strong-field approximation. Expressed in terms of dimensionless time $\phi_T = \omega T$,

$$S_{\text{SFA}}(\phi_T, \mathbf{p}) = \frac{1}{2\omega} \int_{\phi_i}^{\phi_T} [\mathbf{p} + \mathbf{A}(\phi)]^2 d\phi - \frac{I_p}{\omega} \phi_s. \quad (3)$$

Here, I_p is the ionization potential, and $\phi_s = \phi_i + i\phi_T$ denotes the complex solution to the saddle-point equation $[\mathbf{p} + \mathbf{A}(\phi_s)]^2 = -2I_p$. Explicitly, we have

$$\phi_i = \omega t_i = \tan^{-1} \left(\frac{p_y}{p_x} \right), \quad (4)$$

$$\phi_T = \omega \tau_T = \cosh^{-1} \left[\frac{A_0}{2p} \left(\gamma_{\text{eff}}^2 + \frac{p^2}{A_0^2} + 1 \right) \right], \quad (5)$$

where $p = (p_x^2 + p_y^2)^{1/2}$, $\gamma_{\text{eff}} = (\omega/F)(\kappa^2 + p_z^2)^{1/2}$ is the effective Keldysh parameter, and $\kappa = \sqrt{2I_p}$. We interpret t_i as being the ionization time; that is, the time at which the electron emerges in the continuum. Notice that here $\phi_i = \omega t_i$ corresponds to the angle at which we detect our electron. This result neglects corrections to the ionization time (for a given observation angle) due to the core potential. If we take Coulomb interactions into account, the ionization time is modified to $\phi_i = \phi_i^{(0)} - |\Delta\phi_i| = \tan^{-1}(\frac{p_y}{p_x}) - |\Delta\phi_i|$ (see Ref. [11] for details). For the long (CW) pulses considered in this paper, however, the effect of this correction on photoelectron spectra is negligible, and we omit it here for simplicity. Note, also, that we select only a single solution for ϕ_s , which is associated with a single ionization burst in a given direction. The total photoelectron spectrum will be given by the coherent sum of all such ionization bursts occurring within the laser pulse.

For a given ionization angle, $|e^{-iS_{\text{SFA}}(p)}|^2$ is a Gaussian-like distribution in momentum, centered at optimal momentum k_0 , where

$$k_0 = A_0 \sqrt{1 + \gamma^2} \sqrt{\frac{1 - \xi_0}{1 + \xi_0}}, \quad (6)$$

and the parameter $0 \leq \xi_0 < 1$ satisfies [14]

$$\sqrt{\frac{\xi_0^2 + \gamma^2}{1 + \gamma^2}} = \tanh \left(\frac{1}{1 - \xi_0} \sqrt{\frac{\xi_0^2 + \gamma^2}{1 + \gamma^2}} \right).$$

In the adiabatic $\gamma \ll 1$ limit, $k_0 \rightarrow A_0$. As we shall see, this corresponds to the electron appearing in the continuum with zero initial velocity. In general, however, $k_0 > A_0$ and the electron is born with an initial velocity in the direction in which the barrier is rotating.

The next term, e^{-iW_C} , represents the Coulomb correction coming from the interaction between the departing electron and the core. It is given by

$$W_C(\phi_T, \mathbf{p}) = \frac{1}{\omega} \int_{\phi_i + i\phi_K}^{\phi_T} d\phi U(\mathbf{r}_s(\phi)), \quad (7)$$

where $U(\mathbf{r}_s)$ is the core potential of the atom or molecule evaluated along the trajectory of the departing electron,

$$\mathbf{r}_s(\phi) = \frac{1}{\omega} \int_{\phi_i + i\phi_K}^{\phi} d\phi' [\mathbf{p} + \mathbf{A}(\phi')], \quad (8)$$

and $\phi_K = \phi_T - \omega/\kappa^2$. Understanding this term and its effect on ionization rates and electron spectra will form the core of this paper. Notice, for now, that W_C is both momentum and time dependent. This will allow us to study the effect of the core potential on electron spectra and to probe the process of ionization in a time-resolved way.

The final term, $R_{\text{klm}}(\mathbf{p})$ encodes the angular structure of the initial state. Since the aim of this paper is to investigate the role of the Coulomb-correction term e^{-iW_C} , we shall focus on the simplest case of the spherically symmetric state with no angular momentum $l = m = 0$. In this case, $R_{\text{klm}}(\mathbf{p})$ reduces to

$$R_{k00}(\mathbf{p}) \propto \frac{\sqrt{\kappa}}{\sqrt{|\mathbf{E}(\phi_s^{(1)}) \cdot \mathbf{v}_{\mathbf{p}}^C(\phi_s^{(1)})|}}, \quad (9)$$

where $\phi_s^{(1)} = \phi_s^{(1)}(\mathbf{p})$ is the Coulomb-corrected ionization time, and $\mathbf{v}_{\mathbf{p}}^C = (\mathbf{p} + \mathbf{A}) - \Delta\mathbf{p}^C$ is the Coulomb-corrected velocity (see Ref. [11]). This prefactor modifies the shape of the electron momentum distribution very slightly, and we shall neglect this effect here. The case $l = 1$ was considered in Ref. [11], where we investigated the impact of nonadiabatic Coulomb effects on the sensitivity of ionization to the sense of electron rotation in the initial state, originally predicted for short-range potentials in Ref. [14].

So far, we have defined ionization amplitudes asymptotically, projecting onto the free-electron states at large times T after the laser pulse has been switched off. However, it is also possible to define subcycle ionization amplitudes. We do this by propagating our electron wave function back to some earlier time $t > t_i$ and projecting this onto the plane-wave basis $|\mathbf{p} + \mathbf{A}(t)\rangle$. Essentially, this is equivalent to assuming that the long-range potential is negligible from $t \rightarrow T$ and thus ionization is completed by time t . In fact, it is possible to show that such subcycle amplitudes take exactly the same form as above. The derivation is found in Appendix C of Ref [11]. That is,

$$a_{\mathbf{p}}(t) = \langle \mathbf{p} + \mathbf{A}(t) | \Psi(t) \rangle = R_{\text{klm}}(\mathbf{p}) e^{-iW_C(t,\mathbf{p})} e^{-iS_{\text{SFA}}(t,\mathbf{p})}. \quad (10)$$

Note that, for large times $t = T$ after the laser field has been switched off, $\mathbf{A}(T) = 0$ and Eq. (10) reduces to a projection onto field-free states with momentum \mathbf{p} as before. These subcycle ionization amplitudes will allow us to probe the process of ionization in a time-dependent way.

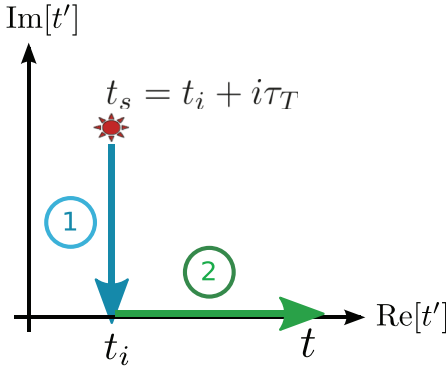


FIG. 1. (Color online) The integration contour we choose when evaluating the Coulomb-correction term W_C [Eq. (7)].

III. EVALUATING THE COULOMB CORRECTION

Let us now turn our attention to the Coulomb-correction term W_C . We would like to evaluate the integral in Eq. (7). As we did in Ref. [9], we choose our integration contour as follows: First, we integrate parallel to the imaginary axis, down from $\phi_i + i\phi_\kappa$ to ϕ_i . Next, we integrate along the real axis, from ϕ_i to our endpoint at ϕ_t (see Fig. 1). That is, we seek to evaluate

$$W_C = \frac{i}{\omega} \int_{\phi_\kappa}^0 d\phi U(\mathbf{r}_s(\phi_i + i\phi)) + \frac{1}{\omega} \int_{\phi_i}^{\phi_t} d\phi U(\mathbf{r}_s(\phi)). \quad (11)$$

A. Analysis of trajectories

In the spirit of Perelomov-Popov-Terent'ev (PPT) theory [15], we can interpret the first leg of this contour as corresponding to the electron's motion under the barrier, while the second leg describes its motion once it emerges in the continuum. Let us consider the trajectories $\mathbf{r}_s(\phi)$ for each of these in turn.

1. Under the barrier

Evaluating $\mathbf{r}_s(\phi_i + i\phi)$ yields the following expressions for the real and imaginary parts of the trajectory for the first leg

of the contour:

$$\mathbf{r}_1(\phi) \equiv \text{Re}[\mathbf{r}_{s,1}] = \frac{F}{\omega^2} (\cosh \phi_\tau - \cosh \phi) \times (\sin \phi_i \hat{\mathbf{x}} - \cos \phi_i \hat{\mathbf{y}}), \quad (12)$$

$$\rho_1(\phi) \equiv \text{Im}[\mathbf{r}_{s,1}] = \left(\frac{F}{w^2} (\sinh \phi_\tau - \sinh \phi) - \frac{p}{\omega} (\phi_\tau - \phi) \right) \times (\cos \phi_i \hat{\mathbf{x}} + \sin \phi_i \hat{\mathbf{y}}) - \frac{p_z}{\omega} (\phi_\tau - \phi) \hat{\mathbf{z}}. \quad (13)$$

Note that ϕ runs between ϕ_κ and 0 here. We think of $\phi = \phi_\kappa$ as corresponding to the “entrance” of the barrier and the start of tunneling, while $\phi = 0$ is associated with the barrier exit, when the electron emerges in the continuum.

Without loss of generality, let us set $p_y = 0$. That is, we place our detector along the x axis. Indeed, for a long laser pulse, all detection directions in the plane of polarization are equivalent. In this case, $\phi_i = 0$ and the electric field points in the positive y direction at the instant of ionization. If we also set $p_z = 0$ (noting that ionization perpendicular to the plane of the laser field is exponentially suppressed), we have

$$\mathbf{r}_1(\phi, \phi_i = 0) = -\frac{F}{\omega^2} (\cosh \phi_\tau - \cosh \phi) \hat{\mathbf{y}}, \quad (14)$$

$$\rho_1(\phi, \phi_i = 0) = \left(\frac{F}{w^2} (\sinh \phi_\tau - \sinh \phi) - \frac{p}{\omega} (\phi_\tau - \phi) \right) \hat{\mathbf{x}}. \quad (15)$$

As expected, the real part of the trajectory implies that the electron starts near the origin and escapes in the negative y direction. The imaginary part of the trajectory, on the other hand, varies from positive to negative x values, depending on the drift momentum of the electron $p = p_x$ (that is, the final momentum registered at the detector). Note, however, that the real and imaginary parts are always perpendicular to each other. Note, also, that for the optimal SFA momentum $p = k_0$, the imaginary part of the trajectory vanishes at the barrier exit.

2. In the continuum

Along the second leg of the integration contour, from ϕ_i to ϕ_t , we have

$$\begin{aligned} \mathbf{r}_2(\phi) \equiv \text{Re}[\mathbf{r}_{s,2}] &= \left(\frac{F}{w^2} (\sin \phi_i \cosh \phi_\tau - \sin \phi) + \frac{p}{\omega} \cos \phi_i (\phi - \phi_i) \right) \hat{\mathbf{x}} \\ &+ \left(-\frac{F}{w^2} (\cos \phi_i \cosh \phi_\tau - \cos \phi) + \frac{p}{\omega} \sin \phi_i (\phi - \phi_i) \right) \hat{\mathbf{y}} + \frac{p_z}{\omega} (\phi - \phi_i) \hat{\mathbf{z}}, \end{aligned} \quad (16)$$

$$\rho_2(\phi) \equiv \text{Im}[\mathbf{r}_{s,2}] = \left(\frac{F}{w^2} \sinh \phi_\tau - \frac{p}{\omega} \phi_\tau \right) (\cos \phi_i \hat{\mathbf{x}} + \sin \phi_i \hat{\mathbf{y}}) - \frac{p_z}{\omega} (\phi_\tau - \phi) \hat{\mathbf{z}}. \quad (17)$$

For $p_y = p_z = 0$, this simplifies to

$$\mathbf{r}_2(\phi, \phi_i = 0) = \left(-\frac{F}{w^2} \sin \phi + \frac{p}{\omega} \phi \right) \hat{\mathbf{x}} + \left(\frac{F}{w^2} (\cos \phi - \cosh \phi_\tau) \right) \hat{\mathbf{y}}, \quad (18)$$

$$\rho_2(\phi, \phi_i = 0) = \left(\frac{F}{w^2} \sinh \phi_\tau - \frac{p}{\omega} \phi_\tau \right) \hat{\mathbf{x}}. \quad (19)$$

From the real part of the trajectory, we see that the electron starts its motion in the continuum at $\mathbf{r}_{\text{exit}} = \mathbf{r}_s(\phi_i) = -(F/\omega)(\cosh \phi_i - 1)\hat{\mathbf{y}}$, with initial velocity $\mathbf{v}_i = (p - A_0)\hat{\mathbf{x}}$. We think of this as the exit of the barrier. It then undergoes circular motion superimposed on an overall drift momentum p in the positive x direction. Note that at the moment of ionization, the barrier also rotates in the positive x direction.

The imaginary part of the continuum trajectory, on the other hand, remains constant and equal to its value at the barrier exit. However, with the exception of the optimal momentum $p = k_0$, it is nonzero in general. As we shall see, this nonzero imaginary component will be directly responsible for a shift towards lower momenta in the electron spectra, which is associated with a deceleration of the electron due to the core potential. It will also lead to small subcycle variations in the total ionization rate in the continuum, which we interpret in terms of the dynamics of electron recapture and release.

B. Analytical continuation of Coulomb potential

As we have seen, the trajectory $\mathbf{r}_s(\phi)$ along both legs of our integration contour is complex in general. Therefore, in order to evaluate W_C [Eq. (11)], we must analytically continue our potential $U(\mathbf{r})$.

Consider the case of the Coulomb potential. For a real vector $\mathbf{r} = (x, y, z)$, we have $V_C(\mathbf{r}) = -Q/\sqrt{\mathbf{r} \cdot \mathbf{r}} = -Q/(x^2 + y^2 + z^2)^{1/2}$. For a complex vector, $\mathbf{r} + i\rho = (x, y, z) + i(\chi, \eta, \xi)$, we defin

$$\begin{aligned} V_C(\mathbf{r} + i\rho) &= \frac{-Q}{\sqrt{(\mathbf{r} + i\rho) \cdot (\mathbf{r} + i\rho)}} \\ &= \frac{-Q}{\sqrt{r^2 - \rho^2 + 2i\mathbf{r} \cdot \rho}} \\ &= \frac{-Q}{\sqrt{(x + i\chi)^2 + (y + i\eta)^2 + (z + i\xi)^2}}, \end{aligned} \quad (20)$$

where $r = |\mathbf{r}|^2$ and $\rho = |\rho|^2$. It is easy to verify that this satisfies the Riemann-Cauchy conditions. We shall choose the branch cut of the complex square root to be infinitesimal above the negative real axis, so that $\sqrt{-1} = -i$. In doing so, we ensure that our contour never crosses a branch cut.

If we let

$$a = r^2 - \rho^2 \text{ and } b = 2\mathbf{r} \cdot \rho, \quad (21)$$

we can explicitly express the Coulomb potential in terms of its real and imaginary parts as follows:

$$\begin{aligned} V_C &= -\frac{Q}{\sqrt{2(a^2 + b^2)}} \left(\sqrt{\sqrt{a^2 + b^2} + a} \right. \\ &\quad \left. - i \text{sgn}(b) \sqrt{\sqrt{a^2 + b^2} - a} \right), \end{aligned} \quad (22)$$

where we defin

$$\text{sgn}(b) = \begin{cases} -1 & \text{for } b \leq 0 \\ +1 & \text{for } b > 0. \end{cases} \quad (23)$$

Note that, in addition to the singularity at the origin that we are familiar with ($r = \rho = 0$), we now have an additional

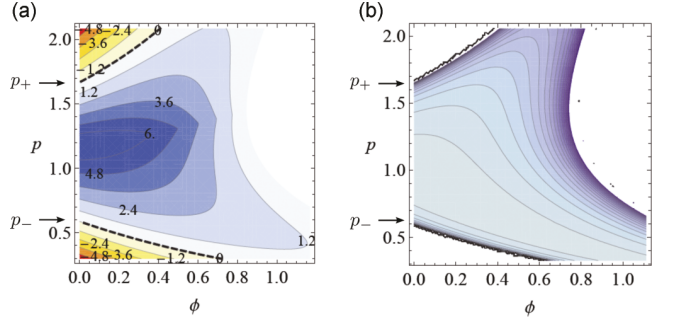


FIG. 2. (Color online) (a) The difference between the magnitude of the real and imaginary part of the trajectory under the barrier $r_1 - \rho_1$, as a function of imaginary time ϕ (in radians) and drift momentum p (in a.u.). In the blue region, $r_1 > \rho_1$ and V_C is purely real. In the red and yellow regions, $r_1 < \rho_1$ and V_C is purely imaginary. The black dashed lines correspond to $r_1 = \rho_1$, where V_C is singular. Note that ϕ evolves from ϕ_k to zero (right to left) as the electron moves away from the atom. (b) The real part of the Coulomb potential under the barrier. It is singular along the lines $r_1 = \rho_1$ and zero where $r_1 < \rho_1$.

singularity when $\mathbf{r} \cdot \rho = 0$ and $r = \rho$. $\mathbf{r} \cdot \rho = 0$, $r < \rho$ corresponds to the branch cut of our square root function. This is an important case to consider since, as we have seen, $\mathbf{r} \cdot \rho = 0$ everywhere under the barrier. Figure 2 shows the difference between the magnitudes of the real and imaginary parts of the under-barrier trajectory $r_1 - \rho_1$, as a function of imaginary time ϕ and momentum p . For momenta near the center of the SFA momentum distribution $p \in (p_-, p_+)$, we see that $r_1 > \rho_1$ everywhere. V_C therefore remains real and there is no singularity or branch cut along our integration contour. However, for momenta outside of this central region, we will pass over the line $r_1 = \rho_1$ as time evolves from ϕ_k to the ionization time $\phi_i = 0$. In this case, we encounter a singularity and V_C changes from real to imaginary as the electron tunnels. Fortunately, unlike the singularity at the origin, this singularity is integrable and the integrals for W_C always converge. Definin our square root such that $\sqrt{-1} = -i$ ensures that our contour never crosses the branch cut. Note that, at p^- and p^+ , define by $r(p_{\pm}, \phi_i) = \rho(p_{\pm}, \phi_i)$, the singularity occurs at the barrier exit.

C. Evaluating the Coulomb phase

Since we are interested in studying the effect of the Coulomb-correction term on electron spectra and ionization rates, the quantity of interest is the ionization probability $|a_p(t)|^2 \sim \exp[2\text{Im}S_{\text{SFA}}] \exp[2\text{Im}W_C]$. We shall therefore focus on the imaginary part of the Coulomb phase. That is, we are interested in $\text{Im}[W_C] = W_{C_1} + W_{C_2}$, where

$$W_{C_1} = \frac{1}{\omega} \int_{\phi_k}^0 d\phi \text{Re}[V_C(\mathbf{r}_{s,1})], \quad (24)$$

$$W_{C_2} = \frac{1}{\omega} \int_{\phi_i}^{\phi_f} d\phi \text{Im}[V_C(\mathbf{r}_{s,2})]. \quad (25)$$

Figure 3 shows these Coulomb-correction terms as a function of the drift momentum of the electron; that is, the fina

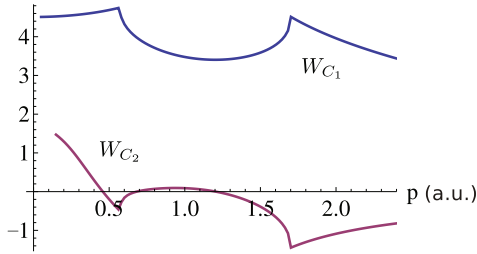


FIG. 3. (Color online) The Coulomb-correction terms W_{C_1} and W_{C_2} plotted against the momentum registered at the detector $p = (p_x^2 + p_y^2)^{1/2}$, for $\lambda = 800 \text{ nm}$, $I = 2.6 \times 10^{14} \text{ W/cm}^2$, $I_p = 0.5$. W_{C_2} is shown at time $\phi_t = 20$ radians.

momentum measured at the detector. Overall, we see that the under-barrier Coulomb term W_{C_1} is always positive and hence leads to an enhancement in ionization rate. The continuum Coulomb correction W_{C_2} can lead to either enhancement or suppression, depending on the momentum. The two sharp points we see in each of the two graphs correspond to p^- and p^+ , the momenta at which the integrable $r = \rho$ singularity occurs at the exit of the barrier. However, note that these sharp points precisely cancel each other out when we compute the total Coulomb correction $\text{Im}[W_C] = W_{C_1} + W_{C_2}$, which is the actual quantity of interest.

Figure 4 shows the total Coulomb correction $\text{Im}[W_C]$ plotted against the drift momentum of the departing electron for a series of three different observation times. Notice that it is smooth everywhere and varies with time. Note, also, that at sufficientl large times, $\text{Im}[W_C]$ increases with decreasing momenta. As we shall see, this will give rise to a shift in the electron momentum distribution. We investigate the effect of this term in greater detail in the next section.

IV. COULOMB EFFECTS: ELECTRON SPECTRA AND SUBCYCLE IONIZATION RATES

Armed with our time- and momentum-dependent Coulomb correction, we are now ready to evaluate the ionization probability $|a_p(t)|^2 \sim \exp[2\text{Im}S_{\text{SFA}}] \exp[2\text{Im}W_C]$. We shall compare this to the standard SFA result $\exp[2\text{Im}S_{\text{SFA}}]$, where the effect of the core is neglected. Doing this, we fin two main effects:

(1) The peak in the electron distribution shifts towards lower momenta. This shift is accumulated as the electron travels in the continuum.

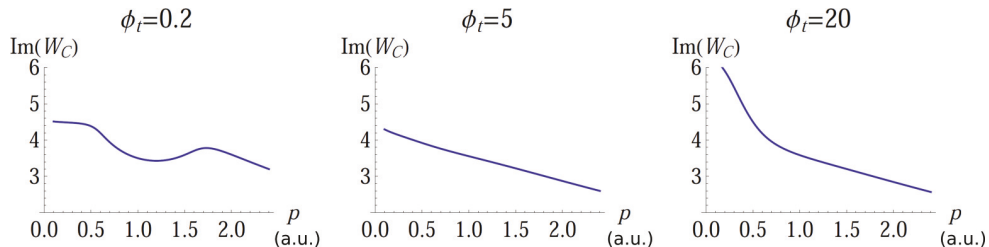


FIG. 4. (Color online) The total Coulomb correction $\text{Im}[W_C] = W_{C_1} + W_{C_2}$, plotted against momentum for three different observation times ϕ_t (in radians), for $\lambda = 800 \text{ nm}$, $I = 2.6 \times 10^{14} \text{ W/cm}^2$, $I_p = 0.5$.

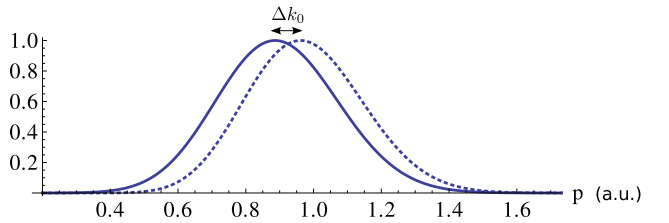


FIG. 5. (Color online) Electron momentum distribution with (solid) and without (dotted) the Coulomb correction, normalized to a height of 1, for $\lambda = 600 \text{ nm}$, $I = 2.6 \times 10^{14} \text{ W/cm}^2$, and $I_p = 0.5$, evaluated at an asymptotic time $\phi_t = 1000$ radians.

(2) In addition to the well-known increase in the total ionization rate acquired under the barrier, we observe further small variations after the electron emerges in the continuum.

A. Electron spectra: A shift to lower momenta

Since our Coulomb correction is momentum dependent, our theory allows us to study the effect of the core on electron spectra. For a given observation angle, we investigate the shape of $|a_p(t)|^2 \sim \exp[2\text{Im}S_{\text{SFA}}(p)] \exp[2\text{Im}W_C(p,t)]$ as a function of canonical momentum p . Note that canonical momentum here always refers to the momentum measured asymptotically at the detector, even though we evaluate $|a_p(t)|^2$ subcycle. As mentioned before, we can think of p as the electron's drift momentum as it moves in the presence of the laser field

Recall, first the SFA case, $|a_p^{\text{SFA}}|^2 \sim \exp[2\text{Im}S_{\text{SFA}}]$. As discussed in Sec. II, the momentum distribution in this instance is a Gaussian-like function centered at $p = k_0$, where k_0 is given by Eq. (6). Short wavelengths, weak fiel strengths, and small ionization potentials correspond to smaller k_0 .

As alluded to in Sec. III C, if we now include the Coulomb-correction factor, we fin that the distribution shifts towards low momenta. Figure 5 shows an example of this shift in the photoelectron spectrum, evaluated at large asymptotic time $\phi_t = 1000$. Figure 6 shows how this shift varies with the system parameters. Notice that we observe the largest shifts at short wavelengths, weak fields and low ionization potentials; that is, when the SFA distribution is centered at low momenta.

Since our theory is time dependent, we can go further and investigate the dynamics associated with these shifts in a time-resolved way. Doing this, we fin that the shift in $|a_p(t)|^2$ is predominantly accumulated while the electron travels in the continuum. Immediately after ionization, at the barrier exit, the peak is very close to the SFA prediction. However, as we allow time to evolve from ϕ_i along the real time axis, the peak

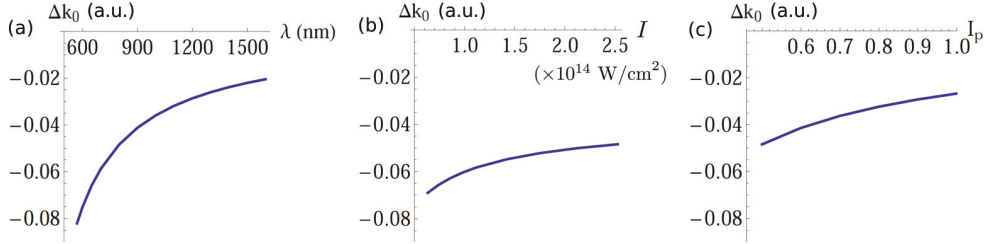


FIG. 6. (Color online) The shift of the peak of the photoelectron spectrum due to the Coulomb correction as a function of (a) wavelength, (b) field intensity, and (c) ionization potential, evaluated at an asymptotic time $\phi_t = 1000$ radians.

moves towards lower momenta and soon approaches its final asymptotic value. Figure 7 shows this subcycle variation for three different wavelengths. Note that, for shorter wavelengths (associated with a smaller initial drift momentum k_0), the peak takes a longer time to reach its final asymptotic value.

Clearly, it is natural to interpret these shifts as the deceleration of the electron wave packet by the core as it moves away from its parent atom or molecule. As discussed in the introduction, this is a well-recognized effect, which is commonly treated by propagating classical trajectories within a two-step model. Within our theory, however, we find that it emerges completely naturally, and is in fact a direct consequence of the imaginary components of the continuum trajectories. Had the continuum trajectories been purely real, we would not observe any such shifts. The imaginary parts of the continuum trajectories are therefore not merely a mathematical curiosity, but encode an important and real physical effect.

We can quantify the shift of the peak in the electron spectrum by differentiating $|a_p(t)|^2$ with respect to p . Solving $\frac{\partial}{\partial p} \{ \text{Im}[S_{\text{SFA}}(k_C)] + \text{Im}[W_C(k_C)] \} = 0$, we find the Coulomb-corrected peak momentum $k_C = k_0 + \Delta k_0$. We can estimate this by expanding about k_0 to lowest order in the Coulomb correction as follows:

$$\Delta k_0^{(0)}(t) = \frac{-\text{Im} \left[\frac{\partial}{\partial p} W_C \Big|_{k_0} \right]}{\text{Im} \left[\frac{\partial^2}{\partial p^2} S_{\text{SFA}} \Big|_{k_0} \right]} \quad (26)$$

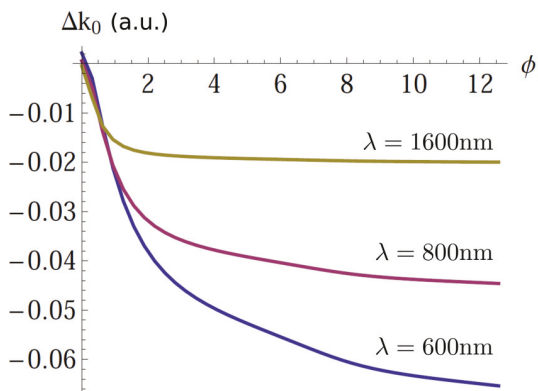


FIG. 7. (Color online) The shift of the peak of the photoelectron spectrum as a function of time in the continuum ϕ_t (in radians).

$$= \frac{1}{\phi_\tau(k_0)} \left(\int_{\phi_k}^0 d\phi \frac{\partial}{\partial p} U(\mathbf{r}_{s,1}(\phi, p)) \Big|_{k_0} - U(\mathbf{r}_{s,1}(\phi_k, k_0)) \frac{\partial \phi_\tau}{\partial p} \Big|_{k_0} + \int_{\phi_i}^{\phi_t} d\phi \text{Im} \left[\frac{\partial}{\partial p} U(\mathbf{r}_{s,2}(\phi, p)) \Big|_{k_0} \right] \right). \quad (27)$$

Note that the first two terms, which come from the under-barrier contribution W_{C1} , approximately cancel each other and, as a result, the shift is primarily accumulated after the electron emerges in the continuum [the final term in Eq. (27)].

B. Total ionization rate: nonadiabatic effects and subcycle variations

It is well established that accounting for the Coulomb potential leads to an overall enhancement in the total ionization rate predicted by SFA. This can be understood by considering the shape of the tunneling barrier. Compared to the short-range potential implicit within the strong-field approximation, the barrier for a Coulomb potential is smoother and lower, making it easier for the electron to tunnel through. In the adiabatic limit, this increase is typically approximated using [15–17]

$$\frac{w}{w_{\text{SFA}}} \approx \left(\frac{2\kappa^3}{F} \right)^{2/\kappa}. \quad (28)$$

Within our ARM formalism, which is valid well into the nonadiabatic regime and enables us to study ionization dynamics in a time-resolved way, we are able to go beyond this result.

To do this, we calculate the total ionization rate in a given direction by integrating over momenta p ,

$$w(t) = \int dp |a_p(t)|^2 \propto \int dp e^{2\text{Im}[S_{\text{SFA}}]} e^{2\text{Im}[W_C]}. \quad (29)$$

We shall again fix $p_z = 0$ here, noting that ionization in the z direction is exponentially suppressed. Without loss of generality, we also set $p_y = 0$ and integrate over $p = p_x$. Since our field is circular and we consider long pulses, the problem is symmetric and this calculation yields the ionization rate for any given direction in the plane of laser polarization.

1. Ionization rates via the saddle-point method: a first approximation

In our preceding paper [11], we approximated the above integral using the saddle-point method, relying on the fact that

the SFA term is a relatively narrow Gaussian-like function centered at k_0 . Within this approximation, to lowest order in W_C , we obtain

$$w \approx \frac{\sqrt{\pi}}{\sqrt{|\text{Im}[\frac{\partial^2}{\partial p^2} S_{\text{SFA}}(k_0)]|}} e^{2\text{Im}[S_{\text{SFA}}(k_0)]} e^{2\text{Im}[W_C(k_0)]}. \quad (30)$$

Here, the correction to the SFA ionization rate is simply $\exp[2\text{Im}W_C(k_0)]$, the Coulomb term evaluated along the optimal trajectory where $p = k_0$. This result coincides with the nonadiabatic Coulomb correction in PPT [18]. Note that, in contrast to the purely static Coulomb correction in Eq. (28), W_{C_1} now also depends on wavelength.

Recalling from Sec. III A that the optimal trajectory is purely real at real times, we see that $W_{C_1}(k_0)$ is zero. Hence, within this approximation, the Coulomb modification of the total ionization rate comes only from the under-barrier part W_{C_1} , and no further changes to the total rate occur as we evolve in real time. This result seems quite intuitive. The total ionization rate depends only on what happens to the electron while it is tunneling, and we can say that ionization is completed at the ionization time t_i when the electron appears in the continuum. As plausible as this picture seems, however, it does not tell the whole story.

2. A more accurate calculation: frequency dependence and time-resolved ionization rates

In order to obtain a more accurate description of the total subcycle ionization rates, we evaluate the integral in Eq. (29) numerically and divide this by the SFA rate $w^{\text{SFA}} = \int dp e^{2\text{Im}[S_{\text{SFA}}]}$. In doing so, we find deviations from the result obtained using the saddle-point method. In particular, our Coulomb correction to the ionization rate acquires a time-dependence and no longer remains constant in the continuum.

Figure 8 shows these time-resolved results for $\lambda = 600$ nm, 800 nm, and 1600 nm. In all cases, we find an

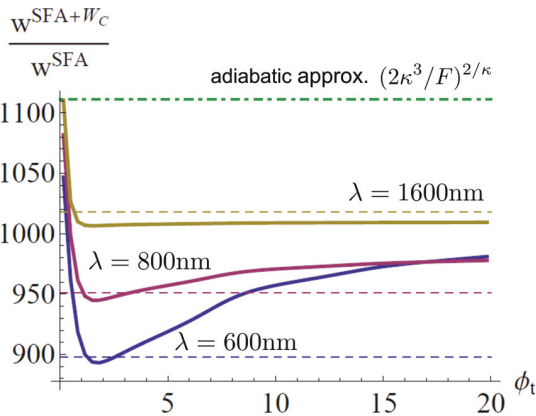


FIG. 8. (Color online) Coulomb enhancement of the total ionization rate as a function of time ϕ_t (in radians), normalized by the SFA rate. Solid lines are the results of numerical integration. Dashed lines show the lowest-order saddle-point approximation (that is, the nonadiabatic Coulomb correction $\exp[W_{C_1}(k_0)]$). The dot-dashed green line indicates the commonly used adiabatic approximation given by Eq. (28).

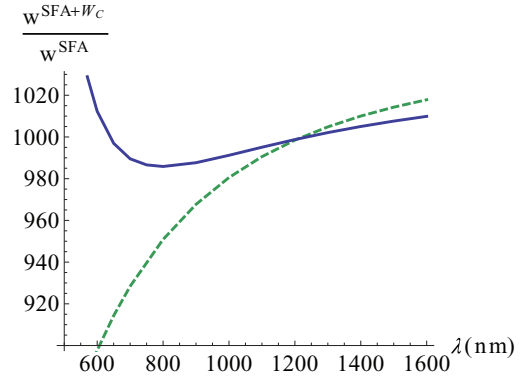


FIG. 9. (Color online) The Coulomb enhancement of the total ionization rate, calculated using the saddle-point approximation (green dashed curve) and by evaluating the integral in Eq. (29) exactly (blue solid curve) as a function of wavelength.

initial decrease in the rate on a timescale of one quarter of a laser cycle or less. We suggest that this could be attributed to the Coulomb trapping of the departing electron into Rydberg states. At shorter wavelengths, as we enter the nonadiabatic $\gamma \gtrsim 1$ regime, we find that this initial decrease is followed by a gradual increase in rate over a longer period of time, where the extra contribution comes from small momenta. This may be explained by electrons being shaken back out of Rydberg states at higher frequencies. Again, note that these subcycle variations arise as a direct consequence of the imaginary parts of the continuum trajectories. That is, the imaginary components again give rise to nontrivial physical effects.

The inaccuracy of the lowest-order saddle-point approximation for the integral over p in Eq. (29) comes about due to the shift of the optimal momentum Δk_0 and the reshaping of the photoelectron distribution. The deviation between the two as a function of wavelength is shown in Fig. 9.

V. CONCLUSION

In this work, we have studied the effect of the core potential in strong-field ionization by circularly polarized fields using ionization amplitudes derived via the time-dependent analytical R -matrix approach [9–11]. Our theory applies well into the nonadiabatic regime, and the Coulomb correction is both momentum and time dependent, which has allowed us to investigate its effect on electron spectra and subcycle ionization rates in a time-resolved way.

Within this approach, we have been naturally led to the concept of complex trajectories. With the exception of the optimal trajectory associated with momentum k_0 , our trajectories have a nonzero imaginary part all the way to the detector. We have shown that these imaginary components, in fact, give rise to real physical effects.

In electron spectra, we find that the Coulomb term shifts the SFA distribution towards low momenta. This effect is accumulated after the ionization time, as the electron travels in the continuum and time evolves along the real axis. It is natural to interpret this as the deceleration of the electron wave packet by the core as it moves away from its parent atom

or molecule. As we would expect, the observed shift is largest when the electron emerges with a smaller drift velocity and hence spends more time in the vicinity of the core.

We also find that our correction leads to subcycle variations of the ionization rate in the continuum. This is in addition to the well-known enhancement of the SFA rate accumulated while the electron is tunneling. We interpret these variations in terms of electron recapture into Rydberg states and their subsequent rerelease due to interaction with the laser field

Both of these effects come about as a direct consequence of the imaginary parts of the continuum electron trajectories in our theory.

ACKNOWLEDGMENTS

We thank M. Ivanov for useful discussions, and D. Bauer for useful comments. L.T. and O.S. gratefully acknowledge the support of the Leibniz graduate school DiNL. J.K. and O.S. gratefully acknowledge the support of the Marie Curie ITN CORINF.

-
- [1] H. G. Muller, *Laser Phys.* **9**, 138 (1999).
 - [2] C. P. J. Martiny, M. Abu-samha, and L. B. Madsen, *Phys. Rev. A* **81**, 063418 (2010).
 - [3] T.-M. Yan, S. V. Popruzhenko, and D. Bauer, *Prog. Ultrafast Intense Laser Sci.* **9**, 1 (2013).
 - [4] T.-M. Yan, S. V. Popruzhenko, M. J. J. Vrakking, and D. Bauer, *Phys. Rev. Lett.* **105**, 253002 (2010).
 - [5] Y. Huismans *et al.*, *Science* **331**, 61 (2011).
 - [6] S. V. Popruzhenko, G. G. Paulus, and D. Bauer, *Phys. Rev. A* **77**, 053409 (2008).
 - [7] S. V. Popruzhenko and D. Bauer, *J. Mod. Opt.* **55**, 2573 (2008).
 - [8] T.-M. Yan and D. Bauer, *Phys. Rev. A* **86**, 053403 (2012).
 - [9] L. Torlina and O. Smirnova, *Phys. Rev. A* **86**, 043408 (2012).
 - [10] L. Torlina, M. Ivanov, Z. B. Walters, and O. Smirnova, *Phys. Rev. A* **86**, 043409 (2012).
 - [11] J. Kaushal and O. Smirnova, *Phys. Rev. A* **88**, 013421 (2013).
 - [12] O. Smirnova, M. Spanner, and M. Ivanov, *Phys. Rev. A* **77**, 033407 (2008).
 - [13] O. Smirnova, M. Spanner, and M. Ivanov, *J. Phys. B* **39**, S307 (2006).
 - [14] I. Barth and O. Smirnova, *Phys. Rev. A* **84**, 063415 (2011); **87**, 013433 (2013).
 - [15] A. M. Perelomov, V. S. Popov, and M. V. Terent'ev, *Sov. Phys. JETP* **24**, 207 (1967).
 - [16] L. Keldysh, *Sov. Phys. JETP* **20**, 1307 (1965).
 - [17] M. V. Ammosov, N. B. Delone, and V. P. Krainov, *Sov. Phys. JETP* **64**, 1191 (1986).
 - [18] A. M. Perelomov and V. S. Popov, *Sov. Phys. JETP* **25**, 336 (1967).

Ab-initio verification of the analytical R-Matrix theory for strong field ionization

Lisa Torlina, Felipe Morales, Harm Geert Muller, and Olga Smirnova
Max Born Institute, Max Born Strasse 2a, 12489, Berlin, Germany

This is an author-created, un-copyedited version of an article published in Journal of Physics B: Atomic, Molecular and Optical Physics. IOP Publishing Ltd is not responsible for any errors or omissions in this version of the manuscript or any version derived from it. The Version of Record is available online at <http://dx.doi.org/10.1088/0953-4075/47/20/204021>.

Abstract

We summarize the key aspects of the recently developed Analytical R-Matrix (ARM) theory for strong field ionization [L. Torlina and O. Smirnova, Phys. Rev. A 86, 043408 (2012), J. Kaushal and O. Smirnova, Phys. Rev. A 88, 013421 (2013)], and present tests of this theory using ab-initio numerical simulations for hydrogen and helium atoms in long circularly polarized laser pulses. We find excellent agreement between the predictions of ARM and the numerical calculations.

I. INTRODUCTION

The ionization of atoms and molecules in the presence of a strong low frequency laser field is at the heart of a wide range of phenomena in the fast-developing field of attosecond science. A good description of this process is therefore vital if we are to correctly interpret experimental results and understand the underlying electron dynamics. However, obtaining such a description poses a considerable challenge. The process is highly nonlinear, and we are faced with the problem of simultaneously accounting for the atomic or molecular core as well as the strong laser field in a regime where conventional perturbation theory fails.

In addition to the direct ab-initio solution of the time-dependent Schrödinger equation (TDSE) – which becomes particularly demanding at high field strengths and long wavelengths – the main theoretical approaches to resolving this problem have generally fallen within two main categories. The first of these relies on the tunnelling picture, which describes ionization in terms of electron tunnelling through a barrier created by the core potential and the electric potential of the laser field. Typically, the process is split into two-steps: first, quantum mechanical tunnelling through a static barrier, and second, the propagation of classical trajectories from the barrier exit to the detector (see e.g. [1, 2]). This approach provides an intuitive and convenient description of the process. However, it suffers from ambiguities which arise when the quantum and classical steps are matched.

The other major class of theoretical approaches is based on the strong field approximation (SFA) or the closely related Keldysh–Faisal–Reiss (KFR) [3–5] and Perelomov–Popov–Terentev (PPT) theory [6–8], together with their extensions and generalizations. Unlike the two-step model, this approach is fully quantum and tunnelling is not explicitly assumed (though the tunnelling rate is indeed reproduced in the appropriate limit). Instead, in its original form, the key approximation of SFA is effectively to neglect the electron–core interaction after the start of ionization. This approx-

imation is only valid for short range potentials and in the length gauge version of the theory [9, 10]. In general, however, neglecting the interaction of the departing electron and the core can lead to results which are both qualitatively and quantitatively incorrect [11]. To resolve this issue, a number of modifications of SFA have been proposed. Of these, Coulomb-corrected SFA (CCSFA) [12–14] is noteworthy for making use of the concept of electron trajectories – familiar from the two-step tunnelling picture – to propose a modification of the SFA ionization amplitude. However, although considerably more advanced than the two-step model, this method is also subject to assumptions regarding trajectories and initial conditions.

In this work, we focus on an alternative theory known as the analytical R-matrix (ARM) [15–18]. Unlike previous approaches, ARM allows us to describe strong field ionization and account for electron–core interactions within a single consistent quantum framework, and requires no ad hoc assumptions to be made. Like CCSFA, this method includes the concept of trajectories. However, rather than being postulated, these trajectories emerge naturally in our theory, and unlike CCSFA or the two step model, we find that these trajectories retain an imaginary component all the way to the detector. These imaginary components, in fact, play a crucial role in determining the shape of the photoelectron spectra.

This paper is organized as follows. In Section II we summarize the main ideas and equations of the ARM theory in a compact form for the benefit of the reader. In Section III, we present the key new results, which compare the predictions of ARM with the ab-initio solution of the TDSE for the ionization of hydrogen and helium in the presence of long circularly polarized laser pulses. Section IV concludes the paper.

II. THE ANALYTICAL R-MATRIX

The ARM approach to strong field ionization is based on a very simple yet powerful idea. In the spirit of R-

matrix theory [20, 21], we divide space into two regions – an inner region and an outer region – and match solutions at the boundary. The power of the method then comes from our ability to make appropriate simplifications within each of these. In particular, although neither the laser field nor the core potential can be neglected or treated perturbatively everywhere, doing so within certain regions of space is indeed justified. The key features of the theory and its derivation are summarized in the following sections.

A. An inner and an outer region

Within the analytical R-matrix approach, we choose the boundary between the inner and outer region to be a sphere of radius a enclosing the atom or molecule. In the inner region, the potential of the core is dominant, which in turn allows us to approximate the solution using bound states. We can express such states in the form

$$\Psi_{\text{in}}(\mathbf{r}, t) = a_g(t) \psi_g(\mathbf{r}) e^{iI_p t}, \quad (1)$$

where I_p is the ionization potential, $\psi_g(\mathbf{r})$ determines the spatial structure of the ground state and $a_g(t')$ accounts for effects of the laser field within the quasistatic approximation (including Stark shifts and depletion).

In the outer region, on the other hand, we are remote from the singularity of the core. This enables us to use eikonal-Volkov solutions, which account for the laser field exactly, and include effects of the core potential within the eikonal approximation [22]. Note that throughout this work, we treat the laser field in the dipole approximation. Eikonal-Volkov solutions take the form

$$\begin{aligned} \Psi_{\mathbf{p}, T}^{\text{EVA}}(\mathbf{r}, t) &= \langle \mathbf{r} | \mathbf{p}_T^{\text{EVA}}(t) \rangle \\ &= \frac{1}{(2\pi)^{3/2}} e^{i(\mathbf{p} + \mathbf{A}(t)) \cdot \mathbf{r}} e^{iS_V(T, \mathbf{p}; t)} e^{iG_C(\mathbf{p}, T; \mathbf{r}, t)}, \end{aligned} \quad (2)$$

and are valid for an arbitrary laser field, described by vector potential $\mathbf{A}(t)$ and electric field $\mathbf{F}(t) = -d\mathbf{A}(t)/dt$. In the expression above, S_V is the Volkov phase, the phase accumulated by an electron in the laser field only,

$$S_V(T, \mathbf{p}; t) = \frac{1}{2} \int_t^T d\tau (\mathbf{p} + \mathbf{A}(\tau))^2, \quad (3)$$

and G_C is the Coulomb phase, the phase due to the interaction of the departing electron with the core,

$$\begin{aligned} G_C(\mathbf{p}, T; \mathbf{r}, t) &= \int_t^T d\tau U(\mathbf{r}_L(\tau; \mathbf{r}, \mathbf{p}, t)) \\ &\quad + G_{0\mathbf{p}}(\mathbf{r}_L(T; \mathbf{r}, \mathbf{p}, t)). \end{aligned} \quad (4)$$

Here, $U(\mathbf{r})$ is the potential of the core, and \mathbf{r}_L is the characteristic laser-driven trajectory of the electron, $\mathbf{r}_L(\tau; \mathbf{r}, \mathbf{p}, t) = \mathbf{r} + \int_t^\tau d\zeta (\mathbf{p} + \mathbf{A}(\zeta))$. The second term in

Eq.(4) is associated with the asymptotic phase distortion of the field-free states and can be neglected provided that T is sufficiently large and the electron's drift momentum \mathbf{p} is non-zero. The eikonal-Volkov approximation is accurate as long as $|\nabla_{\mathbf{r}} G_C(\mathbf{p}, T; \mathbf{r}, t)| \ll |\mathbf{p} + \mathbf{A}(t)|$, and performs well for soft core potentials, i.e away from the singularity of the core [22]. By remaining within the outer region, we ensure that this is the case. Note that this also implies that $G_C \ll S_V$; that is, the Coulomb term is a small correction compared to the Volkov phase.

Having divided space in this way, we observe that the overall Hamiltonian of the system will no longer be Hermitian in both inner and outer regions separately. We restore Hermiticity by adding the Bloch operator [20], following the standard R-matrix approach [21]. Essentially, this operator is responsible for matching the two solutions at the boundary. Upon doing so, we obtain the following expression for the wavefunction in the outer region:

$$\begin{aligned} \Psi_{\text{out}}(\mathbf{r}, T) &= -i \int_{-\infty}^T dt' \int d\mathbf{r}' G^{\text{EVA}}(\mathbf{r}, T, \mathbf{r}', t') \\ &\quad \times \delta(r' - a) \hat{B} \Psi_{\text{in}}(\mathbf{r}', t'). \end{aligned} \quad (5)$$

Here, $\hat{B} = d/dr' + (1 - b)/r'$ is the Bloch operator which acts on Ψ_{in} at the boundary $r' = a$, b is an arbitrary constant, and $G^{\text{EVA}}(\mathbf{r}, T, \mathbf{r}', t') = \theta(t - t') \int d\mathbf{p} \langle \mathbf{r} | \mathbf{p}_T^{\text{EVA}}(t) \rangle \langle \mathbf{p}_T^{\text{EVA}}(t') | \mathbf{r}' \rangle$ is the eikonal-Volkov Greens function which we use to describe propagation in the outer region. To evaluate the wavefunction, we need to integrate over the boundary $r' = a$, and over all possible times t' , which have the natural interpretation of ionization time.

B. Ionization amplitudes within ARM

When describing ionization, our physical quantity of interest will be the ionization amplitude. To evaluate this, we project the outer region wavefunction onto plane-wave continuum states defined by final momentum \mathbf{p} . This yields

$$\begin{aligned} a_{\mathbf{p}}(T) &= \langle \mathbf{p} | \Psi_{\text{out}}(T) \rangle \\ &= \frac{-i}{(2\pi)^{3/2}} \int_{-\infty}^T dt' \int d\mathbf{r}' e^{-i(\mathbf{p} + \mathbf{A}(t')) \cdot \mathbf{r}'} \\ &\quad \times e^{-iG_C(\mathbf{p}, T; \mathbf{r}', t')} e^{-iS_V(\mathbf{p}, T; t')} e^{iI_p t'} \\ &\quad \times a_g(t') \delta(r' - a) \hat{B} \psi_g(\mathbf{r}'). \end{aligned} \quad (6)$$

Notice that the integrand above is of the form $P(\mathbf{r}', t') e^{-iS(\mathbf{r}', t')}$, and the phase S is large provided we have a sufficiently strong laser field of sufficiently low frequency. As a result, the dominant contribution to the integral will be accumulated near stationary solutions for t' and \mathbf{r}' where the derivative of S vanishes. This fact allows us to evaluate the above integral analytically using the saddle point method.

The a -dependence is eliminated by matching the asymptotic tail of the inner-region wavefunction with the Coulomb phase e^{-iG_C} in the outer region. Our ability to do this relies on making a correct choice for the location of the boundary. In particular, we require $1/\sqrt{2I_p} \ll a \ll I_p/F$. Note that, within the tunnelling picture, the exit of the barrier is at I_p/F . This implies that our boundary must be chosen inside the classically forbidden region, which places it closer to the core than boundaries typically used within numerical implementations of the R-matrix method.

Proceeding as above, we obtain the following expression for the ionization amplitude [15, 17]:

$$a_{\mathbf{p}}(T) = a_g(t_s) R_{klm}(\mathbf{p}, t_s) e^{-iW_C(T, \mathbf{p}; t_s)} \times e^{-iS_V((T, \mathbf{p}; t_s))} e^{iI_p t_s}. \quad (8)$$

The first factor, $a_g(t_s)$, which accounts for laser-induced polarization and depletion of the bound inner-region wavefunction, can be omitted provided that the field is sufficiently weak compared to I_p [17]. The second factor, R_{klm} , encodes the angular structure of the initial bound state. For ionization from the spherically symmetric ground states of hydrogen and helium, which we consider in this paper, R_{klm} does not impact the photoelectron spectra and can also be neglected. The third factor is the boundary-matched Coulomb-phase,

$$W_C(T, \mathbf{p}; t_s) = \int_{t_s - i/\kappa^2}^T dt U(\mathbf{r}_s(\mathbf{p}, t, t_s)), \quad (9)$$

where $\kappa = \sqrt{2I_p}$ in the lower limit of the integral comes from the matching of inner and outer region solutions, and $\mathbf{r}_s(\mathbf{p}, t, t_s) = \int_{t_s}^t dt' (\mathbf{p} + \mathbf{A}(t'))$. S_V is the Volkov phase defined in Eq.(3) and I_p is the ionization potential as before.

All terms above are evaluated at the saddle point time t_s , which is the solution to the saddle point equation

$$\frac{\partial S_V}{\partial t'} \Big|_{t_s} + \frac{\partial W_C}{\partial t'} \Big|_{t_s} = I_p. \quad (10)$$

Since the Coulomb phase W_C is small compared to S_V , we can express the solution for t_s as

$$t_s(\mathbf{p}) = t_s^0(\mathbf{p}) + \Delta t_s^C(\mathbf{p}), \quad (11)$$

where t_s^0 solves the Coulomb-free saddle point equation

$$\frac{\partial S_V}{\partial t'} \Big|_{t_s^0} = -\frac{1}{2}[\mathbf{p} + \mathbf{A}(t_s^0)]^2 = I_p, \quad (12)$$

and Δt_s^C represents a small correction due to the departing electron's interaction with the core. Note that Eq.(12) is the standard equation for ionization time that appears in SFA. It can be solved exactly, provided that we allow our saddle point time to be complex $t_s^0 = t_i^0 + i\tau_T^0$.

The correction Δt_s^C can then be calculated perturbatively [17]. To first order in W_C ,

$$\Delta t_s^C(\mathbf{p}) = -\frac{W'_C(t_s^0)}{S''_V(t_s^0)}, \quad (13)$$

and is also complex in general.

Within SFA-based theories, the real part of the saddle point solution $\text{Re}[t_s]$ is interpreted as the time of ionization: that is, the time at which the electron appears in the continuum. The correction $\text{Re}[\Delta t_s^C]$, which we derive within ARM, then expresses the modification to ionization time due to the electron-core interaction.

The ability to evaluate the Coulomb term W_C is vital to this theory. It features in both the corrected saddle point solution for ionization time (Eq.(11),(13)) and in the expression for the ionization amplitude itself (Eq.(8)). In order to evaluate it, we must integrate in the complex plane: the integral in Eq.(9) starts at the complex point $t_s - i/\kappa^2$, and ends at a time T on the real axis. Provided that the function remains analytic and we avoid branch cuts and singularities, we are free to deform our contour of integration as we like. For simplicity, we choose the contour as follows: First, we integrate parallel to the imaginary axis, down from $t_s - i/\kappa^2$ to t_i on the real axis. Next, we integrate along the real axis from t_i to T .

Doing so, we find that the trajectories $\mathbf{r}_s(\mathbf{p}, t, t_s)$ along which we evaluate the integrand are complex in general along both legs of the contour. These complex trajectories, in fact, play a crucial role within our theory: neglecting the imaginary components would lead to incorrect results in general. The complex nature of the trajectories, in turn, makes it necessary to analytically continue the core potential $U(\mathbf{r})$ when evaluating W_C . For the Coulomb potential $U_C(\mathbf{r}) = -Q/r = -Q/\sqrt{\mathbf{r} \cdot \mathbf{r}}$, we define

$$U_C(\mathbf{r} + i\rho) = -\frac{Q}{\sqrt{(\mathbf{r} + i\rho) \cdot (\mathbf{r} + i\rho)}} = -\frac{Q}{\sqrt{r^2 - \rho^2 + 2ir \cdot \rho}}, \quad (14)$$

and choose the branch cut of the complex square root to be infinitesimally above the negative real axis (so that $\sqrt{-1} = -i$). For the case of long circular pulses, this ensures that our contour never crosses a branch cut.

C. ARM as a theory of strong field ionization

The preceding calculations contain the fundamental tools we need to describe strong field ionization and predict photoelectron spectra. The results above can be applied for any pulse shape and polarization, for any given atom or molecule – provided that we have an expression for the initial state ψ_g and the core potential $U(\mathbf{r})$ – and are accurate well into the non-adiabatic regime, where the static tunnelling picture fails. Furthermore, the theory lends itself naturally to further extensions and refinements. Correlation-driven excitations of the core, for

example, have been included in previous work [16], and recollisions could be accounted for in a similar manner.

Comparing Eq.(8) to the standard SFA result, we observe two key differences: 1. We have acquired a new term, W_C , which describes the effect of an arbitrary long range core potential on the departing electron. Evaluating this term involves integrating along complex electron trajectories. 2. The complex saddle point solution t_s (at which each term in Eq.(8) is evaluated) has been modified to account for the effect of the core. This correction plays an important role for ionization in short laser pulses [19].

In contrast to approaches based on the two step model, ARM is a fully quantum theory and makes no assumptions about the way in which ionization proceeds. In particular, it does not assume tunnelling and does not artificially break the process down into distinct steps. By virtue of this, it avoids the issue of choosing initial conditions for the electron's motion in the continuum. The matching procedure for the inner and outer regions leaves no room for ad hoc assumptions.

D. Looking inside the ionization process: ARM and the tunnelling picture

While the results of ARM are entirely independent of tunnelling, there is nevertheless a natural way to connect the theory to the tunnelling picture. This, in turn, makes it possible to look inside the ionization process, and to test some of the assumptions commonly made in two-step models of ionization. The ability to do this comes from the fact that we can associate each of the legs of the integration contour (which we chose in section II B) with one of the steps in the two-step model [7]. In particular, we identify the first leg of the contour (where the electron evolves in imaginary time) with the electron's motion under the tunnelling barrier, and the second leg (where time evolves along the real axis) with the electron's motion in the continuum. The time t_i , where the two legs of the contour meet, is then naturally interpreted as the time at which the electron appeared in the continuum: that is, the time of ionization.

Electron trajectories also arise naturally within ARM. They feature in the eikonal-Volkov solutions used in the outer region and, as a consequence, appear explicitly in the Coulomb phase W_C . However, unlike the trajectories in both the two-step model and in CCSFA, the trajectories within ARM are complex in general along both legs of the integration contour. They have an imaginary component not only during the tunnelling step, but also after the electron emerges in the continuum, all the way to the detector. Note that this fact is not assumed, but emerges naturally in the theory as a result of consistently applying the saddle point method. In this sense, trajectories within ARM are not purely classical; they retain a quantum character throughout the electron's motion.

Rather than being a mere curiosity, the complex nature

of the trajectories is in fact essential to correctly describe the interaction of the departing electron with the core. The imaginary components are responsible for a shift in the photoelectron spectrum towards lower energies during the electron's continuum motion – associated with a deceleration of the electron wavepacket by the core – and for ongoing changes in the total ionization rate after the ionization time t_i [18].

III. RESULTS: LONG CIRCULARLY POLARIZED PULSES

To assess the performance of our theory, we compare photoelectron spectra calculated using ARM with the numerical solution of the TDSE and with predictions based on length-gauge SFA. Figures 1 and 2 show the results for hydrogen and helium respectively, for ionization in a long circularly polarized laser pulse. For helium, we present results for two different wavelengths and two different intensities to test the robustness of our theory across a range of parameters.

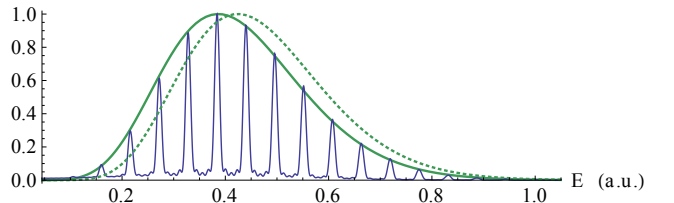


FIG. 1: Photoelectron spectrum for the ionization of hydrogen in a long circularly polarized laser pulse, with $\lambda = 813$ nm and $I = 1.26 \times 10^{14}$ W/cm². Solid and dashed green lines show the predictions of ARM and length-gauge SFA respectively. Blue lines show the spectrum obtained by numerically solving the TDSE. To allow a direct comparison, all results are rescaled such that the maximum of the distribution is at unity.

The solid blue lines, showing sharply peaked ATI spectra, correspond to the numerical results. The calculations were performed following the method described in [23]. The size of the radial box for the results presented in this work was $r_{\max} = 2700$ a.u., followed by a complex absorbing potential for another 300 a.u. The maximum angular momentum used was $L_{\max} = 120$, the step size of the radial grid was $\delta r = 0.15$ a.u. and the time-step was $\delta t = 0.05$ a.u. Convergence was tested against several time-discretization, box, time-step and radial-step sizes. A flat-top laser pulse was used, which consisted of a 2-cycle turn-on, 5 cycles at constant envelope and a two-cycle turn-off. For the hydrogen atom, the exact Coulomb potential was used and the photo-electron spectrum was calculated by projecting the wavefunction onto the exact field-free continuum states of hydrogen after the end of the laser pulse. For helium, a single-active-electron screened potential was used, as described

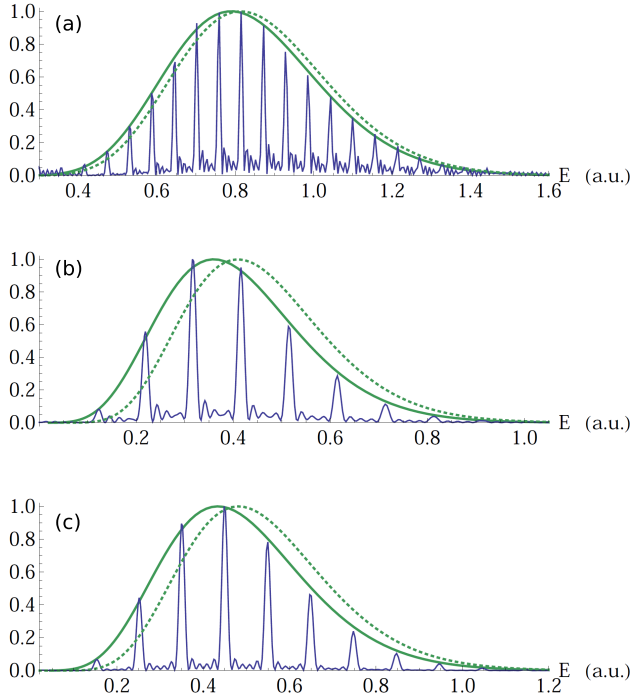


FIG. 2: Photoelectron spectra for the ionization of helium in a long circularly polarized laser pulse, with (a) $\lambda = 800$ nm, $I = 2.53 \times 10^{14}$ W/cm 2 , (b) $\lambda = 456$ nm, $I = 2.53 \times 10^{14}$ W/cm 2 , and (c) $\lambda = 456$ nm, $I = 3.44 \times 10^{14}$ W/cm 2 . Solid and dashed green lines show the predictions of ARM and length-gauge SFA respectively. Blue lines show the spectrum obtained by numerically solving the TDSE. To allow a direct comparison, all results are rescaled such that the maximum of the distribution is at unity.

in [24]. The photoelectron spectrum was then calculated by projecting the wavefunction onto plane waves. This was done three cycles after the end of the pulse to ensure that the electron had time to travel sufficiently far from the core. Before projection, a mask function was applied to get rid of the non-ionizing part of the wavefunction.

The solid and dashed green lines represent results obtained using ARM and length-gauge SFA respectively. For ionization from the symmetric ground state of hydrogen or helium, the length-gauge SFA expression for the ionization rate is simply $|a_{\mathbf{p}}^{\text{SFA}}|^2 = 1/|S_V''(t_s^0)| e^{2\text{Im}S_V(t_s^0)} e^{-2I_p\tau_T^0}$ (neglecting an overall constant factor). The ARM results were calculated based on Eq.(8) using the procedure described in Section II B. All calculations were done for an infinitely long pulse, and using just one saddle point solution $t_s(\mathbf{p})$ at every momentum \mathbf{p} to evaluate the ionization rate $|a_{\mathbf{p}}(T)|^2$. For an infinitely long pulse, there are in fact infinitely many such saddle point solutions, corresponding to identical ionization events at each cycle of the laser field. By choosing one saddle point, we restrict ourselves to one such event at each energy, and as a consequence re-

produce the shape of the spectrum but not the peaked structure (the peaks are a result of interference between equivalent ionization events).

In all cases, we observe excellent agreement between the predictions of ARM and the numerically calculated spectra. Both the shape of the distribution and the location of its maximum coincide very well. Note that for long circular pulses, we find that the shape of the ARM distribution is virtually unaffected by the Coulomb-correction to the saddle point time $\Delta t_s^C(\mathbf{p})$; using the uncorrected time t_s^0 is sufficient. For short pulses, however, this is no longer the case.

In contrast, the predictions of length-gauge SFA produce a notable mismatch: the maximum of the distribution is shifted to higher energies compared to the numerical calculations in all cases. The reason for this mismatch stems from the fact that long range Coulomb effects have been neglected here. As the electron departs, it is decelerated by the attractive potential of the core. This, in turn, gives rise to the relative shift towards lower energies we see in both the numerical and ARM-based results. A similar effect has been observed for linearly polarized fields using the Coulomb-Volkov approximation (CVA) [25, 26]. However, unlike ARM, the CVA approach neglects Coulomb-laser coupling, and as a result becomes inaccurate as we move towards the strong field, low frequency regime [27]. Within ARM, the observed shift originates from the e^{-iW_C} term and is accumulated along the second leg of the integration contour. It arises as a direct consequence of the non-zero imaginary components of electron trajectories in the continuum.

IV. CONCLUSIONS AND OUTLOOK

The analytical R-matrix theory provides us with a flexible and robust quantum framework that can be used to study a variety of phenomena within strong field and attosecond physics. In this work, by comparing its predictions with ab initio numerical calculations, we have shown that ARM can accurately account for Coulomb effects and correctly reproduce photoelectron spectra for strong field ionization in circularly polarized fields, where standard SFA theory fails. Unlike previous attempts to include electron-core interactions, the strength of ARM lies in the fact that very few assumptions are required. The theory does not rely on the tunnelling picture, and does not assume that ionization proceeds in a particular way. As a result, it avoids ambiguities related to the choice of initial conditions which arise in two-step and related models.

An important advantage of the ARM approach stems from its flexibility. The theory can be applied across a broad range of parameters – from the tunnelling limit, well into the non-adiabatic regime – and can readily be generalized and adapted for different situations. For example, the ARM theory has recently been applied to ionization in short circularly polarized pulses, which made it

possible to explain the offset angle observed in attoclock-type experiments and to develop a procedure for reconstructing ionization times from experimental or numerical data [19]. The theory has also been extended to multi-electron systems and used to describe correlation-driven excitations of the ionic core which can occur during the ionization process [16]. Further work on this could provide vital insights into ionization-induced multielectron dynamics.

To complete the picture of strong field ionization, recollisions of the departing electron with the core could also be incorporated into the theory, along with the recombination of the electron back into the parent ion. The latter, in turn, would make it possible to apply ARM in the context of high harmonic generation. Accounting for electron-core interaction and correlation-driven exci-

tations during the high harmonic process, and particularly in multicolour fields, are both important unresolved issues at present. ARM could help us to address both of these, and thereby further our understanding of what is one of the most powerful and widely used tools within attosecond and strong field physics today.

V. ACKNOWLEDGEMENTS

O.S. and L.T. acknowledge the support of DFG grant Sm 292/2-3. F.M. and O.S acknowledge the ERA-Chemistry Project No. PIM2010EEC-00751 (Sm 292/3-1).

-
- [1] P. B. Corkum, Phys. Rev. Lett. 71, 1994 (1993)
 - [2] G. G. Paulus, W. Becker, W. Nicklich, and H. Walther, J. Phys. B: At. Mol. Opt. Phys. 27 L703 (1994)
 - [3] L. V. Keldysh, Zh. Exp. Teor. Fiz. 20 1307 (1965) [Sov. Phys. JETP 47 1945 (1965)]
 - [4] F. H. M. Faisal, J. Phys. B 6 L89 (1973)
 - [5] H. R. Reiss, Phys. Rev. A 22 1786 (1980)
 - [6] A. M. Perelomov, V. S. Popov, M. V. Terent'ev, Zh. Eksp. Teor. Fiz. 50 1393 (1966) [Sov. Phys. JETP 23 924 (1966)]
 - [7] A. M. Perelomov, V. S. Popov, M. V. Terent'ev, Zh. Eksp. Teor. Fiz. 51 309 (1966) [Sov. Phys. JETP 24 207 (1967)]
 - [8] A. M. Perelomov, and V. S. Popov, Zh. Eksp. Teor. Fiz. 52 514 (1967) [Sov. Phys. JETP 25 336 (1967)]
 - [9] M. V. Frolov, N. L. Manakov, E. A. Pronin, and A. F. Starace, Phys. Rev. Lett. 91, 053003 (2003); J. Phys. B 36, L419 (2003).
 - [10] D. Bauer, D. B. Miloevi, and W. Becker, Phys. Rev. A 72, 023415 (2005)
 - [11] O. Smirnova, M. Spanner, and M. Ivanov, J. Phys. B: At. Mol. Opt. Phys. 39 S307 (2006)
 - [12] S. V. Popruzhenko, V. D. Mur, V. S. Popov, and D. Bauer, Phys. Rev. Lett. 101 193003 (2008)
 - [13] S. V. Popruzhenko, and D. Bauer, J. Mod. Opt. 55 2573 (2008)
 - [14] S. V. Popruzhenko, G. G. Paulus, and D. Bauer, Phys. Rev. A 77, 053409 (2008)
 - [15] L. Torlina and O. Smirnova, Phys. Rev. A 86, 043408 (2012)
 - [16] L. Torlina, M. Ivanov, Z. B. Walters, and O. Smirnova, Phys. Rev. A 86, 043409 (2012)
 - [17] J. Kaushal and O. Smirnova, Phys. Rev. A 88, 013421 (2013)
 - [18] L. Torlina, J. Kaushal, and O. Smirnova, Phys. Rev. A 88, 053403 (2013)
 - [19] L. Torlina, F. Morales, J. Kaushal, I. Ivanov, A. Kheifets, A. Zielinski, A. Scrinzi, H. G. Muller, S. Sukiasyan, M. Ivanov, and O. Smirnova, Nat. Phys. 11, 503-508 (2015).
 - [20] C. Bloch, Nuclear Physics, 4, 503, (1957)
 - [21] P. G. Burke, J. Tennyson, Molecular Physics, 103, 2537, (2005)
 - [22] O. Smirnova, M. Spanner, and M. Ivanov, Phys. Rev. A 77, 033407 (2008)
 - [23] H. G. Muller, Laser Physics Vol. 9, No. 1, p. 138 (1999)
 - [24] H. G. Muller, Phys. Rev. Lett. 83, 3158 (1999)
 - [25] M. Jain, and N. Tzoar, Phys. Rev. A 18, 538 (1978)
 - [26] D. G. Arbo, K. L. Ishikawa, K. Schiessl, E. Persson, and J. Burgdrfer, Phys. Rev. A 82, 043426 (2010)
 - [27] Popruzhenko S, J. Phys. B: At. Mol. Opt. Phys. 47 204001 (2014)

Interpreting Attoclock Measurements of Tunnelling Times

Lisa Torlina*,¹ Felipe Morales*,¹ Jivesh Kaushal,¹ Igor Ivanov,² Anatoli Kheifets,² Alejandro Zielinski,³ Armin Scrinzi,³ Harm Geert Muller,¹ Suren Sukiasyan,⁴ Misha Ivanov,^{1,4,5} and Olga Smirnova¹

¹*Max-Born-Institut, Max-Born-Str. 2A, 12489 Berlin*

²*Research School of Physical Sciences, The Australian National University, Canberra ACT 0200, Australia*

³*Ludwig Maximilians University, Theresienstrasse 37, D-80333 Munich, Germany*

⁴*Department of Physics, Imperial College London,
South Kensington Campus, SW7 2AZ London, United Kingdom*

⁵*Institute für Physik, Humboldt-Universität zu Berlin, Newtonstrasse 15, 12489 Berlin, Germany*

This is the accepted version of an article published in Nature Physics 11, 503–508 (2015). The published version is available online at <http://dx.doi.org/10.1038/nphys3340>.

Resolving in time the dynamics of light absorption by atoms and molecules, and the electronic rearrangement this induces, is among the most challenging goals of attosecond spectroscopy. The attoclock is an elegant approach to this problem, which encodes ionization times in the strong-field regime. However, the accurate reconstruction of these times from experimental data presents a formidable theoretical task. Here, we solve this problem by combining analytical theory with ab-initio numerical simulations. We apply our theory to numerical attoclock experiments on the hydrogen atom to extract ionization time delays and analyse their nature. Strong field ionization is often viewed as optical tunnelling through the barrier created by the field and the core potential. We show that, in the hydrogen atom, optical tunnelling is instantaneous. By calibrating the attoclock using the hydrogen atom, our method opens the way to identify possible delays associated with multielectron dynamics during strong-field ionization.

I. INTRODUCTION

Advances in attosecond technology have opened up the intriguing opportunity of timing electron release during photoionization. New experimental techniques such as the attosecond streak camera[1], high harmonic spectroscopy[2], attosecond transient absorption[3] and the attoclock[4–7] are now able to provide the exceptional time-resolution – down to the level of tens of attoseconds ($1 \text{ asec} = 10^{-18} \text{ s}$) – needed to time-resolve ionization. The removal of an electron from an atom or molecule during one-photon ionization creates a non-equilibrium charge distribution which evolves on the attosecond time scale[8]. Ionization time then serves as a sensitive measure encoding the dynamics of core rearrangement triggered by electron removal (see e.g. [9–11]).

Although the use of intense infrared fields as either pump or probe in time-resolved ionization experiments provides access to the time scale of electronic motion, it also introduces a hurdle in interpreting such experiments[10–15]. Identifying and disentangling time delays related to multielectron dynamics from the apparent delays induced by the interaction with the infrared field is challenging both technically and conceptually. In one-photon ionization [1], understanding the nature of the measured delays required the accurate calibration of the measurement schemes, with the hydrogen atom used as a benchmark (see e.g. [12–15]).

Looking beyond the weak field one-photon case, multiphoton ionization can also excite rich multielectron dynamics, which calls for the accurate measurement of ionization times in the strong field regime. What's more,

strong field ionization is often viewed as a tunnelling process, where the bound electron passes through the barrier created by the laser field and the core potential. Consequently, time resolving this process opens the intriguing opportunity [2, 4, 5, 7] to revisit the long-standing problem of tunnelling times.

The measurement of tunnelling times in strong-field ionization has been pioneered by the group of U. Keller [4–7] using the attoclock technique. The attoclock set-up measures angle- and energy- resolved photoelectron spectra produced by ionization in strong, nearly circularly polarized infrared (IR) fields. Essentially, the rotating electric field vector serves as the hand of a clock, deflecting electrons in different directions depending on their moment of escape from the atom. The tunnelling perspective provides a simple picture of how this works. The strong circularly polarized field combined with the binding potential of the atom together create a rotating barrier through which an electron can tunnel (Fig.1(a)). Due to the rotation of the barrier, the electron tunnels in different directions at different times, and is subsequently detected at different angles after the end of the pulse (Fig.1(b)).

Suppose the field rotates counterclockwise and reaches its maximum at $t = 0$ when the field vector $\mathbf{F}_L(t)$ points at an angle of $\phi = 90^\circ$ (Fig.1(b)). In the tunnelling picture, this instant is associated with the thinnest tunnelling barrier and the highest probability of ionization. In the absence of (i) tunnelling delays and (ii) electron–core interaction after tunnelling, we expect that an electron which escapes at time $t_0 = 0$ will be detected at an angle of $\phi = 0^\circ$, orthogonal to $\mathbf{F}_L(t)$. Indeed, if the

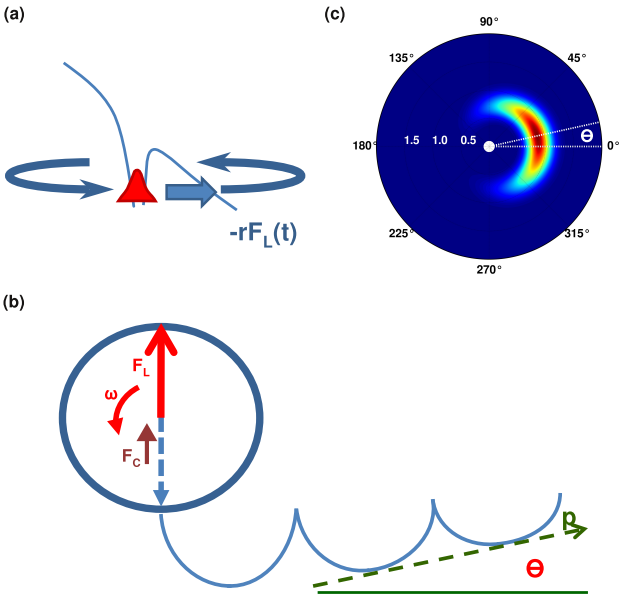


FIG. 1: The attoclock setup. (a) The tunnelling perspective on the attoclock: the laser field and the core potential together create a rotating barrier through which the bound electron can tunnel. As the barrier rotates, the electron will escape in different directions at different times. (b) A cartoon illustrating our ionization geometry. The laser field rotates counter-clockwise and reaches its maximum value when the electric field \mathbf{F}_L points up at an angle of 90° . When the electric field points up, the electron tunnels down, and in the absence of electron-core interaction, we would expect to detect it at an angle of $\phi = 0^\circ$. An offset θ from this angle could be due to the attractive potential of the core (force \mathbf{F}_C) as shown in the figure, and/or possible tunnelling delays. (c) The experimental observable: the angle- and energy-resolved photoelectron spectrum, shown for ionization from the ground state of the hydrogen atom induced by a single-cycle circularly polarized infrared pulse. Dashed lines show the offset angle θ .

electron is released from the barrier with zero initial velocity as suggested by the tunnelling picture (Fig.1(a)), its final momentum at the detector will be $\mathbf{p} = -\mathbf{A}_L(t_i)$, where $\mathbf{A}_L(t_i)$ is the vector-potential of the laser field at the moment of ionization. For circularly polarized pulses, \mathbf{A}_L is orthogonal to \mathbf{F}_L (up to effects of the ultrashort envelope).

An observed deviation of the photoelectron distribution maximum from $\phi = 0^\circ$ could come from the deflection of the outgoing electron by the attractive core potential (Fig.1(b)) and, possibly, from tunnelling delays[4, 5]. This deviation is characterised by the offset angle θ (Fig.1(c)). Experimentally, θ can be measured with high accuracy ($\delta\theta \sim 2^\circ$), which implies the potential to measure ionization delays with accuracy $\delta\tau = \delta\theta/\omega_L \sim 15$ asec for 800 nm radiation.

However, the reconstruction of ionization times from experimentally measured offset angles is sensitive to the

assumptions made about the underlying process. To date, the theoretical approaches used to interpret attoclock results have relied on three assumptions [4–7, 16]. (A1) First, based on the exponential sensitivity of strong-field ionization to the electric field, it is assumed that the highest probability for the electron to tunnel is at the peak of the electric field. (A2) Second, ionization is assumed to be completed once the electron emerges from the barrier. (A3) Third, electron dynamics after the barrier exit are described classically, assuming some point of exit and initial distribution of velocities [7, 17]. Within this classical model, the accuracy of extracting time delays from attoclock measurements depends on the initial conditions assumed for the classical electron dynamics. These initial conditions, however, cannot be established unambiguously. The resulting ambiguity in interpreting attoclock measurements is a major bottleneck for reconstructing ionization times with attosecond precision.

In light of this, we provide a consistent interpretation and calibration for attoclock measurements of ionization times, making no ad hoc assumptions. We do this by combining analytical theory with ab-initio simulations. To calibrate the attoclock, we focus on the hydrogen atom. Doing so, we (i) find very good agreement between our analytical theory and numerical experiments, (ii) show that, for one-electron systems, purely tunnelling delays during strong-field ionization are equal to zero and (iii) reconstruct ionization times for the hydrogen atom, finding deviations from the conventional tunnelling picture expressed by assumptions A1-A3. Finally, we show how the calibration based on single active electron dynamics can be used to identify multielectron contributions to the attoclock observable in multielectron systems.

II. RESULTS

A. Theoretical description

Our theoretical approach is based on the Analytical R-Matrix (ARM) method [19–22]. The key mathematical approximations of this theory and its application to nearly single-cycle pulses are described in the Appendix. In ARM, the probability $w(p, \phi)$ of detecting an electron at an angle ϕ with momentum p is described by an integral over all possible instants of ionization[19–22]. By calculating this time-integral using the saddle point method, we express $w(p, \phi)$ via the contribution of ‘quantum trajectories’ that start from the atom at complex times $t_s(\phi, p)$. Mathematically, the saddle point approach is justified when the electron action S accumulated along the ‘quantum trajectory’ is large, $S \gg \hbar$, which is naturally satisfied in strong low-frequency fields. ARM also requires sufficiently thick tunnelling barriers, restricting analytical work to circularly polarized fields with intensities $I < 4 \times 10^{14} \text{W/cm}^2$. Comparison with ab-initio calculations allows us to judge the accuracy of

the analytical approach.

As time arises naturally along each ‘quantum trajectory’, it becomes possible to establish a connection between the attoclock observable $w(\phi, p)$ and the associated time $t_s(\phi, p)$. It is this mathematically established connection that allows us to calibrate the attoclock. The real part $t_i(\phi, p) \equiv \text{Ret}_s(\phi, p)$ is the ‘ionization time’. In the tunnelling picture, this time corresponds to the moment at which the electron emerges in the classically allowed region. For a ‘zero-range’ binding potential, which supports only a single bound state, we obtain:

$$\text{Ret}_s^{(0)}(\phi, p) \equiv t_i^{(0)}(\phi, p) = \frac{\phi}{\omega} + \Delta t_i^{\text{env}}(\phi, p). \quad (1)$$

Here the superscript (0) denotes the ‘zero-range’ potential. The small correction Δt_i^{env} is due to the ultrashort pulse envelope. It accounts for the fact that, for very short circular pulses, the electric field and the vector potential are not orthogonal at all times during the pulse; Δt_i^{env} disappears for ionization at the peak of the field. In the geometry of Fig.1, the offset angle θ is the angle ϕ associated with the highest photoelectron signal.

For an arbitrary potential, ARM yields (see Appendix):

$$t_i(\phi, p) = \frac{\phi}{\omega} + \Delta t_i^{\text{env}}(\phi, p) + \Delta t_i^C(\phi, p), \quad (2)$$

where $\Delta t_i^C = \text{Re}\Delta t_s^C$ is given by the following expression:

$$\Delta t_s^C = -\frac{dW_C(\phi, p)}{dI_p}, \quad (3)$$

Here W_C is the phase acquired by the laser-driven electron due to its interaction with the core and I_p is the ionization potential (see Appendix for detailed derivation and explicit expression for W_C , including its dependence on the core potential). The derivative is taken with respect to the electron binding energy I_p , keeping the initial and the final electron momenta constant (see Appendix).

B. Attoclock ab-initio

We can now (i) test the ability of ARM to quantitatively describe attoclock measurements, (ii) apply the results Eq.(2,3) to reconstruct ionization times t_i , (iii) investigate the presence of tunnelling delays associated with the electron’s motion in the classically forbidden region. To this end, we perform ab-initio numerical simulations of attoclock measurements for a benchmark system: a hydrogen atom interacting with a perfectly circularly polarized, nearly single-cycle laser pulse with central wavelength $\lambda = 800$ nm. The merit of using ab-initio simulations for hydrogen is the unprecedented accuracy this affords when analysing the attoclock observables: the hydrogen atom is unique in allowing an exact numerical solution of the full time-dependent Schrödinger equation (TDSE) in a circularly polarized field, requiring

no approximations beyond the standard non-relativistic and dipole approximations. Approaching the problem numerically gives us full control of all pulse parameters – intensity, ellipticity, pulse shape and carrier-envelope phase – which is important when time-resolving highly nonlinear processes at the 10 asec level.

Since every numerical scheme must deal with convergence issues related to the finite discretization step, the size of the simulation box, time-propagation routines, etc, we compare three independent calculations of the angle- and energy- resolved photoelectron spectra, done using three different methods and propagation algorithms [16, 23, 24] (see Appendix). The results are in very good agreement. We then compare the numerical results with the analytical theory, to check its validity, and again find very good agreement across a wide range of intensities. Fig.2 shows this comparison for $I = 1.75$, 2.5 and 3.4×10^{14} W/cm². The laser field is defined by $\mathbf{F}_L(t) = -\partial\mathbf{A}_L(t)/\partial t$, where

$$\mathbf{A}_L(t) = -A_0 \cos^4(\omega t/4) (\cos(\omega t) \hat{\mathbf{x}} + \sin(\omega t) \hat{\mathbf{y}}). \quad (4)$$

The field rotates counter-clockwise and points at an angle of 90° when it reaches its maximum at time $t = 0$.

The offset angle θ is extracted by finding the peak of the photoelectron distribution. Fig.3(a) shows the offset angles calculated using the three numerical methods and the ARM approach as a function of laser intensity. The numerical results agree within 0.5°, and the deviation between the analytical and numerical results is within 2°. This slight discrepancy is analysed further in Fig.3(b), where we zoom into the region of intensities between 1×10^{14} W/cm² and 3×10^{14} W/cm². The error bars indicate the angles at which the distribution falls by 0.1% compared to the peak of the signal intensity. Within this deviation, the analytical and numerical offset angles agree. These error bars highlight the extremely flat nature of the distribution around the maximum, even for the single-cycle pulse we have used and gauge the accuracy one has to reach to locate the maximum of photo-electron distribution. The flatness of the spectrum we see here may also challenge the accuracy of identifying θ in experiments.

All calculations show a very interesting trend in intensity. At lower intensities, when the barrier for tunnelling is thicker, there is a bigger deflection angle. Does this trend represent a tunnelling delay, as suggested recently [17, 25]?

C. Delays in tunnelling

In the hydrogen atom, the angular offset may come from two sources: tunnelling delay and the interaction between the departing electron and the nucleus. As a first step towards distinguishing these two possibilities, we replace the Coulomb potential of the hydrogen atom by a short range potential. In this case, the tunnelling barrier will still be present; however, electron-nucleus interaction

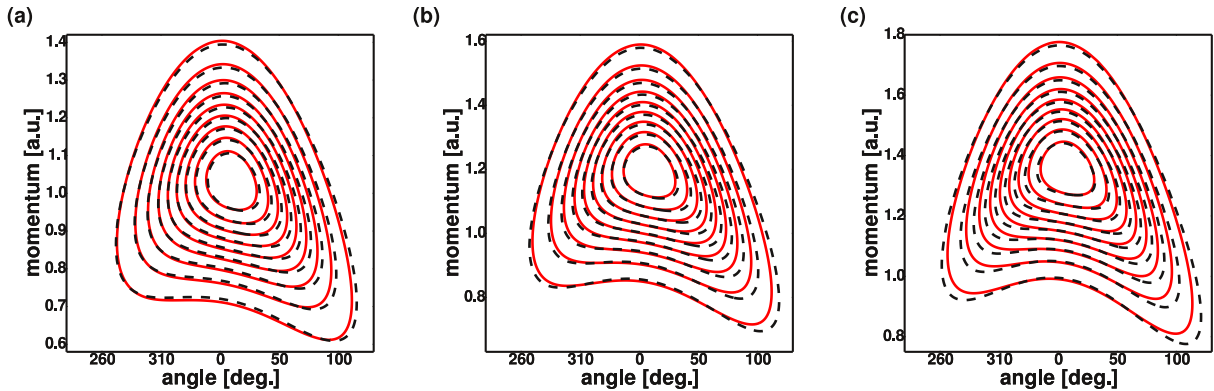


FIG. 2: Comparison of numerical and analytical calculations. Angle- and energy- resolved photoelectron spectra produced by the strong field ionization of the hydrogen atom using a single-cycle circularly polarized laser pulse with wavelength $\lambda = 800$ nm and intensity (a) $I = 1.75 \times 10^{14}$ W/cm 2 , (b) $I = 2.5 \times 10^{14}$ W/cm 2 , and (c) $I = 3.4 \times 10^{14}$ W/cm 2 . The form of the laser pulse is specified in Eq.(4). Solid red contours show spectra obtained analytically using the ARM theory. Dashed black contours are the results of ab initio numerical calculations performed using the method labelled TDSE H1 (see Appendix). The distributions are normalized to 1, and contours correspond to signal intensity changing from 0.1 to 0.9 in steps of 0.1, with the innermost contour at 0.9.

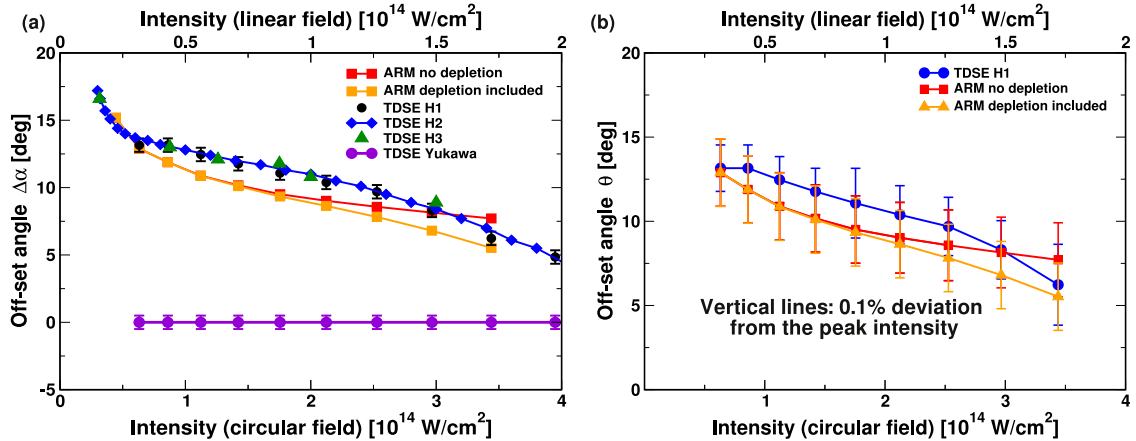


FIG. 3: Offset angles θ extracted from photoelectron spectra as a function of intensity. (a) A comparison of the offset angles obtained for the hydrogen atom using the three different numerical methods (black circles, blue diamonds and green triangles correspond to TDSE H1, H2 and H3 respectively, see Appendix) and the ARM theory (red and yellow squares, the latter include the effect of ground state depletion, see Appendix for details). Violet circles show the numerically obtained offset angles for the short-range Yukawa potential. Error bars are associated with extracting the position of the maximum from angle- and momentum- resolved spectra. (b) A close up of the analytical (red and yellow squares) and numerical (blue circles, TDSE H 1) results for the offset angle for hydrogen. The error bars are used to indicate the angles at which the signal intensity is reduced by a mere 0.1% compared to the peak value.

after tunnelling is turned off. To investigate this, the numerical calculations were repeated for a short-range Yukawa potential, $U_Y = -Ze^{-r/a}/r$, with $Z = 1.94$ and $a = 1.0$ a.u. chosen to yield the ionization potential of the hydrogen atom. The results are summarized in Fig.3(a) and Fig.4. At all intensities, we find that the offset angle θ is equal to zero in this instance. That is, the attoclock measures no tunnelling delays for the short-range Yukawa potential. We now move to the hydrogen atom, where the presence of multiple excited states can, in principle, alter the tunnelling process via electronic

excitations before tunnelling.

D. Reconstruction of ionization times in hydrogen

Having demonstrated very good agreement between photoelectron spectra calculated using the ARM method and ab initio TDSE calculations, we can now apply the mapping (Eq.(2)) to reconstruct ionization times from ab-initio data. In particular, for a given photoelectron spectrum, we extract the most probable time of ioniza-

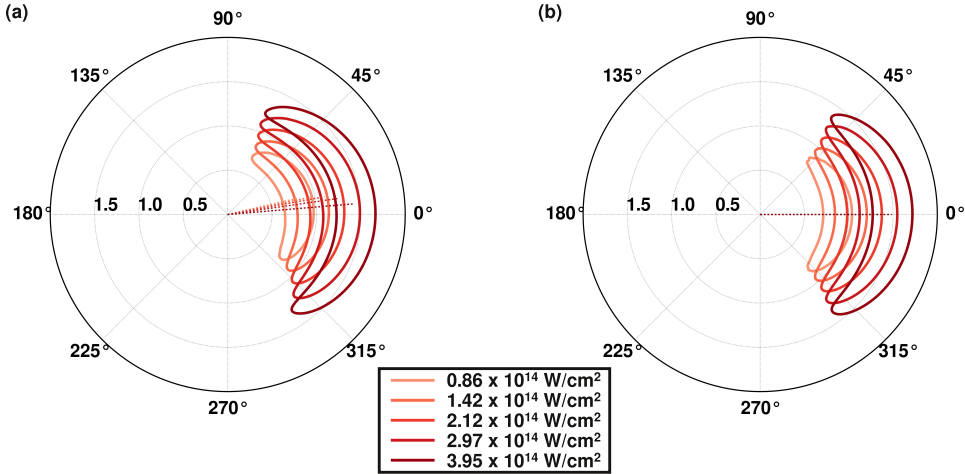


FIG. 4: Attoclock spectra for long and short range potentials. A comparison of the photoelectron spectra calculated numerically using method TDSE H1 for (a) hydrogen and (b) the short-range Yukawa potential. Each contour corresponds to the same signal strength, but a different laser intensity. Pulse shape and wavelength are the same as in Fig.2 and 3. In (b), the offset angle is zero at all intensities, and hence the attoclock measures no tunnelling delays for the Yukawa potential. All spectra include the volume element $\propto p^2$.

tion by evaluating Eq.(2) at the spectrum peak (θ, p_{peak}):

$$t_i(\theta, p_{\text{peak}}) = \frac{\theta}{\omega} - |\Delta t_i^{\text{env}}(\theta, p_{\text{peak}})| - |\Delta t_i^C(\theta, p_{\text{peak}})|, \quad (5)$$

where we have used the fact that Δt_i^C is negative and $\Delta t_i^{\text{env}} < 0$ for $\theta > 0$.

Fig.5(a) shows the results of applying this reconstruction procedure for offset angles θ and momenta p_{peak} obtained numerically using methods TDSE H1 and H2 (see Appendix). Black circles represent the first term in Eq.(5) above: the numerically calculated offset angles, divided by the laser frequency. They correspond to the ionization times we would have reconstructed had we neglected the Coulomb effects and assumed the long pulse limit: $t_i^0 = \theta/\omega$. Orange diamonds represent the above offset angles with the envelope correction $|\Delta t_i^{\text{env}}|$ subtracted: the first two terms in Eq.(5). Essentially, the envelope correction removes the effects of pulse shape from the data: within the analytical approach, we have verified that offset angles corrected in this way become virtually independent of the shape of the envelope used. Blue inverted triangles show the Coulomb correction to the ionization time, the final term in Eq.(5). Finally, green triangles show the reconstructed ionization times t_i themselves.

Across all intensities, we find that the reconstructed ionization times are never positive. The absence of such positive times, in turn, implies the absence of tunnelling delays in the strong field ionization of the hydrogen atom in IR fields.

For $I > 1.5 \times 10^{14} \text{ W/cm}^2$, ionization times become negative, which indicates that the dominant contribution to ionization occurs just before the field reaches its maximum. What could the origin of this effect be? One

possible explanation is the depletion of the ground state: a loss of population before the peak of the field would enhance the relative contribution of early ionization events, decreasing the off-set angle as shown in Fig.3(a) within the ARM theory. The depletion of the ground state, calculated numerically, is shown in Fig.5(b) (see Appendix for details). As expected, depletion increases with intensity, which in turn should give rise to negative t_i . However, as Fig.5(c) shows, if we calculate the expected negative shift of the ionization times based on depletion alone (red circles; see Appendix), we find that it is not sufficient to explain the observed negative ionization times (green triangles). This implies that either the analytical expression Eq.(3) becomes less accurate at higher intensities, or there is another physical effect at play. The latter possibility is explored in the Supplementary Information (available online) using additional numerical tests, which are entirely independent of the analytical theory. These tests confirm the appearance of negative ionization times and show that they may be related to ‘frustrated tunnelling’, a phenomenon well documented for the case of ionization in linearly polarized pulses [26]. Recent theoretical work has suggested that this can also occur in circular fields [27, 28], and the negative ionization times we reconstruct may be a signature of this.

In one-photon ionization, the accurate calibration of time delays for the hydrogen atom made it possible to access delays associated with multielectron effects [12–14, 29, 30]. The same applies to multiphoton ionization time-resolved by the attoclock. It is natural to expect that, as in the one photon case, these may also lead to delays during multiphoton ionization in strong laser fields. The ability to account for the time-shift Δt_i^C associated with single-electron dynamics allows one to identify mul-

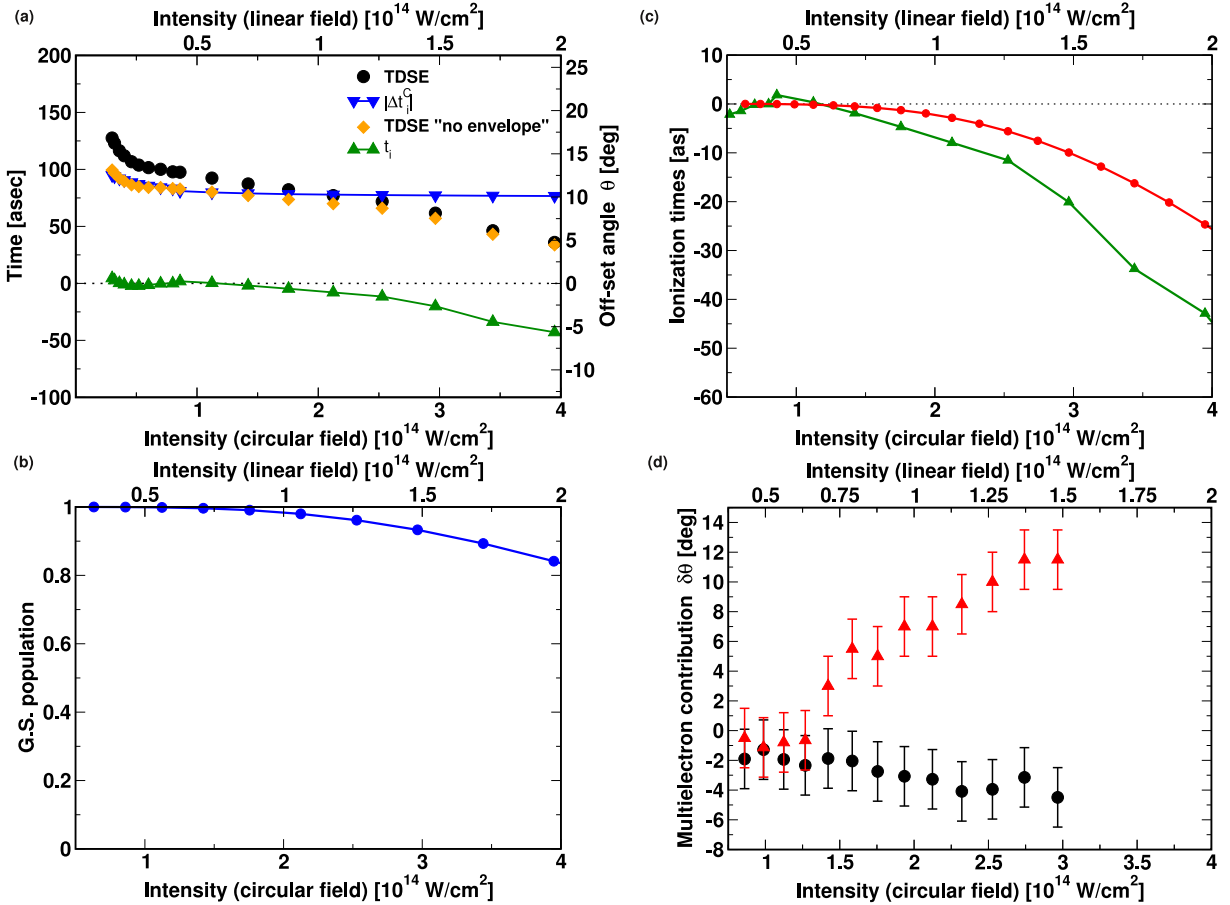


FIG. 5: Reconstruction of ionization times. (a) Ionization times (left axis) reconstructed using the ARM theory from offset angles (right axis) obtained numerically using methods TDSE H1 and H2. Black circles are the numerically calculated offset angles, divided by the laser frequency, θ/ω . Orange diamonds show the offset angles with the correction due to the pulse envelope subtracted, $t_i^0 = \theta/\omega - |\Delta t_i^{\text{env}}(\theta, p_{\text{peak}})|$. Blue inverted triangles show the Coulomb correction to the ionization time evaluated at the peak of the photoelectron distribution, $|\Delta t_i^C(\theta, p_{\text{peak}})|$. Green triangles show the ionization times we obtain by applying reconstruction procedure defined by Eq.(5). In terms of the figure, this is simply the result of subtracting the blue curve from the orange curve. (b) Population of the ground state of the H-atom after the end of the laser pulse as a function of intensity. (c) Ionization times reconstructed using the ARM theory, based on numerically derived offset angles (green triangles), vs corrections to zero ionization times due to effects of depletion alone (red circles; see Appendix). (d) Identification of multielectron effects in attoclock measurements: difference $\delta\theta = \theta_2 - \theta_1$ between the deflection angles for the two-electron (θ_2) and the one-electron (θ_1) systems with the same ionization potential. Black dots: results for a ‘rigid’ model system with high energy of ionic excitations $\Delta E = 0.47$ a.u. Red triangles: results for a model system with reduced energy of ionic excitations $\Delta E = 0.21$ a.u. The error bars indicate the angles at which the signal intensity is reduced by 0.1%

tielectron contributions in attoclock measurements.

Fig.5(d) shows the difference $\delta\theta$ between the numerically calculated offset angles (θ_2, θ_1) for a two-electron and a single electron system with the same binding energy and the same long-range core potential, $\delta\theta = \theta_2 - \theta_1$ (see Supplementary Information for details). We observe two complementary effects. The first is core polarization[7], which shields the core and therefore slightly *reduces* the deflection angle caused by electron-core attraction. This leads to negative $\delta\theta$ (see Fig.5(d), black circles). This is the only effect we see in our numerical simulations when electronic excitations in the ion lie far above the ionization threshold ($\Delta E = 0.47$ a.u. in

our model system).

However, if we reduce the energy of electronic excitation in the ion (to $\Delta E = 0.21$ a.u.), and thereby also the energy of two-electron excitations, while keeping the ionization potential of the neutral fixed at $I_p = 0.5$ a.u., the picture changes (Fig.5(d), red triangles). As laser intensity increases, the multielectron correction $\delta\theta$ of the deflection angle starts to rise quickly and becomes positive. This sharp increase of $\delta\theta$ coincides with onset of double ionization.

This trend is accompanied by a decrease in the relative delay between the removal of the two electrons during double ionization (see Supplementary Information), and

is consistent with two-electron excitations formed during the first ionization step [6, 20] (termed ‘pre-collision’ in [6]). Thus, electronic excitations during ionization may indeed lead to additional positive delays in attoclock measurements of single ionization.

III. CONCLUSIONS AND OUTLOOK

As we have seen, because the ARM method naturally includes the concept of trajectories, it makes it possible to reconstruct ionization times from the experimentally observed offset angles. Applying this method to the single electron system, the hydrogen atom, in turn, has allowed us to calibrate the attoclock, revealing the contribution coming purely from the attractive force of the core. Any additional offset observed in multielectron systems must then be due to multielectron effects. We have shown how these effects can be detected by comparing the offset angles for multielectron systems with the predictions obtained within the standard single-active-electron approximation.

The presence of trajectories within ARM also makes it possible to assess the accuracy of the commonly used assumptions (A1)-(A3). In contrast to (A3), trajectories in ARM are never fully classical. Although the measured quantity (the electron momentum) is real, the trajectories retain an imaginary component of the coordinate all the way to the detector (see Appendix). This property is directly related to the fact that, for long range potentials, ionization is not yet completed at the moment the electron exits the tunnelling barrier, in contrast to (A2) (see discussion and ab-initio numerical tests in Supplementary Information). At high intensities, the dominant contribution to the photoelectron spectrum may come from ionization that starts before the maximum of the electric field, even after effects of depletion are taken into

account, in contrast to (A1). One should therefore be cautious when using assumptions (A1)-(A3) to interpret attoclock measurements at the ~ 10 asec level.

Our results indicate no tunnelling delays associated with the ionization of the ground-state of the hydrogen atom by a strong low-frequency field. However, the situation may be different when real electronic excitations during ionization are involved. For two-electron systems, our results have shown that the two types of multielectron response to the infrared laser field – namely the adiabatic polarization of the electronic cloud and real two-electron excitations – leave distinct and different traces in attoclock measurements, leading to additional delays, either negative or positive. Thus, attoclock experiments with molecules or alkaline-earth atoms, where doubly excited states lie below the first ionization threshold, may uncover rich multielectron response manifested in non-trivial, intensity dependent ionization delays caused by correlation-driven excitations during strong-field ionization.

Acknowledgements

We acknowledge stimulating discussions with U. Keller and A. Landsman. J.K., O. S. and M. I. acknowledge support of the EU Marie Curie ITN network CORINF. F. M. and O. S. acknowledge support of the ERA-Chemistry grant, M. I. acknowledges support of the EPSRC Programme Grant, O.S., L. T. and J.K. acknowledge support of the DFG grant SM 292/2-3. A.K. and I.I. acknowledge support of the Australian Research Council Grant DP120101805. A.Z. and A.S. acknowledge support by the DFG cluster of excellence “Munich Center for Advanced Photonics (MAP)”. H. G. M. acknowledges the hospitality of the Max Born Institute.

* These authors have contributed equally.

-
- [1] Schultze, M. et al. Delay in photoemission. *Science* 328, 1658-1662 (2010).
 - [2] Shafir, D. et al. Resolving the time when an electron exits a tunnelling barrier, *Nature* 485, 343-346 (2012).
 - [3] Goulielmakis, E. et al. Real-time observation of valence electron motion, *Nature* 466, 700-702 (2010).
 - [4] Eckle, P. et al. Attosecond ionization and tunneling delay time measurements in helium. *Science* 322, 1525-1529 (2008).
 - [5] Eckle, P. et al. Attosecond angular streaking, *Nature Phys.* 4, 565-570 (2008).
 - [6] Pfeiffer, A. N. et al. Breakdown of the independent electron approximation in sequential double ionization, *New J. Phys.* 13, 093008 (2011).
 - [7] Pfeiffer, A. N. et al. Attoclock reveals natural coordinates of the laser-induced tunnelling current flow in atoms, *Nature Physics* 8, 7680 (2012).
 - [8] Breidbach, J. & Cederbaum, L. S. Universal attosecond response to the removal of an electron, *Phys. Rev. Lett.* 94, 033901 (2005).
 - [9] Sukiasyan, S., Ishikawa, K. L. & Ivanov, M. Attosecond cascades and time delays in one-electron photoionization, *Phys. Rev. A* 86, 033423 (2012).
 - [10] Kheifets A. S. & Ivanov I. A. Delay in atomic photoionization, *Phys. Rev. Lett.* 105, 233002 (2010).
 - [11] Moore, L. R., Lysaght, M. A., Parker, J. S., van der Hart, H. W. & Taylor, K. T. Time delay between photoemission from the 2p and 2s subshells of neon, *Phys. Rev. A* 84, 061404 (2011).
 - [12] Klunder, K. et al. Probing single-photon ionization on the attosecond time scale, *Phys. Rev. Lett.* 106, 143002 (2011).
 - [13] Ivanov, M. & Smirnova O. How accurate is the attosecond streak camera? *Phys. Rev. Lett.* 107, 213605 (2011).
 - [14] Pazourek, R., Nagele, S. & Burgdorfer, J. Time-resolved photoemission on the attosecond scale: Opportunities and challenges. *Faraday Discuss.* 163, 353-376 (2013).
 - [15] Dahlström, J. M., L'Huillier, A. & Maquet, A. Introduc-

- tion to attosecond delays in photoionization J. Phys. B 45, 183001 (2012).
- [16] Ivanov, I. & Kheifets, A. Strong-field ionization of He by elliptically polarized light in attoclock configuration. Phys. Rev. A 89, 021402 (2014).
- [17] Boge, R. et al. Probing nonadiabatic effects in strong-field tunnel ionization, Phys. Rev. Lett. 111, 103003 (2013).
- [18] Shvetsov-Shilovski, N. I., Dimitrovski, D. & Madsen, L. B. Ionization in elliptically polarized pulses: Multielectron polarization effects and asymmetry of photoelectron momentum distributions. Phys. Rev. A 85, 023428 (2012).
- [19] Torlina, L. & Smirnova, O. Time-dependent analytical R-matrix approach for strong-field dynamics. I. One-electron systems, Phys. Rev. A 86, 043408 (2012).
- [20] Torlina, L., Ivanov M., Walters, Z. B. & Smirnova, O. Time-dependent analytical R-matrix approach for strong-field dynamics. II. Many-electron systems, Phys. Rev. A 86, 043409 (2012).
- [21] Kaushal, J. & Smirnova, O. Nonadiabatic Coulomb effects in strong-field ionization in circularly polarized laser fields, Phys. Rev. A 88, 013421, (2013).
- [22] Torlina, L., Kaushal, J. & Smirnova, O. Time-resolving electron-core dynamics during strong-field ionization in circularly polarized fields, Phys. Rev. A 88, 053403 (2013).
- [23] Muller, H. G. An efficient propagation scheme for the time-dependent Schrödinger equation in the velocity gauge, Laser Phys. 9, 138-148 (1999).
- [24] Tao, L. & Scrinzi, A. Photo-electron momentum spectra from minimal volumes: The time-dependent surface flux method. New J. Phys. 14, 013021 (2012).
- [25] Landsman, A. et al. Ultrafast resolution of tunneling time delay. Optica 1, 343-349 (2014).
- [26] Nubbemeyer, T., Gorling, K., Saenz, A., Eichmann, U. & Sandner, W. Strong-field tunneling without ionization Phys. Rev. Lett. 101, 233001 (2008).
- [27] Kamor, A., Mauger, F., Chandre, C. & Uzer, T. How key periodic orbits drive recollisions in a circularly polarized laser field, Phys. Rev. Lett. 110, 253002 (2013).
- [28] Wang, X. & Eberly, J. H. Elliptical polarization and probability of double ionization. Phys. Rev. Lett. 105, 083001 (2010).
- [29] Carette, T., Dahlström, J. M., Argenti, L. & Lindroth, E. Multiconfigurational Hartree-Fock close-coupling ansatz: Application to the argon photoionization cross section and delays. Phys. Rev. A 87, 023420 (2013).
- [30] Kheifets, A. S. Time delay in valence shell photoionization of noble gas atoms, Phys. Rev. A 87, 063404 (2013).
- [31] Scrinzi, A. t-SURFF: Fully differential two-electron photo-emission spectra, New J. Phys. 14, 085008 (2012).
- [32] Sukiasyan, S. et al. Signatures of bound-state-assisted nonsequential double ionization Phys. Rev. A 80, 013412 (2009).
- [33] Smirnova, O., Spanner, M. & Ivanov, M. Analytical solutions for strong field-driven atomic and molecular one- and two-electron continua and applications to strong-field problems. Phys. Rev. A 77, 033407 (2008).

Appendix: Methods

1. Ab initio simulations

Our numerical simulations have used three different algorithms to produce ab-initio spectra of strong-field ionization induced by a nearly single-cycle 800 nm laser pulse. The data labeled ‘TDSE H 1’ (F. Morales and H. G. Muller) have used the numerical procedure and the code described in detail in [23]. The data labeled ‘TDSE H 2’ (A. Zielinski and A. Scrinzi) were obtained using the t-SURFF method described in [24]. The data labelled ‘TDSE H 3’ (I. Ivanov and A. Kheifets) have used the numerical procedure and the code described in detail in [16].

Our numerical simulations have used three different algorithms to produce ab-initio spectra of strong-field ionization induced by a nearly single-cycle 800 nm laser pulse. The data labeled ‘TDSE H 1’ (F. Morales and H. G. Muller) have used the numerical procedure and the code described in detail in [23]. The data labeled ‘TDSE H 2’ (A. Zielinski and A. Scrinzi) were obtained using the t-SURFF method described in [24]. The data labelled ‘TDSE H 3’ (I. Ivanov and A. Kheifets) have used the numerical procedure and the code described in detail in [16].

The method used for the calculations labeled ‘TDSE H 1’ (F. Morales and H. G. Muller) has been monitored for convergence by changing the maximum angular momentum up to $L_{max} = 120$, while the radial grid size was increased up to $r_{max}=2700$ a.u. The spectrum was obtained by projection on the exact field-free continuum states of the H-atom after the end of the laser pulse. The step size of radial grid was $\delta r=0.15$ a.u. and the time-step was $\delta t=0.05$ a.u. Convergence was monitored by varying δr down to 0.05 a.u. and the time-step δt down to 0.04 a.u.

T-SURFF (‘TDSE H 2’, A. Zielinski and A. Scrinzi) combines numerical solutions in an inner region with approximate analytical solutions in terms of Volkov states outside. The method is efficient since the numerical part of the solution can be kept comparatively small: converged results were obtained with an inner region $|\vec{r}| < r_{max} = 120$ a.u. using a finite-element radial discretization with 310 coefficients and an expansion into spherical harmonics up to $L_{max} = 95$. The dominant error in the offset-angle θ arises from the absence of electron-ion interaction in the Volkov states. It is $\lesssim 0.3^\circ$ at the lowest intensities and drops below 0.01° for intensities $> 10^{14}$ W/cm². A detailed description of method and code, as well as numerical examples can be found in [24, 31].

The method used for the calculations labeled ‘TDSE H 3’ (I. Ivanov and A. Kheifets) has been monitored for convergence by changing the maximum angular momentum up to $L_{max} = 80$, while the radial grid size was increased up to $r_{max}=300$ a.u. for calculations in both the length and the velocity gauge (with full agreement between the

two). The spectrum was obtained by projection onto the exact field-free continuum states of the H-atom after the end of the laser pulse. The step size of radial grid was $\delta r=0.1$ a.u. and the time-step was $\delta t=0.01$ a.u.. Convergence was monitored by varying δr down to 0.05 a.u. and the time-step δt down to 0.005 a.u..

The method used for two-electron systems has been described in detail in [32] and is based on the Heidelberg MCTDH code, adapted to two electrons. It uses time-dependent basis functions, variationally optimized to the electron dynamics, see [32]. The electrons are treated in two dimensions each, with basis functions set on the Cartesian grid with step-size $\delta x=0.2$ a.u., covering ± 280 a.u. for each dimension. To achieve convergence 30 time-dependent basis functions per dimension are used, leading to leading to 810,000 total configurations propagated at each time step.

2. The ARM theory applied to short circularly-polarized pulses

a. General expressions

The ARM approach has been described in detail in Refs.[19–22], where it was originally developed for long laser pulses. Here we apply the same method for short pulses, taking into account effects of the pulse envelope. These effects are very important when considering the nearly-single cycle pulses required to perform atto-clock measurements.

The ARM method yields the following expression for the photoelectron spectrum[21, 22]:

$$|a_{\mathbf{p}}(T)|^2 = |R_{\kappa l m}(\mathbf{p})|^2 e^{2\text{Im}S(T, \mathbf{p}, t_s)}, \quad (\text{A.1})$$

where $T \rightarrow \infty$. The first term, $R_{\kappa l m}(\mathbf{p})$, encodes the angular structure of the initial state. For the spherically symmetric ground state of hydrogen, which we focus on in this work, $R_{\kappa l m}(\mathbf{p})$ does not impact the angle-resolved spectra. The action S in the second term is comprised of three components,

$$S(T, \mathbf{p}, t_s) = S_V(T, \mathbf{p}, t_s) + W_C(T, \mathbf{p}, t_s) - I_p t_s. \quad (\text{A.2})$$

The first of these is the so-called Volkov phase, the phase accumulated by the electron in the laser field only:

$$S_V(T, \mathbf{p}, t_s) = \frac{1}{2} \int_{t_s}^T dt [\mathbf{p} + \mathbf{A}(t)]^2. \quad (\text{A.3})$$

The second component is the phase accumulated due to the interaction of the departing electron with the core:

$$W_C(T, \mathbf{p}, t_s) = \int_{t_s - i\kappa^{-2}}^T dt U(\mathbf{r}_s(\mathbf{p}, t, t_s)), \quad (\text{A.4})$$

where $U(\mathbf{r}_s)$ is the potential of the atom or molecule evaluated along the electron's laser-driven quantum trajec-

tory,

$$\mathbf{r}_s(\mathbf{p}, t, t_s) = \int_{t_s}^t dt' (\mathbf{p} + \mathbf{A}(t')). \quad (\text{A.5})$$

The third component comes from the evolution of the initial bound state, where I_p is the ionization potential of this state. Finally, $\kappa = \sqrt{2I_p}$ in the lower limit of the integral in Eq.(A.4) comes from the matching of inner and outer region solutions. Each of the terms above is evaluated at the complex time $t_s = t_i + i\tau_T$, which is the solution to the saddle-point equation

$$\begin{aligned} \left. \frac{\partial S(T, \mathbf{p}, t')}{\partial t'} \right|_{t_s} &= \left. \frac{\partial S_V(T, \mathbf{p}, t')}{\partial t'} \right|_{t_s} - I_p \\ &+ \left. \frac{\partial W_C(T, \mathbf{p}, t')}{\partial t'} \right|_{t_s} = 0 \end{aligned} \quad (\text{A.6})$$

The time t_s defines the starting point of the electron trajectory, and the presence of the imaginary component in t_s reflects the quantum nature of the electron's motion.

The above expressions are obtained by solving the time-dependent Schrödinger equation for the problem of strong-field ionization. The solution makes no assumptions about the nature of the ionization process and is gauge-invariant [19, 20]. The core part of the method relies on the rigorous R-matrix-type separation of coordinate space into inner and outer regions, with the wavefunction transferred between the two using the Bloch operator – a standard R-matrix technique. The approximations used by the analytical method are as follows: (B1) The wavefunction in the inner region is approximated by the bound state from which ionization occurs. (B2) In the outer region, the method uses strong-field eikonal-Volkov states [33] to describe the electron dynamics. The validity of the eikonal approximation sufficiently far from the core has been thoroughly checked in [33]. Its accuracy has been further verified for the case of delays in one-photon ionization measured by the attosecond streak-camera [13] – the use of eikonal-Volkov states in the continuum yielded excellent agreement between analytical and ab-initio results. (B3) The derivation also makes use of the saddle point method when evaluating the integrals that arise. Our ability to do so stems from the large action accumulated by the electron in the presence of a strong laser field.

The key to our ability to reconstruct ionization times from photoelectron spectra comes from the fact that $t_i = \text{Re}[t_s]$, the real part of the saddlepoint solution above, is naturally interpreted as the time of ionization (see e.g.[2] and references therein). Consequently, the analysis of ionization times in strong-field ionization is concerned with saddle-point times and the corrections to these times introduced by the core potential.

b. Coulomb corrections to saddle-point times

It is instructive to start with the case where the electron-core interaction is negligible, which is appropriate e.g. for the short-range Yukawa potential. If we neglect the term due to the Coulomb phase, Eq.(A.6) reduces to

$$\frac{\partial S_V(T, \mathbf{p}, t')}{\partial t'} \Big|_{t_s^0} - I_p = 0, \quad (\text{A.7})$$

which can be easily solved with no approximations. For electron momentum $\mathbf{p} = \{p, \phi\}$, we obtain

$$\omega t_i^0(\mathbf{p}) = \omega \text{Re}[t_s^0(\mathbf{p})] = \phi + \Delta\phi^{\text{env}}(\mathbf{p}), \quad (\text{A.8})$$

where ϕ is the angle at which the electron is detected and $\Delta\phi^{\text{env}}$ is a small correction due to the shape of the pulse envelope. The sign of this correction depends on ϕ : it is negative for $\phi > 0$, positive for $\phi < 0$, and zero for $\phi = 0$. For sufficiently long pulses, $\Delta\phi^{\text{env}}$ vanishes, and we are left with the simple mapping $t_i^0 = \phi/\omega$. That is, if we neglect electron-core interaction, we find that the angle of detection is orthogonal to the direction of the field at the moment of ionization. This is fully consistent with the ab-initio numerical results obtained for the Yukawa potential, where the majority of the electrons are detected orthogonal to the field direction at the peak of the laser pulse.

In the absence of electron-core interaction, the real part t_i^0 of the saddle point solution t_s^0 has a clear meaning. It corresponds to the so-called ionization time, since for all times $t > t_i^0$ both the photoelectron spectrum $|a_{\mathbf{p}}^0(t)|^2 \propto e^{2\text{Im}S_{SFA}(t, \mathbf{p}, t_s^0)}$ and the ionization probability $\int |a_{\mathbf{p}}^0(t)|^2 d\mathbf{p}$ remain constant: ionization is completed by time t_i^0 . Indeed, the imaginary component of the action $S_{SFA}(t, \mathbf{p}, t_s^0)$ is only accumulated while integrating from t_s^0 to t_i^0 in Eq.(A.3). This property of the integral in Eq.(A.3) has prompted the perspective that tunnelling corresponds to motion in imaginary time from $\text{Im}t_s^0$ to zero. $\text{Re}t_s^0 = t_i^0$ then corresponds to the exit time: the time at which the electron leaves the tunnelling barrier. Within this approach, in the absence of electron-core interaction, tunnelling from the bound state starts and finishes at the same real time t_i^0 . This result is fully consistent with the ab-initio calculations for the Yukawa potential presented in the main body of the paper. We note that the potential used in the numerical calculations has a single bound s-state, which ensures that scattering phases in all ionization channels other than the s-channel are equal to zero.

With this result in mind, we can express the full solution to Eq.(A.6) as

$$t_s = t_s^0 + \Delta t_s^C, \quad (\text{A.9})$$

where t_s^0 is the solution of the Coulomb-free saddlepoint equation (Eq.(A.7)) and Δt_s^C is the correction due to the electron-core interaction. Expanding Eq.(A.6) in a

Taylor series around t_s^0 and keeping all terms up to first order in the electron-core interaction W_C , we obtain

$$\Delta t_s^C = -\frac{\partial W_C(T, \mathbf{p}, t_s^0)}{\partial t_s^0} \left(\frac{\partial^2 S_V(T, \mathbf{p}, t_s^0)}{\partial t_s^0} \right)^{-1}. \quad (\text{A.10})$$

Next, we note that Eq.(A.7) establishes a functional dependence $t_s^0 = t_s^0(I_p)$. With this in mind, differentiating both sides of Eq.(A.7) with respect to I_p , we have

$$\left(\frac{\partial^2 S_V(T, \mathbf{p}, t_s^0)}{\partial t_s^0} \right)^{-1} = \frac{dt_s^0}{dI_p}. \quad (\text{A.11})$$

Combining Eq.(A.10) and (A.11), we obtain

$$\Delta t_s^C = -\frac{\partial W_C(T, \mathbf{p}, t_s^0)}{\partial t_s^0} \frac{dt_s^0}{dI_p}. \quad (\text{A.12})$$

To derive a practical way of calculating Δt_s^C , we recall that $W_C(T, \mathbf{p}, t_s^0)$ (Eq.(A.4)) depends on I_p only via $t_s^0 = t_s^0(I_p)$ and $\kappa = \sqrt{2I_p}$ in the lower limit of the integral. The full derivative of $W_C(T, \mathbf{p}, t_s^0)$ with respect to I_p can therefore be expressed as

$$\begin{aligned} \frac{dW_C(T, \mathbf{p}, t_s^0)}{dI_p} &= \frac{\partial W_C(T, \mathbf{p}, t_s^0)}{\partial t_s^0} \frac{dt_s^0}{dI_p} \\ &\quad + \frac{\partial W_C(T, \mathbf{p}, t_s^0)}{\partial \kappa} \frac{d\kappa}{dI_p}. \end{aligned} \quad (\text{A.13})$$

Thus, we can evaluate Δt_s^C by differentiating $W_C(T, \mathbf{p}, t_s^0)$ with respect to I_p , while keeping κ in the lower limit of the integral constant:

$$\Delta t_s^C = -\frac{dW_C(T, \mathbf{p}, t_s^0)|_{\kappa=\text{const}}}{dI_p}. \quad (\text{A.14})$$

Recalling that the real part of the saddlepoint solution, $t_i = \text{Re}[t_s]$, represents the time of ionization, our analysis has established a mapping between the angle and momentum at which the electron is detected and its ionization time $t_i = \text{Re}[t_s]$:

$$t_i(\phi, p) = \frac{\phi}{\omega} + \Delta t_i^{\text{env}}(\phi, p) + \Delta t_i^C(\phi, p), \quad (\text{A.15})$$

where Δt_i^{env} is obtained by solving Eq.(A.7), and $\Delta t_i^C = \text{Re}\Delta t_s^C$ is calculated using Eq.(A.14) above.

Finally, we discuss the dependence of W_C (SM, Eq.(A.4)) on the range a of the short-range Yukawa potential. The integral Eq.(A.4) is calculated from t_s down to the real time axis, $t_i = \text{Re}(t_s)$, and then along the real time axis. In the classically forbidden region, between t_s and t_i , the differential dt is purely imaginary and thus, for real-valued $U(r)$, no real-valued contribution to W_C is accumulated. (The potential U evaluated along the complex trajectory remains real-valued in the classically forbidden region between t_s and t_i as long as $\text{Re}r_s > \text{Im}r_s$. This condition is met for the peak of the

electron distribution.) The real-valued contribution to W_C is accumulated at $t > t_i$. If $r_s(p, t_i, t_s)$ exceeds the range of the potential, then $U(r_s(p, t \geq t_i, t_s)) = 0$, and $\text{Re}W_C = 0$, leading to no correction to the real part of the saddle point. Obviously, the same applies to the zero-range potential. As the range a of the potential becomes comparable to $r_s(p, t_i, t_s)$, $\text{Re}W_C$ will start to deviate from zero, leading to non-zero Δt_i .

c. Effect of ground state depletion on ionization times

Fig. 5 (b) (see main text) shows the population of the ground state after the end of the pulse, calculated using the ‘TDSE H1’ approach (F. Morales and H. Muller). The population is obtained by projecting the wavefunction of the system on the ground state after the end of the pulse. The depletion of the ground state remains very small until $I = 2 \times 10^{14} \text{ W/cm}^2$, and is below 10^{-3} when negative ionization times become apparent. However, these times (Fig. 5 (a,c)) are also small. At higher intensities, ionization reaches a few percent and depletion of the ground state population must contribute to the increasing values of negative ionization times. To quantify this effect, we take advantage of the attoclock mapping between the ionization times t_i and the electron deflection angle θ . We also take into account that both the depletion of the ground state and the negative ionization times are very small.

Consider the photoelectron distribution integrated over energy, $P(\phi)$, and let us denote by $P_0(\phi)$ the photoelectron distribution in the absence of depletion. According to the ARM theory, their relationship is $P(\phi) = P_0(\phi)W_g(t_i(\phi))$, where $W_g(t_i(\phi))$ is the ground state population at the moment of ionization $t_i(\phi)$, which is mapped to the detection angle ϕ . If ground state depletion is the sole origin of the negative ionization times, then $P_0(\phi)$ should have its maximum at the angle which corresponds to an ionization time of zero: that is, at the angle $\phi = \theta_0$ which satisfies $t_i(\theta_0) = 0$. The decreasing function $W_g(t_i)$ will then skew this distribution towards $t_i < 0$. Note that, according to the attoclock principle, $\phi - \theta_0 = \omega t_i$, where ω is the laser frequency.

For small ionization times near the peak of the laser field $t = 0$, we have $W_g(t_i) = W_g(0)[1 - \Gamma_0 t_i]$, where $\Gamma_0 = \Gamma(t = 0)$ is ionization rate at the peak of the field, and $W_g(0)$ is the ground state population at the peak of the field. To determine how the decreasing value of $W_g(t_i)$ shifts the maximum of $P(\phi)$, we expand $P(\phi)$ in a Taylor series around θ_0 , the angle at which $P_0(\phi)$ is maximized:

$$P(\phi) = P_0(\phi)W_g(0)[1 - \Gamma_0 t_i] \quad (\text{A.16})$$

$$= \left[P_0(\theta_0) - \frac{1}{2}P_0''(\phi - \theta_0)^2 \right] W_g(0)[1 - \Gamma_0 t_i]. \quad (\text{A.17})$$

Here we have used the fact that $P_0(\phi)$ has its maximum at $\phi = \theta_0$ and hence $P_0'(\theta_0) = 0$. Using $\phi - \theta_0 = \omega t_i$ we

obtain:

$$P(\phi) = P_0(\phi)W_g(0)[1 - \Gamma_0 t_i] \quad (\text{A.18})$$

$$= \left[P_0(\theta_0) - \frac{1}{2}P_0''\omega^2 t_i^2 \right] W_g(0)[1 - \Gamma_0 t_i]. \quad (\text{A.19})$$

We can now find the maximum of the function $P(\phi)$ by solving the equation $dP(\theta)/d\phi = 0$, or equivalently $dP/dt_i = 0$, given the linear dependence $\phi - \theta_0 = \omega t_i$. For small time shifts t_i , where $\Gamma_0 t_i \ll 1$, this yields

$$\omega t_i = -\frac{P_0(\theta_0)}{P_0''(\theta_0)}W_g(0)\Gamma_0\frac{1}{\omega} \quad (\text{A.20})$$

In our numerical simulations, $\Gamma_0 t_i \leq 4 \times 10^{-3}$ for all intensities shown in Fig.5. We can now use our ab-initio photoelectron distributions to extract the required quantities, the ratio P_0/P_0'' and the ionization rate Γ_0 .

First, we integrate each ab-initio energy- and angle- resolved photoelectron distribution over energy to obtain an angle-resolved electron yield, to which we fit a Gaussian:

$$P(\phi) = C \exp \left[-\frac{(\phi - \theta_{\max})^2}{2\Delta^2} \right], \quad (\text{A.21})$$

where θ_{\max} corresponds to the maximal photoelectron signal. Again, making use of $\Gamma_0 t_i \ll 1$, and using Eq.(A.16), we have

$$\frac{P_0(\theta_0)}{P_0''(\theta_0)} = \frac{P(\theta_{\max})}{P''(\theta_{\max})} = \Delta^2, \quad (\text{A.22})$$

where the relative error in the first equality in the above equation is $\Gamma_0 t_i/2 \leq 2 \times 10^{-3}$. Eq.(A.22) yields the following expression for ωt_i :

$$\omega t_i = -\frac{\Delta^2}{\omega}\Gamma_0 W_g(0). \quad (\text{A.23})$$

Finally, we note that the attoclock mapping $\theta(t_i)$ reflects the sub-cycle dependence of the ionization rate, which follows the same Gaussian-shaped distribution as the photoelectron spectrum,

$$\Gamma(\theta) = \Gamma_0 \exp \left[-\frac{(\phi - \theta_0)^2}{2\Delta^2} \right] = \Gamma_0 \exp \left[-\frac{(\omega t_i)^2}{2\Delta^2} \right] \quad (\text{A.24})$$

Here, we explicitly use the assumption that Γ is maximized at the peak of the field, i.e. depletion is the only reason for negative ionization times (θ_0 corresponds to the peak of the field $t = 0$). For a circularly polarized field, we can obtain the total ionization yield W_i by integrating $\Gamma(\phi)$ over all angles ϕ or, equivalently, over all t_i . This yields

$$W_i = \Gamma_0 \sqrt{2\pi} \frac{\Delta}{\omega}. \quad (\text{A.25})$$

This equation can be used to obtain the ionization rate Γ_0 from the total ionization signal or from the depletion

of the ground state $W_{\text{Loss}} \simeq W_i$ (in all our numerical simulations these quantities differ by less than 1%):

$$\Gamma_0 = \frac{W_{\text{Loss}}}{\sqrt{2\pi}} \frac{\omega}{\Delta}, \quad (\text{A.26})$$

Thus, numerically finding the depletion of the ground state and the angular width of the photoelectron distribution, we have all the quantities necessary to obtain the negative ionization times due to ground state depletion:

$$\omega t_i = -W_g(0)W_{\text{Loss}} \frac{\Delta}{\sqrt{2\pi}}. \quad (\text{A.27})$$

The equation above was used to obtain the depletion-

corrected ionization times in Fig. 5 (c) of the main text (red circles). We have used $W_g(0) = 1$, which provides an upper bound for the effect: at the highest intensity shown, substituting $W_g(0) = 1$ leads to an error below 0.25° (at lower intensities, the error is considerably less). The same equation can also be used to correct the ARM offset angles as shown in Fig. 3 (orange squares) of the main text. Figure 5 (c) of the main text indicates that although depletion is indeed partially responsible for the appearance of negative times, it cannot explain them fully. This suggests that there could be additional effects at play. These effects, and the corresponding numerical tests, are discussed in the Supplementary Information (available online).

Part III

CONCLUSIONS

5

CONCLUSIONS AND THE FUTURE

As we have seen, the analytical R-matrix approach provides us with a new theoretical framework for studying the electron dynamics induced when an atom or molecule is subjected to a strong low frequency laser field. In this thesis, we have introduced the basic formalism of ARM, verified its accuracy and started to investigate some of its capabilities.

At this stage, it is reasonable to ask what we have gained as a result. How does ARM compare to other approaches to strong field ionization and what advantages does it offer? To answer these questions, it is natural to return to the criteria (C1-C6) we set out in Section 3.6. Upon doing so, we find that ARM performs very well indeed.

- C₁ Like the SFA, the basic equations of ARM are derived from first principles, starting directly from the Schrödinger equation. No assumptions are made about the mechanism by which ionization proceeds and the boundary matching procedure leaves no room for ambiguity or free parameters. This gives ARM a considerable advantage over two-step models of ionization and the CCSFA.
- C₂ Like the CCSFA and the SFA before it, and in contrast to the two-step approach, ARM is a fully quantum theory (as far as the electron is concerned) and as such is naturally able to account for interference effects. Although our analysis has so far neglected this by considering only a single saddlepoint for any given \mathbf{p} , the interference of different trajectories can readily be incorporated if we coherently sum over all solutions $t_s^\alpha(\mathbf{p})$.
- C₃ Within the strong field regime, we find that ARM is accurate across a broad range of parameters. Its domain of applicability can be estimated by recalling the key approximations we have made. First, the matching of inner and outer region solutions requires that the field strength is sufficiently small compared to the atomic field and, second, the saddlepoint method demands that the phase of our integrand over t' is sufficiently large. Both of these requirements are shared by the SFA (when evaluated via saddlepoint) and the CCSFA. Importantly, in contrast to two-step models, ARM at no point assumes quasistatic tunnelling. As a result, it is able to fully account for non-adiabatic effects and faces no restriction to the $\gamma \ll 1$ tunnelling limit.
- C₄ As in the SFA, in ARM we again encounter an integral over a time t' that can be thought of as the time of ionization and a

phase that can be identified as a classical action. As a result, the PPT argument that made it possible to interpret the SFA in terms of the tunnelling picture is equally well motivated in this case. In the context of the attoclock experiment, we have already seen how much we can gain as a result. While fully numerical calculations can inherently tell us only about photo-electron spectra, the interpretation of the saddlepoint solution in ARM makes it possible to probe the underlying physics directly. It was this that allowed us to reconstruct the time of ionization – the quantity that the experiment ultimately set out to measure. In addition to this, the PPT interpretation enables us to directly assess some of the assumptions typically made by two-step models, which – in contrast to ARM – rely on the tunnelling picture from their outset.

- C5** The ability to account for the interaction between the outgoing electron and the core in a rigorous, unambiguous way is one of the most important advances of the ARM theory and the one on which we have focussed most in this thesis. As comparisons with numerical calculations in both [D] and [E] have shown, the Coulomb correction term ensures that the ARM theory is quantitatively accurate and represents a marked improvement over the SFA. In this regard, ARM has a lot in common with the CCSFA; indeed, the Coulomb corrections in both theories are of a very similar form. However, in ARM it comes with a crucial difference: the trajectories along which the correction is evaluated have an imaginary component not only under the barrier, but in the continuum as well. This fact stems directly from the boundary matching argument and, as we have seen, gives rise to real physical consequences.
- C6** Finally, we have shown how the ARM theory can be extended to multielectron systems and used to describe ionic excitations induced by the outgoing electron. The ability to go beyond the single active electron approximation in this way sets ARM apart from all other analytic theories we have considered in this thesis. Such correlation-driven dynamics are highly interesting from the perspective of attosecond science and our preliminary results indicate that they could indeed play a role in the strong field ionization of molecules.

It is clear, of course, that in this thesis we have only just begun to explore the capabilities of the ARM theory. In practical terms, much of our work has focussed on the simplest possible scenario: the ionization of the hydrogen atom by a circularly polarized pulse. In this instance there are no multielectron effects to account for, our initial ground state is spherically symmetric and we do not have to worry about recollisions or subcycle interference effects. Even in this most

basic case – and in the context of the attoclock experiment in particular – the ARM approach has already yielded a great deal of interesting physics. However, given its scope and flexibility, it is apparent that ARM can offer us a lot more.

One of the most pressing issues to look into is recollisions. What happens in instances when the electron returns to its parent ion? As we have seen, such processes are responsible for an assortment of important phenomena, including high harmonic generation, the high energy plateau in photoelectron spectra and non-sequential double ionization. Applying ARM to such cases is clearly an intriguing prospect, and vital if we are to achieve a complete description of strong field physics.

Besides this, there is undoubtedly much to be done in developing the work on multielectron dynamics and ionic excitations beyond the single active electron approximation. In the context of the attoclock, preliminary numerical calculations in [E] have already shown how multielectron interactions can manifest themselves in photoelectron spectra. Investigating the mechanism responsible for the observed effects would certainly be a fascinating avenue to explore. On the other hand, given that it was high harmonic spectroscopy that provided much of the original impetus for studying correlation-driven excitations, it would be natural to examine how excitations of this sort might imprint themselves upon HHG spectra.

As experimental techniques develop – yielding results with ever higher resolution and making it possible access new physical phenomena – it is vital that theoretical approaches develop with them. Given its fully quantum nature and lack of free parameters, its intuitive physical interpretation, its accuracy well into the non-adiabatic regime and its ability to be extended and refined in various ways, the ARM theory is very well positioned to fulfil this role and to serve as a powerful tool for attosecond science.

Part IV
APPENDIX

A

ATOMIC UNITS

Throughout this thesis we work in atomic units (a.u.), as defined in Section 1.2.1: $m_e = 1$, $e^2 = 1$, $\hbar = 1$, $k_c = 1/(4\pi\epsilon_0) = 1$. The relationship between atomic and S.I. units is summarized in Table 1 below. Note that, based on this, it is easy to check that the speed of light is given by $c = 1/\alpha \approx 137$, where α is the fine structure constant.

Table 1: Atomic Units

Quantity	Unit	Physical Significance	Value in SI Units
Mass	m_e	Mass of an electron	9.10938×10^{-31} kg
Charge	e	Charge of an electron	1.60218×10^{-19} C
Angular momentum	\hbar	Planck's constant divided by 2π	1.05457×10^{-34} J s
Length	$\hbar^2/(m_e k_c e^2)$	Bohr radius	5.29177×10^{-11} m
Velocity	$e^2 k_c / \hbar$	Velocity of electron in first Bohr orbit	2.18769×10^6 m/s
Time	$\hbar^3 / (m_e k_c^2 e^4)$	Time electron in first Bohr orbit would take to travel one Bohr radius	2.41888×10^{-17} s
Energy	$m_e e^4 k_c^2 / \hbar^2$	Twice the ionization potential of the hydrogen atom	4.35974×10^{-18} J
Electric field strength	$m_e^2 k_c^3 e^5 / \hbar^4$	Field experienced by electron in first Bohr orbit	5.14221×10^{11} V/m

BIBLIOGRAPHY

- [1] P. Agostini and L. F. DiMauro, The physics of attosecond light pulses, *Reports Prog. Phys.* **67**, 813–855 (2004).
- [2] J. Itatani, J. Levesque, D. Zeidler, H. Niikura, H. Pépin, J. C. Kieffer, P. B. Corkum, and D. M. Villeneuve, Tomographic imaging of molecular orbitals, *Nature* **432**, 867–871 (2004).
- [3] O. Smirnova, Y. Mairesse, S. Patchkovskii, N. Dudovich, D. Villeneuve, P. Corkum, and M. Y. Ivanov, High harmonic interferometry of multi-electron dynamics in molecules, *Nature* **460**, 972–977 (2009).
- [4] Y. Mairesse, J. Higuet, N. Dudovich, D. Shafir, B. Fabre, E. Mével, E. Constant, S. Patchkovskii, Z. B. Walters, M. Y. Ivanov, and O. Smirnova, High Harmonic Spectroscopy of Multichannel Dynamics in Strong-Field Ionization, *Phys. Rev. Lett.* **104**, 213601 (2010).
- [5] S. Haessler, J. Caillat, W. Boutu, C. Giovanetti-Teixeira, T. Ruchon, T. Auguste, Z. Diveki, P. Breger, A. Maquet, B. Carré, R. Taïeb, and P. Salières, Attosecond imaging of molecular electronic wavepackets, *Nat. Phys.* **6**, 200–206 (2010).
- [6] S. Haessler, J. Caillat, and P. Salières, Self-probing of molecules with high harmonic generation, *J. Phys. B At. Mol. Opt. Phys.* **44**, 203001 (2011).
- [7] E. Goulielmakis, Z.-H. Loh, A. Wirth, R. Santra, N. Rohringer, V. S. Yakovlev, S. Zherebtsov, T. Pfeifer, A. M. Azzeer, M. F. Kling, S. R. Leone, and F. Krausz, Real-time observation of valence electron motion, *Nature* **466**, 739–743 (2010).
- [8] M. Spanner, O. Smirnova, P. B. Corkum, and M. Y. Ivanov, Reading diffraction images in strong field ionization of diatomic molecules, *J. Phys. B At. Mol. Opt. Phys.* **37**, L243–L250 (2004).
- [9] M. Meckel, D. Comtois, D. Zeidler, A. Staudte, D. Pavičić, H. C. Bandulet, H. Pépin, J. C. Kieffer, R. Dörner, D. M. Villeneuve, and P. B. Corkum, Laser-Induced Electron Tunneling and Diffraction, *Science* **320**, 1478–1482 (2008).
- [10] C. I. Blaga, J. Xu, A. D. DiChiara, E. Sistrunk, K. Zhang, P. Agostini, T. a. Miller, L. F. DiMauro, and C. D. Lin, Imaging ultrafast molecular dynamics with laser-induced electron diffraction, *Nature* **483**, 194–197 (2012).

- [11] Y. Huismans, A. Rouzée, A. Gijsbertsen, J. H. Jungmann, A. S. Smolkowska, P. S. W. M. Logman, F. Lépine, C. Cauchy, S. Zamith, T. Marchenko, J. M. Bakker, G. Berden, B. Redlich, a. F. G. van der Meer, H. G. Muller, W. Vermin, K. J. Schafer, M. Spanner, M. Y. Ivanov, O. Smirnova, D. Bauer, S. V. Popruzhenko, and M. J. J. Vrakking, Time-resolved holography with photoelectrons, *Science* **331**, 61–64 (2011).
- [12] P. Eckle, A. N. Pfeiffer, C. Cirelli, and A. Staudte, Attosecond ionization and tunneling delay time measurements in helium, *Science* **322**, 1525–1529 (2008).
- [13] P. Eckle, M. Smolarski, P. Schlup, J. Biegert, A. Staudte, M. Schöffler, H. G. Muller, R. Dörner, and U. Keller, Attosecond angular streaking, *Nat. Phys.* **4**, 565–570 (2008).
- [14] A. N. Pfeiffer, C. Cirelli, M. Smolarski, D. Dimitrovski, M. Abu-samha, L. B. Madsen, and U. Keller, Attoclock reveals natural coordinates of the laser-induced tunnelling current flow in atoms, *Nat. Phys.* **8**, 76–80 (2012).
- [15] G. S. Voronov and N. B. Delone, Ionization of the xenon atom by the electric field of ruby laser emission, *JETP Lett.* **1**(2), 66 (1965).
- [16] P. Agostini, F. Fabre, G. Mainfray, G. Petite, and N. K. Rahman, Free-free transitions following six-photon ionization of xenon atoms, *Phys. Rev. Lett.* **42**(17), 1127–1130 (1979).
- [17] P. Agostini, M. Clement, F. Fabre, and G. Petite, Multiphoton ionisation involving multiphoton continuum-continuum transitions, *J. Phys. B At. Mol. Phys.* **14**, L491–L495 (1981).
- [18] P. Kruit, J. Kimman, and M. J. Van der Wiel, Absorption of additional photons in the multiphoton ionisation continuum of xenon at 1064, 532 and 440 nm, *J. Phys. B At. Mol. Phys.* **14**, L597–L602 (1981).
- [19] P. Agostini and G. Petite, Photoelectric effect under strong irradiation, *Contemp. Phys.* **29**(1), 57–77 (1988).
- [20] Y. Gontier, M. Poirier, and M. Trahin, Multiphoton absorptions above the ionisation threshold, *J. Phys. B At. Mol. Phys.* **13**, 1381–1387 (1980).
- [21] G. G. Paulus, W. Nicklich, and H. Xu, Plateau in above threshold ionization spectra, *Phys. Rev. Lett.* **72**(18), 2851–2854 (1994).
- [22] M. J. Nandor, M. A. Walker, and L. D. Van Woerkom, Angular distributions of high-intensity ATI and the onset of the plateau, *J. Phys. B At. Mol. Opt. Phys.* **31**, 4617–4629 (1998).

- [23] B. Yang, K. Schafer, B. Walker, K. Kulander, P. Agostini, and L. DiMauro, Intensity-dependent scattering rings in high order above-threshold ionization, *Phys. Rev. Lett.* **71**(23), 3770–3773 (1993).
- [24] P. H. Bucksbaum, M. Bashkansky, R. R. Freeman, T. J. McIlrath, and L. F. Dimauro, Suppression of multiphoton ionization with circularly polarized coherent light, *Phys. Rev. Lett.* **56**(24), 2590–2593 (1986).
- [25] U. Mohideen, M. H. Sher, H. W. K. Tom, G. D. Aumiller, O. R. Wood II, R. R. Freeman, J. Bokor, and P. H. Bucksbaum, High Intensity Above-Threshold Ionization of He, *Phys. Rev. Lett.* **71**(4), 509–512 (1993).
- [26] M. Bashkansky, P. H. Bucksbaum, and D. W. Schumacher, Above-Threshold Ionization with Elliptically Polarized Light, *Phys. Rev. Lett.* **59**(3), 274–277 (1987).
- [27] X. F. Li, A. L’Huillier, M. Ferray, L. A. Lompré, and G. Mainfray, Multiple-harmonic generation in rare gases at high laser intensity, *Phys. Rev. A* **39**(11), 5751–5761 (1989).
- [28] A. L’Huillier and P. Balcou, High-order harmonic generation in rare gases with a 1-ps 1053-nm laser, *Phys. Rev. Lett.* **70**(6), 774–777 (1993).
- [29] J. J. Macklin, J. D. Kmetec, and C. L. Gordon, High-order harmonic generation using intense femtosecond pulses, *Phys. Rev. Lett.* **70**(6), 766–769 (1993).
- [30] J. Krause, K. Schafer, and K. Kulander, High-order harmonic generation from atoms and ions in the high intensity regime, *Phys. Rev. Lett.* **68**(24), 3535–3538 (1992).
- [31] W. Zernik and R. W. Klopfenstein, Two-Photon Ionization of Atomic Hydrogen. II, *J. Math. Phys.* **6**(2), 262–270 (1965).
- [32] K. J. Schafer, B. Yang, L. F. Dimauro, and K. C. Kulander, Above threshold ionization beyond the high harmonic cutoff, *Phys. Rev. Lett.* **70**(11), 1599–1602 (1993).
- [33] M. Protopapas, C. H. Keitel, and P. L. Knight, Atomic physics with super-high intensity lasers, *Reports Prog. Phys.* **60**, 389–486 (1997).
- [34] N. B. Delone and V. P. Krainov, *Atoms in Strong Light Fields*, Springer-Verlag, Berlin Heidelberg, 1985.
- [35] C. J. Joachain, N. J. Kylstra, and R. M. Potvliege, *Atoms in Intense Laser Fields*, Cambridge University Press, Cambridge, 2012.

BIBLIOGRAPHY

- [36] A. L'Huillier, L. A. Lompre, G. Mainfray, and C. Manus, Multiply charged ions induced by multiphoton absorption in rare gases at 0.53 um, *Phys. Rev. A* **27**(5), 2503–2512 (1983).
- [37] D. N. Fittinghoff, P. R. Bolton, B. Chang, and K. C. Kulander, Observation of nonsequential double ionization of helium with optical tunneling, *Phys. Rev. Lett.* **69**(18), 2642–2645 (1992).
- [38] B. Walker, E. Mevel, B. Yang, P. Breger, J. P. Chambaret, A. Antonetti, L. F. Dimauro, and P. Agostini, Double ionization in the perturbative and tunneling regimes, *Phys. Rev. A* **48**(2), R894–R897 (1993).
- [39] I. Litvinyuk, F. Légaré, P. Dooley, D. Villeneuve, P. B. Corkum, J. Zanghellini, A. Pegarkov, C. Fabian, and T. Brabec, Shakeup Excitation during Optical Tunnel Ionization, *Phys. Rev. Lett.* **94**, 033003 (2005).
- [40] P. B. Corkum, Plasma perspective on strong field multiphoton ionization, *Phys. Rev. Lett.* **71**(13), 1994–1997 (1993).
- [41] P. Dietrich, N. H. Burnett, M. Ivanov, and P. B. Corkum, High-harmonic generation and correlated two-electron multiphoton ionization with elliptically polarized light, *Phys. Rev. A* **50**(5), 3585–3588 (1994).
- [42] R. Moshammer, B. Feuerstein, W. Schmitt, A. Dorn, C. Schröter, J. Ullrich, H. Rottke, C. Trump, M. Wittmann, G. Korn, K. Hoffmann, and W. Sandner, Momentum Distributions of Ne+ Ions Created by an Intense Ultrashort Laser Pulse, *Phys. Rev. Lett.* **84**(3), 447–450 (2000).
- [43] B. Feuerstein, R. Moshammer, D. Fischer, A. Dorn, C. D. Schröter, J. Deipenwisch, J. R. Crespo Lopez-Urrutia, C. Höhr, P. Neumayer, J. Ullrich, H. Rottke, C. Trump, M. Wittmann, G. Korn, and W. Sandner, Separation of recollision mechanisms in nonsequential strong field double ionization of Ar: the role of excitation tunneling, *Phys. Rev. Lett.* **87**(4), 043003 (2001).
- [44] M. Weckenbrock, D. Zeidler, A. Staudte, T. Weber, M. Schöffler, M. Meckel, S. Kammer, M. Smolarski, O. Jagutzki, V. R. Bhardwaj, D. M. Rayner, D. M. Villeneuve, P. B. Corkum, and R. Dörner, Fully differential rates for femtosecond multiphoton double ionization of neon, *Phys. Rev. Lett.* **92**(21), 213002 (2004).
- [45] A. N. Pfeiffer, C. Cirelli, M. Smolarski, R. Dörner, and U. Keller, Timing the release in sequential double ionization, *Nat. Phys.* **7**, 428–433 (2011).

- [46] A. N. Pfeiffer, C. Cirelli, M. Smolarski, X. Wang, J. H. Eberly, R. Dörner, and U. Keller, Breakdown of the independent electron approximation in sequential double ionization, *New J. Phys.* **13**, 093008 (2011).
- [47] H. Akagi, T. Otobe, A. Staudte, A. Shiner, F. Turner, R. Dörner, D. M. Villeneuve, and P. B. Corkum, Laser tunnel ionization from multiple orbitals in HCl, *Science* **325**, 1364–1367 (2009).
- [48] D. M. Wolkow, Über eine Klasse von Lösungen der Diracschen Gleichung, *Zeitschrift für Phys.* **94**(3-4), 250–260 (1935).
- [49] K. J. Schafer, Numerical Methods in Strong Field Physics, in *Strong F. Laser Phys.*, edited by T. Brabec, pages 111–147, Springer, New York, 2008.
- [50] T. F. Gallagher, Above-threshold ionization in low-frequency limit, *Phys. Rev. Lett.* **61**(20), 2304–2307 (1988).
- [51] P. B. Corkum, N. H. Burnett, and F. Brunel, Above-threshold ionization in the long-wavelength limit, *Phys. Rev. Lett.* **62**(11), 1259–1262 (1989).
- [52] K. C. Kulander, K. J. Schafer, and J. L. Krause, Dynamics of short-pulse excitation, ionization and harmonic conversion, in *Super-Intense Laser-Atom Phys.*, pages 95–110, 1993.
- [53] L. V. Keldysh, Ionization in the field of a strong electromagnetic wave, *Sov. Phys. JETP* **20**(5), 1307–1314 (1965).
- [54] M. V. Ammosov, N. B. Delone, and V. P. Krainov, Tunnel ionization of complex atoms and of atomic ions in an alternating electromagnetic field, *Sov. Phys. JETP* **64**, 1191 (1986).
- [55] A. M. Perelomov, V. S. Popov, and M. V. Terent'ev, Ionization of Atoms in an alternating electric field, *Sov. Phys. JETP* **23**(5), 924–934 (1966).
- [56] X. M. Tong, Z. X. Zhao, and C. D. Lin, Theory of molecular tunneling ionization, *Phys. Rev. A* **66**, 033402 (2002).
- [57] X. M. Tong and C. D. Lin, Empirical formula for static field ionization rates of atoms and molecules by lasers in the barrier-suppression regime, *J. Phys. B At. Mol. Opt. Phys.* **38**, 2593–2600 (2005).
- [58] B. Walker, B. Sheehy, K. Kulander, and L. DiMauro, Elastic Rescattering in the Strong Field Tunneling Limit, *Phys. Rev. Lett.* **77**(25), 5031–5034 (1996).

BIBLIOGRAPHY

- [59] G. G. Paulus, W. Becker, W. Nicklich, and H. Walther, Rescattering effects in above-threshold ionization: a classical model, *J. Phys. B At. Mol. Opt. Phys.* **27**(21), L703–L708 (1994).
- [60] T. Brabec, M. Ivanov, and P. Corkum, Coulomb focusing in intense field atomic processes, *Phys. Rev. A* **54**(4), R2551–R2554 (1996).
- [61] G. L. Yudin and M. Y. Ivanov, Physics of correlated double ionization of atoms in intense laser fields: Quasistatic tunneling limit, *Phys. Rev. A* **63**, 033404 (2001).
- [62] D. Comtois, D. Zeidler, H. Pépin, J. C. Kieffer, D. M. Villeneuve, and P. B. Corkum, Observation of Coulomb focusing in tunneling ionization of noble gases, *J. Phys. B At. Mol. Opt. Phys.* **38**, 1923–1933 (2005).
- [63] T. Nubbemeyer, K. Gorling, A. Saenz, U. Eichmann, and W. Sandner, Strong-field Tunneling without Ionization, *Phys. Rev. Lett.* **101**, 233001 (2008).
- [64] C. Lemell, K. I. Dimitriou, X. M. Tong, S. Nagele, D. V. Kartashov, J. Burgdörfer, and S. Gräfe, Low-energy peak structure in strong-field ionization by midinfrared laser pulses: Two-dimensional focusing by the atomic potential, *Phys. Rev. A* **85**, 011403 (2012).
- [65] C. Liu and K. Hatsagortsyan, Origin of Unexpected Low Energy Structure in Photoelectron Spectra Induced by Midinfrared Strong Laser Fields, *Phys. Rev. Lett.* **105**, 113003 (2010).
- [66] J. Cohen, Reexamination of over-the-barrier and tunneling ionization of the hydrogen atom in an intense field, *Phys. Rev. A* **64**, 043412 (2001).
- [67] K. I. Dimitriou, D. G. Arbó, S. Yoshida, E. Persson, and J. Burgdörfer, Origin of the double-peak structure in the momentum distribution of ionization of hydrogen atoms driven by strong laser fields, *Phys. Rev. A* **70**, 061401 (2004).
- [68] N. I. Shvetsov-Shilovski, D. Dimitrovski, and L. B. Madsen, Ionization in elliptically polarized pulses: Multielectron polarization effects and asymmetry of photoelectron momentum distributions, *Phys. Rev. A* **85**, 023428 (2012).
- [69] A. N. Pfeiffer, C. Cirelli, A. Landsman, M. Smolarski, D. Dimitrovski, L. Madsen, and U. Keller, Probing the Longitudinal Momentum Spread of the Electron Wave Packet at the Tunnel Exit, *Phys. Rev. Lett.* **109**, 083002 (2012).

- [70] N. I. Shvetsov-Shilovski, D. Dimitrovski, and L. B. Madsen, Ehrenfest's theorem and the validity of the two-step model for strong-field ionization, *Phys. Rev. A* **87**, 013427 (2013).
- [71] N. B. Delone and V. P. Krainov, Energy and angular electron spectra for the tunnel ionization of atoms by strong low-frequency radiation, *J. Opt. Soc. Am. B* **8**(6), 1207–1211 (1991).
- [72] L. Arissian, C. Smeenk, F. Turner, C. Trallero, A. Sokolov, D. Villeneuve, A. Staudte, and P. B. Corkum, Direct Test of Laser Tunneling with Electron Momentum Imaging, *Phys. Rev. Lett.* **105**, 133002 (2010).
- [73] M. Y. Ivanov, M. Spanner, and O. Smirnova, Anatomy of strong field ionization, *J. Mod. Opt.* **52**(2-3), 165–184 (2005).
- [74] A. Rudenko, K. Zrost, T. Ergler, A. B. Voitkiv, B. Najjari, V. L. B. de Jesus, B. Feuerstein, C. D. Schröter, R. Moshammer, and J. Ullrich, Coulomb singularity in the transverse momentum distribution for strong-field single ionization, *J. Phys. B At. Mol. Opt. Phys.* **38**, L191–L198 (2005).
- [75] A. M. Perelomov, V. S. Popov, and M. V. Terent'ev, Ionization of atoms in an alternating electric field: II, *Sov. Phys. JETP* **24**(1), 207–217 (1967).
- [76] F. H. M. Faisal, Multiple absorption of laser photons by atoms, *J. Phys. B At. Mol. Phys.* **6**, L89–L92 (1973).
- [77] H. R. Reiss, Effect of an intense electromagnetic field on a weakly bound system, *Phys. Rev. A* **22**(5), 1786–1813 (1980).
- [78] S. V. Popruzhenko, Keldysh theory of strong field ionization: history, applications, difficulties and perspectives, *J. Phys. B At. Mol. Opt. Phys.* **47**, 204001 (2014).
- [79] G. F. Gribakin and M. Y. Kuchiev, Multiphoton detachment of electrons from negative ions, *Phys. Rev. A* **55**(5), 3760–3771 (1997).
- [80] G. Paulus, F. Zacher, H. Walther, a. Lohr, W. Becker, and M. Kleber, Above-Threshold Ionization by an Elliptically Polarized Field: Quantum Tunneling Interferences and Classical Dodging, *Phys. Rev. Lett.* **80**(3), 484–487 (1998).
- [81] A. Lohr, M. Kleber, R. Kopold, and W. Becker, Above-threshold ionization in the tunneling regime, *Phys. Rev. A* **55**(6), R4003–R4006 (1997).
- [82] D. Milošević and F. Ehlotzky, Influence of screening of the Coulomb potential on the plateau in above-threshold ionization, *Phys. Rev. A* **57**(6), 5002–5005 (1998).

BIBLIOGRAPHY

- [83] D. Milošević, A. Gazibegović-Busuladžić, and W. Becker, Direct and rescattered electrons in above-threshold detachment from negative ions, *Phys. Rev. A* **68**, 050702 (2003).
- [84] M. Lewenstein, P. Balcou, M. Y. Ivanov, A. L'Huillier, and P. B. Corkum, Theory of high-harmonic generation by low-frequency laser fields, *Phys. Rev. A* **49**(3), 2117–2132 (1994).
- [85] M. Lewenstein, K. C. Kulander, K. J. Schafer, and P. H. Bucksbaum, Rings in above-threshold ionization: A quasiclassical analysis, *Phys. Rev. A* **51**(2), 1495–1507 (1995).
- [86] W. Becker, F. Grasbon, R. Kopold, D. B. Milosevic, G. G. Paulus, and H. Walther, Above-threshold ionization: from classical features to quantum effects, *Adv. At. Mol. Opt. Phys.* **48**, 35–98 (2002).
- [87] O. Smirnova and M. Y. Ivanov, Multielectron High Harmonic Generation: simple man on a complex plane, arXiv:1304.2413 (2013).
- [88] W. Becker, J. K. McIver, and M. Confer, Total multiphoton-ionization rates for an extremely short-ranged potential, *Phys. Rev. A* **40**(12), 6904–6912 (1989).
- [89] M. Dörr, R. M. Potvliege, D. Proulx, and R. Shakeshaft, Multi-photon detachment of H- and the applicability of the Keldysh approximation, *Phys. Rev. A* **42**(7), 4138–4150 (1990).
- [90] D. B. Gazibegović-Busuladžić, A. Milošević, W. Becker, B. Bergues, H. Hultgren, and I. Y. Kiyan, Electron rescattering in above-threshold photodetachment of negative ions, *Phys. Rev. Lett.* **104**, 103004 (2010).
- [91] M. V. Frolov, N. L. Manakov, E. A. Pronin, and A. F. Starace, Model-independent quantum approach for intense laser detachment of a weakly bound electron., *Phys. Rev. Lett.* **91**(5), 053003 (2003).
- [92] D. Bauer, D. Milošević, and W. Becker, Strong-field approximation for intense-laser-atom processes: The choice of gauge, *Phys. Rev. A* **72**, 023415 (2005).
- [93] B. Bergues, Z. Ansari, D. Hanstorp, and I. Y. Kiyan, Photodetachment in a strong laser field: An experimental test of Keldysh-like theories, *Phys. Rev. A* **75**, 063415 (2007).
- [94] H. R. Reiss, Spectrum of atomic electrons ionised by an intense field, *J. Phys. B At. Mol. Phys.* **20**, L79–L83 (1987).

- [95] L. Guo, S. S. Han, X. Liu, Y. Cheng, Z. Z. Xu, J. Fan, J. Chen, S. G. Chen, W. Becker, C. I. Blaga, A. D. Dichiara, E. Sistrunk, P. Agostini, and L. F. Dimauro, Scaling of the low-energy structure in above-threshold ionization in the tunneling regime: Theory and experiment, *Phys. Rev. Lett.* **110**, 013001 (2013).
- [96] A. M. Perelomov and V. S. Popov, Ionization of atoms in an alternating electrical field: III, *Sov. Phys. JETP* **25**(2), 336–343 (1967).
- [97] D. Bauer, D. B. Milošević, and W. Becker, On the validity of the strong field approximation and simple man's theory, *J. Mod. Opt.* **53**(1-2), 135–147 (2006).
- [98] D. G. Arbó, J. E. Miraglia, M. S. Gravielle, K. Schiessl, E. Persson, and J. Burgdörfer, Coulomb-Volkov approximation for near-threshold ionization by short laser pulses, *Phys. Rev. A* **77**, 013401 (2008).
- [99] M. Bashkansky, P. H. Bucksbaum, and D. W. Schumacher, Asymmetries in above-threshold ionization, *Phys. Rev. Lett.* **60**(24), 2458–2461 (1988).
- [100] I. Barth and O. Smirnova, Nonadiabatic tunneling in circularly polarized laser fields: Physical picture and calculations, *Phys. Rev. A* **84**, 063415 (2011).
- [101] S. V. Popruzhenko and D. Bauer, Strong field approximation for systems with Coulomb interaction, *J. Mod. Opt.* **55**(16), 2573–2589 (2008).
- [102] S. V. Popruzhenko, V. D. Mur, V. S. Popov, and D. Bauer, Strong Field Ionization Rate for Arbitrary Laser Frequencies, *Phys. Rev. Lett.* **101**, 193003 (2008).
- [103] S. V. Popruzhenko, V. D. Mur, V. S. Popov, and D. Bauer, Multiphoton ionization of atoms and ions by high-intensity X-ray lasers, *J. Exp. Theor. Phys.* **108**(6), 947–962 (2009).
- [104] S. V. Popruzhenko, G. G. Paulus, and D. Bauer, Coulomb-corrected quantum trajectories in strong-field ionization, *Phys. Rev. A* **77**, 053409 (2008).
- [105] T.-M. Yan, S. V. Popruzhenko, M. J. J. Vrakking, and D. Bauer, Low-Energy Structures in Strong Field Ionization Revealed by Quantum Orbits, *Phys. Rev. Lett.* **105**, 253002 (2010).
- [106] T.-M. Yan and D. Bauer, Sub-barrier Coulomb effects on the interference pattern in tunneling-ionization photoelectron spectra, *Phys. Rev. A* **86**, 053403 (2012).

BIBLIOGRAPHY

- [107] M. Jain and N. Tzoar, Compton scattering in the presence of coherent electromagnetic radiation, *Phys. Rev. A* **18**(2), 538–545 (1978).
- [108] R. Shakeshaft and R. M. Potvliege, Approximate theory for multiphoton ionization of an atom by an intense field, *Phys. Rev. A* **36**(11), 5478–5481 (1987).
- [109] S. Basile, F. Trombetta, and G. Ferrante, Twofold symmetric angular distributions in multiphoton ionization with elliptically polarized light, *Phys. Rev. Lett.* **61**(21), 2435–2437 (1988).
- [110] A. Jaron, J. Z. Kaminski, and F. Ehlotzky, Asymmetries in the angular distributions of above threshold ionization in an elliptically polarized laser field, *Opt. Commun.* **163**, 115–121 (1999).
- [111] G. Duchateau, E. Cormier, H. Bachau, and R. Gayet, Coulomb-Volkov approach of atom ionization by intense and ultrashort laser pulses, *Phys. Rev. A* **63**, 053411 (2001).
- [112] D. G. Arbó, K. L. Ishikawa, K. Schiessl, E. Persson, and J. Burgdörfer, Diffraction at a time grating in above-threshold ionization: The influence of the Coulomb potential, *Phys. Rev. A* **82**, 043426 (2010).
- [113] A. S. Kornev and B. A. Zon, Testing of Coulomb-Volkov functions, *J. Phys. B At. Mol. Opt. Phys.* **35**, 2451–2458 (2002).
- [114] P. G. Burke, *R-Matrix Theory of Atomic Collisions*, Springer, 2011.
- [115] O. Smirnova, M. Spanner, and M. Ivanov, Analytical solutions for strong field-driven atomic and molecular one- and two-electron continua and applications to strong-field problems, *Phys. Rev. A* **77**, 033407 (2008).
- [116] J. Kaushal and O. Smirnova, Nonadiabatic Coulomb effects in strong-field ionization in circularly polarized laser fields, *Phys. Rev. A* **88**, 013421 (2013).